IACMI/R0011-2021/4.2

IACMI Project 4.2: Thermoplastic Composite Development for Wind Turbine Blades

Author: David Snowberg
Date: December 7, 2021

Final Technical Report
PA16-0349-4.2-01

Approved for Public Release.
Distribution is Unlimited.

The Institute for iacmi Advanced Composites Manufacturing Innovation
THE COMPOSITES INSTITUTE

U.S. DEPARTMENT OF ENERGY

IACMI Project 4.2: Thermoplastic Composite Development for Wind Turbine Blades

Principal Investigator:	David Snowberg
Organization:	NREL
Address:	15013 Denver West Parkway, Golden, CO 80401
Phone:	(303) 275-3000
Email:	david.snowberg@nrel.gov
Co-authors:	Derek Berry, Dana Swan, Zhang Mingfu, Steve Nolet, Douglas Adams, Johnathan Goodsell, Dayakar Penumadu, Aaron Stebner

Date Published: (December, 2021)

Prepared by:
Institute for Advanced Composites Manufacturing Innovation
Knoxville, TN 37932
Managed by Collaborative Composite Solutions, Inc.
For the
U.S. DEPARTMENT OF ENERGY
Under contract DE- EE0006926

Project Period:
(07/2015 to 12/2019)

Approved For Public Release

TABLE OF CONTENTS

1 LIST

1.1 LIST OF ACRONYMS & NOMENCLATURE

AMO	Advanced Manufacturing Office
°C	Degrees Celsius
CFRP	carbon fiber reinforced plastic
CLC	combined loading compression
CMSC	Composites Manufacturing and Simulation Center (at Purdue)
CoMET	Composites Manufacturing Education and Technology (at NREL)
cP	centipoise
DOE	Department of Energy
EERE	Energy Efficiency and Renewable Energy
FRP	fiberglass reinforced plastic
IACMI	Institute for Advanced Composites Manufacturing Innovation
IITRI	Illinois Institute of Technology Research Institute
ILSS	interlaminar shear strength
KoP	King of Prussia (Pennsylvania)
LASIR	Laboratory for Systems Integrity and Reliability (at Vanderbilt)
LCOE	levelized cost of energy
MHK	marine hydrokinetic
NDE	non-destructive evaluation
OEM	original equipment manufacturer
PAM-RTM (resin infusion modeling software by ESI Group)	
Pre-preg	pre-impregnated reinforced fabric
SCB	single cantilever beam
TE model	techno-economic model
VARTM	vacuum assisted resin transfer molding
Wind TA	Wind Technology Area

1.2 List of Figures

1.3 List of Tables

1.4 Acknowledgements

This material is based on work supported by the U.S. Department of Energy's (DOE's) Office of Energy Efficiency and Renewable Energy (EERE) under the support of Task 4.2 of the Institute for Advanced Composites Manufacturing Innovation (IACMI), Award Number DE-EE006926 managed by John Winkel from DOE and John Unser from IACMI. Academic and national laboratory partners for this project are Derek Berry and David Snowberg (NREL), Aaron Stebner (Colorado School of Mines), Nathan Sharpe and Drew Sommer (Purdue), Dayakar Penumadu and Stephen Young (University of Tennessee), and Douglas Adams (Vanderbilt). The industrial consortium for this project was led by Dana Swan (Arkema), Mingfu Zhang (Johns Manville), and Stephen Nolet (TPI Composites). The views and opinions of authors expressed in this paper or referenced documents do not necessarily state or reflect those of the U.S. government or the identified collaborating partners. Authors acknowledge that important insight and ideas were obtained from academic and industrial collaborators during the project activities who are not being formally acknowledged in this manuscript as co-authors. Materials supplied, and manufacturing methods developed by the industrial collaborators are gratefully acknowledged.

2. EXECUTIVE SUMMARY

(Section 5.1) Composites made from Arkema's Elium® thermoplastic resin and Johns Manville fiberglass were researched during this project for applications in wind blade manufacturing. A techno-economic model was developed to model this wind blade manufacturing process using these materials in place of traditional composites made with thermoset resin. This model was based on manufacturing a 61.5-meter wind blade, which showed a 4.7% reduction in wind blade cost as compared traditional thermoset materials. These cost savings were not from the thermoplastic material costing less than traditional thermoset materials, but rather from decreased capital costs, faster cycle times and reduced energy requirements and labor costs.

(Section 5.2) An infusion and curing model was developed for thermoplastic composite wind blades using PAM-RTM. The primary goal was to demonstrate the infusion simulation for the Elium® resin system on a 13-meter wind blade. Additionally, the exotherm temperature was predicted and compared to measurements, which showed model results within 10% of actual measurements.

(Section 5.3) Composite laminate panels and composite sandwich panels with a balsa core were produced; specimens were cut and characterized. Similar composite specimens were made with Elium® thermoplastic resin and Hexion thermoset epoxy (RIMR135/RIMH1366) to enable comparisons between these resin systems. The static test methods included: tensile, compression, in-plane shear, interlaminar shear, flexural, sandwich core shear flexure, and single cantilever beam tests for sandwich beams. Fatigue testing at room temperature was completed to composite laminate panels at a stress ratio of R=0.1 and R=10. In addition, fatigue testing to laminate panels was completed at -30°C, and at room temperature after conditioning specimens at 70°C and 90% relative humidity. Overall, mechanical test results from Elium® composites are similar to epoxy composites.

(Section 5.4) Elium composite panels were produced with intentional defects such as voids and nonwetting of fibers to begin to understand performance sensitivity to defects. A thermal digital image correlation (TDIC) method provides high spatial resolution strain field at elevated temperatures and can be used to identify defective regions within composite panels. Flexural modulus differences of 21% were seen between defect and non-defect panels. Other Elium® composite panels were forced to be defective by boiling the resin after infusion, which created voids throughout the composite laminate. X-ray computed tomography scanning was used to view the internal structure of the defect panels. Defect panels had a significant reduction in fatigue life as compared to baseline panels produced without intentional defects.

(Section 5.5) Lap shear specimens were fabricated to compare the lap shear strength of an off-the-shelf adhesive (Plexus MA590) and two new adhesives developed by Arkema (Bostik SAF30 90 and Bostik SAF30 120). ISO standard 4587:2003 was used to standardize the testing method and sample fabrication. Lap shear specimens were made at 1mm, 3mm, and 10mm thicknesses. The Bostik adhesive lap shear test results were similar to Plexus for all thicknesses.

(Section 5.6) Fiber-reinforced polymer (FRP) composites are typically used in high-performance applications (e.g., aerospace), and their expansion into high-volume industries (e.g. consumer automotive and wind turbine blade manufacturer or similar) is hindered by their cost and a lack of efficient manufacturing techniques. Monitoring the curing process of these composites during manufacturing can improve the efficiency of the process, and therefore reduce the manufacturing cost. Cure monitoring techniques were developed that use probabilistic estimation methods and surface temperature measurements made using infrared cameras. These techniques enable real-time monitoring of the infusion

process to locate manufacturing flaws, and they can, potentially, estimate residual stresses in the part. Their commercialization will help facilitate expansion of FRP composites in high-volume industries.

(Section 5.7) A 13-meter composite wind blade was produced with Elium® resin and Johns Manville fiberglass; this blade was made with VARTM processing similar to how megawatt-scale wind blades are currently manufactured, but no post-mold heating was used for this thermoplastic composite blade. The wind blade underwent full-scale validation for static loading (4-different load orientations) and flapwise fatigue loading to simulate 20-years of operational loads. The thermoplastic composite wind blade withstood the loading without any noted issues and performed similar to results from a previous full-scale validation to an equivalent epoxy composite wind blade produced with the same blade molds.

(Section 5.8) A study was conducted to determine the feasibility of recycling composite wind turbine blade components fabricated with glass fiber reinforced Elium® thermoplastic resin. Dissolution, which is a process unique to thermoplastic matrices, allows recovery of both the polymer matrix and full-length glass fibers, while maintaining their stiffness and strength throughout the recovery process. The economics of recycling is favorable if 50% of the glass fiber is recovered and resold for a process of $0.28/kg, and 90% of the resin is recovered and resold at a price of $2.50/kg.

(Section 10) Recommendations are outlined for commercializing thermoplastic resin for composite wind blade production, in addition to recommended areas for future research.

3. INTRODUCTION

The research undertaken in the execution of the IACMI Wind Technology Area Project 4.2, *Thermoplastic Composites Manufacturing*, focused on the innovative use of advanced thermoplastic resin systems in the design and manufacturing of utility scale wind turbine blades. As discussed further in Section 4 – Background – below, virtually all wind turbine blades produced for megawatt-sized wind turbines are currently manufactured using thermoset resin systems, usually epoxy, polyester or vinyl ester. Although thermoplastic resins have been in wide use in other industries for composite structures, the US and global wind industry has not made use of thermoplastics due primarily to the challenges of processing and material properties. Up to this point, thermoplastics never offered a suitable ‘drop-in’ solution to be used in conjunction with the prevailing vacuum assisted resin transfer molding (VARTM) infusion manufacturing methods favored by almost all wind blade producers.

The overarching goal of this project was to identify potential thermoplastic resin solutions for wind turbine blade design and production, down select the identified candidates based on several key factors – including comparison to baseline thermoset material properties, processability in traditional blade manufacturing environments, ability to lower overall blade cost, and potential for recyclability – develop a material property database through extensive coupon testing, validate resin processing at several scales, and finalize the effort with the production and full-scale structural validation of a 13 meter thermoplastic wind turbine blade. In addition to these main project goals, additional activities planned for the effort included the development of advanced non-destructive evaluation (NDE) of thermoplastic wind turbine blade manufacturing, innovative manufacturing models simulating the processing of thermoplastic resins in the blade production environment, and identifying unique opportunities for thermoplastic wind turbine blades – such as thermal welding, thermal forming, advanced repairs and recycling potential. All of these efforts will be presented in subsequent sections of this report.

As mentioned above, one of the challenging underlying problems with traditional thermoset resin wind

turbine blades lies primarily with the difficulty of solving end-of -life issues. It is with this challenge in mind that the IACMI 4.2 project was launched – to develop an alternative to traditional thermoset resin systems in the production of wind turbine blades thus enabling the potential to reuse, downcycle, recycle or upcycle blades after they have been decommissioned from service. As the overall circular economy for manufacturing has become a focus for industry globally and in the United States, and specifically the sustainability of the US wind industry has come to the forefront of wind turbine OEMs and wind blade manufacturers, the challenge of producing wind blades that do not end up in landfills at the end-of-life has become a higher research priority. However, in solving this challenge, the solution must be cost effective, serve to reduce levelized cost of energy (LCOE) for wind power, and potentially enable other wind turbine blade manufacturing advances. Therefore, the goals of this research sought to improve the design and production of utility scale wind turbine blades with the development and eventual deployment of a recyclable and cost-effective thermoplastic resin system to be adopted in the state-of-the-art blade manufacturing.

While the advances made in the research activities to advance thermoplastic resin systems for wind turbine blades have the potential to transform the sustainability of the US and global wind industry, these innovations could also be adopted by other established and nascent industries that utilize thermoset composites as a basis for structural components. For example, the marine hydrokinetic (MHK) industry has developed wave and tidal energy devices with composite structures primarily produced using thermoset resin systems. The adoption of thermoplastics in that growing global industry could further the impact of this research on sustainability, economic viability and the reduction of energy usage across several renewable energy fields. Furthermore, these advances could also impact non-renewable industries, such as marine, aerospace, automotive and infrastructure composites.

It has been recognized from the beginning of this research that the impact of the efforts will not be fully realized without a comprehensive commercialization plan to enable the adoption of promising innovative and viable technology across the wind industry as well as other composite industries. This plan, further presented in Section 7 of this report, begins with the integral involvement of the entire supply chain in the execution of the research for this project. This includes resin suppliers, fiberglass suppliers, wind turbine blade manufacturers and wind turbine OEMs – as well as other IACMI organizations such as national laboratories and universities. An important part of this approach is the development of a techno-economic model to determine the commercial viability of various resin system solutions. This model, populated by comprehensive empirical and analytical data from the research, will aid the project's industry partners in developing business models, making market decisions, and successfully deploying this new technology in the wind market as well as other composite markets.

4. BACKGROUND

Since the beginning of the global and US utility wind industry in the 1970's, thermoset composites have been the primary materials used in the design and production for wind turbine blades and other structural composites used for wind turbines. Although early wind turbine blade designs experimented with the use of other materials, such as aluminum, wood laminate and concrete, industry engineers quickly converged on composites - typically fiberglass reinforced plastics with the occasional use of carbon fiber – as a solution for large, high cycle and high strain structures. Fiberglass and carbon reinforced thermosets provided a relatively lightweight and directional material that enabled the continued growth in the length of wind turbine blades as wind turbines were scaled to increase energy production and reduce LCOE. It is this environment of thermoset resin systems - including polyesters, vinyl esters and epoxies – used as the predominate matrix in the vast majority of utility scale wind turbine blades for most of the history of the wind industry, that existed when wind turbine OEMs and blade manufacturers began to seriously consider

the sustainability of blade materials and manufacturing in the mid 2010's.

While the use of thermoset resin systems for megawatt scale wind turbine blades has remained fairly constant for almost fifty years, the method of production for blades has evolved over time. Having emerged primarily from marine composite manufacturing, early wind turbine blade production was most often accomplished with an open molding 'hand-layup' process – wetting out fiberglass fabric and placing the saturated laminates into wind turbine blade tooling. However, with the need for improved laminate properties, increased reliability in the field, reduced volatile emissions in the factory, and better working conditions for workers, the wind blade industry looked to more advanced methods for blade production. While a small percentage of manufacturers turned to out-of-autoclave, room-temperature-cure pre-preg systems, most developed or adopted some version of vacuum assisted resin transfer molding – or VARTM. This allowed the wind industry to continue to scale turbine technology with the associated increase in the length and mass of blades. This advanced process continued to use thermoset resin systems as the base matrix for the structural composite wind blades. The most common thermoset resin used in the design and production of blades is epoxy, which requires the addition of heat – usually through the use of heated molds – during the initial resin curing phase. In addition, in order to realize maximum material properties, thermoset epoxy blades require a heated post cure cycle – typically through an extended period of elevated temperature soak in an oven that is able to fit the entire blade inside.

It is with this history and environment that wind turbine OEMs and blade producers began research efforts into developing advanced materials for wind blade design and production that could enable the recycling of blades at the end of service life. As mentioned above, thermoset resin blades are currently difficult to recycle and therefore have often been disposed of in landfills. While some effort has been focused on the reuse or recycling of thermoset composites, this IACMI project and a few other efforts around the world have begun to explore the use of thermoplastic resin systems in wind turbine blades as a way to augment recyclability and increase sustainability of the global wind industry. Due to the rapid growth of the wind industry since the early 2000's, the amount of composite waste that will be generated by the decommissioning of wind turbines will increase significantly over the next several decades. One study by Pu Liu and Claire Y. Barlow at the University of Cambridge, entitled "Wind turbine blade waste in 2050" and published in *Waste Management* in February 2017, estimated that composite waste generated by end-of-life wind turbine blades will exceed 50 million metric tons by the year 2050. The yearly estimates of wind blade composite waste broken down by geographic region is shown in Figure 1.

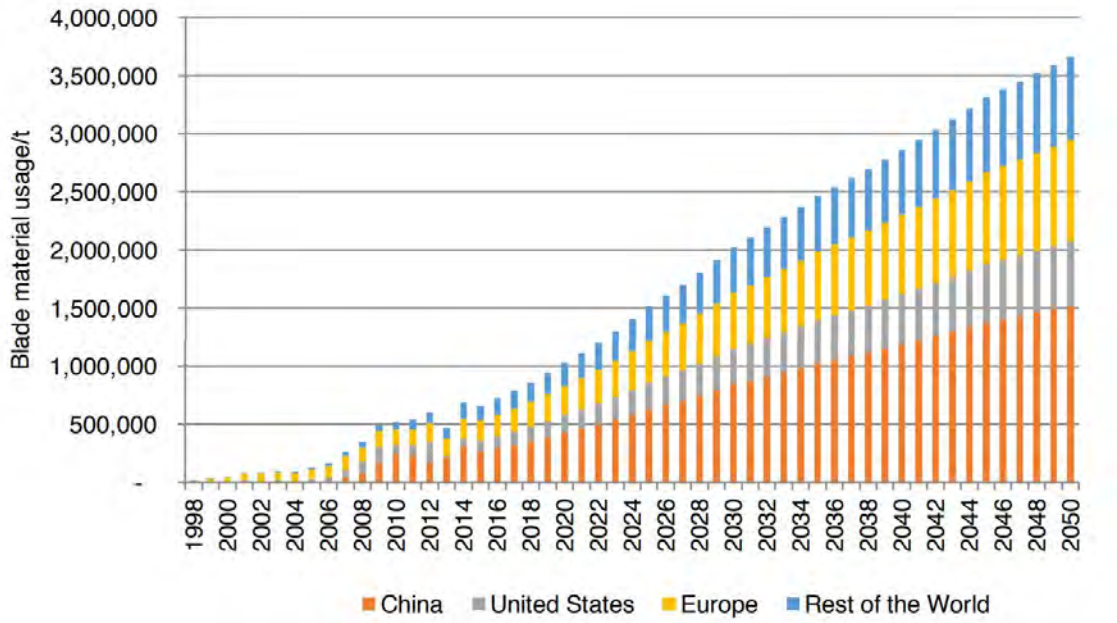

Figure 1. Annual composite waste from decommissioned wind turbine blades.

Because thermoplastic resins are inherently more recyclable than thermoset resin systems, one approach to increasing the potential for recycling future wind turbine blades is to identify a thermoplastic alternative for the production of utility scale blades. However, in order to be a viable replacement for the current thermoset resin systems used in blade production, an acceptable thermoplastic system would have to meet baseline blade design material properties, not increase the overall production cost of blades, and would have to possess similar processing specifications to existing thermoset resin systems to enable a fairly seamless transition into the omnipresent VARTM manufacturing environment in most wind blade factories. Traditional thermoplastic resin systems often utilize solid polymers that are melted through the addition of thermal energy, requiring high melt temperatures (greater than 200°C) and elevated consolidation pressures - and resulting in relatively high viscosity. These parameters are not well suited for the traditional VARTM approach to wind turbine blade manufacturing. In order to comport with state-of-the-art blade processing techniques, an ideal thermoplastic resin system would possess many of the following characteristics:

- Multi-part mixing system with in-situ polymerization;
- A liquid phase with a viscosity below 100 cP at 20°C;
- A maximum exotherm during polymerization of 80°C;
- Compatibility with current fiberglass and carbon fiber sizing;
- Exhibit modulus and tensile strength very similar to the incumbent thermoset resins with equal or better cyclic load performance;
- A volume price point competitive with current VARTM thermoset resin systems.

As described briefly in Section 3, the objective of this research was to identify potential thermoplastic resin solutions for wind turbine blade design and production, down select the identified candidates based on key parameters listed above, develop a material property database through extensive coupon testing, validate resin processing at several scales, and finalize the effort with the production and full-scale structural validation of a thermoplastic composite wind turbine blade. These steps would also be verified by the creation of a techno-economic model accounting for, among other parameters, material cost, labor

cost, cycle time, capital cost, percentage waste, material properties, and potential for recyclability.

The IACMI team assembled for this project possessed unique capabilities and previous relevant experience to enable a successful outcome of this research effort, including the potential commercialization of an innovative wind turbine blade material and manufacturing approach to transform the end-of-life options for decommissioned wind turbine blades. These organizational capabilities and relevant experiences are presented in Table 1.

Table 1. IACMI Project 4.2 Partners with Relevant Capabilities and Experiences.

Project 4.2 Partner	**Relevant Capabilities and/or Experiences**
TPI Composites	Over 40 years of design, manufacturing and testing of wind turbine blades ranging from 9 meters to 70 meters in length; extensive development and sourcing of materials for wind blade production, including resin systems and reinforcements; longstanding relationships with top wind turbine OEMs in global wind industry
Arkema S.A.	Global specialty chemicals and advanced materials company headquartered in France with U.S. headquarters and research facility in King of Prussia (KoP), Pennsylvania; developer and supplier of Elium® thermoplastic resin system; extensive research in both US (KoP) and France (GRL in Lacq) with thermoplastics for wind turbine blades
Johns Manville	A Berkshire Hathaway company headquartered in Denver, Colorado specializing in insulation, roofing materials, and engineered products; develops and produces high performance fiberglass with specialized sizing for use in wind turbine blade industry and other markets
NREL	Over 40 years history in research in all aspects of wind turbine technology, including materials and manufacturing; broad collaboration across entire supply chain of wind industry partners, including wind turbine OEMs, blade manufacturers, and material suppliers; engineers, scientists and technicians with extensive experience in the wind industry in the areas of composite design, manufacturing and validation
Colorado School of Mines	Expertise in kinetics, thermodynamics, and rheology of polymer synthesis, as well as static and fatigue mechanical property characterization, together with failure analysis.
University of Tennessee	Multi-scale fiber and composites characterization facilities were utilized to evaluate the suitable fiber reinforcement and form, resin-fiber interfacial shear strength, optimal methods to extract coupon scale specimens for thermoplastic resin based composites from panel and component scale parts, mechanical testing including tensile, flexural, compression, and fatigue loading. Non-destructive characterization techniques including high resolution micro x-ray computed tomography and radiography to evaluate quality of composite panels and parts, local fiber orientation, and failure modes, and effects of defects on manufactured composite design parts

Vanderbilt University	Vanderbilt's Laboratory for Systems Integrity and Reliability (LASIR) led by co-PI Dr. Douglas Adams has pioneered sensor and data analysis approaches for integrated diagnostics/prognostics in composites manufacturing and composites lifecycle management. LASIR has deployed these approaches in manufacturing, energy, and national security settings including in several national initiatives (DOE IACMI, US Army COSTA rotorcraft and PAM munitions programs, US Marine Corps 53K). Specifically, LASIR has developed technologies to sense, model, and improve the performance and cost of composite body armor and helmets, missiles, ground and air vehicles, wind power structures, and other equipment. LASIR is equipped with a wide range of multi physics sensing systems (optical, infrared, kinematic, inertial) for instrumenting and testing composite materials/structures and composite manufacturing processes. LASIR has deployed its mobile NDE laboratory as part of IACMI to support a number of industry partners including in the 4.2 project by bringing its process monitoring and NDE technologies (eg, infrared flaw imaging system) to NREL's COMET facility.
Purdue University	The Composites Manufacturing and Simulation Center (CMSC) at Purdue University leads in cutting-edge composites manufacturing simulation for high-rate and high-performance applications across aerospace, automotive, and other sectors. CMSC is dedicated to the future of composites manufacturing, including the promises of additive manufacturing. Sitting side-by-side, CMSC team members have capabilities spanning manufacturing, modeling and simulation, performance prediction, characterization, experimental validation, design and prototyping, including rapid fabrication of composites tooling. With this full complement of capabilities, CMSC is the locus for composites design, manufacturing and simulation.

5. RESULTS AND DISCUSSION

5.1 Techno-Economic Model

The techno-economic model developed during this project was published in the Journal of Renewable Energy in February 2019 (Murray, Jenne, Snowberg, Berry, & Cousins, 2019); it is reprinted in its entirety in Appendix A, with permission from the publisher. A link to this published journal article is available here:

https://www.sciencedirect.com/science/article/pii/S0960148118308292

The abstract for this journal article is copied below:

Abstract—**Two-part, in-situ reactive thermoplastic resin systems for composite wind turbine blades have the potential to lower the blade cost by decreasing cycle times, capital costs of both tooling and equipment, and energy consumption during manufacturing, and enabling recycling at the end of the blade life. This paper describes a techno-economic model used to estimate the cost of a thermoplastic wind turbine blade relative to a baseline thermoset epoxy blade. It was shown that a 61.5-m thermoplastic blade costs 4.7% less than an equivalent epoxy blade. Even though the thermoplastic**

resin is currently more expensive than epoxy, this cost reduction is primarily driven by the decreased capital costs, faster cycle times, and reduced energy requirements and labor costs. Although thermoplastic technology for resin infusion of wind turbine blades is relatively new, these results suggest that it is economically and technically feasible and warrants further research.

5.2 Process Modelling and Simulation

The following sections describe the development of an infusion and curing model for thermoplastic wind blades using PAM-RTM. The primary goal was to demonstrate the infusion simulation for the newly developed Elium® resin system on the 13m blade. Additionally, the exotherm temperature is predicted and compared to measurements.

Material characterization

Before developing the infusion simulation, the relevant material properties were collected experimentally or obtained from academic partners on the project. Those properties that could not be measured within the scope of the project were either estimated or taken from the literature. The primary properties required to begin preliminary model development included permeability of the fabric and a chemo-rheological model for the matrix.

Permeability

Permeability is a measure of how easily a liquid can flow through a porous material such as a glass fiber fabric. Permeability is strongly dependent on fiber volume fraction, which is a function of pressure of the fabric. Therefore, the first step in measuring permeability is to run a fiber bed compaction test to find out how much compression is necessary when measuring the permeability in order to be comparable to the 1 atmosphere of pressure that is applied to the fabric during a VARTM process. This test is performed by stacking fabric in a compression fixture of a load cell and measuring the amount the fabric compresses as a function of the applied pressure.

The in-plane permeability is measured by introducing oil with a known viscosity into the fabric at a specific, measured pressure, and observing the flow front of the oil as a function of time. More information about permeability of textiles can be found in (Arbter, et al., 2011) (Parnas, Howard, Luce, & Advani, 1995). Permeability can then be backed out using Darcy's Law:

$$K = \frac{v\mu L}{P}$$

where K is permeability, v is velocity (measured), μ is viscosity (known), L is flow front distance (measured), and P is pressure (fixed). Figure 2 shows a series of images showing the advancement of the oil flow front with time. The flow front distances are gathered in the fiber direction and transverse direction in a series of images and are plotted to get a least squares solution for the in-plane permeabilities.

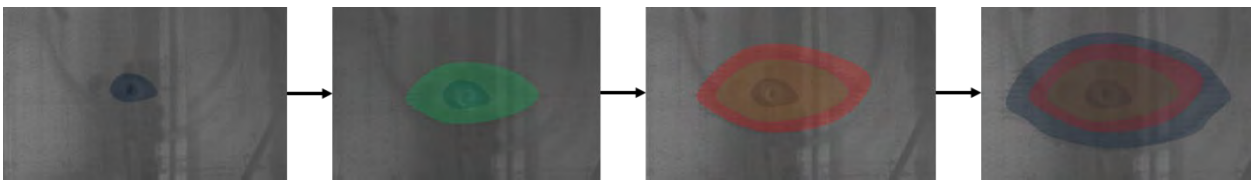

Through thickness permeability cannot be measured in this way; instead, a thick stack of glass fabric (9.5

mm) is placed between the transparent blocks and the time between the start of infusion and when the oil reaches the bottom plate is measured (image shown in Figure 3).

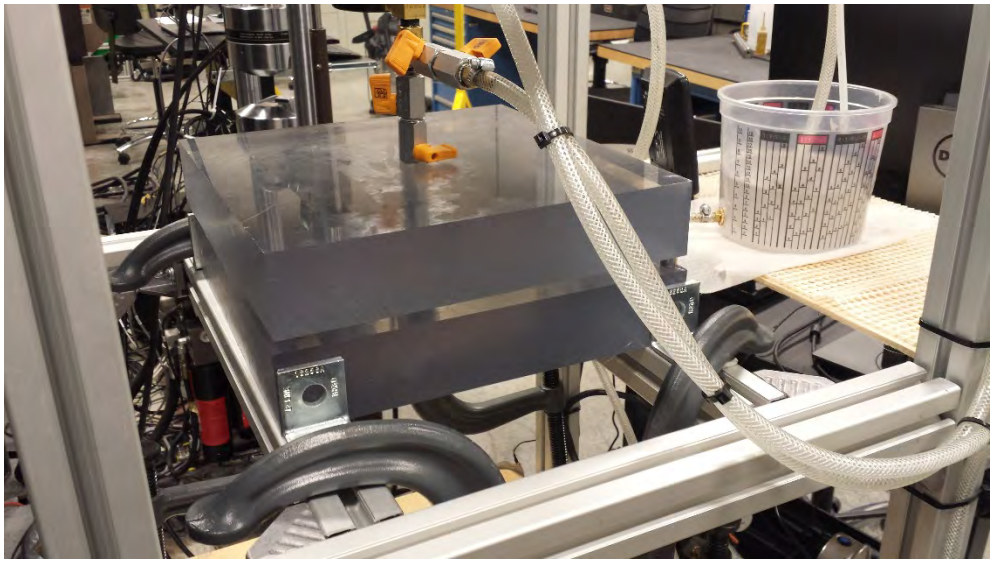

Figure 3. Through thickness permeability setup

The permeability is then estimated using a derivation from Darcy's Law of the time required for the oil to travel a given distance, *x*:

$$K = \frac{\mu \Delta x^2}{P \Delta t}.$$

The measured permeabilities are reported in Table 2. These data are consistent with previous experience.

Table 2. Fabric permeability

Direction	Permeability (m^2)	
	Unidirectional	**Biaxial**
1 (fiber direction)	$9.9x10^{-10}$	$5.8x10^{-10}$
2 (transverse)	$1.7x10^{-10}$	$5.8x10^{-10}$
3 (through-thickness)	$1.7x10^{-10}$	$5.9x10^{-12}$

A physics-based reactivity model for the Elium®188 resin system was developed by academic partners at Colorado School of Mines (Suzuki, et al., 2018). This model was used to generate a lookup table for the conversion rate, $\dot{\alpha}(\alpha, T)$, which could be readily implemented into the infusion model. The reactivity surface is shown in Figure 4. The evolution of the degree of crystallinity for several temperatures is shown in Figure 5.

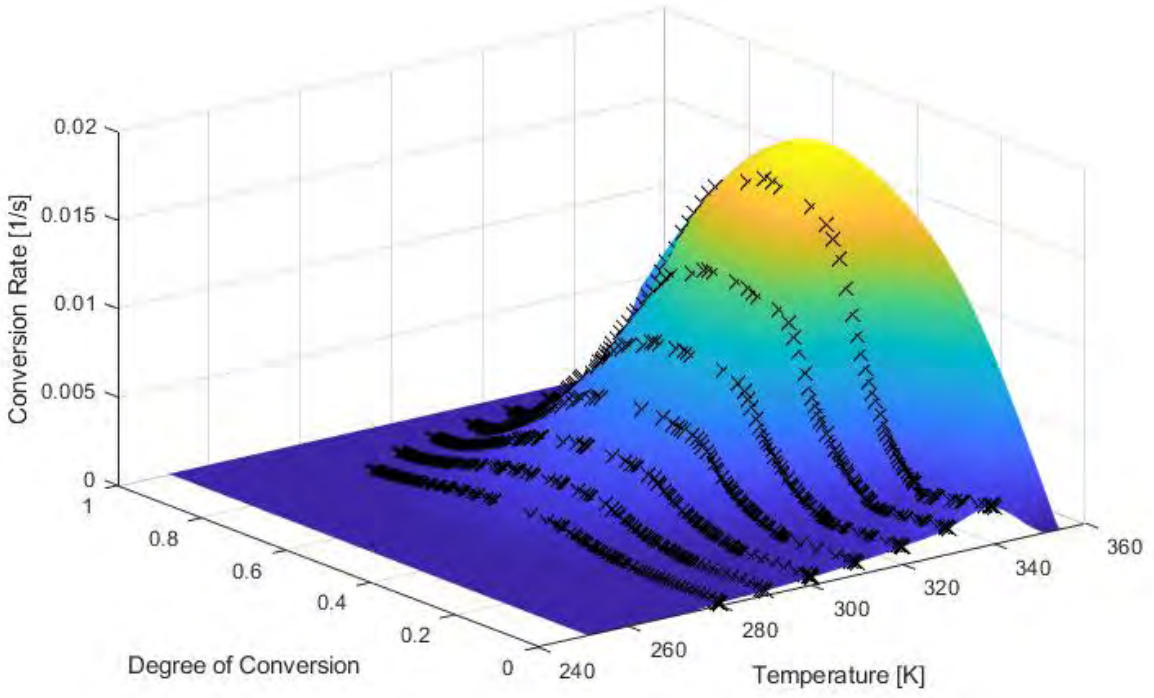

Figure 4. Reactivity surface for Elium®188

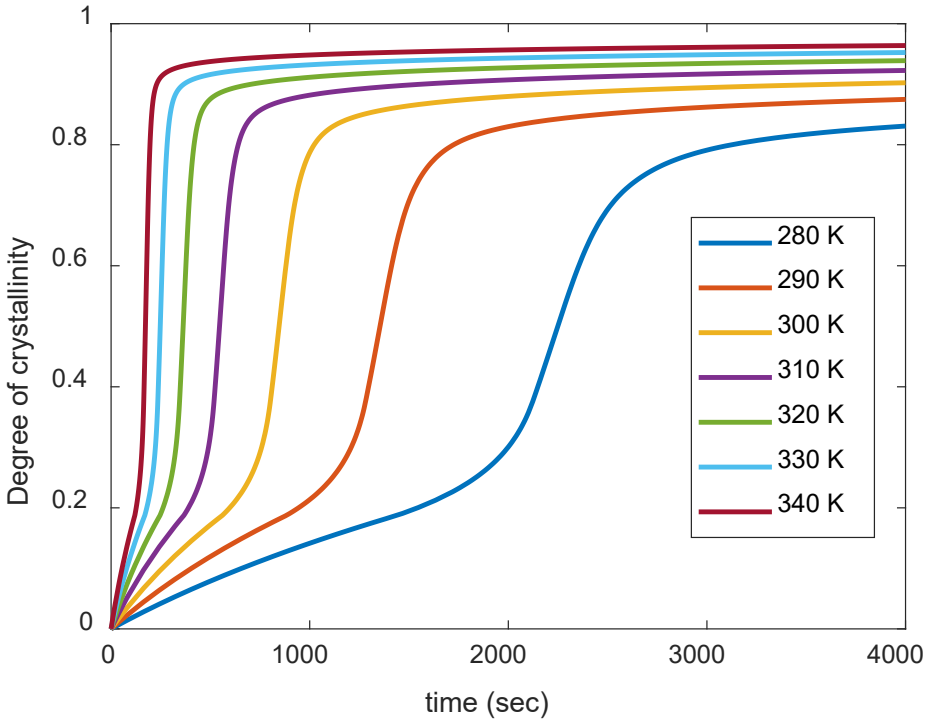

Figure 5. Degree of crystallinity evolution

During infusion, the viscosity evolves with time, temperature, and degree of crystallinity. The viscosity evolution of Elium®188 is shown in Figure 6 for several isothermal histories. These data were measured with a parallel plate rheometer.

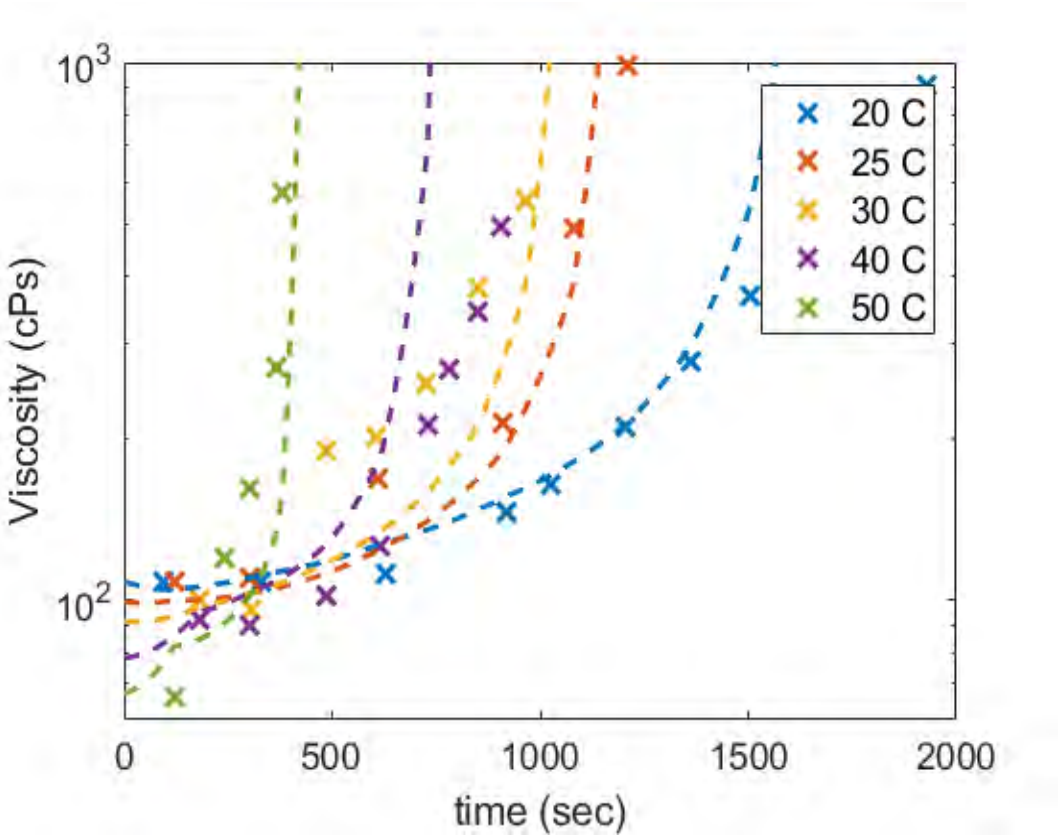

Figure 6. Viscosity evolution during crystallization of Elium®188.

A Castro-Macosko viscosity model, given by Equation 1, was fit to the experimental data. The performance of the viscosity model is shown as the dashed lines in Figure 6. The viscosity, μ, depends on the temperature, T, and degree of crystallinity, α. Five fitting parameters are required for this type of viscosity model and are reported in Table 3 for Elium®188.

$$\mu = \mu_0 \exp\left(\frac{E}{T}\right)\left(\frac{\alpha_g}{\alpha_g - \alpha}\right)^{(C_1 + C_2\alpha)} \quad 1$$

Table 3. Parameters for viscosity model for Elium®188.

Property	Value
μ_0	0.65 [cP]
E	1500 [K]
α_g	0.3
C_1	-0.5
C_2	9

Infusion model development and implementation

After compiling the material models and data, the infusion model for the resin transfer molding (RTM) process was developed. PAM-RTM software from Pacific Engineering Systems International (ESI) was used to model the infusion of the blade. A simplified 2D model of one side of a 13 m wind blade was developed to demonstrate the modeling capability and verify the implementation of the material model for Elium® into the simulation. The 2D model neglects flow through the thickness, so a 3D model is typically preferred for situations with flow media. The simulation coupled both infusion and curing in a "heated filling" analysis to account for the influence of the exothermic reaction, temperature, and degree of crystallinity on the viscosity and the infusion history. This type of model assists in evaluating the filling performance of a certain infusion geometry. The primary components of the infusion model include the material properties, part geometry, infusion layout, and boundary conditions. The material models were described in the previous section. Now, the other steps for creating an infusion model are discussed.

First, the CAD of the blade geometry is taken from the tooling surface as seen in Figure 7. The skin surface is then imported to PAM-MESH (meshing module within the ESI software suite) and a mesh is generated. In PAM-RTM, the material properties are input as described in the previous section.

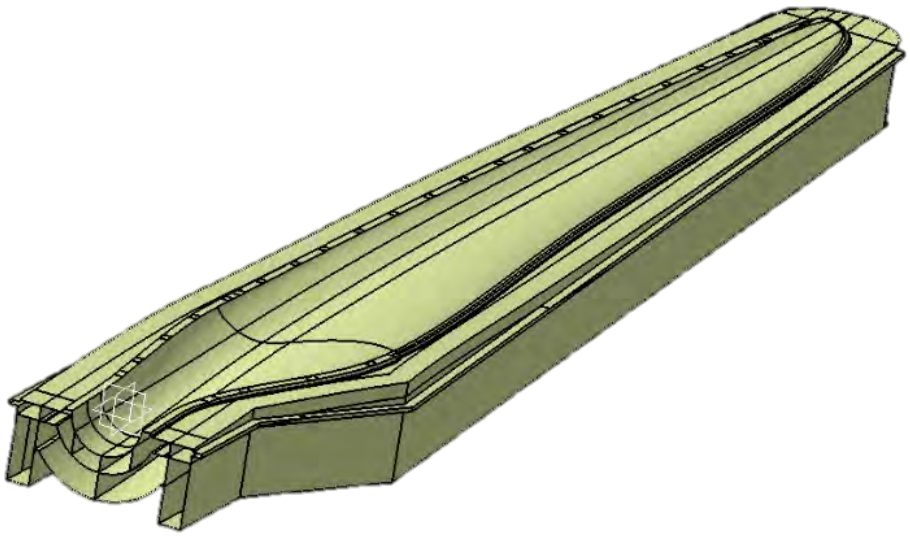

Figure 7. Tooling surfaces used to extract the blade geometry.

An approximation of the dry fabric layup is depicted in Figure 8. The layup schedule in Table 4 helped guide the model creation.

Table 4. Layup schedule for the 13 m wind blade skin.

	Layer	ply	Material	start (mm)	end (mm)	ply length (mm)	Area (m²)
A-side	1	1	EDB	-50	13000	13050	17.75
	2	2	EDB	-50	13000	13050	13.04
	3	3	EUD	-50	2500	2550	3
	4	4	EUD	-50	1850	1900	2.01
	5	5	EDB	-50	1400	1450	1.41
	6	6	EUD	-50	1200	1250	1.18
	7	7	EDB	-50	1100	1150	1.07
B-side	8	1	EDB	-50	12940	12990	17.75
	9	2	EUD	-50	2450	2500	3
	10	3	EUD	-50	1800	1850	2.01
	11	4	EDB	-50	1350	1400	1.41
	12	5	EUD	-50	1150	1200	1.18
	13	6	EDB	-50	1050	1100	1.07

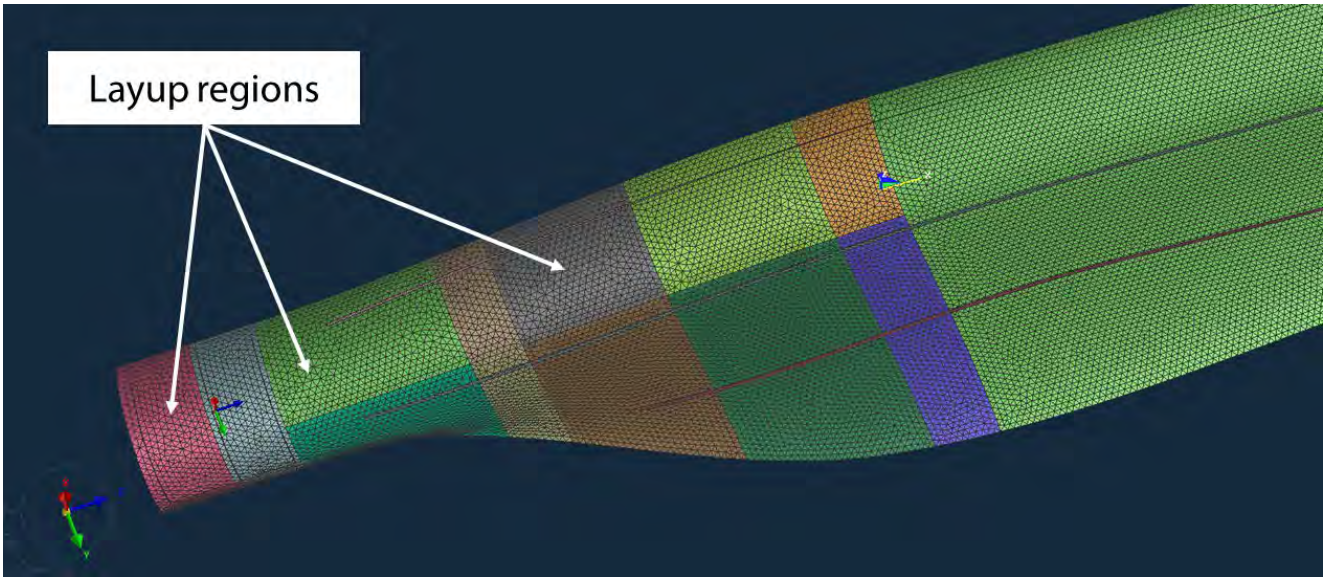

Figure 8. Regions of the finite element mesh, which approximates the layout of the dry fabric.

On the left side of Figure 9, the resin channels and the infusion layout of the blade infusion process is shown. This layout was approximated on the right side of Figure 9 in the RTM simulation. Three infusion channels were located in the root zone, two in the trailing edge zone, and one channel was located in the

leading edge of the blade. Figure 10 shows a close up view of the infusion lines in the RTM shell model that were constructed by adding shell elements perpendicular to the blade surface. These resin channels were created using native PAM-RTM tools. Pressure inlet conditions were applied at the resin channels to introduce the material. Vent conditions were modeled at the leading and trailing edges of the blade.

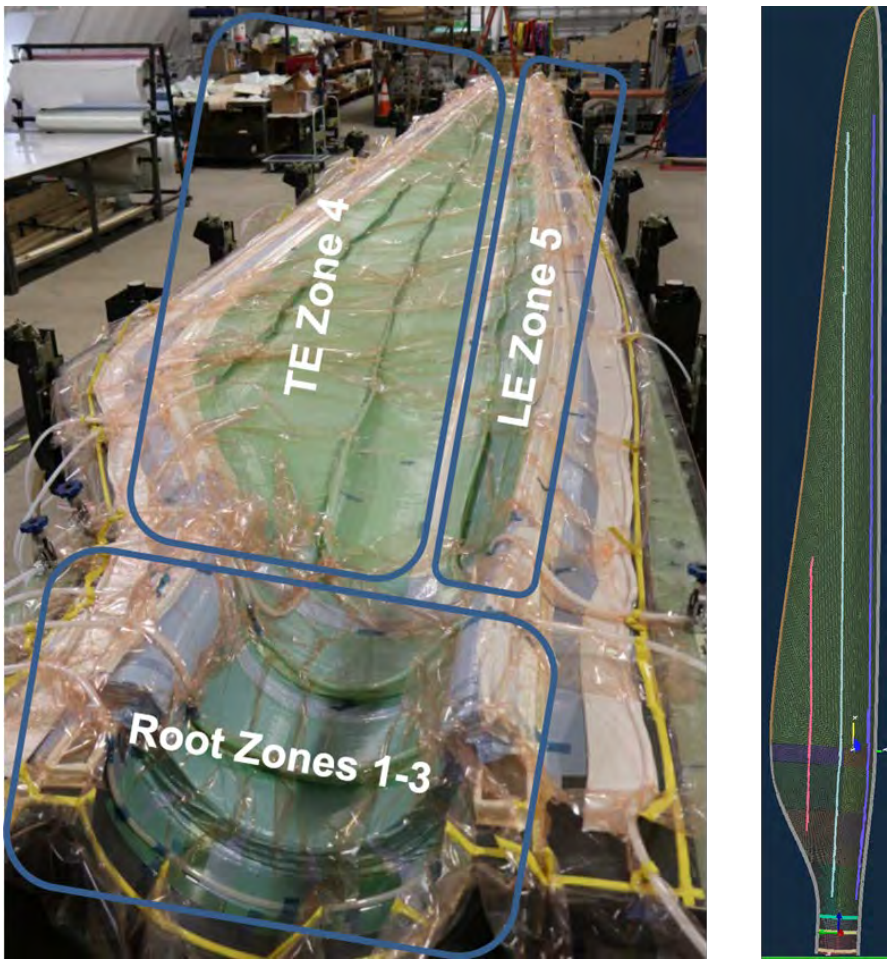

Figure 9. Infusion layup (left) and approximation in the RTM simulation (right).

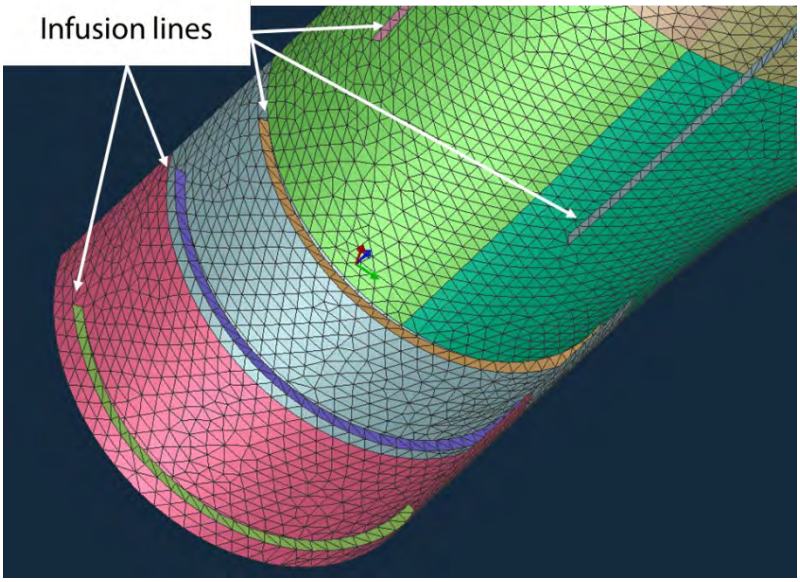

Figure 10. Close-up of the resin infusion channels in the RTM simulation.

Results

The flow front evolution is shown in Figure 11 at several time points. The permeability of the infusion lines is high, so the resin flows rapidly through these channels before filling the blade. The blade was successfully filled in this simulation. Other outputs include the degree of crystallinity, the filling time, temperature, and local viscosity.

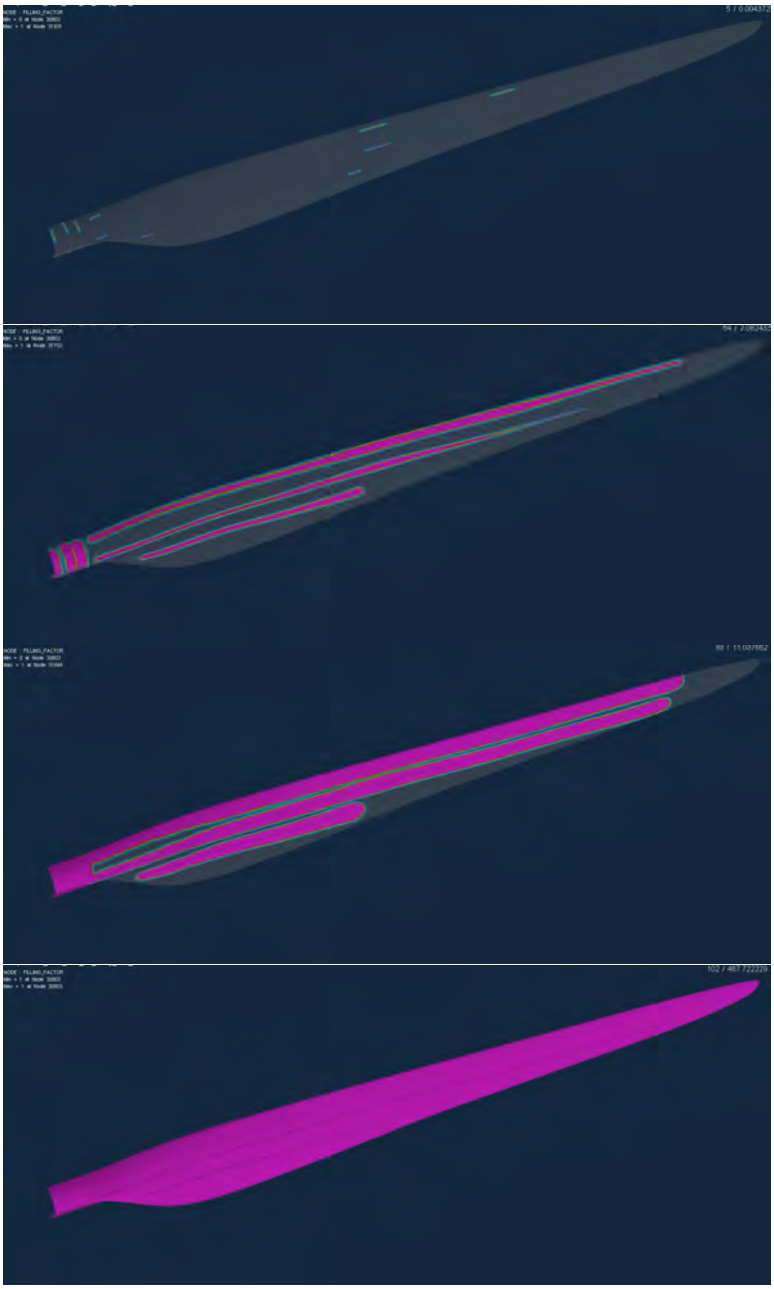

Figure 11. Flow front progression of the infusion simulation.

Conclusions

This section summarized the process modeling performed for simulation the infusion of a thermoplastic wind blade. First, material characterization was performed to collect the relevant material properties and material models required for the infusion simulation. Material characterization was primarily performed at Purdue or by academic partners working on the project. PAM-RTM was used to perform the infusion analysis. The material model for the thermoplastic resin system, Elium®188, was readily implemented into PAM-RTM in a similar fashion to other commonly used resins. The model was successfully demonstrated using a 2D simulation of the infusion of a thermoplastic, 13 m wind blade skin.

Future Work

There are several aspects of this work that could be the focus of future study and further improvements. The simulation method was demonstrated here with a 2D model, but future iterations could be performed using a 3D simulation. This would allow more explicit definition of the infusion layout, fabric preform, and balsa. Additional characterization may be required to appropriately account for the balsa during infusion. The permeability measurements could be improved to account for fabric shear angle. Through thickness permeability measurements can also be improved. A more thorough heat transfer analysis could also be performed. Closer investigation of the simulation outputs such as local temperature and degree of crystallinity should be performed to mitigate defect formation or chance of a short shot. These improvements could render the model useful for optimization of the infusion layout to reduce cycle time and ensure part quality.

Modeling Comparisons with Measurements

Exotherm during crystallization of the Elium® resin system was studied by Vanderbilt on the max chord and root sections of the 13 m blade. The temperature was measured using an IR imaging system and thermocouples. A model was constructed to predict the peak temperature that occurs during crystallization of the blade, and the experimental measurements were used to validate the model.

A 2D model of the blade cross section was constructed to analyze the heat transfer during cure of the max-chord section near the spar cap. The analyzed region was ~7 mm thick. Convection was assumed on the top surface of the part. The mesh and convection surface are shown in Figure 12. The mold was not modeled explicitly, but heat was only allowed to be conducted away from the part through the top surfaces.

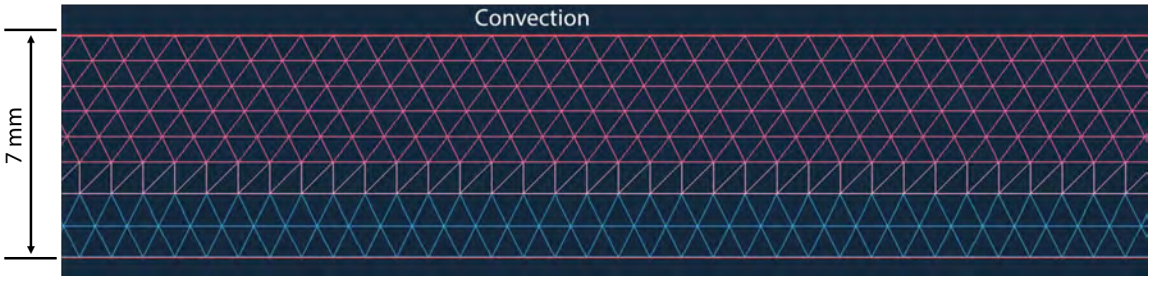

Figure 12. Mesh used for the crystallization simulation.

The experimental measurements showed limited sensitivity to the through thickness position within the part. The predicted temperature history from the simulation is compared to the measurement in Figure 13. The peak temperatures are in good agreement (predicted ~80° C vs measured ~75° C). The temperature increases and drops before and after the peak more quickly in the simulation than in reality. This is likely a result of the simplifying assumptions. Future efforts could involve increasing the modeling fidelity and improving the modeling approximations employed in this model to more closely capture the temperature history during crystallization.

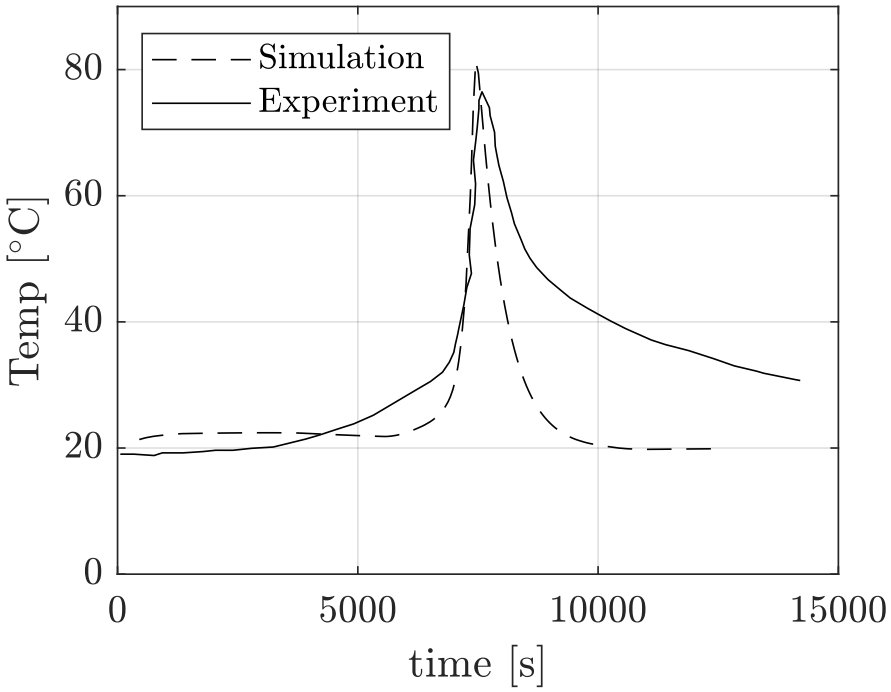

Figure 13. Comparison of measured and predicted temperature during crystallization.

5.3 Elium® Composite Material Characterization

Sample Preparation

Four-ply unidirectional (0_{2s} and 90_{2s} fiber layup) and biaxial ($0/90_s$ and $\pm 45_s$ fiber layup) glass (JM 086 fiber) reinforced polymer panels (Elium®188 thermoplastic and RIMR135/ RIMH1366 thermoset epoxy resin systems) approximately 457 x 457 x 3 mm were obtained from TPI Composites, Warren, RI (Figure 14). To ensure proper fiber orientation, micro X-ray computed radiographs were taken of each panel using lead (Pb) tape to mark an apparent fiber axis, where the fiber angle was measured using ImageJ imaging processing software (Figure 15). The panels were coarse cut using a band saw equipped with a DoAll premium welded blade (Figure 16), and the radiographs were collected to visualize the fiber bundle alignment. Samples were coarse cut from the panels using a Jet 10" Tilting Arbor Saw equipped with a Freud Plexiglass and Plastic 80T blade (Figure 17); then, the samples were precision milled using a SHARP brand vertical knee mill equipped with milling bits engineered for use with composite materials (Figure 18).

Figure 14. Elium-glass fiber composite panel as received from TPI with lead (Pb) tape applied to mark the apparent fiber orientation confirmed by radiography.

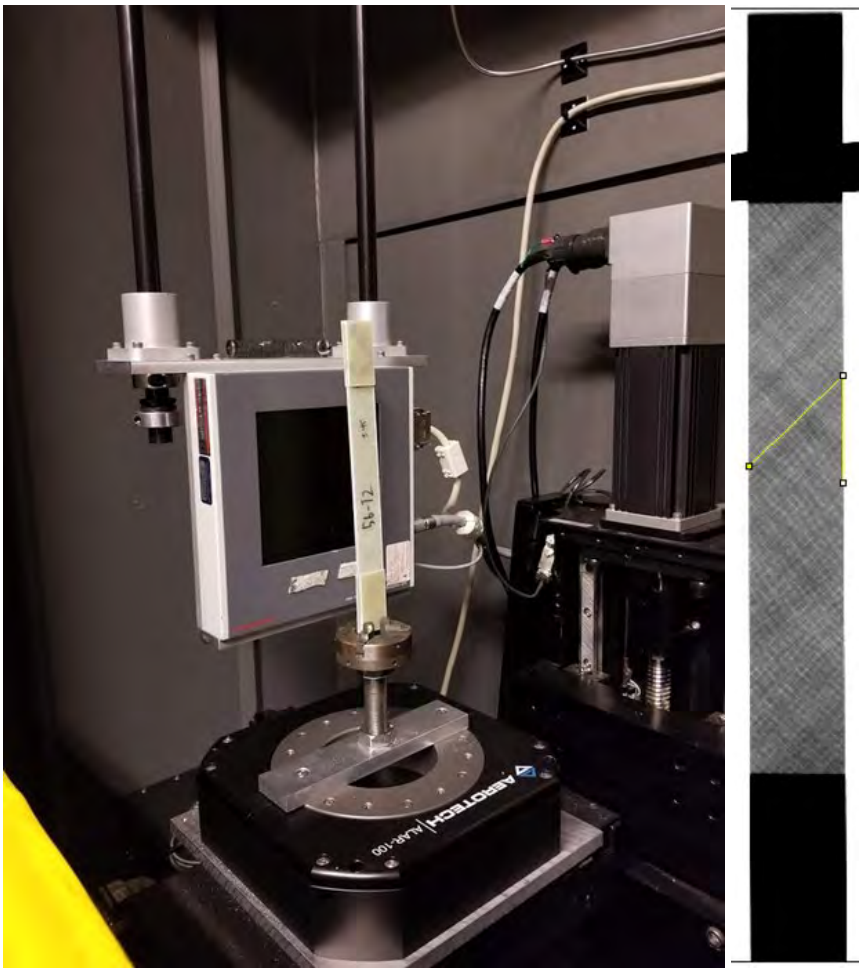

Figure 15. Sample placed in the XCT cabinet for radiography to determine fiber orientation.

Figure 16. Band saw used to square panels and facilitate XCT scanning to determine fiber orientation.

Figure 17. Jet tilting arbor table saw equipped with plexiglass blade used to rough cut samples.

Figure 18. SHARP vertical knee mill utilized for precision cutting of all laminate samples.

Samples were prepared according to the corresponding testing standards, as specified in Table 5; here, round robin testing was performed at two facilities: the University of Tennessee, Knoxville (UTK) and Colorado School of Mines (CSM), with the exception of single cantilever beam (SCB) for the sandwich

structures, where the in-plane shear (Iosipescu) was performed at UTK and flexure at CSM. Prior to testing, all tensile, IITRI compression, and longitudinal fiber direction of the CLC specimens were tabbed with G10 biaxial ($\pm 45_s$ fiber layup) epoxy/glass fiber tabs cut utilizing a Tensilsaw model 60-62 table router equipped with a diamond-plated blade (Figure 19). Tabs were adhered to the specimens by applying a cyanoacrylate based adhesive, Loctite 401 (Figure 20), to the sample and by applying pressure by hand until the adhesive cured. Samples (tabbed or nontabbed) were kept at room temperature in sealed plastic sample bags after preparation until mechanical testing was initiated.

Table 5. Testing standards for various static property determinations.

Test Type	**Testing Standard**	Facility
Tension	ISO 527	UTK/CSM
CLC Compression	ASTM D6641	UTK/CSM
IITRI Compression	ASTM D3410	UTK
Shear (Iosipescu)	ASTM D5379	UTK
Shear (Rail)	ASTM D7078	UTK/CSM
ILSS	ASTM D2344	UTK/CSM
Flexure	ASTM D7264	CSM
Sandwich Core Shear	ASTM C393	UTK/CSM
Sandwich delamination Fracture (SCB)	SCB Test Method for Sandwich Structures (Davies, 1994)	UTK

Figure 19. G10 fiberglass material cut into tabs for tensile specimens and select compression specimens using a Tensilsaw model 60-62 with a diamond-plated blade.

Figure 20. Cyanoacrylate adhesive (Loctite 401) used for bonding tabs to laminate specimens.

Sandwich panels consisting of E-glass fiber reinforced polymer facings (Elium® and epoxy matrix systems) and 25 mm balsa wood cores (Figure 21) were received from TPI with dimensions of 61 cm length x 61 cm x 31 mm thickness for the Elium® sandwich panel (Figure 22) and 122 cm length x 61 cm width x 30 mm thickness for the epoxy-based sandwich panels (Figure 23). Samples (200 mm length x 75 mm width) were extracted from these panels in accordance with geometric specifications of ASTM C393 using the arbor saw shown in Figure 17.

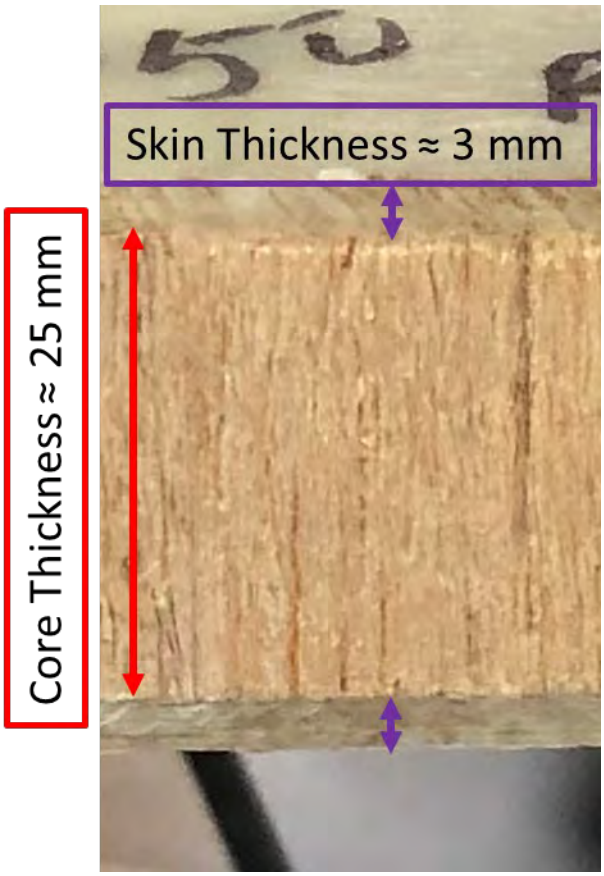

Figure 21. Cross-section of the sandwich panel. (Elium-gf skin shown in the photo)

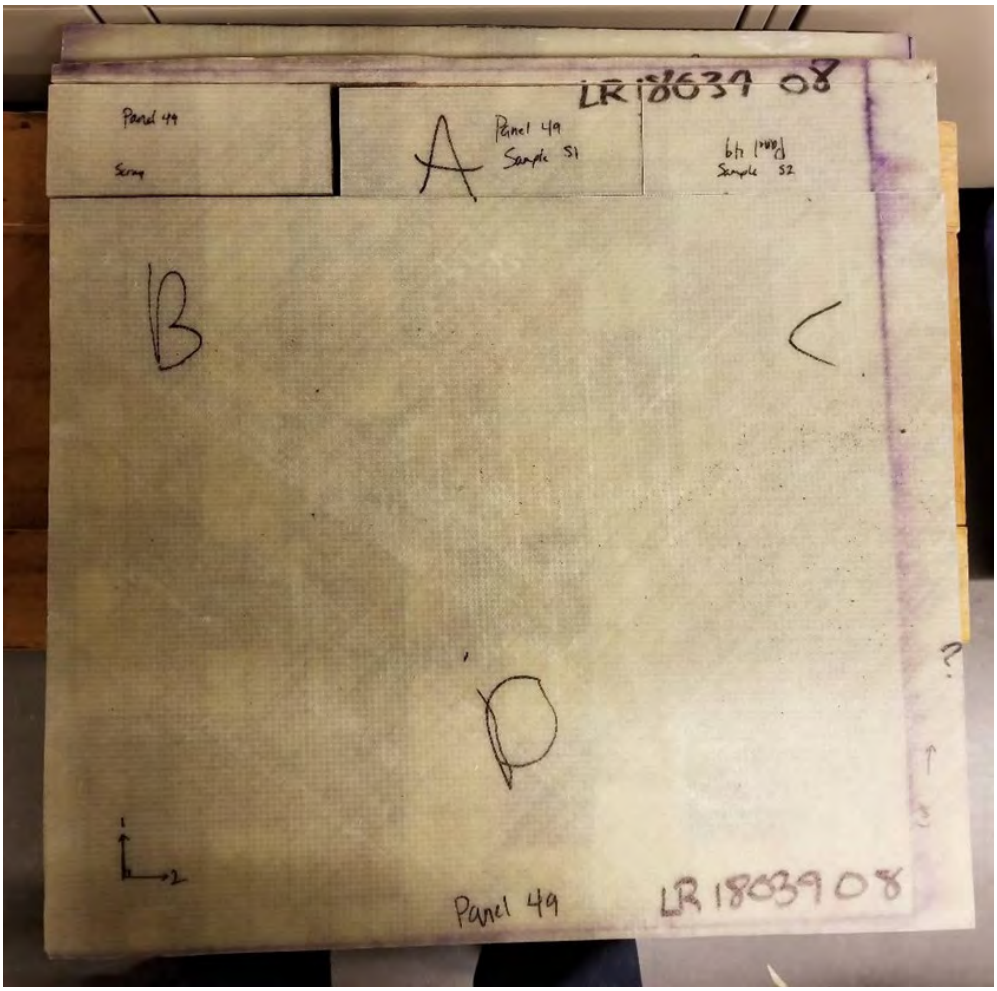

Figure 22. Example 61 x 61 cm Elium-gf-facing sandwich panel with balsa core received from TPI with standard dimension samples cut from one edge.

Figure 23. Example of 122 x 61 cm epoxy-gf-facing sandwich panel with balsa core received from TPI.

Material Composition and Properties

Table 6. Composition overview

Elium® + Glass Fiber	
Material Family	Thermoplastic
Base Material (Resin)	Elium®188 (Tensile Modulus = 3.1 GPa, Tensile Strength = 66 MPa, Flexural Strength = 110 MPa)
Reinforcement	JM 086 Glass Fiber
Reinforcement form	Unidirectional, Biaxial Layup
Glass Fiber Density	2567.5 kg/m^3

Table 7. Physical properties for unidirectional (0 degree) Elium® fiber reinforced composite

Physical Properties	Mean	Std Dev	Units	Qty	Standard(s)
Fiber content (by volume)	55	0.6	%	4	ASTM D792
Void content	0	-	%	4	ASTM D792
Cured ply thickness	0.865	0.0003	mm	4	ASTM D3171
Laminate density	1956	12	kg/m^3	4	ASTM D792

Table 8. Physical properties for biaxial (0/90 degree) Elium® fiber reinforced composite

Physical Properties	Mean	Std Dev	Units	Qty	Standard(s)
Fiber content (by volume)	54.7	2.2	%	4	ASTM D792
Void content	0	-	%	4	ASTM D792
Cured ply thickness	0.825	0.014	mm	4	ASTM D3171
Laminate density	1953	8	kg/m^3	4	ASTM D792

Table 9. Physical properties for biaxial (±45 degree) Elium® fiber reinforced composite

Physical Properties	Mean	Std Dev	Units	Qty	Standard(s)
Fiber content (by volume)	54.9	0.1	%	4	ASTM D792
Void content	0	-	%	4	ASTM D792
Cured ply thickness	0.368	0.005	mm	4	ASTM D3171
Laminate density	1954	0.003	kg/m^3	4	ASTM D792

The density, fiber volume, and void content of the laminates were performed based on ASTM D792; here, four specimens (101.6 mm length x 50.8 mm width x ~3.5 mm thickness) were evaluated for each fiber degree orientation. As shown in Table 7, Table 8, and Table 9, the fiber volume for the 0 degree composite (55%) was marginally higher (0.18%) than ±45 degree (54.9%) and 0.55% higher than the 0/90

degree (54.7%) composite. Similarly, the density of the 0 degree composite (1956 kg/m^3) was slightly higher (0.1%) than ±45 degrees (1954 kg/m^3) and 0.15% higher than the 0/90 degree (1953 kg/m^3). The void content was 0 for the 0 degree, ±45 degree, and 0/90 degree panels, indicating good quality panels with low to no porosity. The cured ply thickness was performed in accordance with ASTM D3171, where four specimens were evaluated. The cured ply thickness for 0/90 fiber degree (0.825 mm) was lower (5%) than the 0 degree (0.865 mm), both of which consisted of four layers. The ±45 degree, which consisted of eight layers cured ply thickness, was approximately 81% lower than the 0 degree panel and 61% lower than the 0/90 degree panel. A non-evasive technique, high-resolution micro X-ray computed tomography (micro-XCT), was performed for each fiber degree specimen to further evaluate the manufactured quality of the panels. Micro-XCT affords the ability to spatially observe in 3D the microstructures features of interest, including fiber orientation and presence of voids. Specimens for 0, ±45, and 0/90 fiber degrees were scanned in a tomography unit (Siemens, in Vitro) at 80 keV and 200 uA over 183 or 360 degrees in 0.12 degree increments to collect 2D projections at 1x binning (2048 pixel x 2048 pixel) in transmission mode. The 2D projects were image processed by normalization and reconstructed using the commercial reconstructed software Octopus (Ghent University, Belgium, version 8.9). The cross-section plane views of the panels were visualized using Fiji image processing software (https://fiji.sc/). Figure 25 shows typical 2D cross sectional plane 0 degree, ±45 degree, and 0/90 degree views. For the 0 degree view, the fiber orientation of the fiber bundles can be clearly observed, showing the unidirectional orientation with cross stitching of the glass fiber spacing at inconsistent increments along the bundles to support the structural integrity of the composite. In Figure 27 and Figure 28, the alternating layup for the 0/90 and ±45 layups are clearly shown. No voids were detected for the specimens, showing good agreement with the void content calculated in for 0 degrees, ±45 degrees, and 0/90 degrees using ASTM D3171, as shown in Table 7, Table 8, and Table 9.

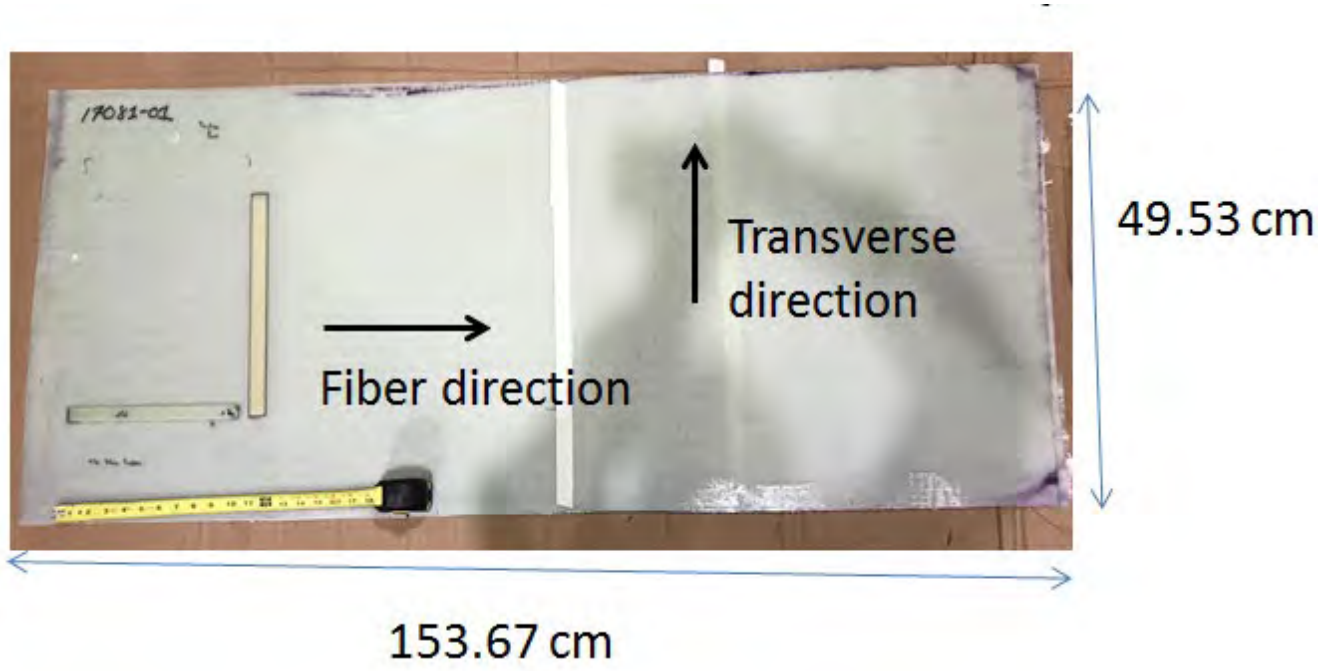

Figure 24. Unidirectional (0 degree) panel.

Note: dark regions on the panel are from the shadow of the photographer.

Figure 25. Micro X-ray tomography and 2D reconstructed cross sections for the unidirectional (0 degree) panel showing low void content.

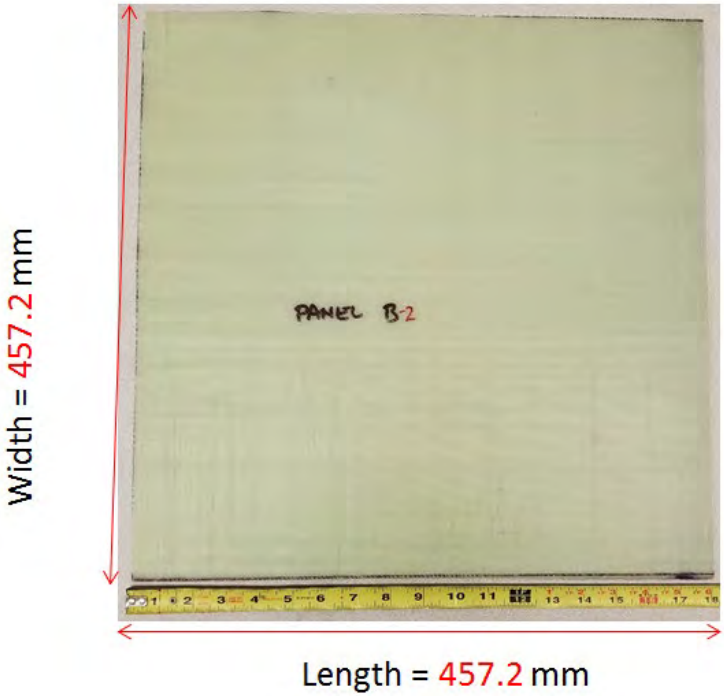

Figure 26. Biaxial (0/90 degree) panel.

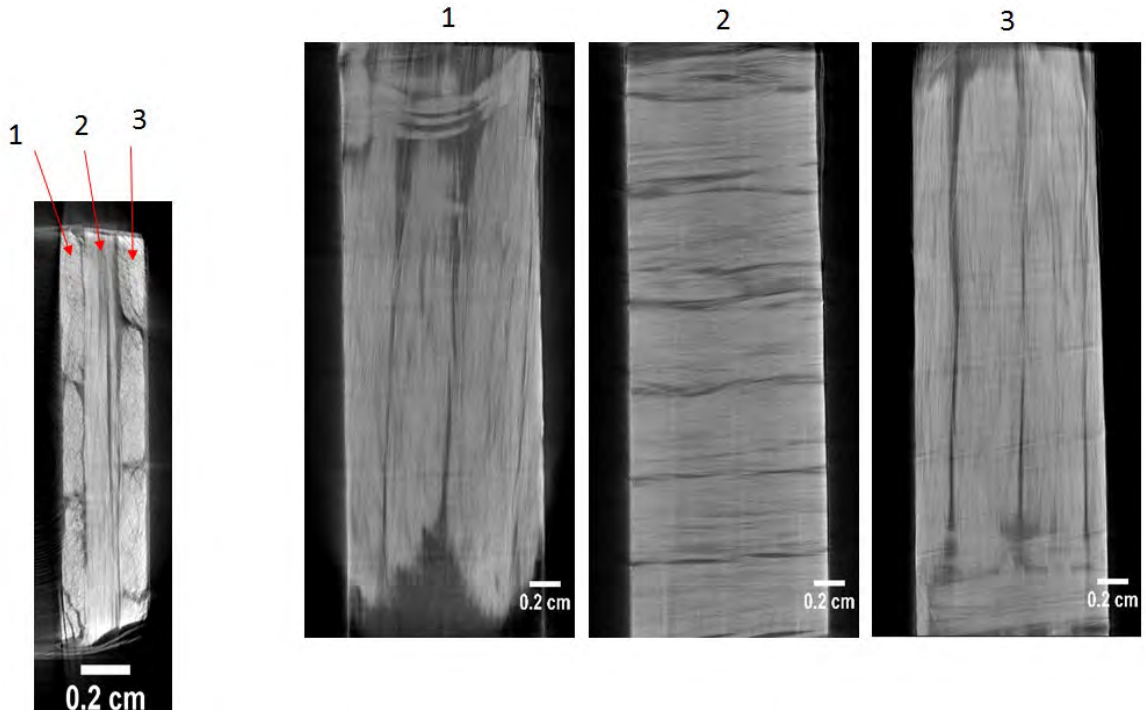

Figure 27. Micro X-ray tomography and 2D reconstructed cross sections for the biaxial (0/90 degree) panel showing low void content.

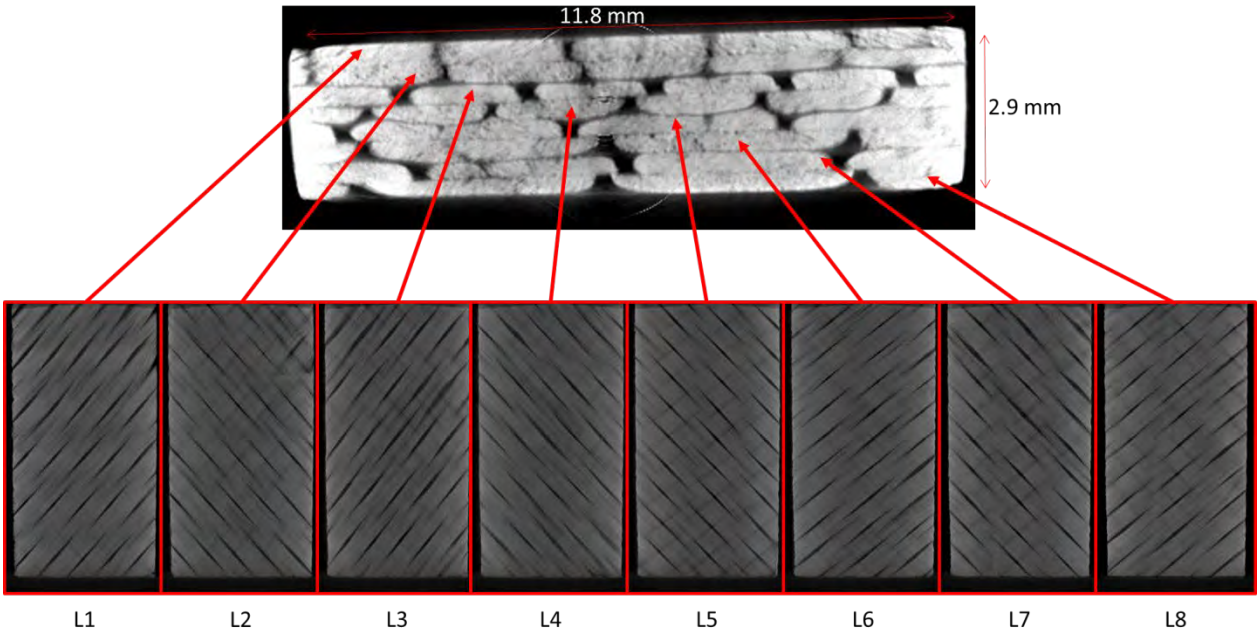

Figure 28. Micro X-ray tomography and 2D reconstructed cross sections for the biaxial (±45 degree) panel showing low void content.

Static Testing

Tensile Results

In accordance with ISO 527, tensile tests were performed for two resin systems, Elium®188 and epoxy to determine baseline tensile composite properties. Testing was performed using a hydraulic mechanical testing load frame (MTS 810 Material Test System) equipped with a 100 kN capacity load cell and 25.4 mm gage length extensometer, as shown in Figure 29. The tensile samples were monotonically loaded in tension with a crosshead rate of 2 mm/minute with extensometer attached to measure the modulus in the elastic region. The extensometer was then removed where the sample was loaded until mechanical tensile failure.

Figure 29. Example tensile specimen loaded in MTS testing machine with extensometer attached.

Approximately eight tensile specimens per facility—UTK and CSM—were tested for each resin system and fiber orientation (0, 90, and ±45 degrees off-loading axis), as shown in Table 10 and Table 11.

Table 10. Tabulated monotonic tensile testing results for the tests performed at UTK.

RESIN SYSTEM	FIBER LAYUP	NUMBER OF SPECIMENS	TENSILE STRENGTH (MPA)	CHORD MODULUS (GPA)	FAILURE STRAIN (%)
ELIUM	0_{2s}	8	820	39	3.0
	90_{2s}	8	44.5	10	0.74
	$\pm45_{s}$	8	131	12	16
	$0/90_{s}$	8	505	26	3.0
	$90/0_{s}$	8	534	28	3.5
EPOXY	0_{2s}	7	763	40	2.8
	90_{2s}	8	45	12	0.49
	$\pm45_{s}$	N/A	N/A	N/A	N/A
	$0/90_{s}$	9	420	24	2.9
	$90/0_{s}$	8	478	25	3.4

Table 11. Tabulated monotonic tensile testing results for the tests performed at CSM.

RESIN SYSTEM	FIBER LAYUP	NUMBER OF SPECIMENS	TENSILE STRENGTH (MPA)	CHORD MODULUS (GPA)	FAILURE STRAIN (%)
ELIUM	0_{2s}	8	917	41	3.8
	90_{2s}	8	47.9	11	0.61
	$\pm45_s$	8	148	12	N/A
	$0/90_s$	8	441	22	3.2
	$90/0_s$	8	502	24	3.8
EPOXY	0_{2s}	8	723	37	N/A
	90_{2s}	8	40.3	11	N/A
	$\pm45_s$	8	147	13	N/A
	$0/90_s$	8	387	22	N/A
	$90/0_s$	8	463	22	N/A

Variations in the results between testing facilities were investigated based on the grip pressures applied to the samples during testing. However, the failure modes remained consistent, and variations between the facilities persisted; therefore, the decision was made to utilize the results specific to the facility to determine the stress levels used for fatigue testing. Tensile specimens with a 0_{2s} fiber layup exhibited splitting along the fibers and transverse fiber breaks during failure (Figure 30 and Figure 31). Tensile specimens with a 90_{2s} fiber layup exhibited matrix failure coupled with interfacial shear failure mechanisms (Figure 32 and Figure 33). Tensile specimens with $\pm45_s$ fiber layup exhibited interlaminar and interfacial shear failures coupled with matrix failure (Figure 34).

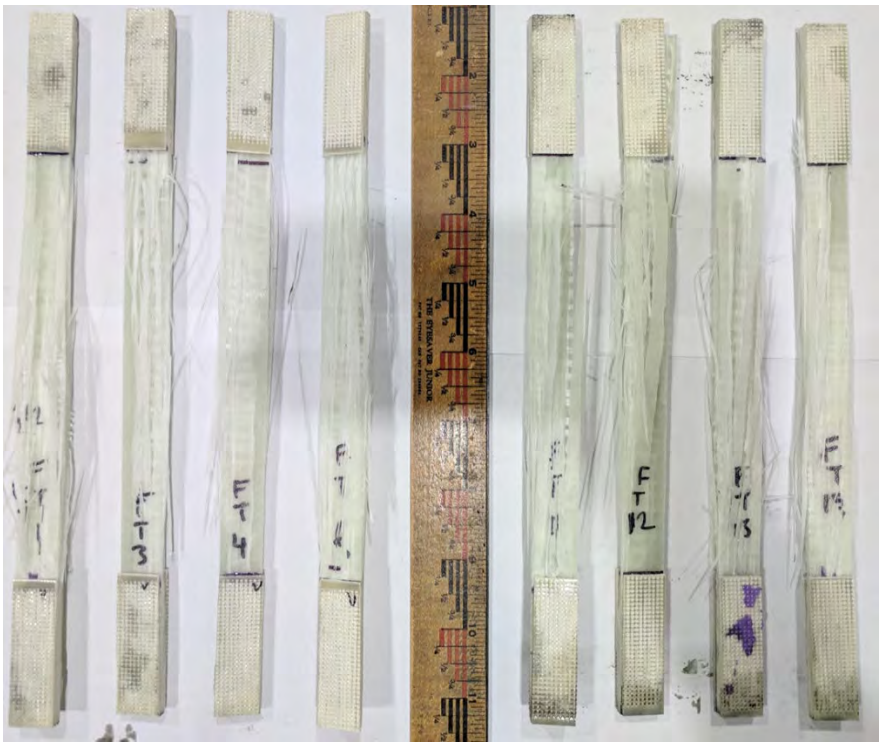

Figure 30. Elium-gf 0_{2s} samples failed in the interlaminar and interfacial shear coupled with transverse fiber breakage.

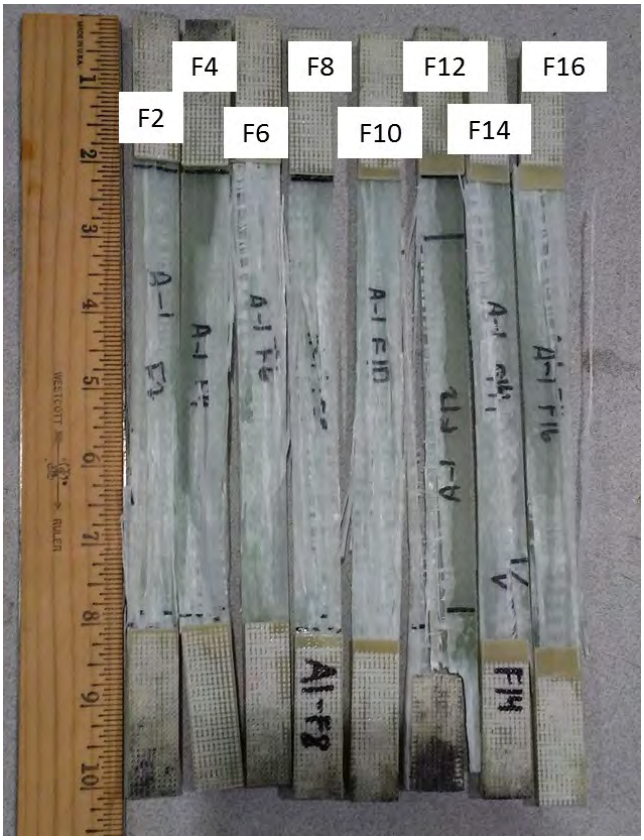

Figure 31. Epoxy-gf 02s samples failed in the interlaminar and interfacial shear coupled with transverse fiber breakage.

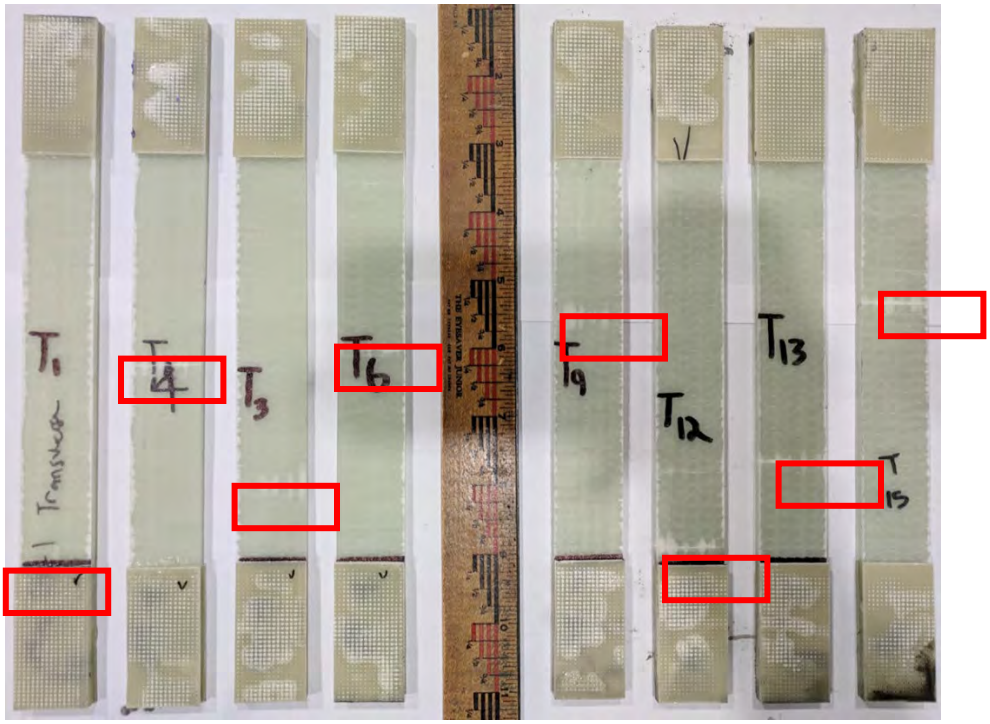

Figure 32. Elium-gf 90_{2s} samples after failure. Samples failed along fiber orientation in the interfacial shear and matrix failure modes.

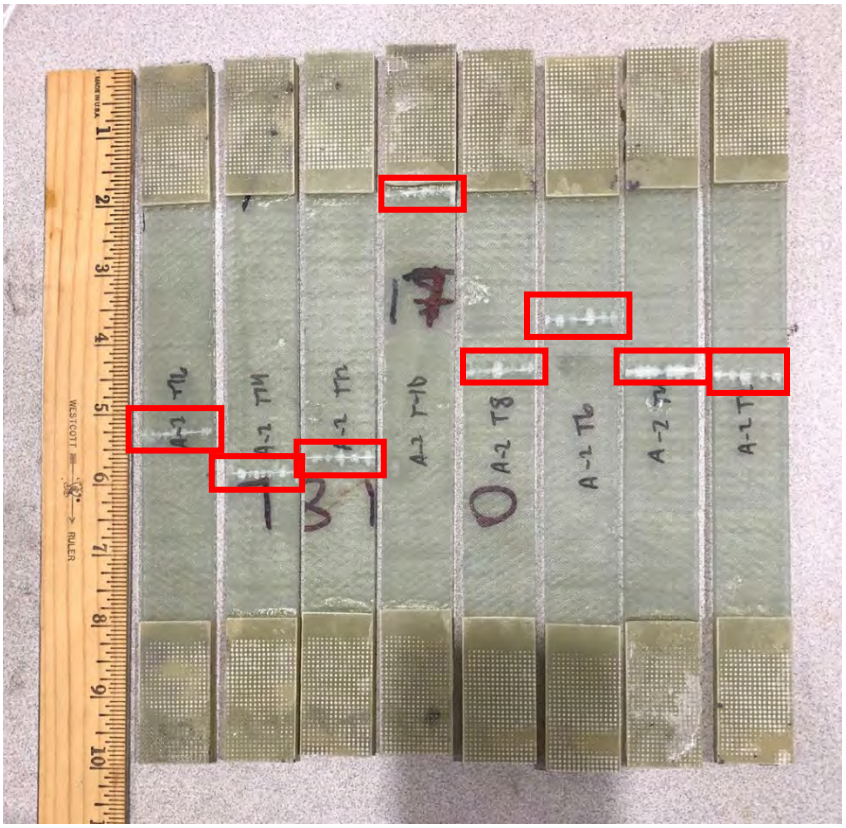

Figure 33: Epoxy-gf 90_{2s} samples after failure. Samples failed along fiber orientation in the interfacial shear and matrix failure modes.

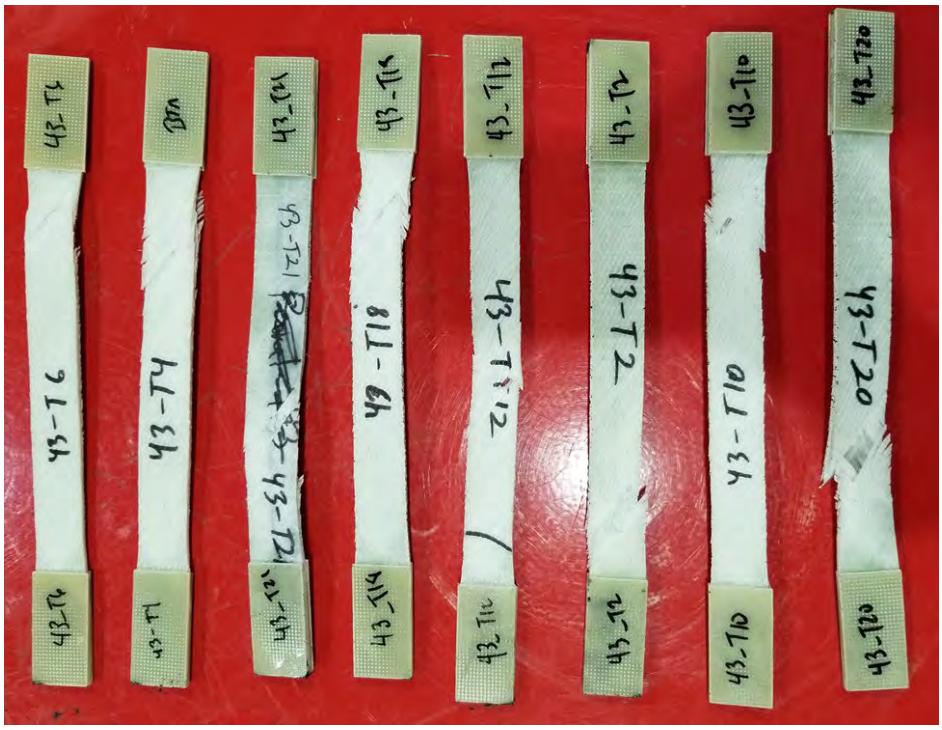

Figure 34. Failed tensile ±45$_s$ Elium-gf specimens exhibiting interlaminar and interfacial shear failure mechanisms.

Compression Results

Monotonic compression tests were performed for two resin systems (Elium® and epoxy) with identical glass fiber reinforcement and were done in accordance with ASTM D6641(CLC, Figure 35) and ASTM D3410 (IITRI, Figure 36); these tests were conducted to determine the baseline compression properties. CLC specimens with fiber aligned with the loading axis and all IITRI specimens were tabbed using G10 fiberglass tabs. Testing was performed using a hydraulic mechanical testing load frame (MTS 810 Material Test System) equipped with a 50 kN capacity load cell. Linear strain gages (350 Ohm resistance) were adhered to each side of the sample aligned with the loading axis to measure strain and buckling during compression loading. Approximately eight specimens were prepared and subjected to compression loading until compression mechanical failure was achieved for each resin system and fiber orientation (0, 90, and ±45 degree off-loading axis). The results of the tests performed at UTK are summarized in Table 12, and the results from the tests performed at CSM are in Table 13.

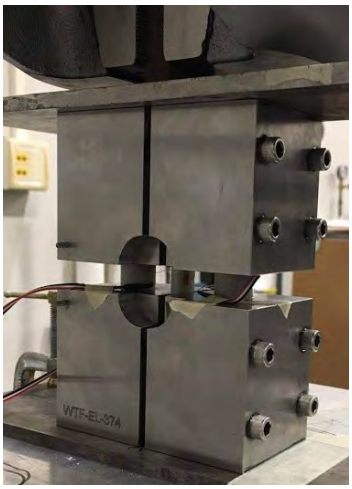

Figure 35. Compression specimen in the CLC fixture with strain gages mounted to opposing faces.

Figure 36. Compression specimen in the IITRI fixture with strain gages mounted to opposing faces.

Table 12. CLC monotonic compression test results from testing performed at UTK.

RESIN SYSTEM	FIBER LAYUP	NUMBER OF SPECIMENS	TENSILE STRENGTH (MPA)	CHORD MODULUS (GPA)	FAILURE STRAIN (%)
ELIUM	0_{2s}	13	680	41	1.9
	90_{2s}	8	149	12	1.3
	$\pm45_s$	9	122	12	*13.6
EPOXY	$\pm45_s$	10	118	13	*11.9

Table 13. CLC monotonic compression results from testing performed at CSM.

RESIN SYSTEM	FIBER LAYUP	NUMBER OF SPECIMENS	TENSILE STRENGTH (MPA)	CHORD MODULUS (GPA)	FAILURE STRAIN (%)
ELIUM	0_{2s}	7	599	34	3.8
	90_{2s}	7	150	9.8	N/A
	$\pm45_s$	8	96.4	5.61	N/A
	$0/90_s$	9	343	34	N/A
	$90/0_s$	8	359	40	N/A
EPOXY	0_{2s}	8	569	34	N/A
	90_{2s}	8	135	10	N/A
	$\pm45_s$	N/A	N/A	N/A	N/A
	$0/90_s$	6	384	26	N/A
	$90/0_s$	6	395	29	N/A

Table 14. IITRI monotonic compression results from testing performed at UTK.

RESIN SYSTEM	FIBER LAYUP	NUMBER OF SPECIMENS	TENSILE STRENGTH (MPA)	CHORD MODULUS (GPA)	FAILURE STRAIN (%)
ELIUM	0_{2s}	10	693	41	1.8
	90_{2s}	10	156	13	2.3
	$\pm45_s$	9	145	12	4.7
EPOXY	$\pm45_s$	16	143	13	4.4

In-plane Shear Results

To determine baseline shear properties, monotonic in-plane shear tests were performed for two resin systems (Elium® and epoxy) with various glass fiber reinforcement layups; the tests were done in accordance with ASTM D5379 (Iosipescu, Figure 37) and ASTM D7078 (V-notched rail shear, Figure 38). Testing was performed using a hydraulic mechanical testing load frame (MTS 810 Material Test System) equipped with a 50 kN capacity load cell or a MTS 808 Material Test System hydraulic load frame equipped with a 25 kN capacity load cell. Rosette strain gages (350 Ohm resistance) were adhered to each side of the samples (Figure 39) with two gage axes aligned to the ±45° off-axis to the load line to measure the shear strain during testing, and the other gage axis was aligned perpendicular to the load line axis. The in-plane shear mechanical testing was coupled with DIC, which was utilized to measure the strain field compared with the rosette strain gages for a selective number of samples, as shown in Table 15 and Table 16. Approximately 10 specimens of each type (Iosipescu and V-notched rail) were prepared and subjected to shear loading until catastrophic failure was achieved for each resin system and fiber orientation (0, 90, and ±45 degree off-loading axes). The results of the Iosipescu and V-notched rail shear testing performed at UTK are in Table 15 and Table 16, and the results of the tests performed at CSM are in Table 17.

Figure 37. Example of the Iosipescu specimen in the test fixture with a speckle pattern for DIC strain analysis.

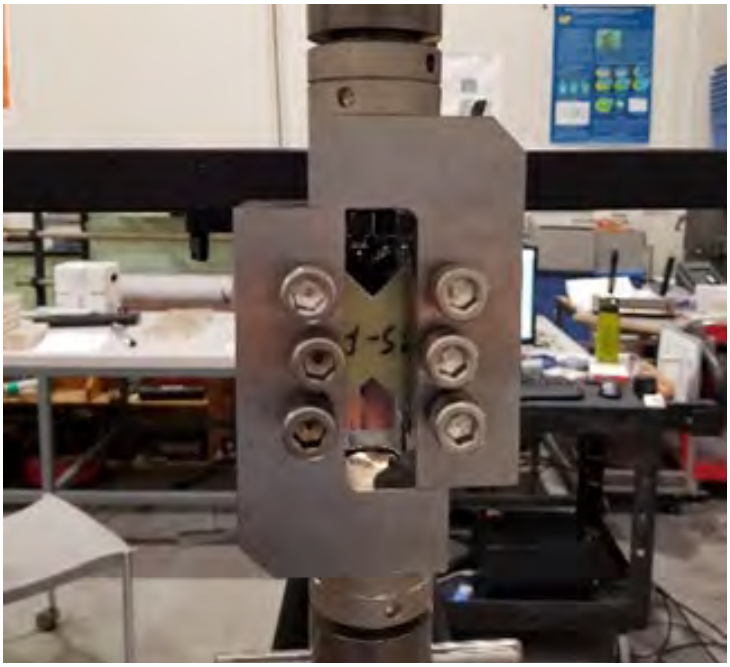

Figure 38. Example of the V-notch rail shear specimen in the test fixture.

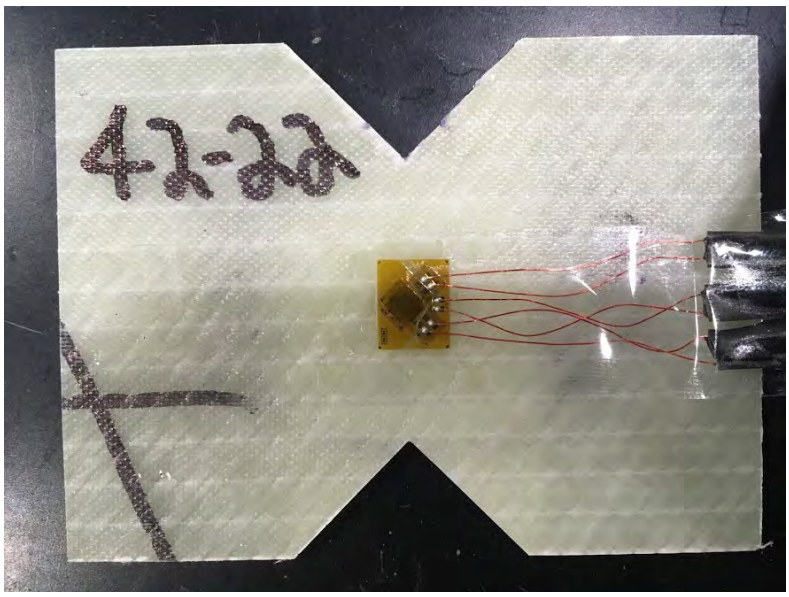

Figure 39. Example of the V-notched rail shear sample with rosette strain gage mounted.

Table 15. Iosipescu in-plane shear results from testing performed at UTK. Shear stress shown for $\pm 45_s$ samples is the true shear strength because the specimens failed before reaching 5% shear strain.

RESIN SYSTEM	FIBER LAYUP	NUMBER OF DIC SPECIMENS	NUMBER OF STRAIN GAGE SPECIMENS	0.2% OFFSET SHEAR STRENGTH (MPA)	SHEAR STRESS @ 5% SHEAR STRAIN (MPA)	CHORD SHEAR MODULUS (GPA)	FAILURE STRAIN (%)
ELIUM	0_{2s}	6	7	38.6	60.8	3.8	N/A
	90_{2s}	5	7	37.4	53.6	3.5	N/A
	$\pm 45_s$	5	10	*N/A *(Linear elastic until failure)	**121 **(True Shear Strength)	11	1.2

Table 16. V-notched rail shear in-plane shear testing results from the tests performed at UTK.

RESIN SYSTEM	FIBER LAYUP	NUMBER OF DIC SPECIMENS	NUMBER OF STRAIN GAGE SPECIMENS	0.2% OFFSET SHEAR STRENGTH (MPA)	SHEAR STRESS @ 5% SHEAR STRAIN (MPA)	CHORD SHEAR MODULUS (GPA)	FAILURE STRAIN (%)
ELIUM	0_{2s}	9	5	39.9	58.2	3.7	N/A
	90_{2s}	10	4	39.4	53.6	3.7	N/A
	$\pm 45_s$	10	4	*N/A *(Linear elastic until failure)	**290 **(True Shear Strength)	13	2.6

Table 17. V-notched rail shear in-plane shear testing results from the tests performed at CSM.

RESIN SYSTEM	FIBER LAYUP	NUMBER OF SPECIMENS	0.2% OFFSET SHEAR STRENGTH (MPA)	SHEAR STRESS @ 5% SHEAR STRAIN (MPA)	CHORD SHEAR MODULUS (GPA)	FAILURE STRAIN (%)
ELIUM	0_{2s}	6	N/A	56.0	4.2	N/A
	90_{2s}	6	N/A	52.5	3.8	N/A
	$\pm 45_s$	7	N/A	**237 **(True Shear Strength)	13	N/A
EPOXY	0_{2s}	7	N/A	57.7	3.6	N/A
	90_{2s}	7	N/A	**51.1 **(True Shear Strength)	4.0	N/A
	$0/90_s$	3	N/A	**54.9	3.9	N/A
	$90/0_s$	3	N/A	51.1	3.4	N/A

The Iosipescu results for 0_{2s} and 90_{2s} fiber layups shown in Table 15 do not exhibit visible shear failure strain because of the specifications of the ASTM standard (D5379), which states that the failure strain is denoted as the strain at maximum strength or 5% shear strain. Therefore, only the $\pm 45_s$ layup samples failure strain could be clearly observed. However, because of distortion of the sample near the location of the strain gages prior to catastrophic failure, a failure strain was typically unobtainable for samples without DIC strain analysis. As such, the value listed in Table 15 is based on five samples only.

DIC analysis revealed strain concentrations across the notched section, as should be expected for

Iosipescu and V-notched rail shear specimens. Here, 0_{2s} specimens failed with lateral (horizontal) shearing along the fiber axes at the notch edge (Figure 40 and Figure 41), an acceptable failure mode according to ASTM D5379. The 90_{2s} specimens typically failed across the V-notch region (Figure 42) along the fiber axes (vertical shearing), with some specimens failing in multiple locations, as shown in Figure 43. V-notched rail shear testing yielded similar shear strength results as the Iosipescu shear for the 0_{2s} and 90_{2s} layups. The $\pm45_s$ specimens failed in the notched region via fiber breakage and matrix failure. The Iosipescu samples exhibited crushing at the loading shoulders, as shown in Figure 44, before 5% shear strain was reached and true shear strength could not be determined. However, the V-notched rail shear specimens failed in pure shear only (Figure 45), allowing true shear strength to be obtained. Therefore, in agreement with ASTM D5379, Iosipescu shear is not considered a good representation of shear strength assessment for $\pm45_s$ layups, and V-notch rail shear strength should be considered closer to true shear strength because the crushing failure mechanism is removed.

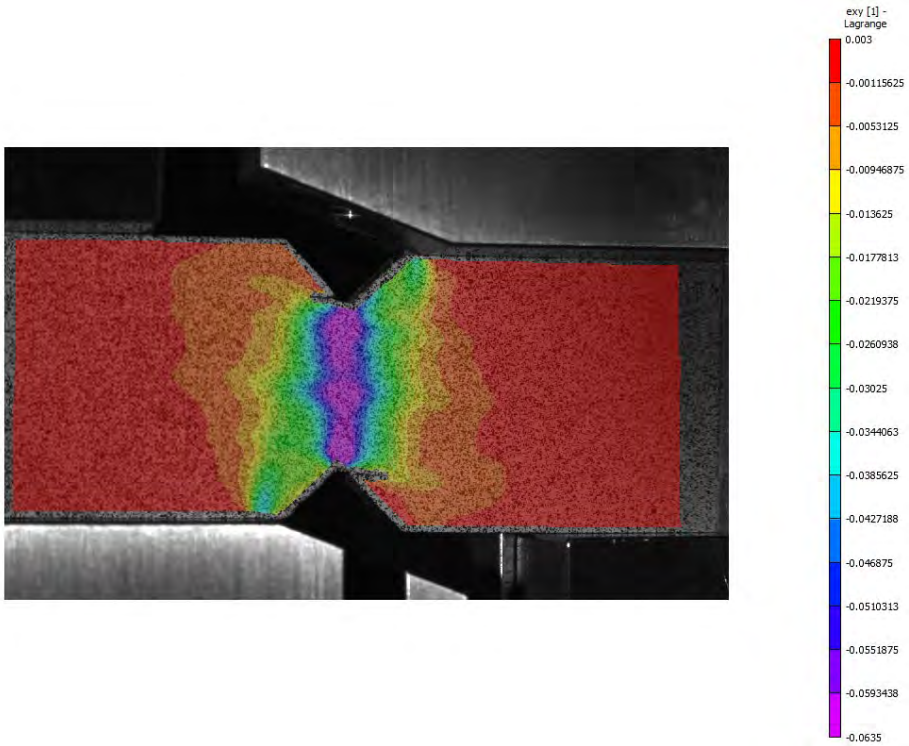

Figure 40. 0_{2s} Elium-gf Iosipescu in-plane shear specimen at failure. The shear strain is concentrated across the V-notch, with splitting along the fiber axis at notch edges, an acceptable failure mode for this specimen, according to ASTM D5379.

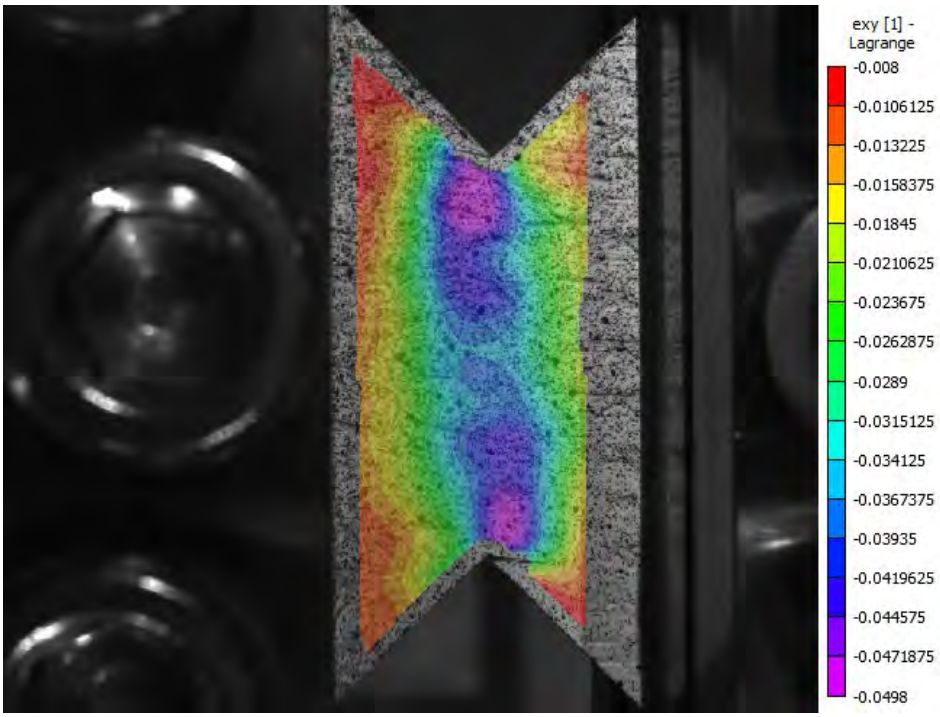

Figure 41. 0_{2s} Elium-gf V-notched rail shear in-plane shear specimen prefailure. The shear strain is concentrated across the V-notch, with splitting along the fiber axis at notch edges, an acceptable failure mode for this specimen, according to ASTM D7078.

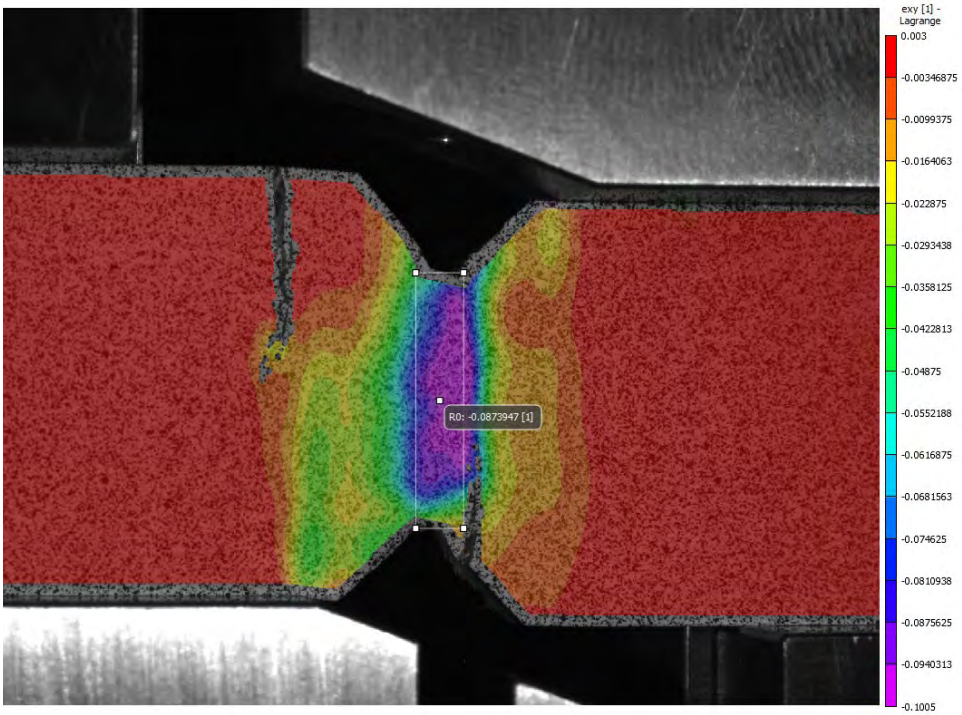

Figure 42. 90_{2s} Elium-gf Iosipescu in-plane shear specimen at failure. The shear strain is concentrated across the V-notch, with splitting along the fiber axis within notched region and outside the notched region, an unacceptable failure mode for this specimen according to ASTM D5379.

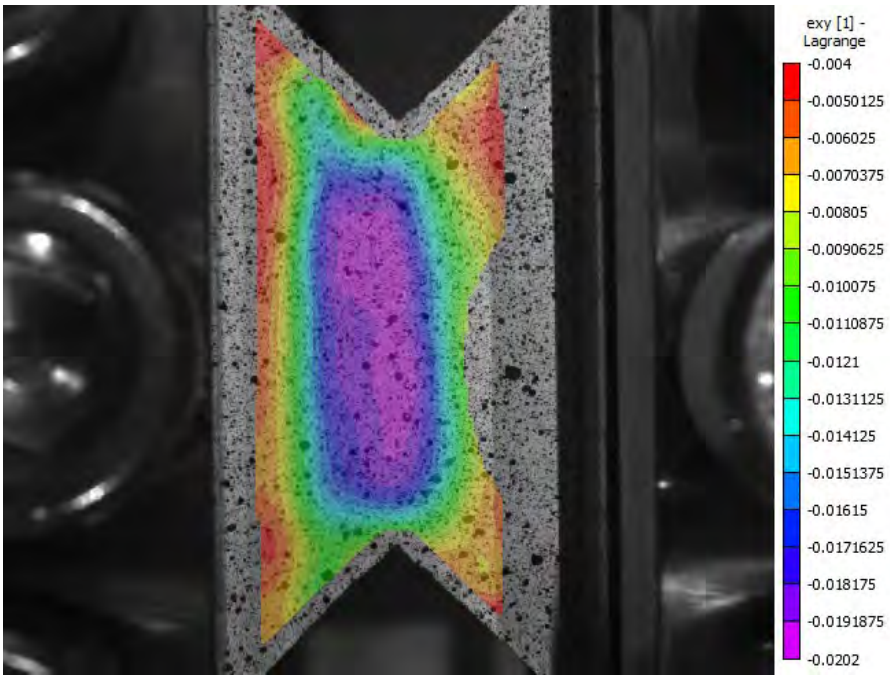

Figure 43. 902s Elium-gf V-notched rail shear in-plane shear specimen at failure. The shear strain is concentrated across the V-notch, with splitting along the fiber axis within notched region, an acceptable failure mode for this specimen according to ASTM D7078.

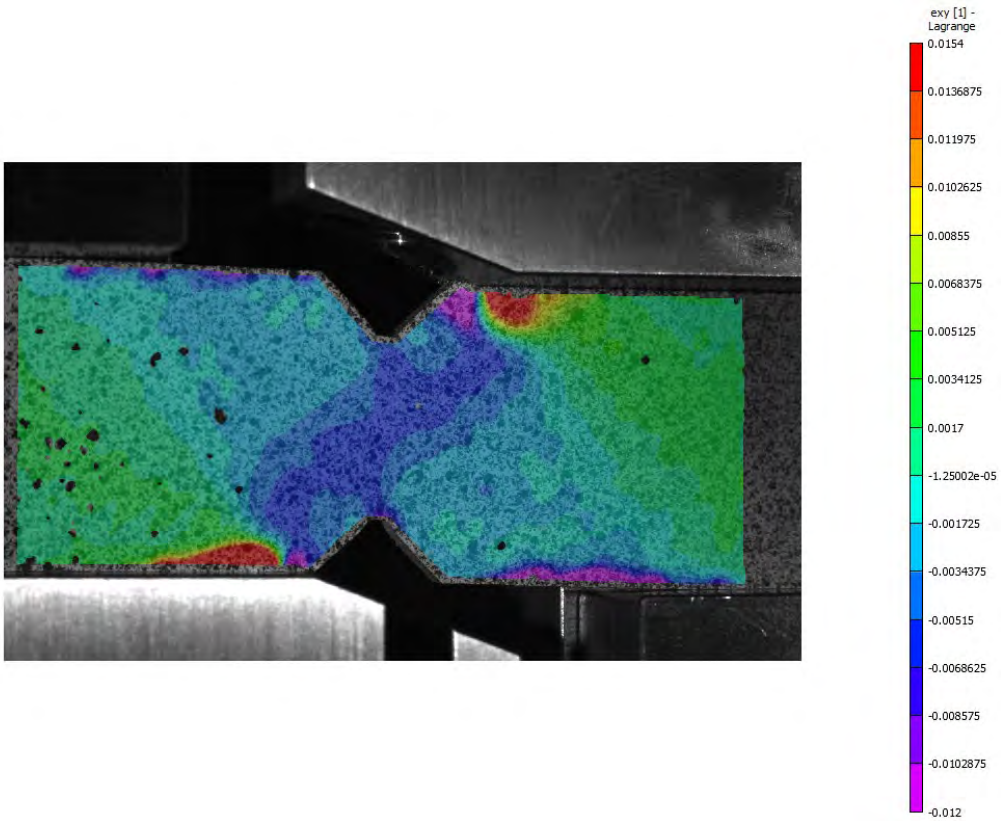

Figure 44. ±45$_s$ Elium-gf Iosipescu in-plane shear specimen at failure. The shear strain follows the fiber axis across the V-notch, with strain concentrations at loading shoulders because of crushing mechanism. Because crushing occurred at loading shoulders, the true shear stress was not obtained from this test.

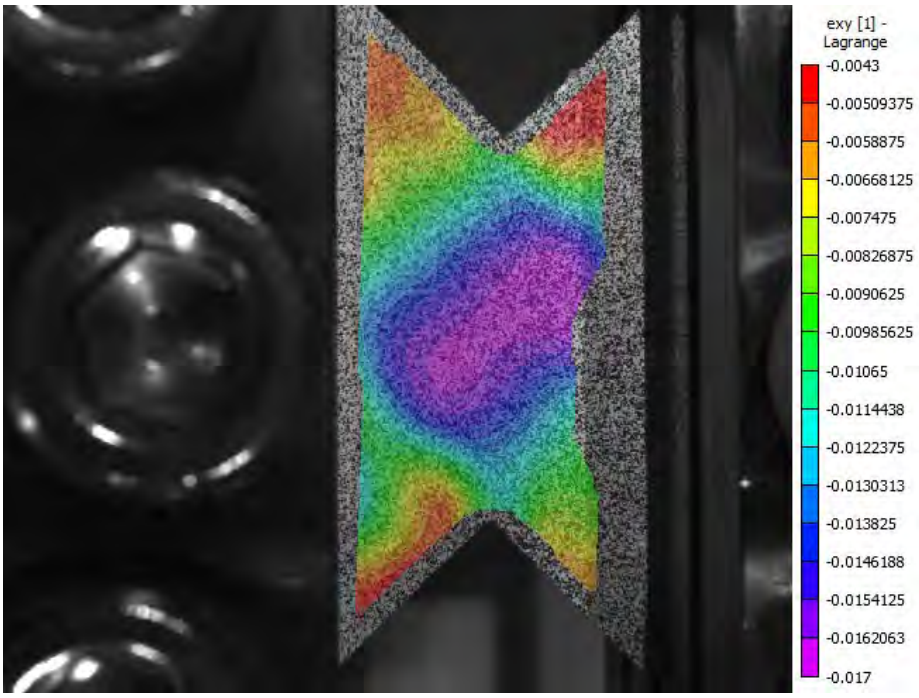

Figure 45. ±45s Elium-gf V-notched rail shear in-plane shear specimen at failure. The shear strain follows the fiber axis across the V-notch.

Interlaminar Shear Strength (ILSS) Results

To determine the interlaminar bond strength of the laminate samples, monotonic short beam interlaminar shear tests were performed for two resin systems (Elium® and epoxy) with various glass fiber reinforcement layups; this was done in accordance with ASTM D2344 (Figure 46). Approximately 10 ILSS samples for each fiber orientation (0_{4s} and $0/90_{2s}$) and resin system were machined from eight-ply laminate panels. Testing was performed using a hydraulic mechanical testing load frame (MTS 858 Material Test System) equipped with a 25 kN capacity load cell, where the samples were subjected to short-beam shear loading until mechanical failure. The ILSS properties are summarized Table 18, which shows the comparable properties for Elium® and epoxy resin systems, with 0_{4s} epoxy-gf samples trending slightly higher regarding the interlaminar shear strength than the 0_{4s} Elium-gf samples.

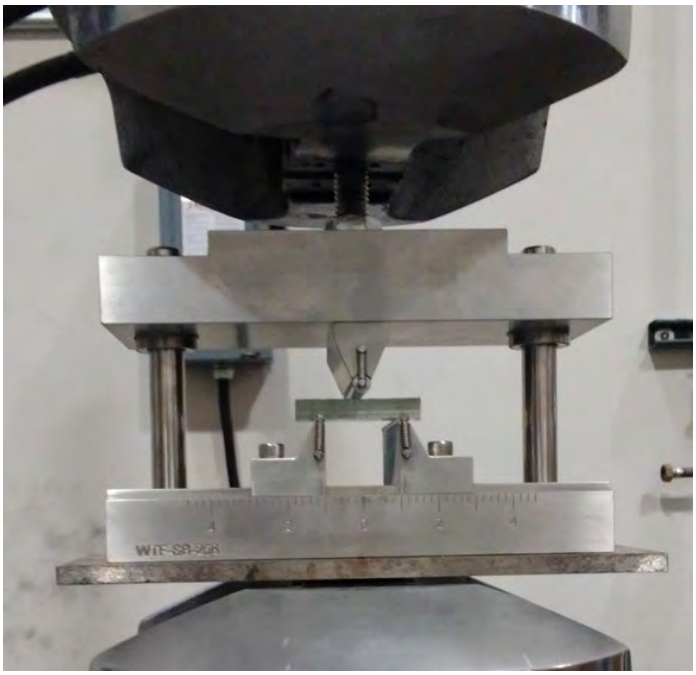

Figure 46. ILSS short-beam shear specimen loaded in fixture.

Table 18. ILSS results from UTK and CSM.

RESIN SYSTEM	FACILITY	FIBER LAYUP	NUMBER OF SPECIMENS	SHORT-BEAM SHEAR STRENGTH (MPA)
ELIUM	UTK	0_{4s}	12	49
		$0/90_{2s}$	12	48
	CSM	0_{4s}	10	50
		$0/90_{2s}$	12	47
EPOXY	UTK	0_{4s}	26	54
		90_{4s}	12	12
		$0/90_{2s}$	12	48
	CSM	0_{4s}	10	54
		90_{4s}	12	11
		$0/90_{2s}$	11	43
		$90/0_{2s}$	12	50

Flexural Results

Flexural specimens were fabricated with eight-ply unidirectional layups using Johns Manville StarRov 086–1200 fiberglass. The thermoplastic resin system was Elium® 188 O with a Luperox AFR40 initiator, and the thermosetting system was Hexion RIMR135 with RIMH1366 hardener at a mixing ratio of 100:30. The specimens were cut using a water-cooled tile saw to produce specimens with longitudinal fiber orientation (fibers parallel to the length of the specimen). Six specimens of each resin type were tested. The specimens were tested in accordance with ASTM D7264 in three-point bending (Procedure A). The specimens were tested on an MTS 370.25 servohydraulic load frame.

The tangent flexural modulus of elasticity is shown in Figure 47. The interquartile range of the moduli for these two systems overlap, but the mean of the Elium® system is 37.0 ± 2.0 GPa, while the mean of the epoxy system is 34.7 ± 2.3 GPa. The flexural strength of the composite laminates is shown in Figure 48.

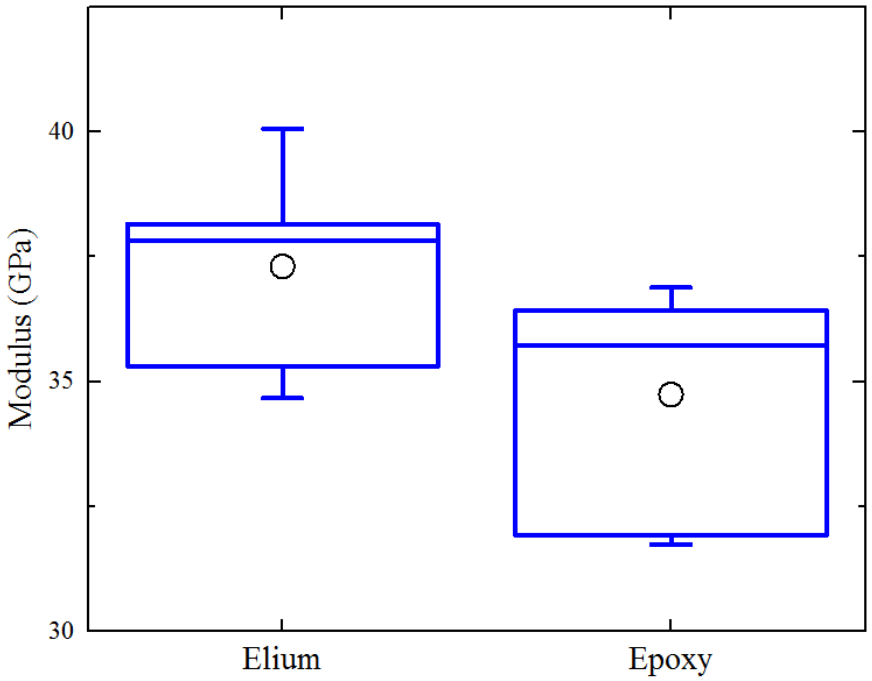

Figure 47. Flexural tangent modulus of elasticity for unidirectional longitudinal Elium® and Epoxy systems. The center point (○) represents the mean, the center line is the median, the box is the inter-quartile range, and the whiskers are 1.5 times the standard deviation.

Neither the IQR nor the standard deviations of the flexural strengths for these systems overlap. The mean flexural strength of Elium® is 1006 ± 85 MPa and for epoxy 809 ± 49 MPa.

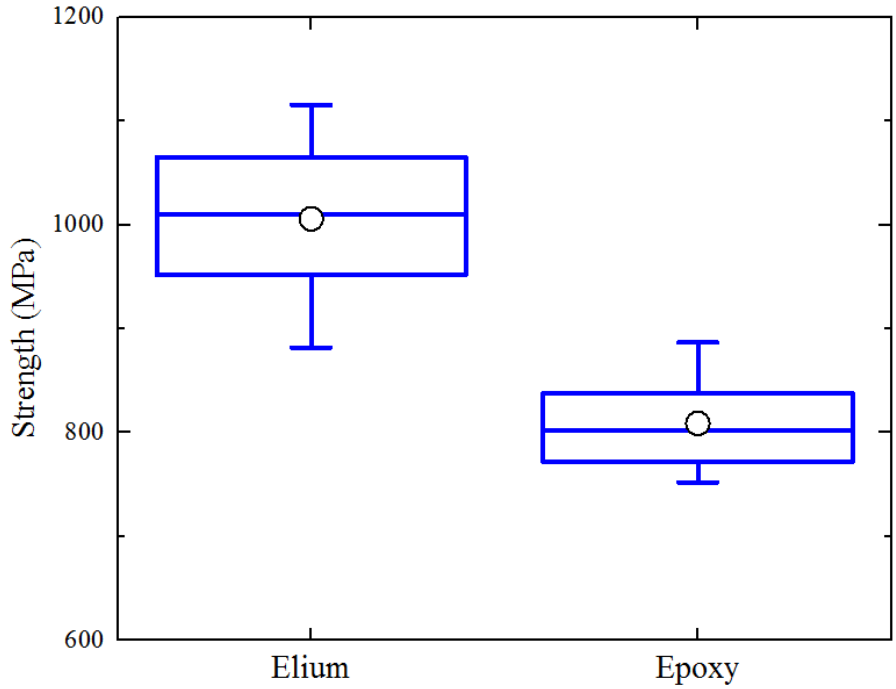

Figure 48. Flexural strength of the unidirectional longitudinal Elium® and Epoxy systems. The center point (○) represents the mean, the center line is the median, the box is the inter-quartile range, and the whiskers are 1.5 times the standard deviation.

Sandwich Core Shear Flexure Test Results

Sandwich core shear flexure tests were performed in accordance with the ASTM C393 three-point bend configuration to determine the baseline flexural properties of the panels consisting of balsa wood cores and glass fiber (0_{2s}, 90_{2s}, and $\pm 45_s$ fiber layups) with reinforced polymer (Elium® or epoxy) skins. DIC was utilized to track strain concentrations and determine failure (Figure 49). As seen in Table 19, for some sample types, large variations in the test results among the panels were noticed with coefficients of variation greater than 20%. Sandwich samples persistently failed because of the core shear near the loading or support noses and/or skin to core delamination, as shown in Figure 50.

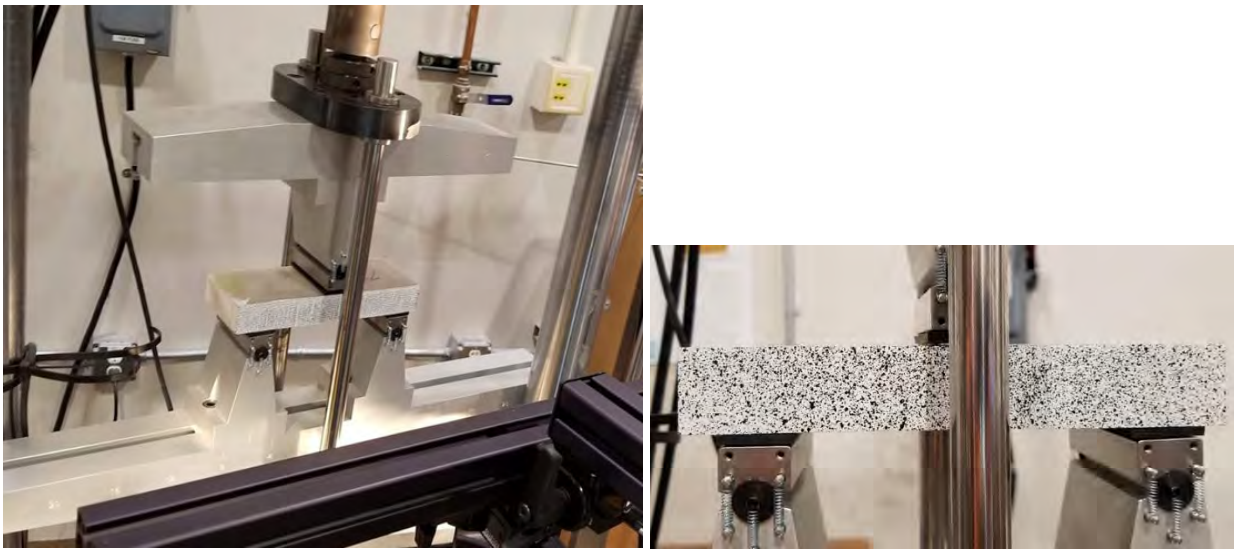

Figure 49. Sandwich panel flexure test setup with DIC specimen.

Table 19. Results of sandwich flexure/core shear testing.

RESIN SYSTEM	FACILITY	FIBER LAYUP	CSUS (MPA)	CSU STD DEV	FACING STRESS (MPA)	FACING STRESS STD DEV
ELIUM	UTK	0_{2s}	1.1	0.3	30	7.0
		90_{2s}	1.7	0.1	43	2.3
		$\pm45_s$	2.2	0.3	71	10
	CSM	0_{2s}	1.1	0.2	30	5.9
		90_{2s}	1.8	0.1	46	3.1
		$\pm45_s$	1.7	0.4	55	13
EPOXY	UTK	0_{2s}	2.4	0.4	68	10
		90_{2s}	1.9	0.1	52	3.8
		$\pm45_s$	2.3	0.2	79	8.1
	CSM	0_{2s}	2.7	0.5	75	12
		90_{2s}	N/A	N/A	N/A	N/A
		$\pm45_s$	N/A	N/A	N/A	N/A

Figure 50. Sandwich sample after core shear and skin-to-core delamination failure.

SCB (Single Cantilever Beam) Test Results for Sandwich Beams

SCB tests were performed for balsa core sandwich panels with skins consisting of two different resin systems (Elium® and epoxy) and an 0_{2s} glass fiber layup. Samples were cut 254 mm in length and 25.4 mm in width, with an initial crack made using a band saw to cut away a 40 mm section of the core from the top skin (Figure 51), followed by sharpening the crack with a razor knife blade (Figure 52). Specimens were glued to stiff plates with Loctite 401 and clamped with a vice until adhesive fully cured to ensure optimum bonding. Before loading, mechanical clamps were attached to help keep the specimen attached to the rigid plate. A hinge was clamped to the top skin and pulled at a 1 mm/min displacement rate until fracture occurred. The crack tip was marked, and the load was removed using a displacement control. Each specimen yielded the approximate cycles of loading and unloading before complete delamination of the skin from the core.

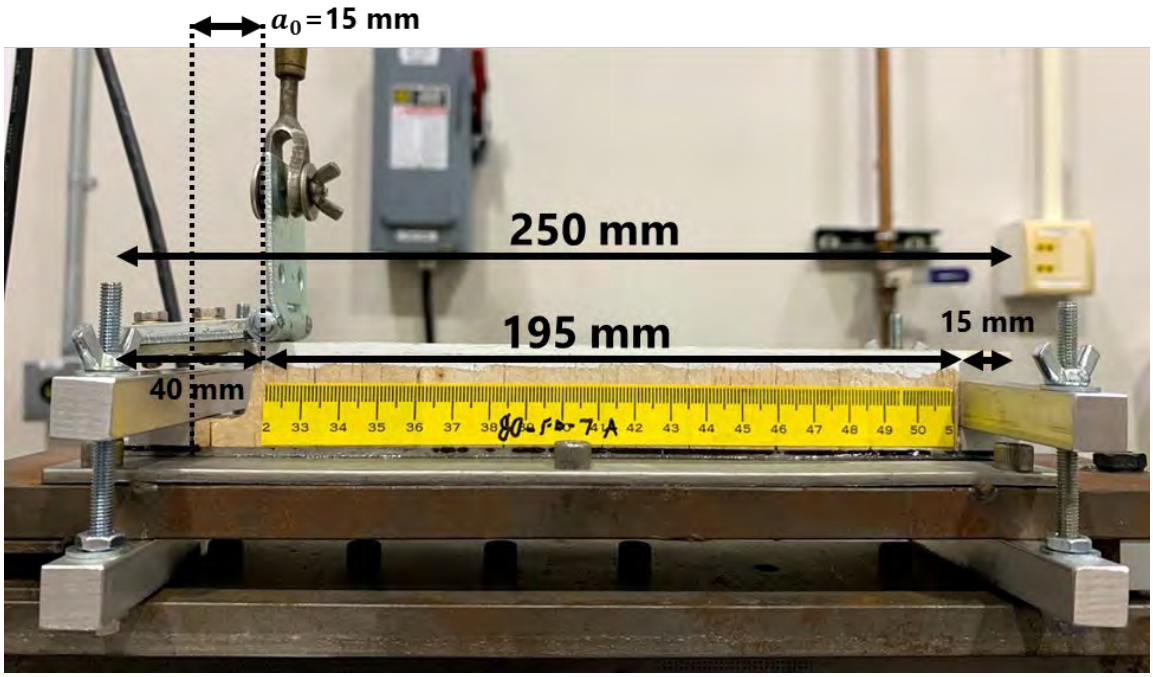

Figure 51. SCB specimen with dimensions.

Figure 52. Crack front at 5x magnification.

Figure 53. SCB test setup for delamination energy release rate determination, with Side A shown.

The strain energy release rate, G_{1c}, was calculated from the load/displacement curve using the trapezoidal method to calculate the area enclosed by a single loop (Figure 54) and then dividing this by the average width of the specimen and the change in crack length for the loop (Equation 2). The crack opening was measured on the near side (Side A) of the specimen, as well as the far side (Side B). The mean G_{1c} was calculated for each specimen and recorded in Table 20.

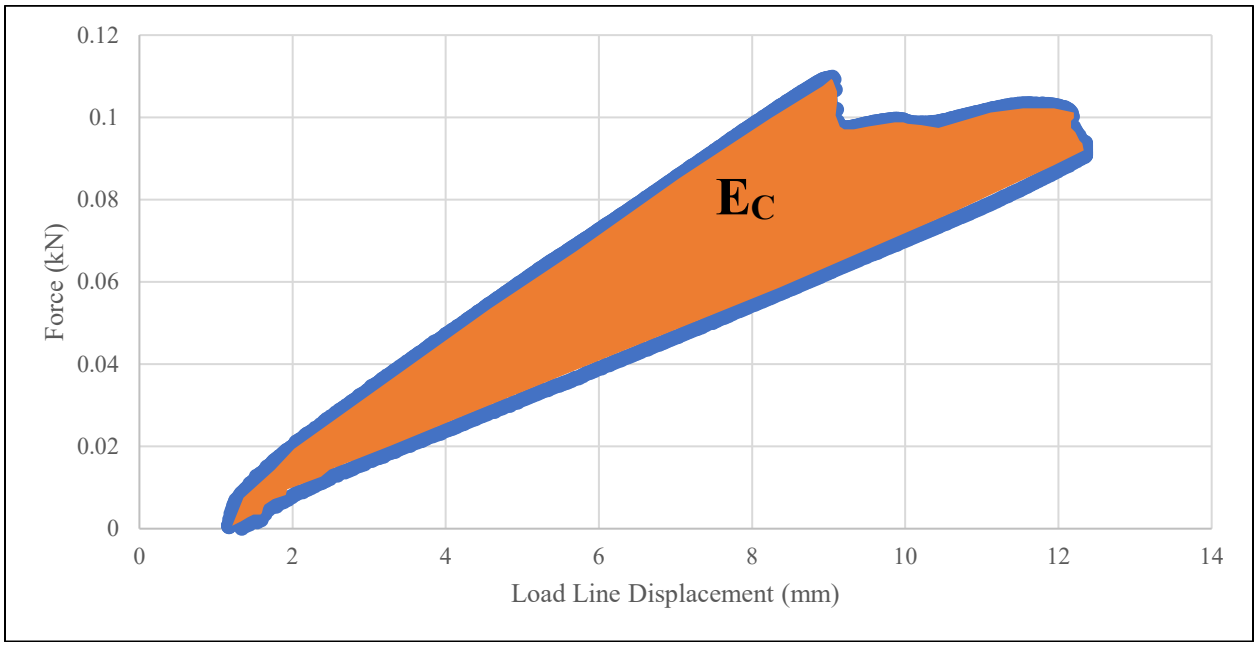

Figure 54. Interpretation of the graphical data for the delamination test.

Equation 2. Energy release rate equation for the SCB test, where E_c is defined in Figure 54.

$$J_{1c} = \frac{E_c}{b\Delta a}$$
$$\Delta a = change\ in\ crack\ length$$
$$b = average\ specimen\ width$$
$$E_c = area\ enclosed\ in\ Force - LLD\ curve$$

Table 20. Energy release rates for the delamination samples.

RESIN TYPE	PANEL ID	SAMPLE ID	SCRIM? (YES/NO)	G_{1C} SIDE A (MPA-M)	G_{1C} SIDE B (MPA-M)
ELIUM	80	FD11	Yes	459	464
		FD13	Yes	668	669
		FD15	Yes	922	902
		FD12	No	1192	1171
		FD14	No	1105	1071
		FD16	No	898	949
EPOXY	71	FD1	Yes	1109	1058
		FD3	Yes	1295	1298
		FD5	Yes	969	975
		FD7	Yes	886	807
		FD9	Yes	1124	1120
		FD4	No	1177	1114
		FD6	No	524	565
		FD10	No	1163	1157

Scrim backing was placed between the bag side skin and the balsa core during manufacturing, as shown in Figure 55. The scrim appeared to have little effect on G_{1c} for the samples with epoxy skins but reduced the G_{1c} values as much as 49% for samples with Elium® skins. In addition, the Elium® sandwich specimens tested on the non-scrim face showed comparable G_{1c} values to those of the epoxy sandwich specimens.

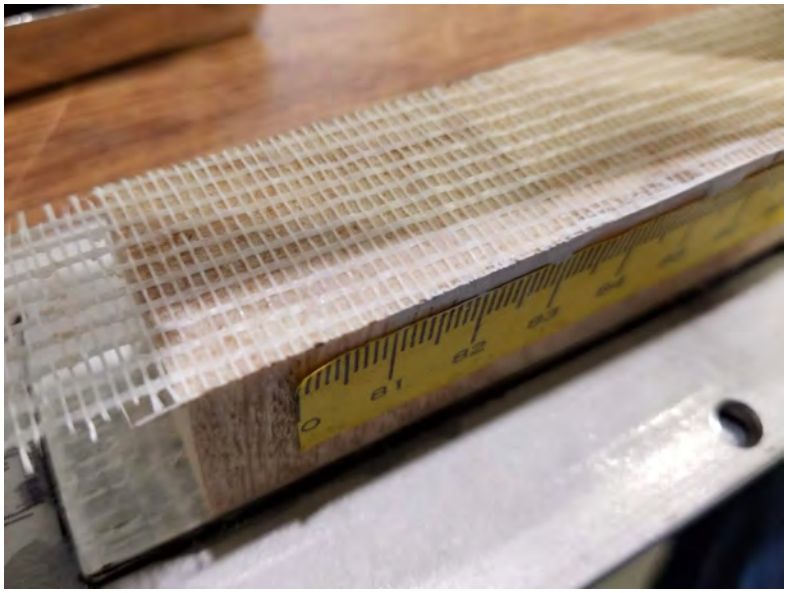

Figure 55. Sandwich delamination sample with scrim backing.

Fatigue Test Results

Round robin fatigue testing of the Elium® thermoplastic system was conducted at two facilities—UTK and CSM—and all specimens were constructed with four glass fiber plies. Longitudinal unidirectional (UD) and transverse UD specimens were fabricated along with panels constructed in a [45/-45/-45/45] layup. G10 epoxy tabs were subsequently adhered to all tensile and compression specimens using Loctite 401 adhesive. Tensile specimens tested at a stress ratio of R = 0.1 were fabricated according to ISO 527, and compression specimens for a stress ratio of R = 10 were fabricated according to ASTM D6641. Fatigue testing was conducted in accordance with ISO 13003. Environmental fatigue testing was conducted at -30 °C.

Figure 56 through Figure 60 show the maximum stress in the cyclic loading curve versus the number of cycles to failure for a stress ratio of R = 0.1. Also included in several of the plots are data from the Sandia National Labs (SNL)/ Montana State University (MSU)/ Department of Energy (DOE) Fatigue Database for Wind Turbine Blade Materials.

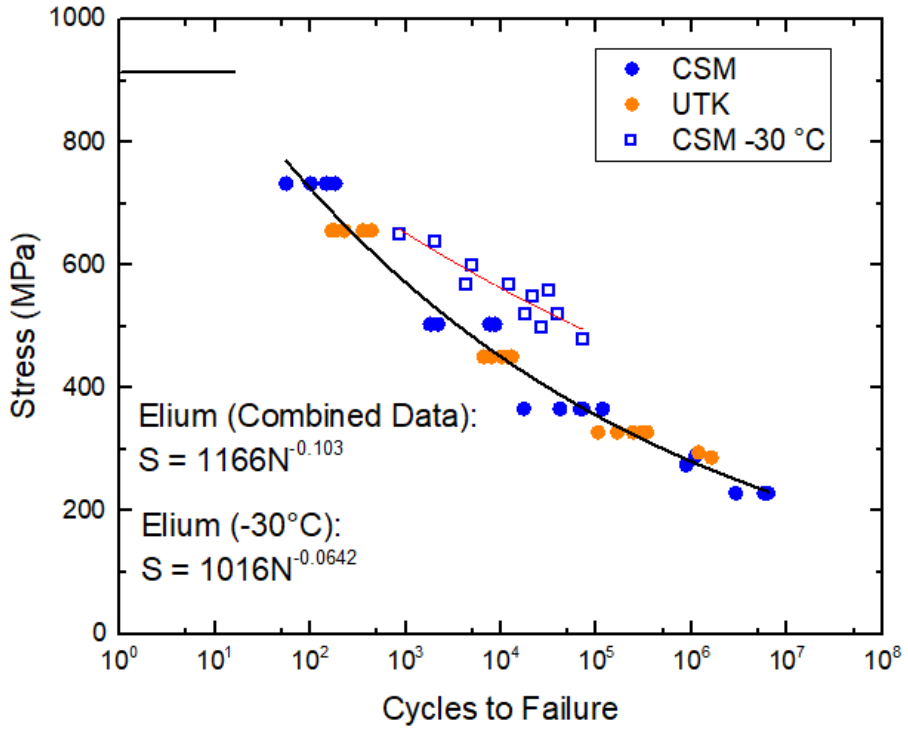

Figure 56. S-N curve for UD longitudinal (0°) Elium® laminates tested at UTK and CSM.

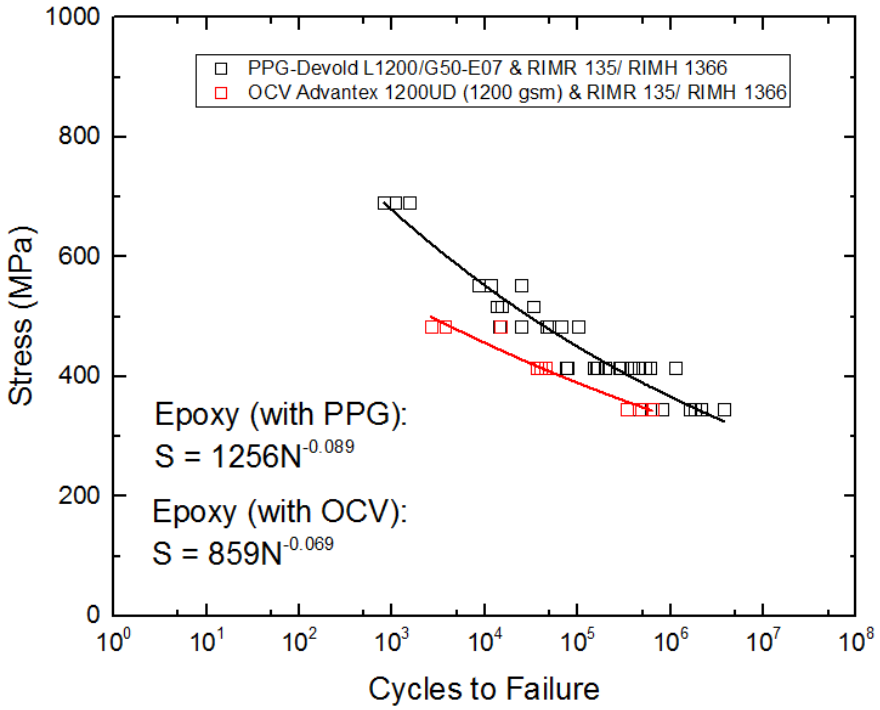

Figure 57. S-N curve for UD longitudinal (0°) epoxy laminates from the SNL/MSU/DOE Fatigue Database for Wind Turbine Blade Materials.

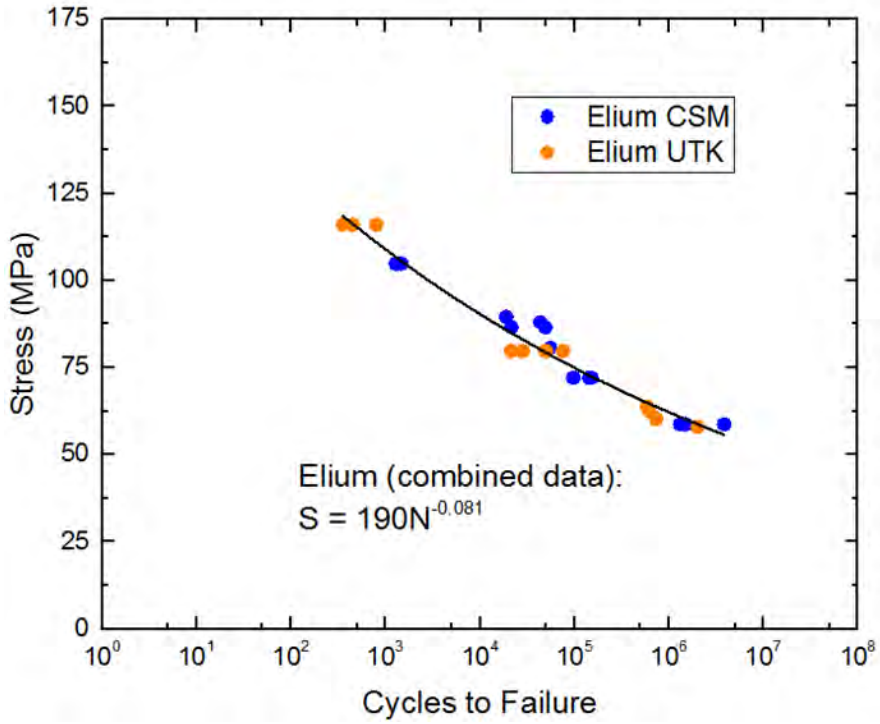

Figure 58. S-N curve for biaxial (±45°) Elium® laminates tested at UTK and CSM.

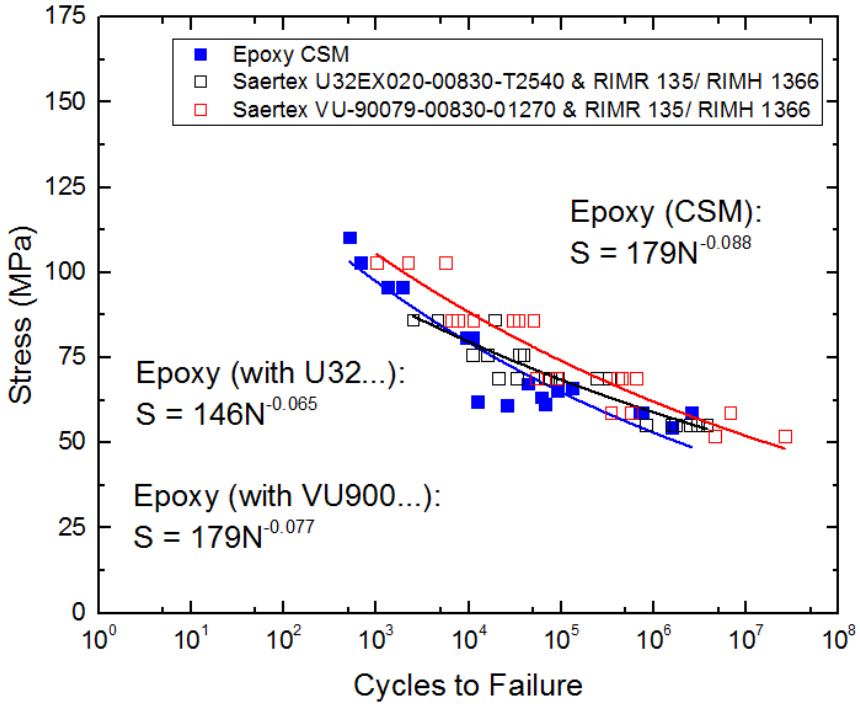

Figure 60. S-N curve for biaxial (±45°) epoxy laminates tested at CSM compared with similar materials from the SNL/MSU/DOE Fatigue Database for Wind Turbine Blade Materials.

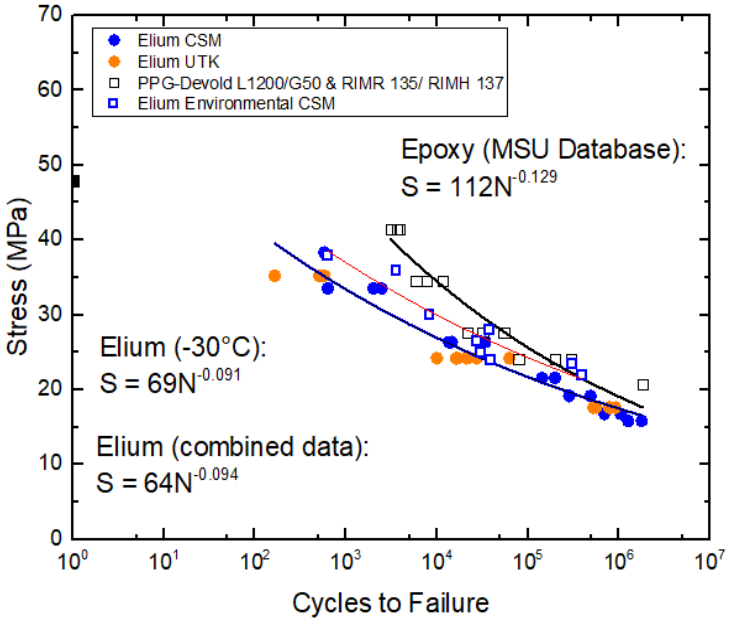

Figure 59. S-N curve for UD transverse (90°) Elium® laminates tested at UTK and CSM compared with similar epoxy material from the SNL/MSU/DOE Fatigue Database for Wind Turbine Blade Materials.

Table 21 gives the maximum stress in the sine curve that is anticipated to yield 10^9 cycles to failure for the various systems investigated. In the case of the UD longitudinal materials, the epoxy systems allow for a higher stress for the 10^9 cycles to failure. However, these systems are dominated by the properties of the glass fibers and not by the fiber/matrix interaction or by the matrix itself. Therefore, it is more informative to consider the case of the UD transverse and biaxial (±45°) material. In each of these cases, the Elium® system gives extrapolated values that are consistent with industry standard epoxy systems. In the case of the biaxial (±45°) materials tested at CSM, Elium® is found to have a higher load capability for a fatigue life that extends to 10^9 cycles. The 086 sizing of the JM fibers may be better suited for the thermoplastic system in this case. This is seen in Figure 61, which shows the optical microscopy images of a glass fiber from a UD transverse fracture surface for Elium® fiber (left) and an epoxy (right). The Elium® adheres better than the epoxy to the fiber, and this was widely observed across the specimens. This demonstrates the drop-in capability that Elium® can afford wind turbine blade OEMs.

Table 21: Extrapolated stress values that lead to failure at 10^9 cycles for various laminates and resin types at a stress ratio of R = 0.1.

Material	Source	Stress for 10^9 cycles (MPa)
UD Longitudinal (0°) Elium	**CSM/UTK**	**137.9**
UD Longitudinal (0°) Epoxy with PPG Fibers	**SNL/MSU/DOE Database**	**198.6**
UD Longitudinal (0°) Epoxy with OCV Fibers	**SNL/MSU/DOE Database**	**205.6**
UD Transverse (90°) Elium	**CSM/UTK**	**9.1**
UD Transverse (90°) Epoxy with PPG Fibers	**SNL/MSU/DOE Database**	**7.7**
±45° Elium	**CSM/UTK**	**35.5**
±45° epoxy (CSM)	**CSM**	**28.9**
±45° epoxy with Saertex U32…	**SNL/MSU/DOE Database**	**38.0**
±45° with Saertex VU900…	**SNL/MSU/DOE Database**	**36.3**

Figure 62 through Figure 64 shows the results of a compression–compression fatigue protocol with a stress ratio of R = 10.

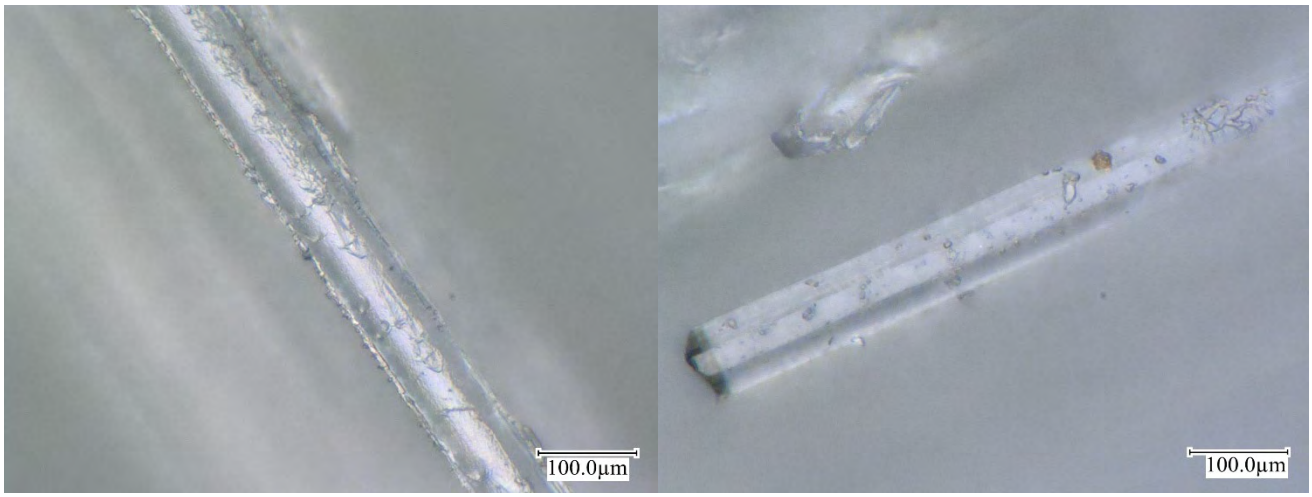

Figure 61. Optical micrographs of the fibers from UD transverse tensile fracture surfaces of Elium® (left) laminate and epoxy (right) laminate. The fiber from the Elium® system is completely coated in resin, while the epoxy system has only polymer particulate left on the surface, a phenomenon observed across these specimens.

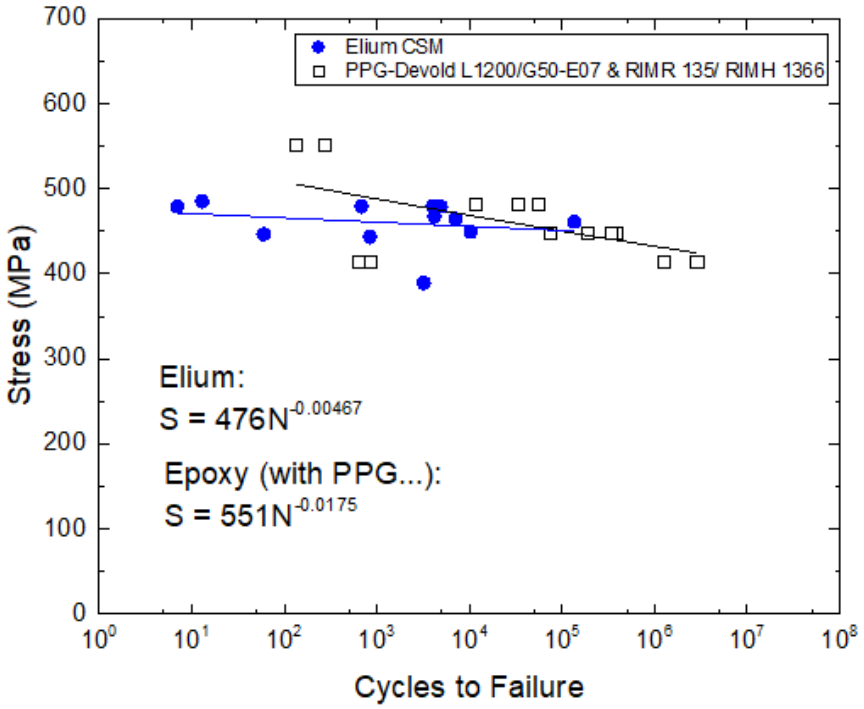

Figure 62. S-N curve (R=10) for the UD longitudinal (0°) Elium® laminates tested at CSM compared with epoxy material with the same laminate layup from the SNL/MSU/DOE Fatigue Database for Wind Turbine Blade Materials. The power regression is for the epoxy system.

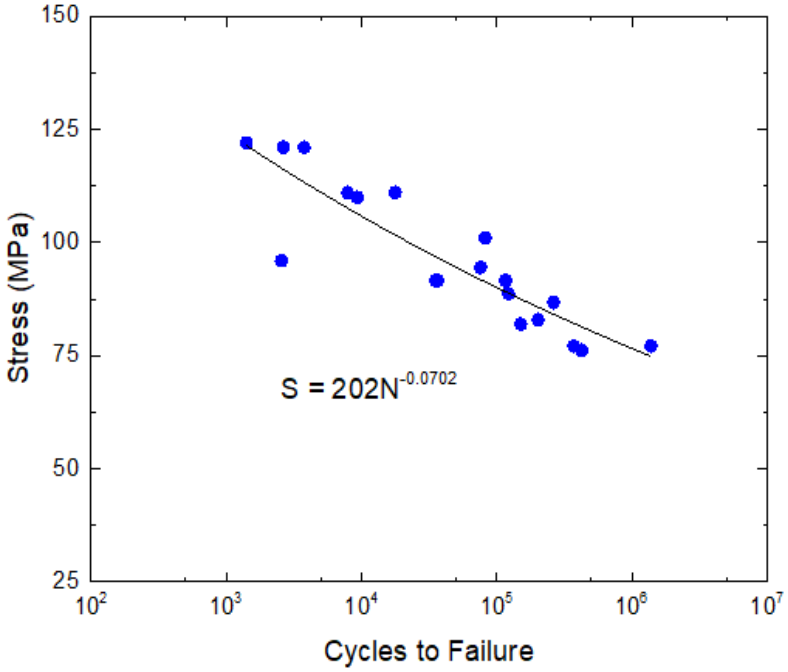

Figure 63. S-N curve (R=10) for the biaxial (±45°) Elium® laminates tested at CSM.

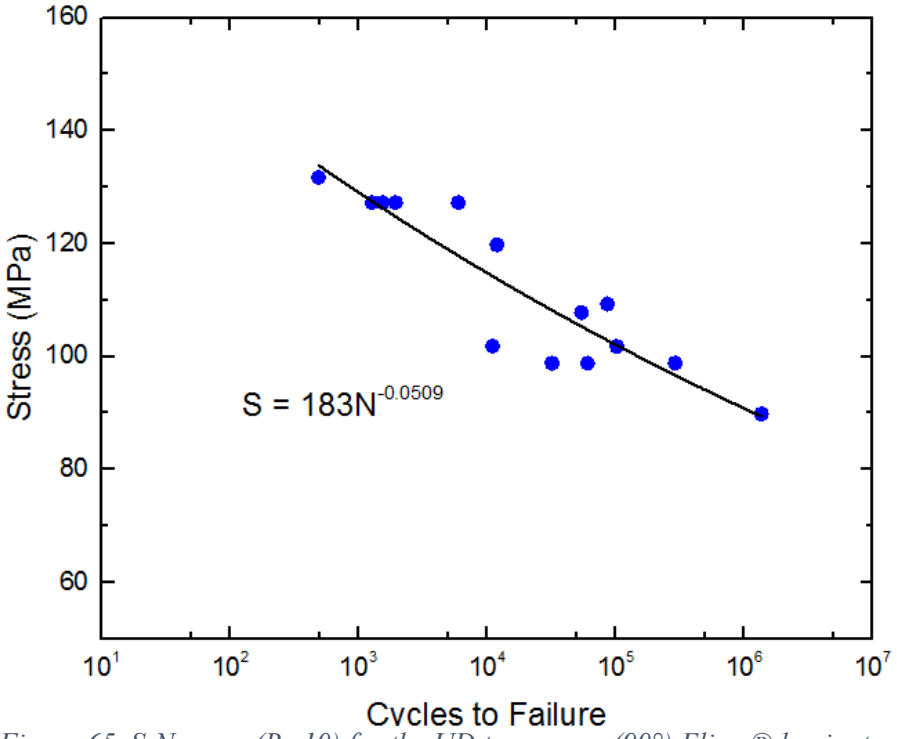

Figure 65. S-N curve (R=10) for the UD transverse (90°) Elium® laminates tested at CSM.

Figure 65 shows the same results as those found in Figure 58 but with the results for the biaxial (±45°) Elium® laminates subjected to fatigue at -30 °C. Interestingly, these data show an increase in fatigue life by roughly one order of magnitude for a given maximum stress.

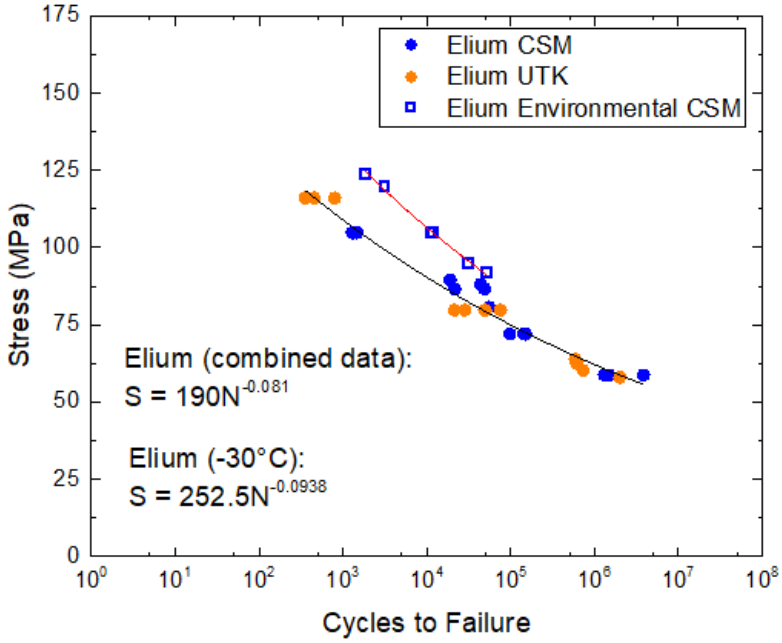

Figure 64. S-N curve for the biaxial (±45°) Elium® laminates tested at UTK (orange circles) and CSM (blue circles). The blue squares show the data for R = 0.1 fatigue testing on this material system conducted at -30 °C.

Effects of Temperature and Humidity Conditioning on Fatigue of $[\pm 45°]_s$ GF/Elium® Laminate Coupons

The effects of increased temperature and humidity on tension-tension fatigue were studied for $[\pm 45°]_s$ E-glass fiber (Johns Manville StarRov 086 – 1200 fiberglass) reinforced thermoplastic (Elium® 188 O with Luperox AFR40 initiator) laminate coupons (GF/Elium). The test coupons were tabbed with G10 material in accordance with standards used for static and non-conditioned fatigue samples (Figure 66), after which the samples were placed in an environmental chamber (Tenney) for 21 days at 70°C and 90% relative humidity (RH) shown in Figure 67. Prior to fatigue testing, the samples were removed from the environmental chamber and kept in a sealed plastic bag for 2 hours at room temperature to allow coupons to cool. The coupons were tested in an MTS universal testing machine with 100 kN capacity load cell, as shown in Figure 68, utilizing a stress ratio of R=0.1, with maximum stress to ultimate tensile strength ratios (UTS taken as 145 MPa, unconditioned static strength) of 0.8, 0.65, 0.55, and 0.4 chosen to directly compare against virgin fatigue coupons. The testing parameters used for these tests are summarized in Table 22, and the corresponding S-N curve is shown in Figure 69 for the conditioned fatigue samples.

Figure 66. Example GF/Elium® coupon after conditioning at 70°C and 90% RH, before fatigue testing.

Figure 67. GF/Elium® coupons inside environmental chamber at 70°C and 90% RH.

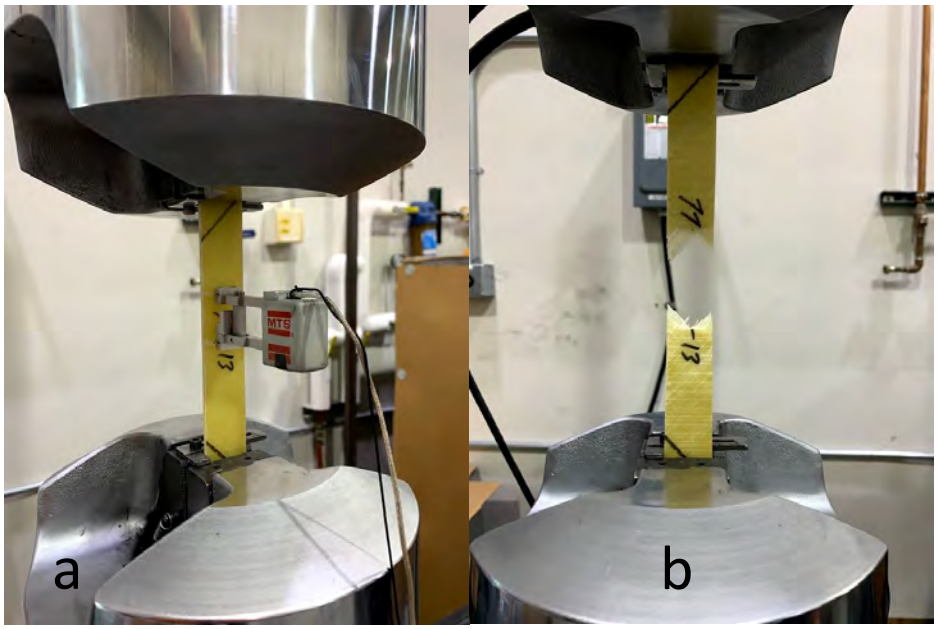

Figure 68. Example GF/Elium® coupon in testing machine before failure (a) and (b) after failure.

Table 22. Test parameters for fatigue testing of $[\pm 45]_s$ coupons.

Percent UTS (%)	Max Stress (MPa)	R ratio	Frequency (Hz)	Number of Samples Tested
80	52	0.1	0.25	8
65	42	0.1	0.25	8
55	36	0.1	1	6
40	26	0.1	3	6

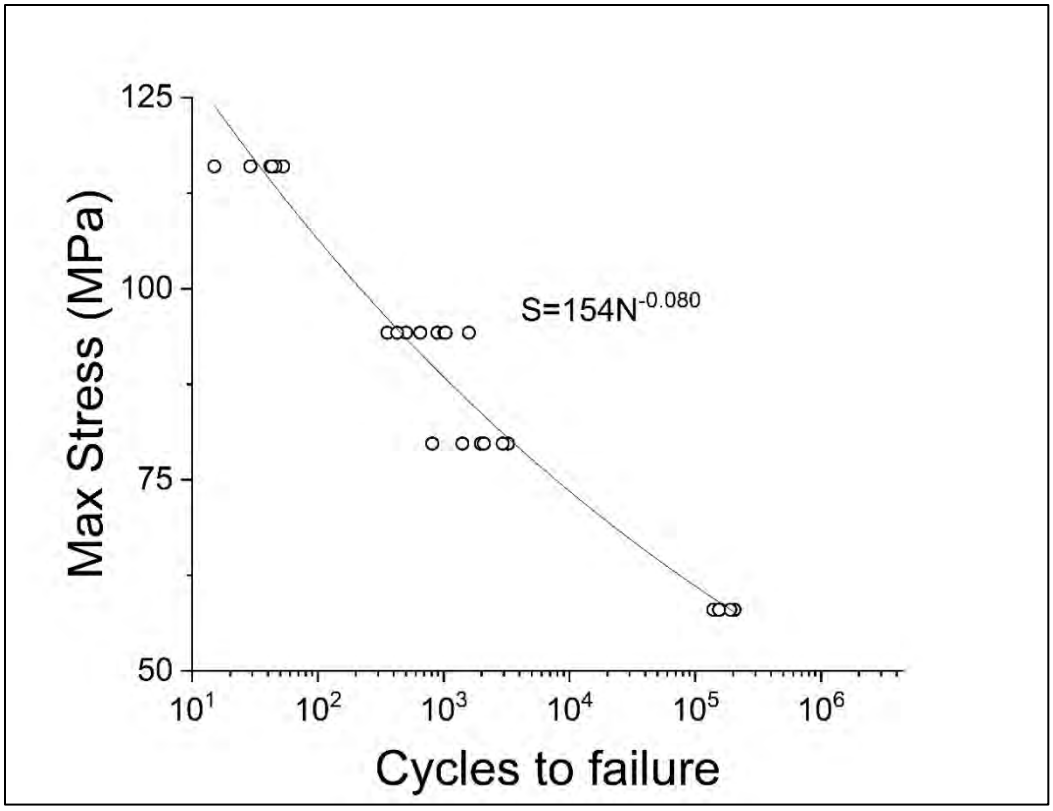

Figure 69. S-N curve for [±45]$_s$ GF/Elium® samples conditioned at 70°C and 90% RH for 21 days.

Additional coupons manufactured utilizing Hexion RIMR135 epoxy resin mixed with RIMH1366 hardener at a ratio of 100:30 and same E-glass reinforcement (GF/epoxy) were tested in T-T fatigue employing the same parameters specified for GF/Elium® coupons. Comparing S-N curves for virgin GF/Elium, conditioned GF/Elium, and virgin GF/epoxy samples, conditioning at 70°C and 90% RH resulted in an order of magnitude reduction in cycles to failure as seen in Figure 70. However, when comparing the maximum stress level at 10^9 cycles, conditioned GF/Elium® was nearly identical to GF/epoxy, but a 5% decrease was observed when compared with virgin GF/Elium® samples as shown in Table 23. It must be noted that projections at 10^9 cycles are gross estimations considering no samples were tested beyond $2*10^6$ cycles for virgin GF/Elium, $2.5*10^6$ for virgin GF/epoxy, and $2*10^5$ for conditioned GF/Elium® systems, and further testing at lower stress levels need to be performed to verify these estimations.

Dynamic mechanical analysis (DMA) of the Elium® unidirectional composites were performed on TA DMA 800 with a single cantilever, using a frequency of 1 Hz over a temperature range from room temperature to 200ºC with scan rate of 3ºC/minute. GF/Elium® specimens approximately 35 mm length by 12 mm width x 3.58 mm were machine cut for DMA testing to evaluate the modulus effects for this material. Due to ±45 fiber orientation of the GF/Elium® coupons, the tensile failure mechanisms typically exhibit a matrix dominated behavior. Based on this failure mode, DMA results included in this study focused on the unidirectional GF/Elium® specimens with transverse fiber orientation (where failure mechanisms are highly matrix dominated) were evaluated to observe the effects of the storage modulus behavior as a function of temperature shown in Figure 71. It is worth noting that DMA results for transverse (matrix dominated) specimens showed a decrease of approximately 30% in the storage modulus of GF/Elium® samples at 70°C (Figure 71). A decrease of approximately 25% in the initial stiffness is shown in Figure 72 when comparing a conditioned sample versus a virgin sample. Failure mechanisms between conditioned and virgin samples were virtually identical on the macroscale as seen in

Figure 73, Figure 74, Figure 75, and Figure 76. Yet, the conditioned GF/Elium® coupon samples are clearly distinguishable from the virgin samples indicating degradation effects of the material are present for the conditioned samples. Investigation of fibers in the failure zone show matrix adhesion along the fibers as well as fiber breakage (Figure 77), similar to failures in virgin samples. These failure mechanisms support JM 086 fiber sizing as well-suited for the Elium® resin matrix.

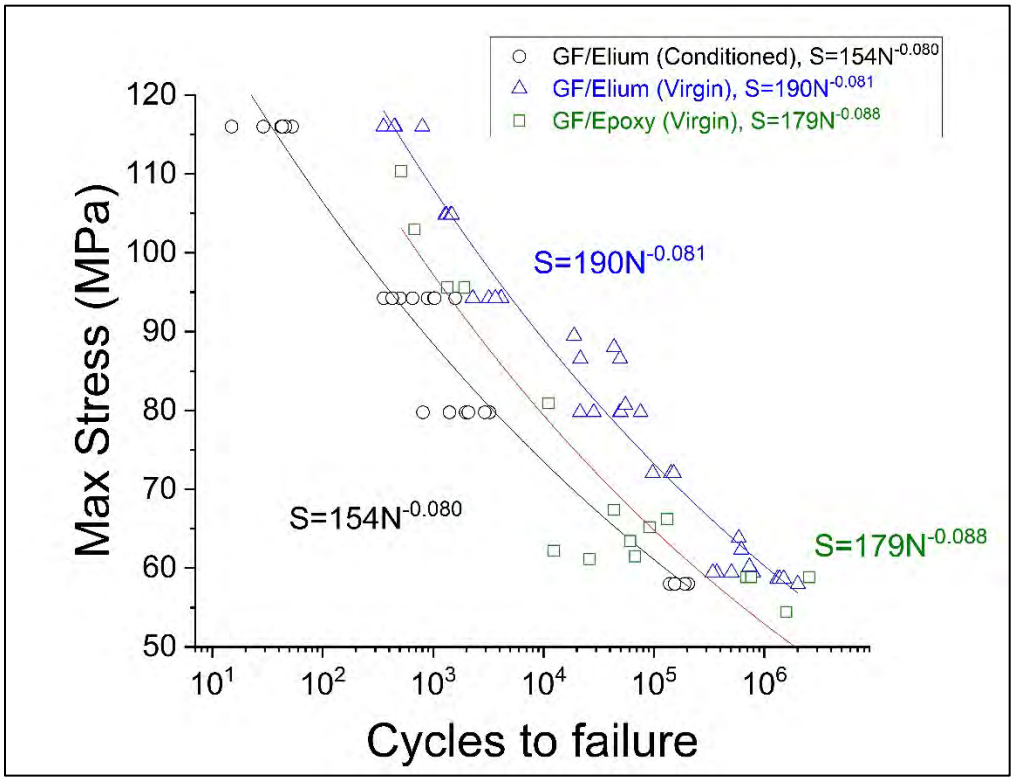

Figure 70. S-N curves for [±45]s conditioned GF/Elium, not conditioned GF/Elium, and not conditioned GF/epoxy.

Table 23. Projected maximum stress level based on S-N curve equation for 10^9 cycles. These projections are gross estimations based on tests with cycle maximums of $2*10^6$, $2*10^5$, and $2.5*10^6$, respectively.

MATERIAL	CONDITIONING	MAX STRESS FOR 10^9 CYCLES (MPA)	PERCENT OF UTS AT 10^9 CYCLES (%)
$[\pm45°]_s$ GF/Elium	**Not conditioned**	**35.5**	**24.5**
$[\pm45°]_s$ GF/Elium	**70°C, 90% RH, 21 days**	**29.3**	**20.2**
$[\pm45°]_s$ GF/Epoxy	**Not conditioned**	**28.9**	**19.6**

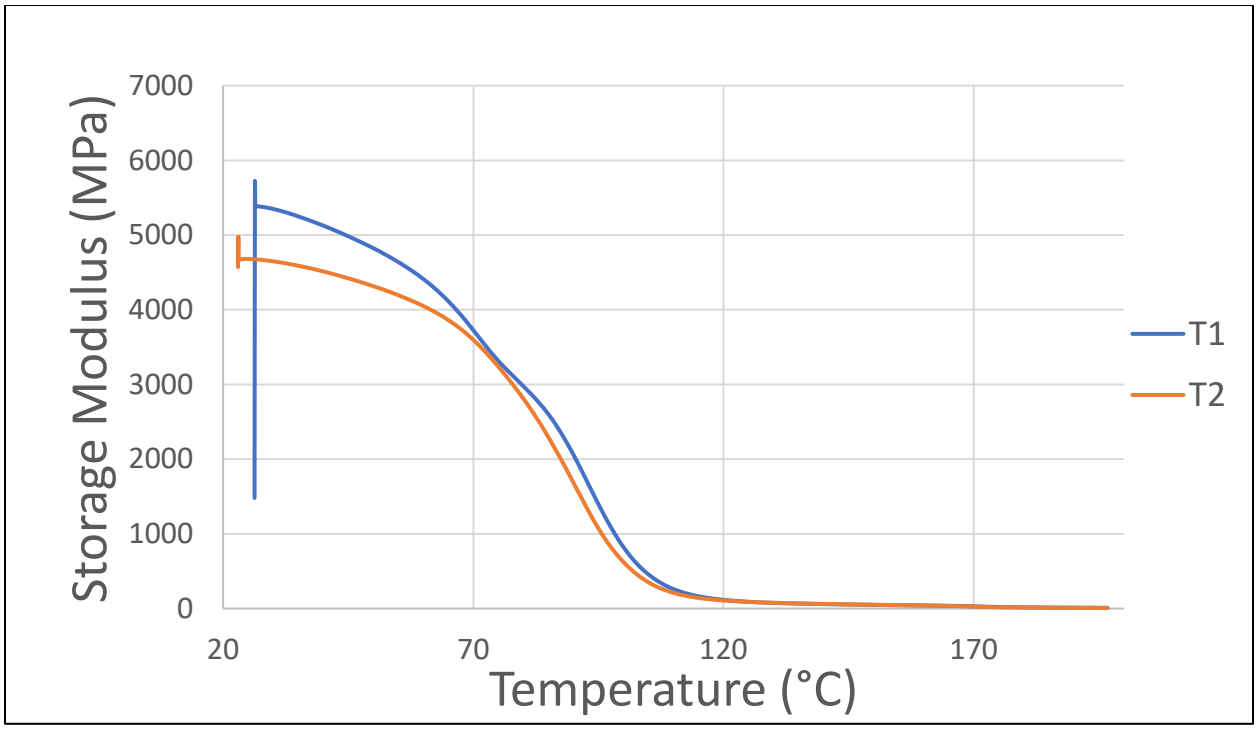

Figure 71. DMA results for transverse [90_4] GF/Elium® samples. A decrease of approximately 30% was shown at 70°C.

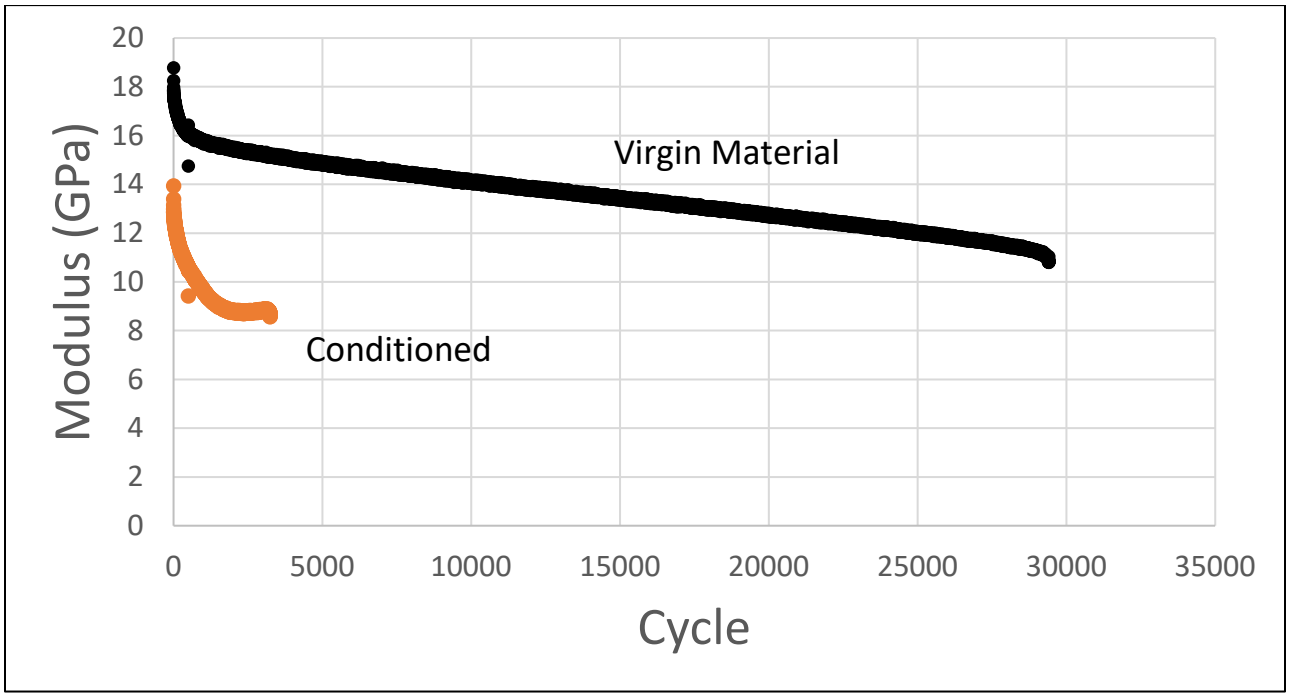

Figure 72. Modulus degradation of conditioned and not conditioned GF/Elium® fatigue samples tested at 55% max stress to UTS ratio. A difference of nearly 20% can be seen in the initial stiffness of the material.

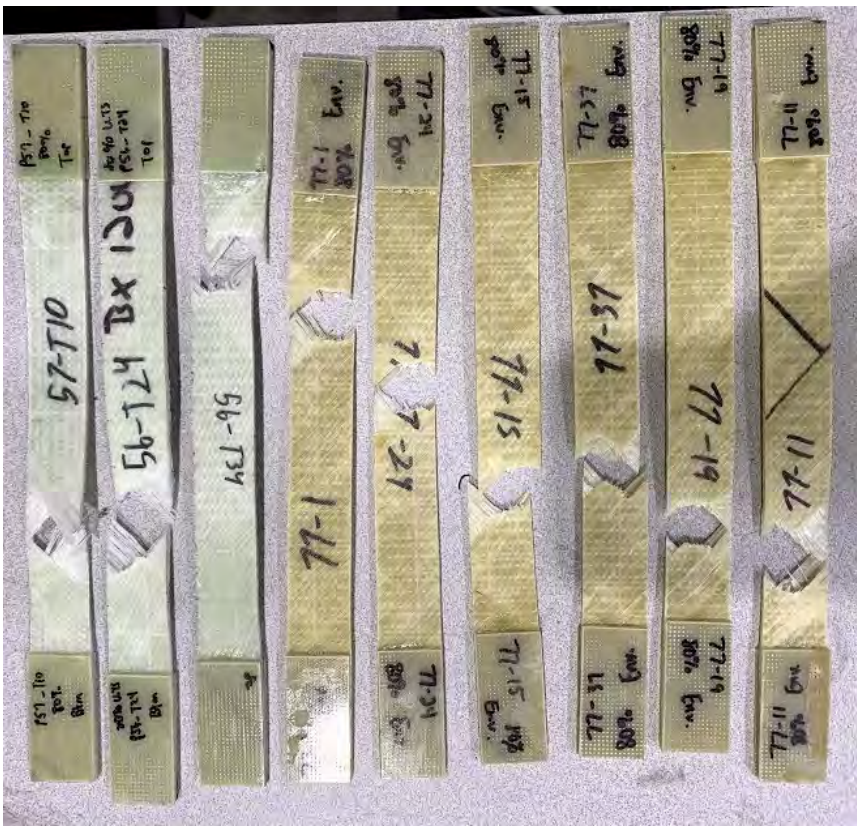

Figure 73. Typical failures of 80% UTS $[\pm 45]_s$ GF/Elium® fatigue samples. Discolored samples were conditioned, while white samples were virgin material.

Figure 74. Typical failures of 65% UTS $[\pm 45]_s$ GF/Elium® fatigue samples. Discolored samples were conditioned, while white samples were virgin material.

Figure 75. Typical failures for 55% UTS $[\pm 45]_s$ GF/Elium® samples. Discolored samples were conditioned, while white samples were virgin material.

Figure 76. Typical failures for 40% UTS $[\pm 45]_s$ GF/Elium® samples. Discolored samples were conditioned, while white samples were virgin material.

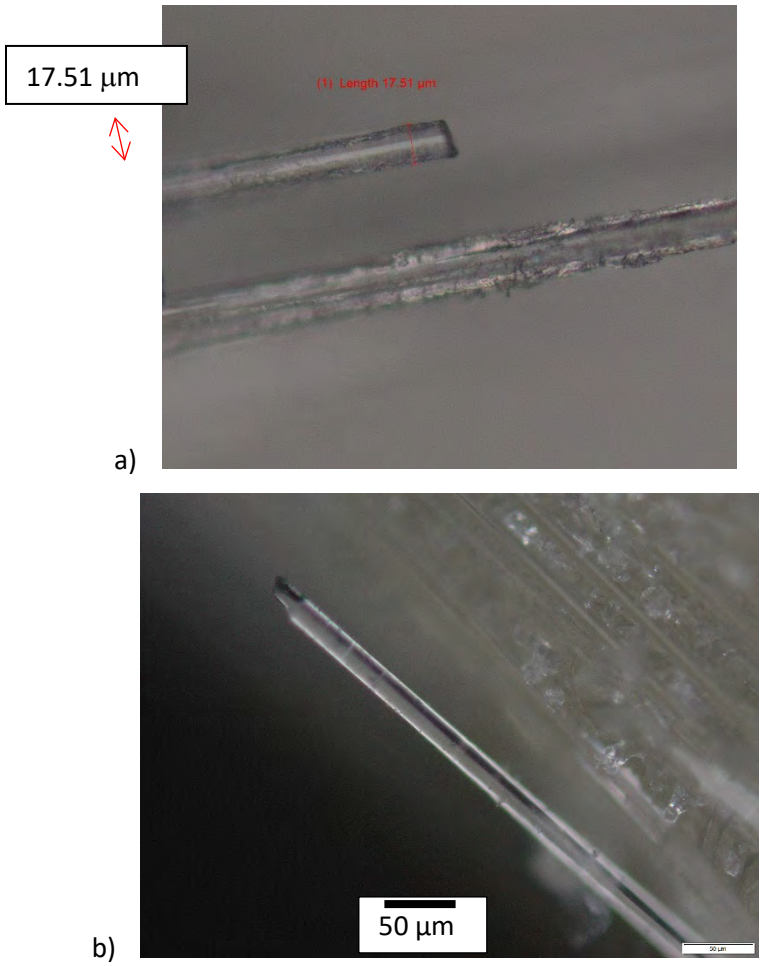

Figure 77. Optical micrographs of failure surfaces for conditioned GF/Elium® samples. Matrix adhesion can be seen across the fiber surface (a), but certain fibers presented obvious pullout characteristics. Figure (b) shows a fractured fiber with shear fracture surface, an uncommon observation.

5.4 Effects of Defects for Elium® Composite Materials

UTK research

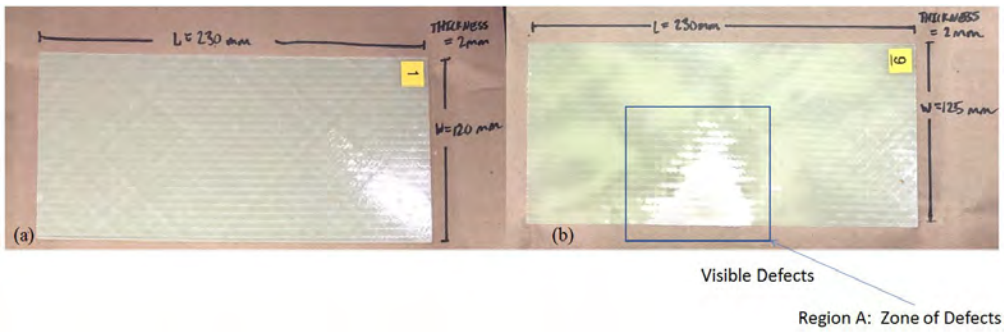

Figure 78: ±45 fiber orientation degree Elium® fiber reinforced panels (a) without visible defects and (b) visible zone of defects.

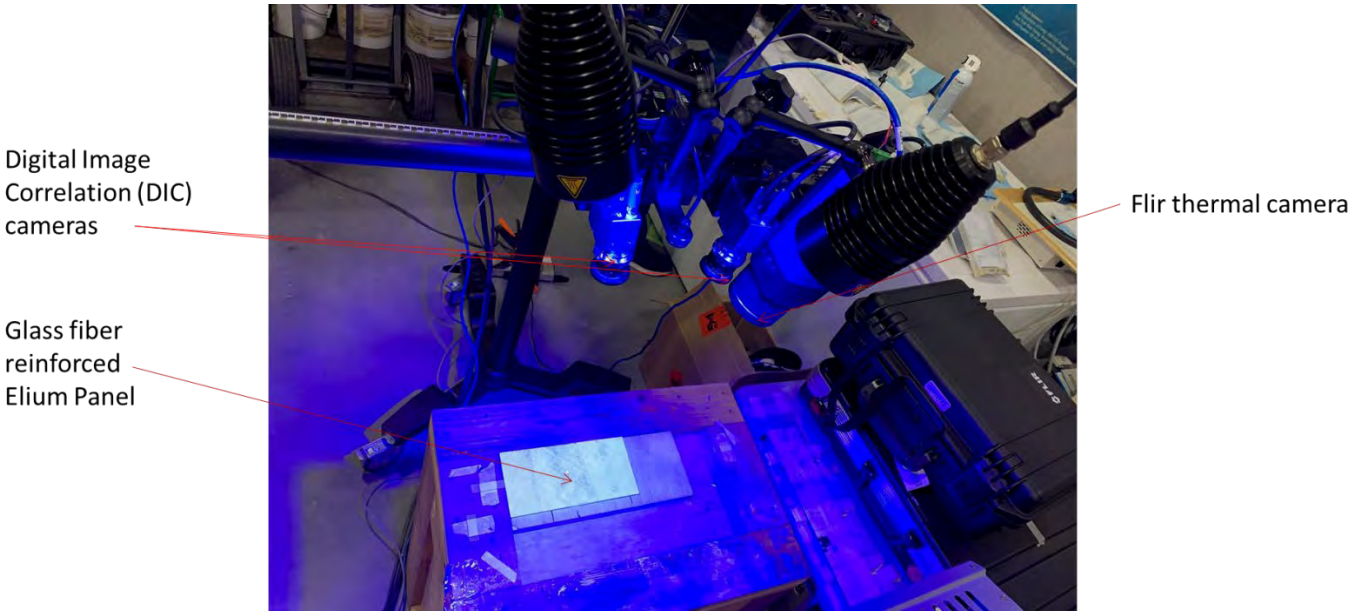

Figure 79. Experimental setup for mechanical flexural testing of ±45 fiber orientation degree Elium® fiber reinforced panels using thermal digital image correlation (TDIC).

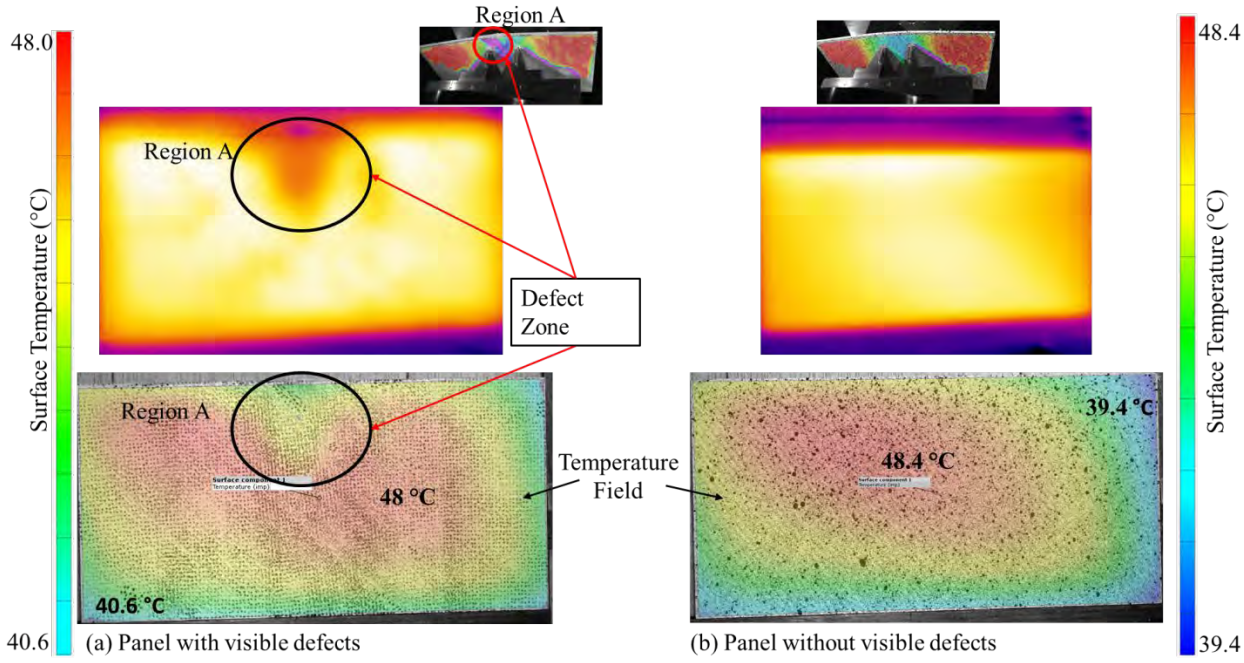

Figure 80. Thermal map of the surface of ±45 fiber orientation degree Elium® fiber reinforced panels using thermal digital image correlation (TDIC) (a) with visible defects and (b) without visible zone of defects.

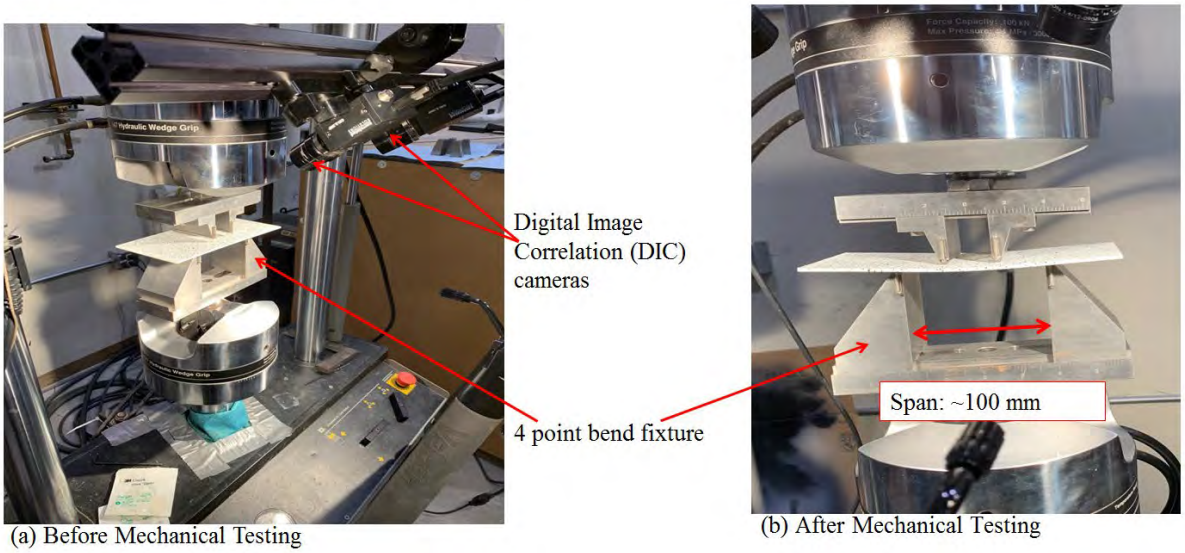

Figure 81. Experimental setup for the mechanical flexural testing of ±45 fiber orientation degree Elium-gf reinforced panels.

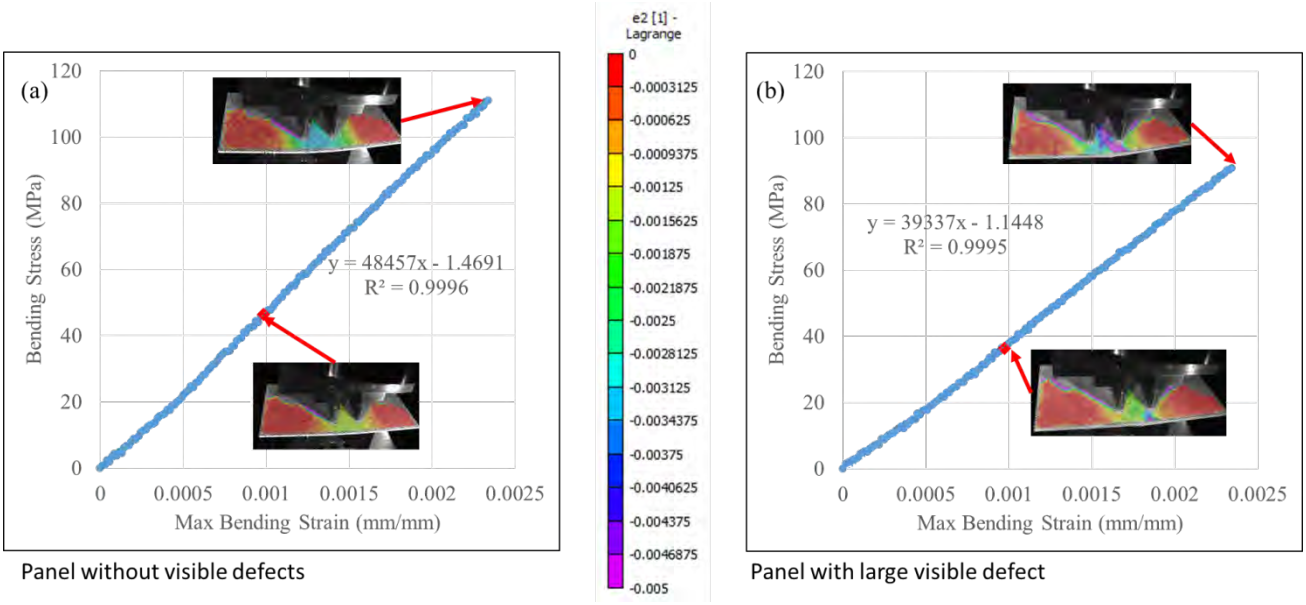

Figure 82. Stress-strain flexural behavior of ±45 fiber orientation degree Elium® fiber reinforced panels using digital image correlation (DIC) (a) with no visible defects and (b) visible zone of defects.

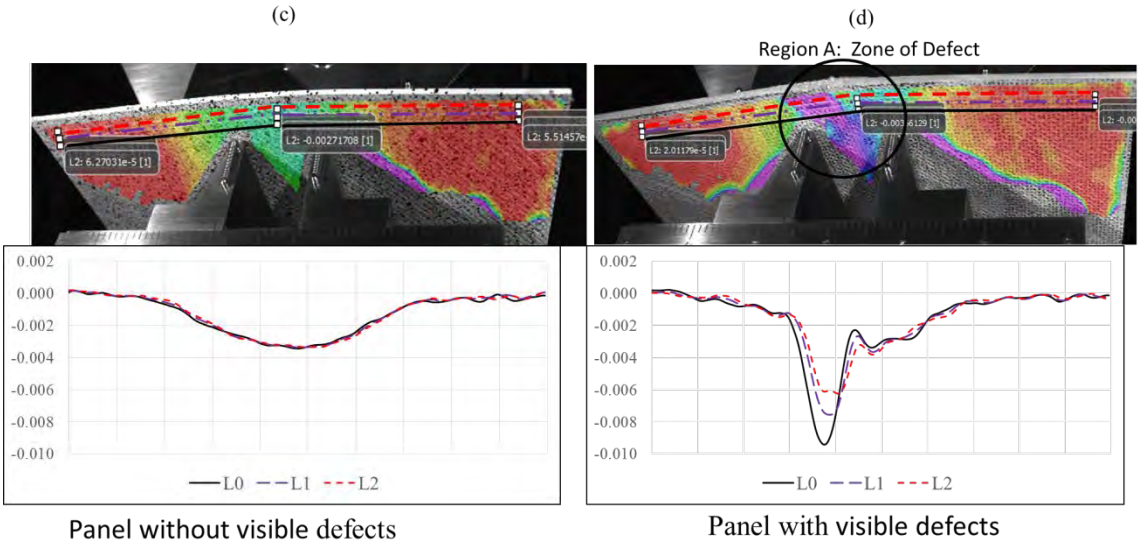

Figure 83. Strain profile comparison of panel (c) with no visible defects and (d) visible zone of defects.

It is critical to investigate defects, such as voids and nonwetting of fibers, that can occur during the manufacturing of the panel resulting from poor infusion. The effects of the defective regions were investigated using a panel with no visible defects (230 mm length x 120 mm width x 2 mm thickness) and a panel with visible defects (230 mm length x 125 mm width x 2 mm) as shown in Figure 78. A novel nondestructive technique called thermal digital image correlation (TDIC) provides a unique ability to provide high spatial resolution strain fields at elevated temperatures and can be used as a predictive method to quickly identify defective regions within fiber reinforced panels. TDIC consists of a thermal camera (Flir) to thermally map the panels, monitoring temperature regions within the panel and DIC utilizing a technique where the panels are speckled with a random pattern and two stereo cameras (Aramis) track the displacement of the speckles to calculate the strain of panel subject to thermal or mechanical loading. The panels were placed in an oven at 90 °C for 30 minutes and then promptly removed and placed onto a substrate beneath TDIC cameras to thermally map the strain fields as the panels cooled to room temperature, as shown in Figure 79. As shown in Figure 80a, the panel with defective regions can clearly be observed when compared with the panel without visible defects (Figure 80b). Flexural mechanical testing coupled with DIC (Correlated Solutions) was performed on the panels, where the panels were mounted on a three-point test fixture (Wyoming Test Fixtures WTF-FL, Salt Lake City, UT), as shown in Figure 81. The flexural tests were performed on a servohydraulic load frame with 88.9 kN load cell capacity at a crosshead rate of 9.25 mm/min and loaded until a maximum deflection of 2.5 mm was reached. Figure 82. shows example stress-strain behavior and strain evolution for the panels, where the modulus panel without visible defect (48.457 GPa) was 21% higher than the panel with visible defects (39.337 GPa). Furthermore, the strain development comparison between the panels be can clearly observed in Figure 83, where the panel without defects exhibited uniform strain field deformation (0.003 mm/mm) and where the panel with visible defects showed significantly more strain variations, as much as approximately two to three (0.006 to 0.009 mm/mm) times higher compared with the panel without visible panels.

CSM Research

Methods

Fabrication of test panels

Two rounds of defect panels were fabricated at the National Wind Technology Center (NWTC) in Boulder, Colorado. In the first round, four defect panels and one "baseline" panel were fabricated at the NWTC. Test specimens were cut using a water-cooled tile saw at the Colorado School of Mines (CSM). G10 epoxy tabs were adhered using Loctite 401 adhesive at CSM. Table 24 summarizes the defect type that was introduced to each of the panels.

Table 24. Methods of defect introduction for the panels produced for the first round of testing.

Panel Designation	Defect
D001	Resin boiled
D002	No defect; same procedure as developed by TPI
D003	No degassing of resin
D004	Resin boiled AND no degassing of resin
Baseline	No defect; same procedure as developed by TPI

For panel D001, the resin was boiled *after* infusion by heating the table on which the panel was fabricated. For panel D002, no defects were purposely introduced. For this panel, the resin was degassed and the VAP membrane was used during fabrication as in the procedure developed by TPI Composites. The resin for panel D003 was not degassed prior to infusion which is the standard fabrication procedure. In panel D004, the resin was not degassed prior to infusion and the table was also heated after infusion to further introduce boiling. The Baseline panel, similar to panel D002, was fabricated by the standard procedure developed by TPI that includes degassing the resin and using a VAP membrane.

In the second round, panels were fabricated at the NWTC using a method established by TPI composites that was the same as that used in fabrication of the panels for the mechanical testing portion of this report. Specimens were cut at the NWTC using a water-cooled tile saw. G10 epoxy tabs were adhered using Loctite 401 at CSM. Table 25 summarizes the defects that were introduced to these panels.

Table 25. Methods of defect introduction for the panels produced for the second round of testing.

Panel Designation	Defect
014	No Defect
015	No Defect
016	VAP membrane used.
017	No VAP membrane used. Leak in infusion line.

Mechanical Testing

An MTS Landmark servohydraulic load frame was used from mechanical testing. Specimens were tested in fatigue by sinusoidal cyclic loading according to ISO 13003. A stress ratio ($\sigma_{min}/\sigma_{max}$) of 0.1 was targeted for all tests. An ultimate tensile strength (UTS) was assumed to be 146.7 MPa based on monotonic testing of panels fabricated using the same layup and material at TPI composites. The imposed σ_{max} was 55% of this UTS. A frequency of 0.25 Hz was used for testing. A FLIR A325sc infrared (IR) camera was used to monitor the heating of the specimens as the test progressed.

X-ray Computed Tomography

X-ray CT scans were taken using a Zeiss Verso 520 instrument with X-rays produced from electrons at 40 kV for the low-energy scan and from electrons at 80 kV for the high-energy scan. For the low-energy scan, an LE1 filer was used to narrow the X-ray spectrum and this resulted in an average X-ray energy of 15 kV. Similarly, at the high-energy level, and HE4 filter was used resulting in an average X-ray energy of 50 kV. Using these sources, the sample was scanned twice without removing the sample or changing its position in the instrument. The dual energy scan allows a better segmentation between the air and polymer and between the polymer and glass compared to using a single source. Additionally, the void content can be calculated by summing the volume elements associated with air. A Deben (Suffolk, UK) load frame was used to load a small tensile specimen from panel D003 in-situ so that the void distribution in the specimen could be elucidated before and after loading. The specimen loaded into the frame is shown in Figure 84. After an initial scan of the unloaded specimen, it was loaded at 0.5 mm/min to 1 kN, then returned to a neutral position (2 N of force) for the next scan. Subsequently, the specimen was loaded to 1.2 kN at 0.5 mm/min, returned to a neutral position at the same rate, and then scanned for a third time.

Figure 84. Deben in-situ X-ray computed tomography load frame. At left, the specimen can be seen loaded into the frame and on the right, the instrument is loaded in the XCT cabinet.

Results

Fatigue Testing

Table 26 summarizes the results of the defect panel fatigue testing. The baseline panels failed on the order of 10^3 to 10^4 cycles. Panels D001, D003 and D004 failed on the order of 10^2 cycles. Despite the fact that no defects were intended to be introduced to panel D002, it is shown to have the worst fatigue life lasting only 10^0 to 10^1 cycles. Since these materials are oriented in a ±45° orientation, the difference between the 0° and 90° testing directions should be minimal. Therefore, on average, the defect panels D001, D003, and D004 lose an order of magnitude or more fatigue life compared to the baseline panels.

Table 26. Cycles to failure for the various panels from the first round of fabrication.

Panel	Specimen	Cycles to Failure
Baseline	0° 1	2,569
Baseline	0° 2	7,357
Baseline	90° 1	1,486
Baseline	90° 2	2,631
D001	0° 1	155
D001	0° 2	152
D001	90° 1	198
D001	90° 2	65
D002	0° 1	16
D002	0° 2	16
D002	90° 1	1
D002	90° 2	3
D003	0° 1	60
D003	0° 2	63
D003	90° 1	113
D003	90° 2	10
D004	0° 1	77
D004	0° 2	67
D004	90° 1	165
D004	90° 1	37

Table 27 gives the cycles to failure for specimens cut from panels from the second round of fabrication. Panels 014 and 015 are seen to have fatigue life that is about an order of magnitude higher than panels 016 and 017. The voids originating in the defect specimens cause delamination between the fiber and the matrix to form more quickly, because those voids are, in effect, "pre-delamination" that doesn't exist initially in the baseline panels (014 and 015).

Table 27. Cycles to failure for the various panels from the second round of fabrication.

Panel	Specimen	Cycles to Failure
014	1	8,260
014	2	6,293
014	3	6,274
014	4	3,732
015	1	8,794
015	2	18,827
015	3	10,833
015	4	7,362
016	1	507
016	2	578
016	3	635
016	4	546
017	1	388
017	2	62
017	3	1,090
017	4	273

IR Imagery

Videos from the IR camera show that damage tends to accumulate in 45° strata along the specimen and this is where heating is observed as shown in Figure 85. The temperature of the hot spots for representative specimens of each panel are presented in Figure 86. All specimens show a spike in temperature into the high 30's °C that is associated with the failure event.

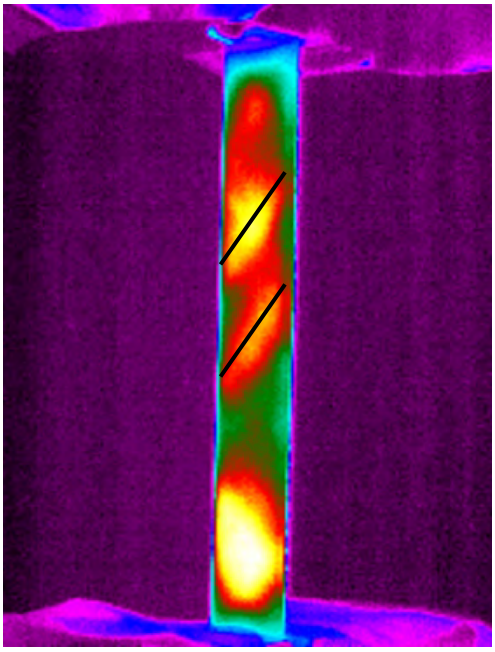

Figure 85. IR image of a defect specimen before failure during mechanical testing. The black lines are inserted to highlight the 45° striations formed where damage accumulates.

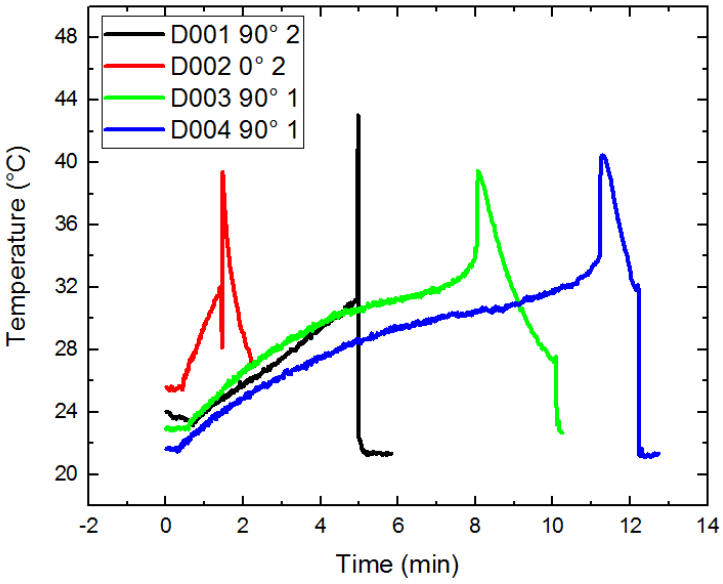

Figure 86. Temperature profiles of "hot spots" for defect panel specimens over the course of the fatigue tests. Note that the cyclic loading frequency is the same for all samples so the time is proportional to the number of cycles.

X-ray Computed Tomography Scanning

The internal structure of the defect panels may be elucidated by X-ray computed tomography scanning. Figure 87 and Figure 88 show the internal void structure (polymer and glass fibers omitted) of defect panels and the Baseline panel. The voids are shown to nucleate along the fiber bindles in the positive and negative 45° directions. The voids content of the representative volume element may therefore be calculated. Table 28 presents the void volume fractions for the defect panels and baseline panel investigated in this work.

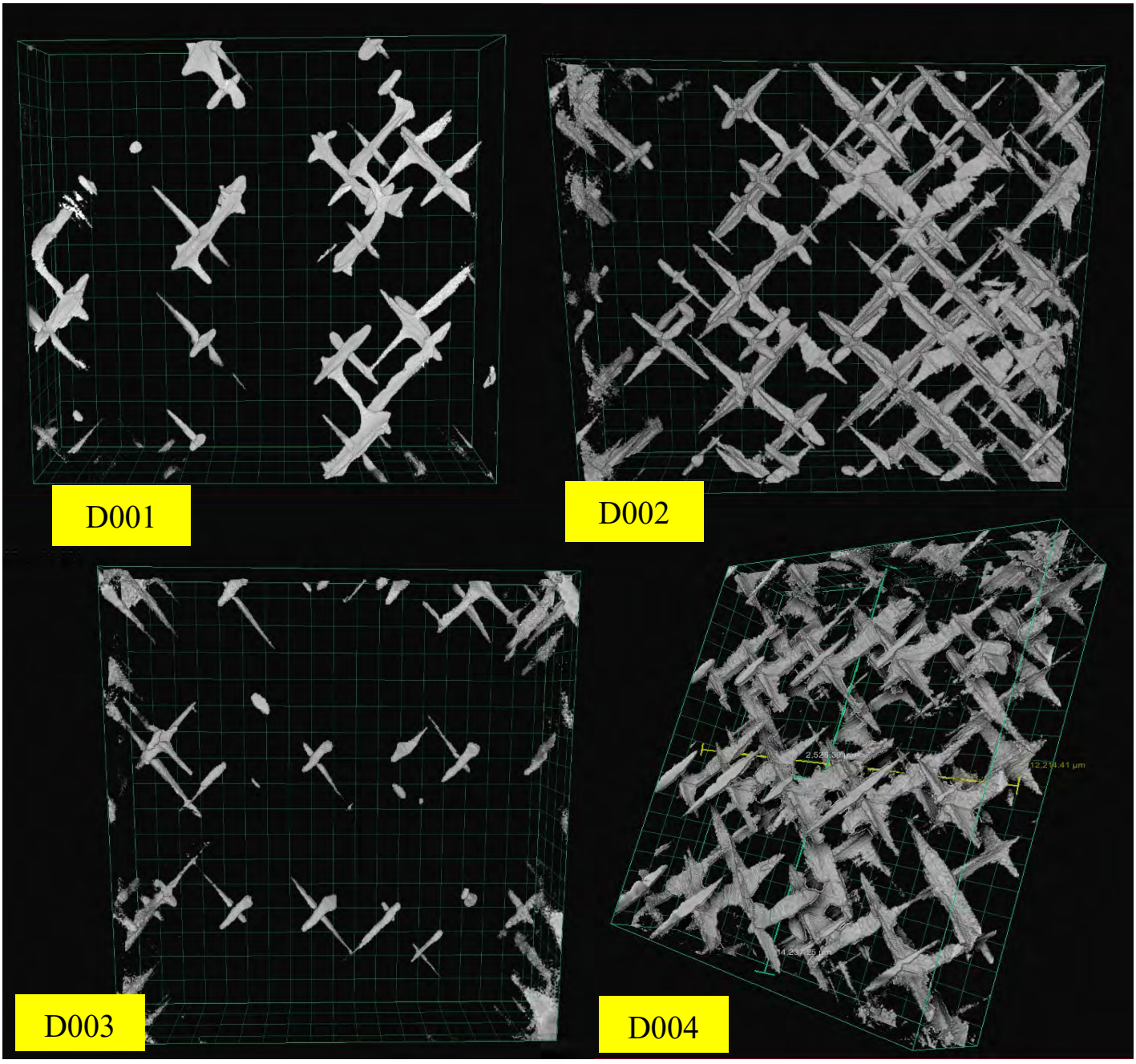

Figure 87. Voids in various defect panels. The glass and polymer are omitted so that the void structure can be easily seen.

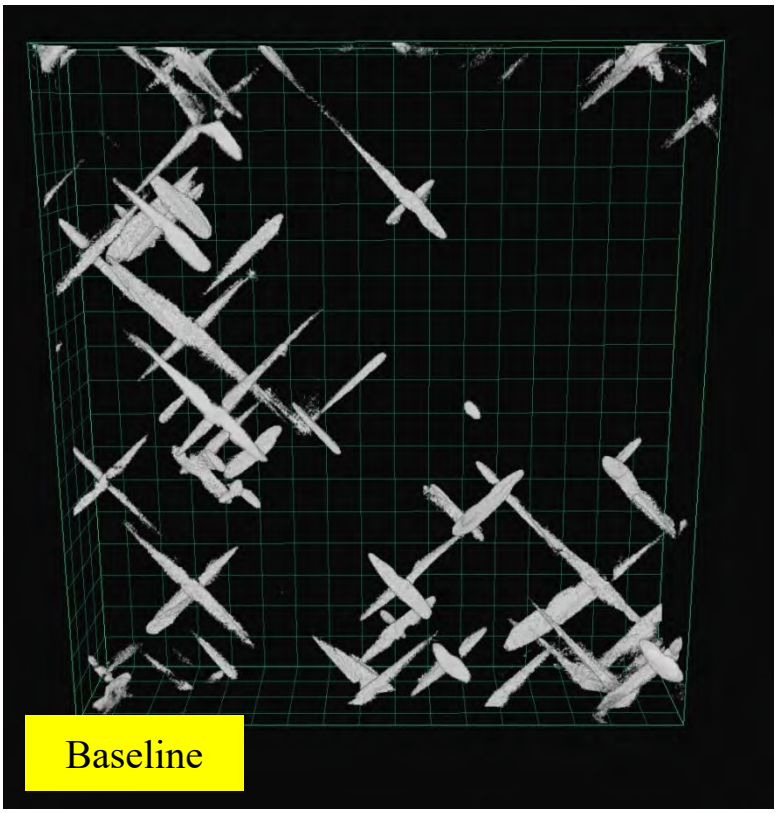

Figure 88. Voids in the "Baseline" panels. The glass and polymer are omitted so that the void structure can be easily seen.

Table 28. Void volume fractions of panels investigated in this study.

Sample	Void Volume Fraction (%)
D001	0.94
D002	3.1
D003	0.76
D004	5.4
Baseline	1.2

The void volume fractions presented in Table 28 are only for small volumes (about 0.25 mm^3), nonetheless, panels D002 and D004 can be concluded to have high porosity (over 1%) due to the extensive void structure observed here.

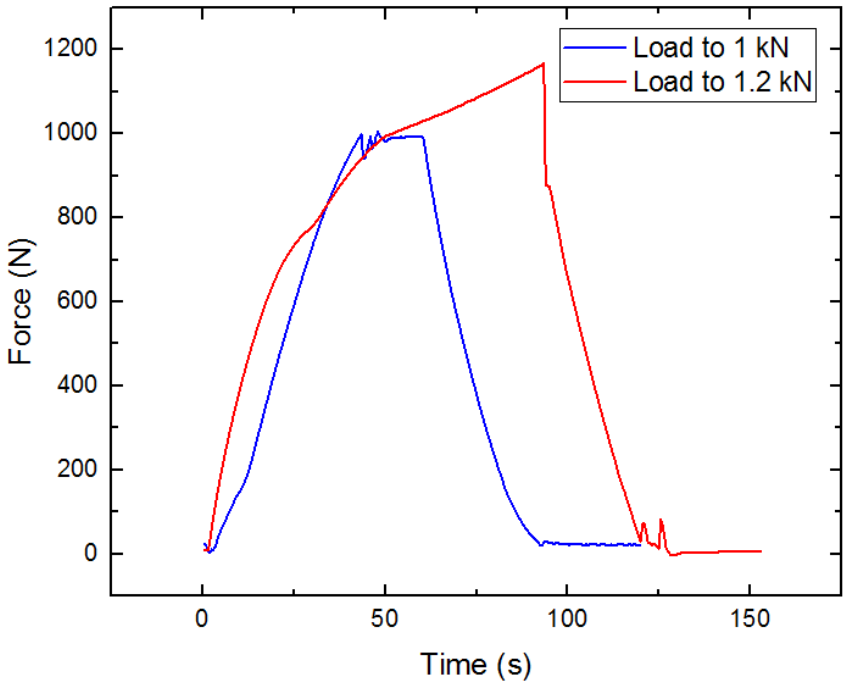

Figure 89. Load profiles for subsequent cycles (1kN load first) on the in-situ XCT sample.

The load profiles for the specimen loaded in the in-situ Deben frame are shown in Figure 89. After each loading cycles, the volume of the void area in the specimen increased. The void volume area in the gauge region is given in Table 29.

Table 29. Void volume and percentages of the void volume in the gauge region of the in-situ XCT tensile specimen before and after the load cycles.

Loading Step	Void Volume	Void Volume %
Pre Load	2.07E+09	1.43%
After 1 kN	2.32E+09	1.61%
After 1.2 kN	3.78E+09	2.53%

The initial void content of the specimen was close to that found for the measurement on a different region (0.76%). However, after loading, the void content is shown to increase significantly, as is expected due to the opening and propagation of cracks. Already, the second loading curve (to 1.2 kN) shown in Figure 6 shows that the slope of the load curve is diminishing around 37 seconds relative to the first loading cycle.

Broadly, due to the significantly diminished fatigue life of the defect panels with voids, these structures should be regarded as a failed part. If parts cannot be designed without such defects, then they will need to be significantly overdesigned to compensate for the reduced fatigue life.

5.5 Adhesive Material Characterization

Methods

Fabrication of lap shear specimens

Lap shear specimens were fabricated to compare the lap shear strength of an off-the-shelf adhesive (Plexus MA590) and two new adhesives developed by Arkema (Bostik SAF30 90 and Bostik SAF30 120). ISO standard 4587:2003 was used to standardize the testing method and sample fabrication. The National Wind Technology Center (NWTC) fabricated lap shear panels at 1mm, 3mm, and 10mm thicknesses. These samples were cut from panels and tested at the Colorado School of Mines (CSM) and tested to compare lap shear response that would likely be seen in wind turbine blade gaps where adhesives are used. Figure 90 below shows the specimen dimensions as described in ISO 4587.

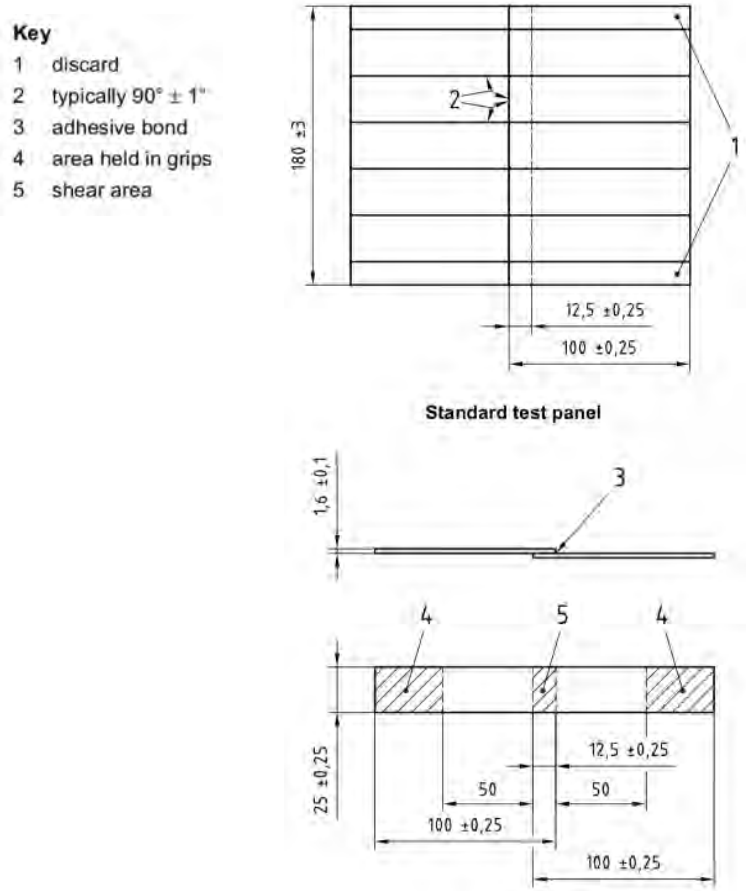

Figure 90. Shape and dimensions for single slap shear test (ISO, 2003-03)

In order to accommodate for the varying gap thicknesses, Teflon spacers were used. Figure 91 shows the process to create a panel from which the lap shear specimens can be cut. Part a) shows the spacers being applied to the bottom panel. Teflon is an excellent spacer for these adhesives as the adhesive does not bond to the Teflon, making the bond gap substantially cleaner. The second step is to purge the adhesive from the guns. This is due to a couple of reasons; firstly, for the adhesive to flow out, allowing any initial trapped air to escape. Secondly, to ensure that proper ratios of the adhesive are flowing from the adhesive tube. The next step is to apply the adhesive in the bond area. It is essential that a steady stream of adhesive flows from the gun to create a clean adhesive gap, free of voids and inconsistencies. With too little adhesive, voids will form in the bond area, with too much adhesive, the bond gap will be larger than desired. The last step is to clamp the panels together and allow the adhesive to cure. Large clamping

pressures were necessary at first to allow the extra adhesive to flow over the Teflon inserts, so the desired bond gap could be achieved. It was also found that making the bond gap longer than specified in the standard and cutting away the excess adhesive post-cure created a substantially better adhesive surface. After the adhesive cured, a precision saw is used to cut the panel to the necessary dimensions for testing (as shown in Figure 91). For the adhesive length, a stop was applied to the saw at the surface of the laminate and the undesired adhesive was cut away.

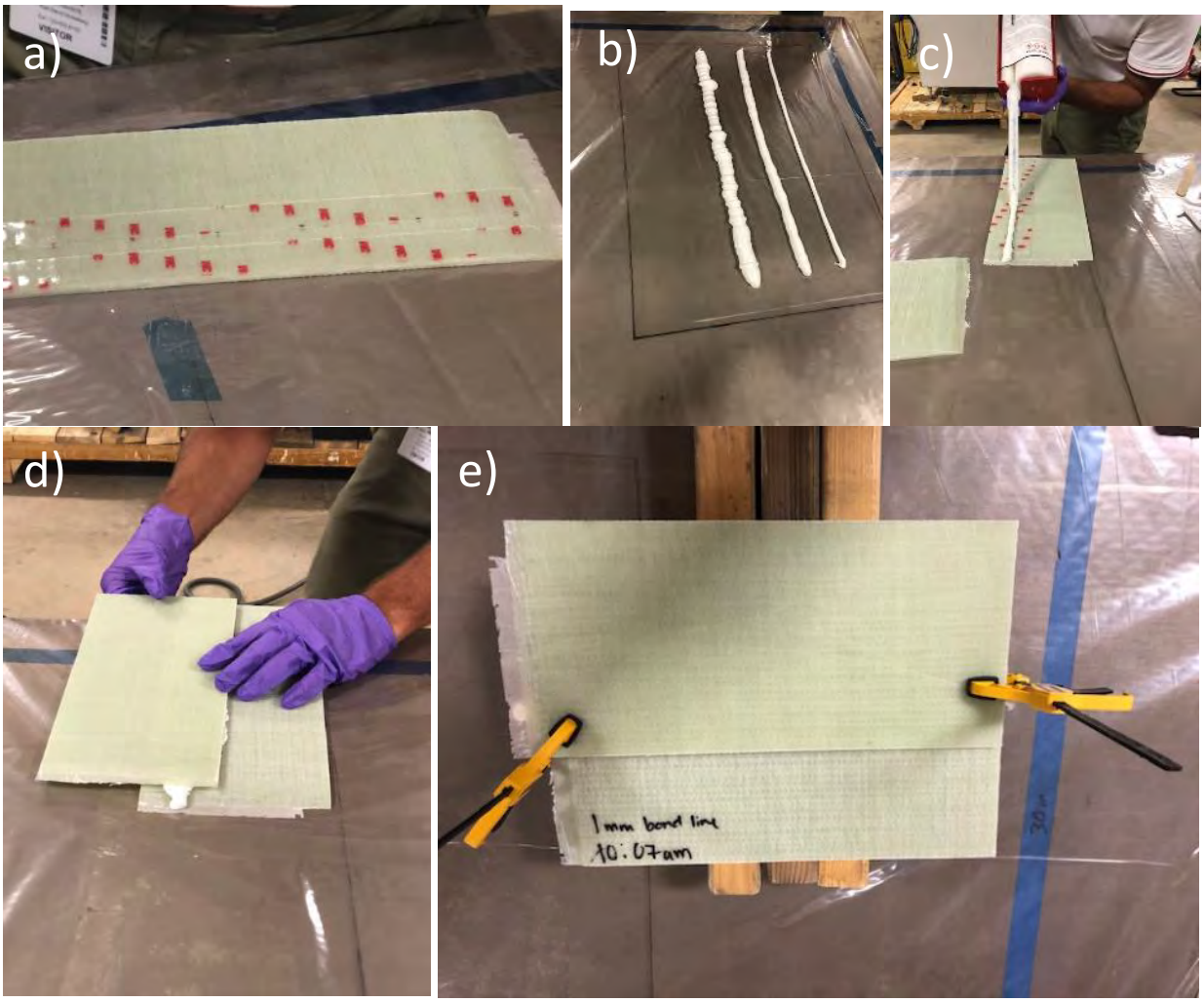

Figure 91. a) Apply spacers. b) Purge adhesive. c) Apply adhesive. d) Overlap panels. e) Clamp panel.

An MTS Landmark 370.10 was used to complete the lap shear testing of the 1mm and 3mm samples and an MTS Landmark 370.25 was used for the 10mm samples. Spacers were fabricated to account for the rotation that would occur within the adhesive during clamping of the sample. The samples were run at a constant head displacement rate of 1mm/min for the 1mm and 3mm samples, and 1.5mm/min for the 10mm samples to achieve a failure at 65 s ± 20 s as indicated in the standard.

Results

1mm Lap Shear Tests

Below in Figure 92-Figure 94 are the post-test images of the samples. For these tests, the adhesive failed cohesively (failure of the adhesive) rather than adhesively (failure of adhesive to substrate). This indicates

that the shear results of these tests are likely to be very close to the actual maximum shear stress the adhesive can withstand before failure. The tests at larger gap thicknesses consistently failed either adhesively or from a surface ply delamination, which will be discussed in more detail in the following sections.

The Plexus MA590 and Bostik SAF30 90 adhesives both failed cohesively, with more adhesive collecting on one side of the sample as can be seen below. For some of the Bostik SAF30 120 samples however, the adhesive itself was split; roughly half separating to one side, and half to another as seen in T8 through T10 in Figure 94. This indicates a more brittle adhesive than the others as failure caused the adhesive to split to both sides of the sample.

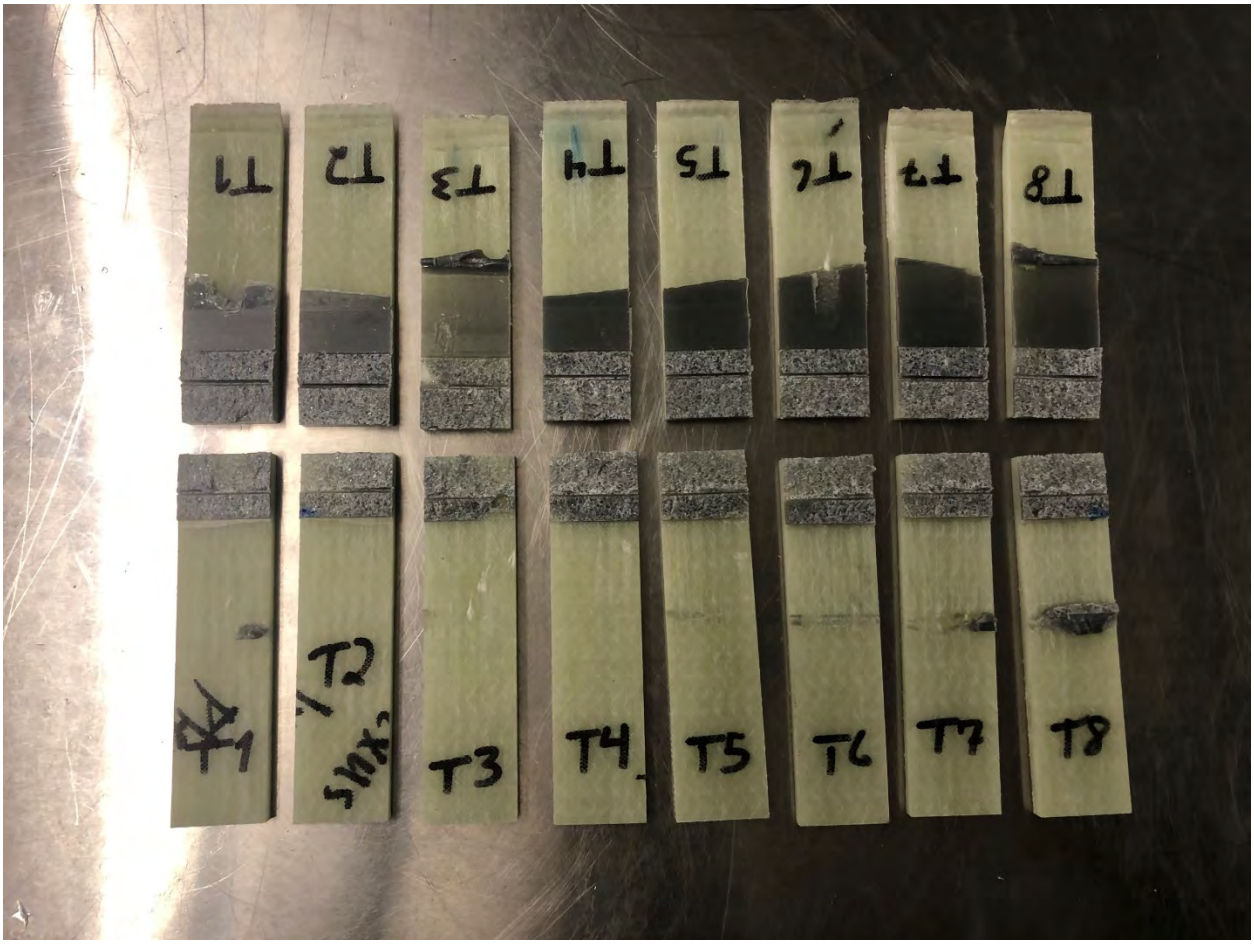

Figure 92. Plexus MA590 1mm samples post-test

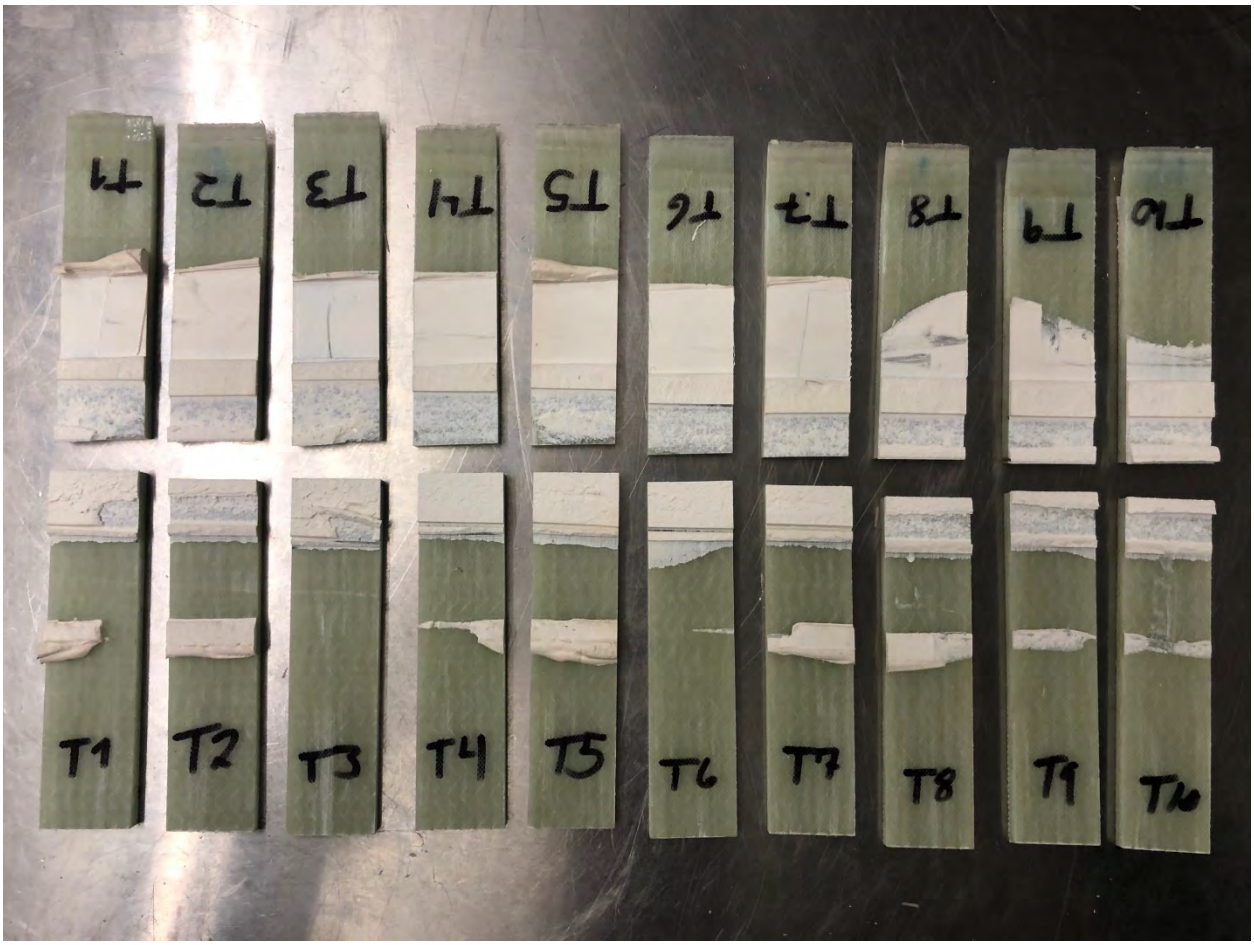

Figure 93. Bostik SAF30 120 1mm samples post-test

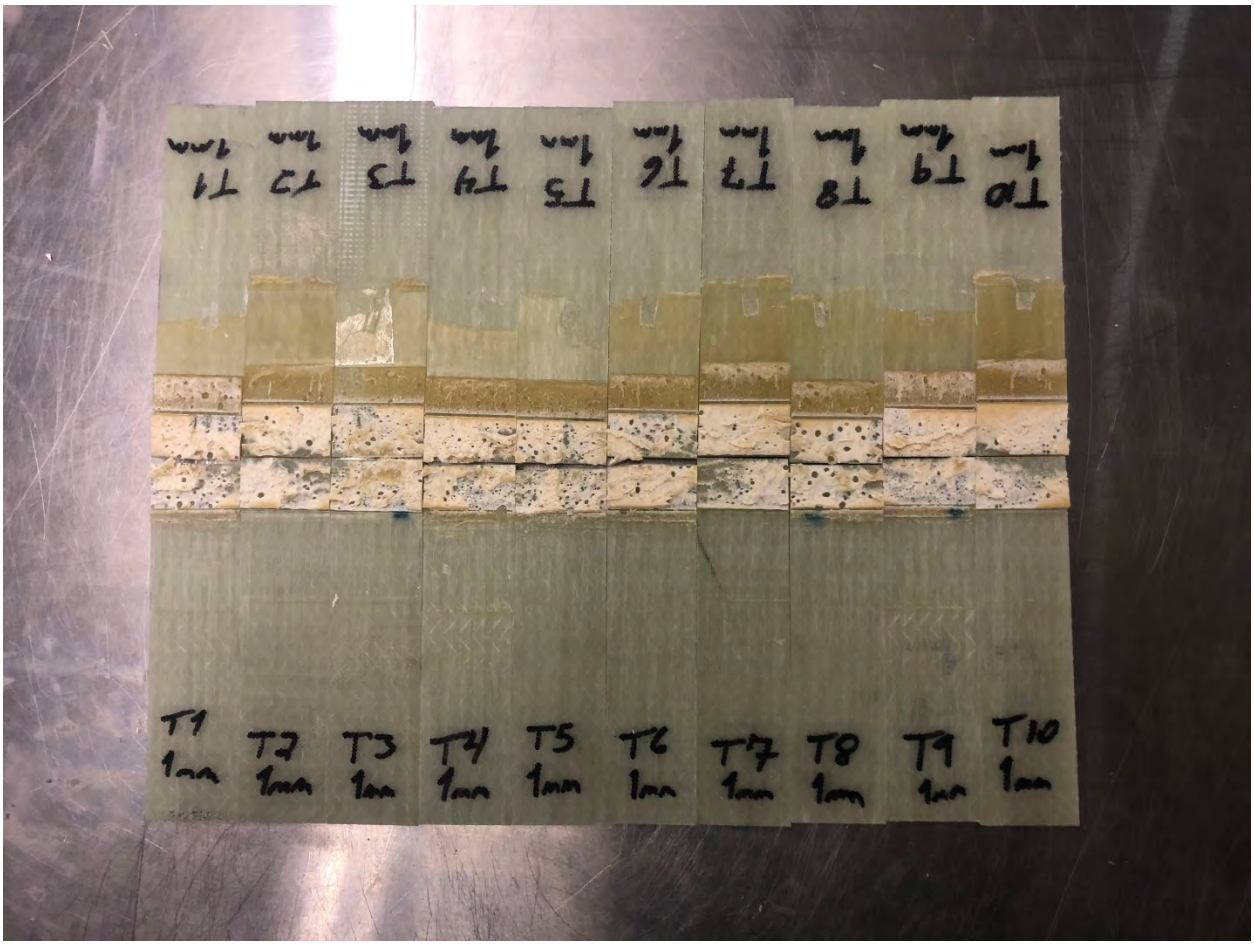

Figure 94. Bostik SAF30 90 1mm samples post-test

The raw test results of the adhesives at a 1mm gap thickness can be seen in Figure 95-Figure 97. The Plexus MA590 adhesive consistently failed around 12 MPa, with very tight data. The Bostik adhesives had a wider range of failure, where the Bostik SAF30 90 failed at a similar stress as the Plexus adhesive, while the Bostik SAF30 120 adhesive failed closer to 10 MPa. It is important to note that the Plexus MA590 adhesive exhibited brittle behavior up to failure, which can be seen by the steep upward slope and sudden change to a drop in stress and then failure. The Bostik adhesives on the other hand, demonstrated a ductile failure, which can be seen by the flat and upward slopes after the adhesive has transitioned from elastic deformation to plastic deformation. This indicates that the Bostik adhesives can maintain their strength under more substantial loading than the Plexus adhesive.

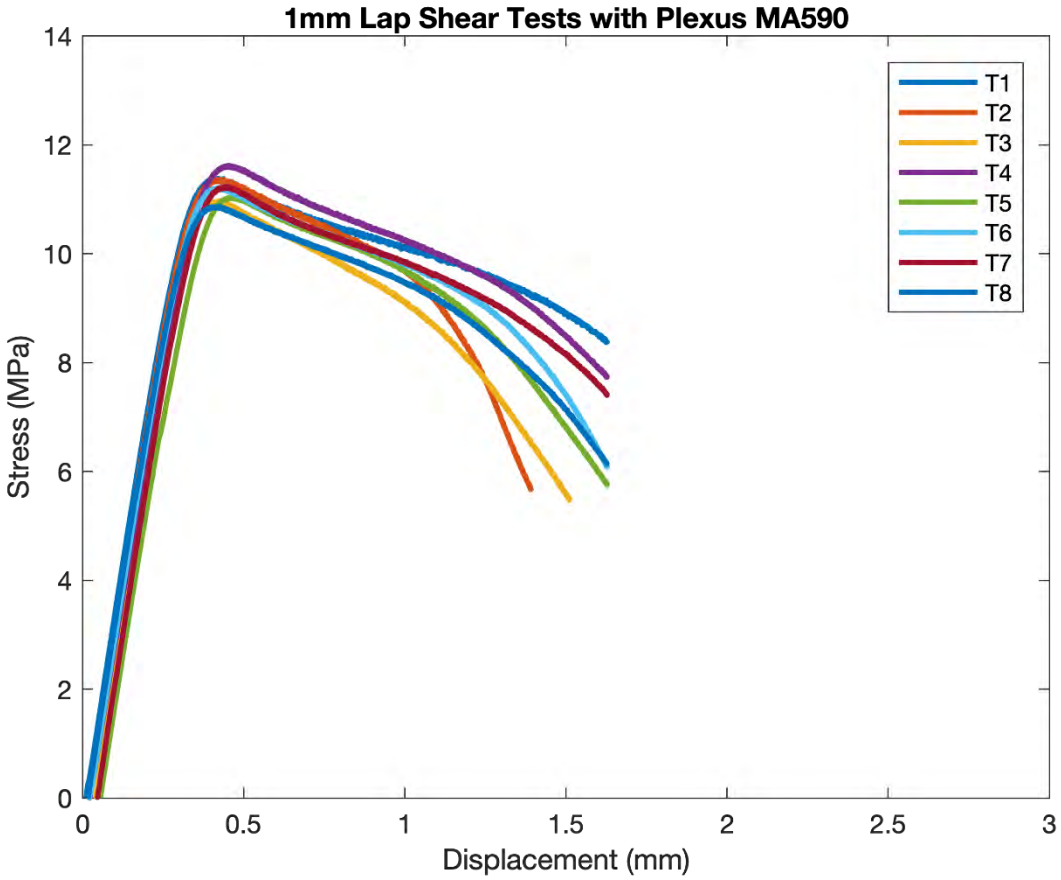

Figure 95. Plexus MA590 1mm lap shear results

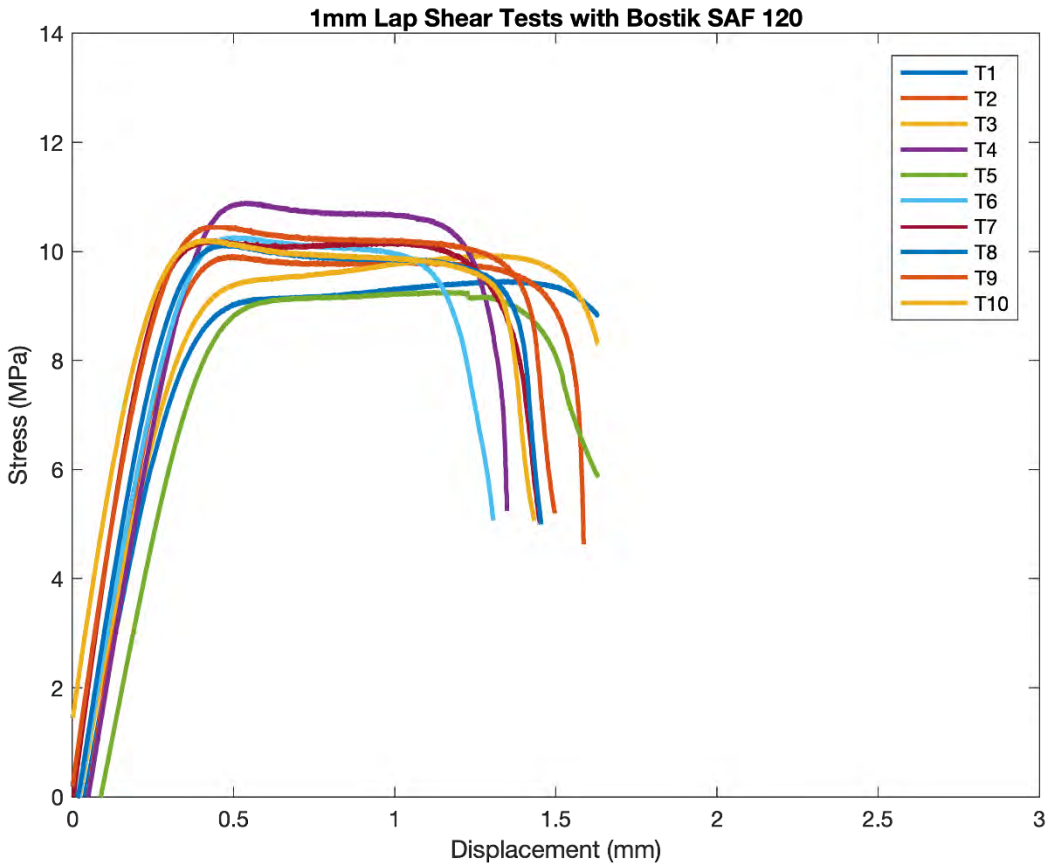

Figure 96. Bostik SAF30 120 1mm lap shear results

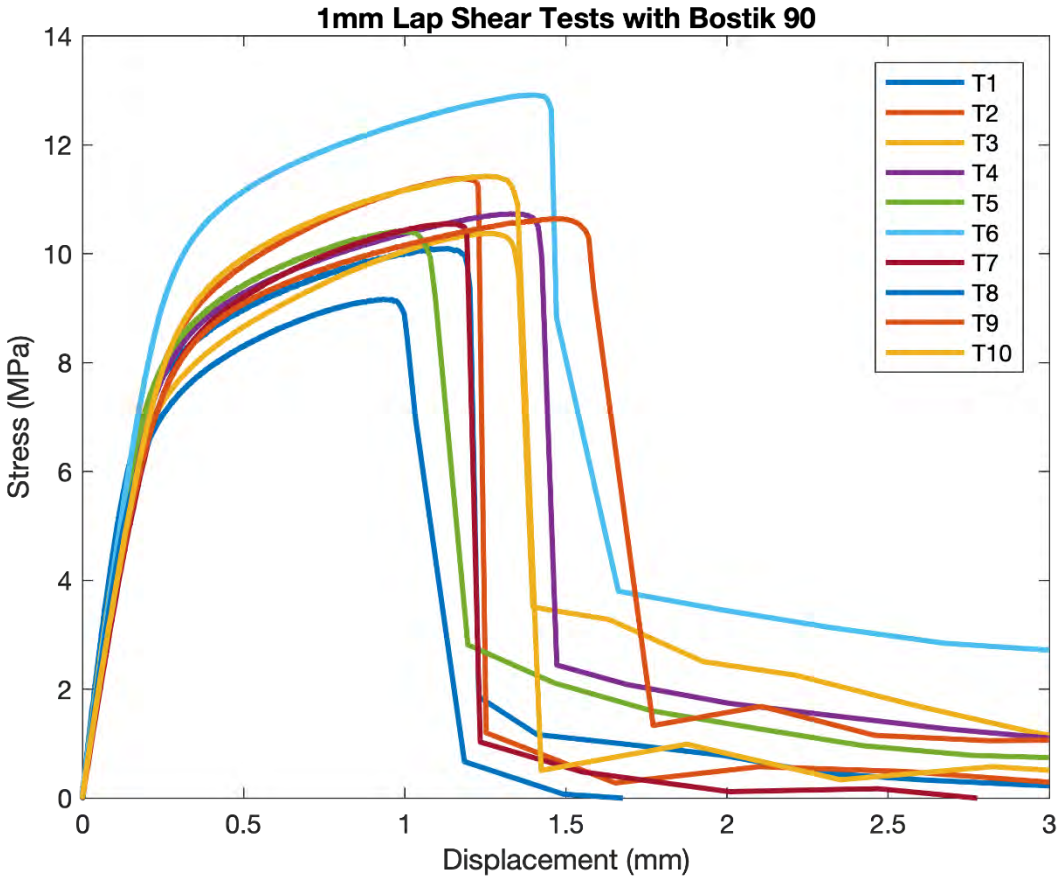

Figure 97. Bostik SAF30 90 1mm lap shear results

Next, the comparison of each of the adhesives is shown in Figure 98. As discussed above, the adhesives exhibited similar strengths. The Bostik SAF30 90 adhesive had slightly more range in the data, however it is within the acceptable limits. The most likely reason for this is due to the bubbles that formed within the adhesive as can be seen in Figure 94. It is unclear whether these bubbles formed during the application of the adhesive, or while curing. It is most likely that the process of applying pressure to remove excess adhesive causes bubbles to form, which is more prevalent in the 1mm and 3mm samples, than the 10mm samples. While the voids in the adhesive lowered the overall strength, it is likely they also contributed to the ductility exhibited by the adhesive.

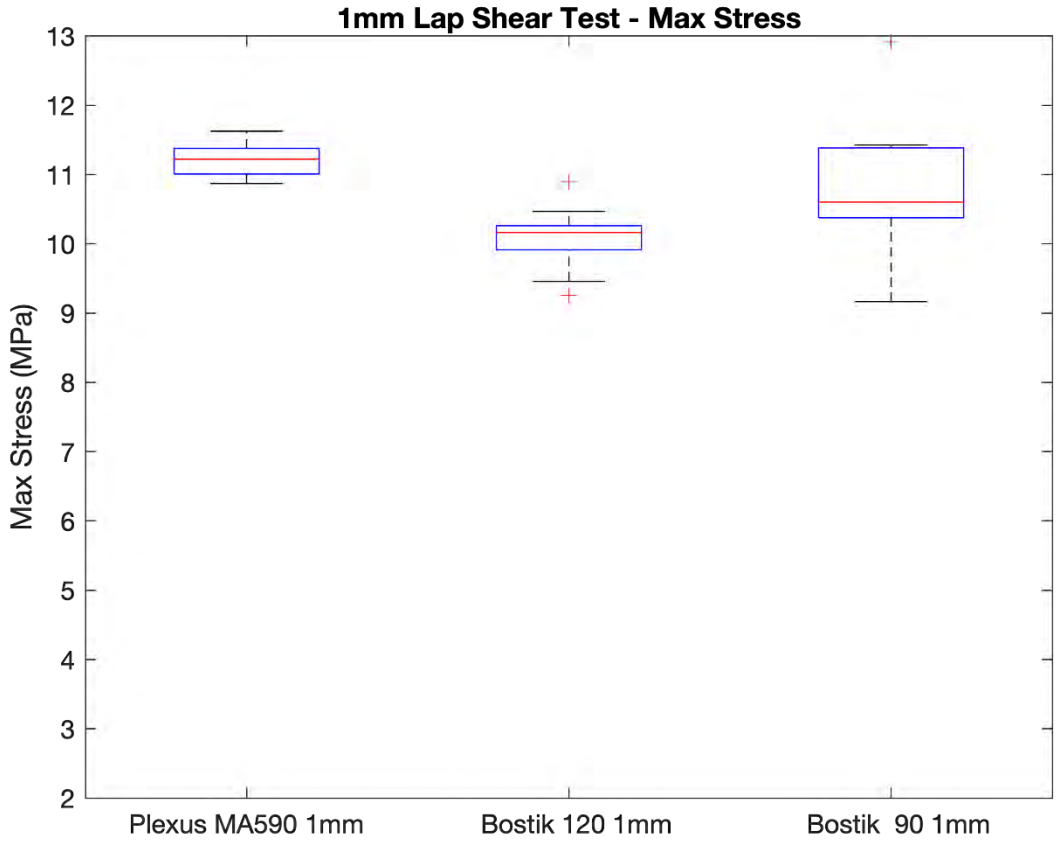

Figure 98. 1mm lap shear test comparison

3mm Lap Shear Tests

The post-test 3mm samples are shown in Figures 99-101 below. The Plexus MA590 samples failed from ply delamination, apart from T2. The Bostik SAF30 120 samples in Figure 100 showed a mixture of cohesive and ply delamination failure. The Bostik SAF 90 samples in Figure 101 however failed almost completely cohesively, with some mixture of ply delamination and cohesive failure within a single bond. The most likely reason this adhesive differs from the others is due once again to the voids that formed within the adhesive. Samples T2 and T4 in Figure 103 had a large number of voids, and the adhesive was separated between the two pieces of the sample. Even with these voids however, the strength of the adhesive was still similar to the Plexus adhesive, as discussed further below. It is also important to note that for these tests, even though there was large amounts of adhesive seepage below the spacers, the excess was separated from the testing area of the specimen using a LECO precision saw (set to stop at the surface of the laminate) to ensure accurate results.

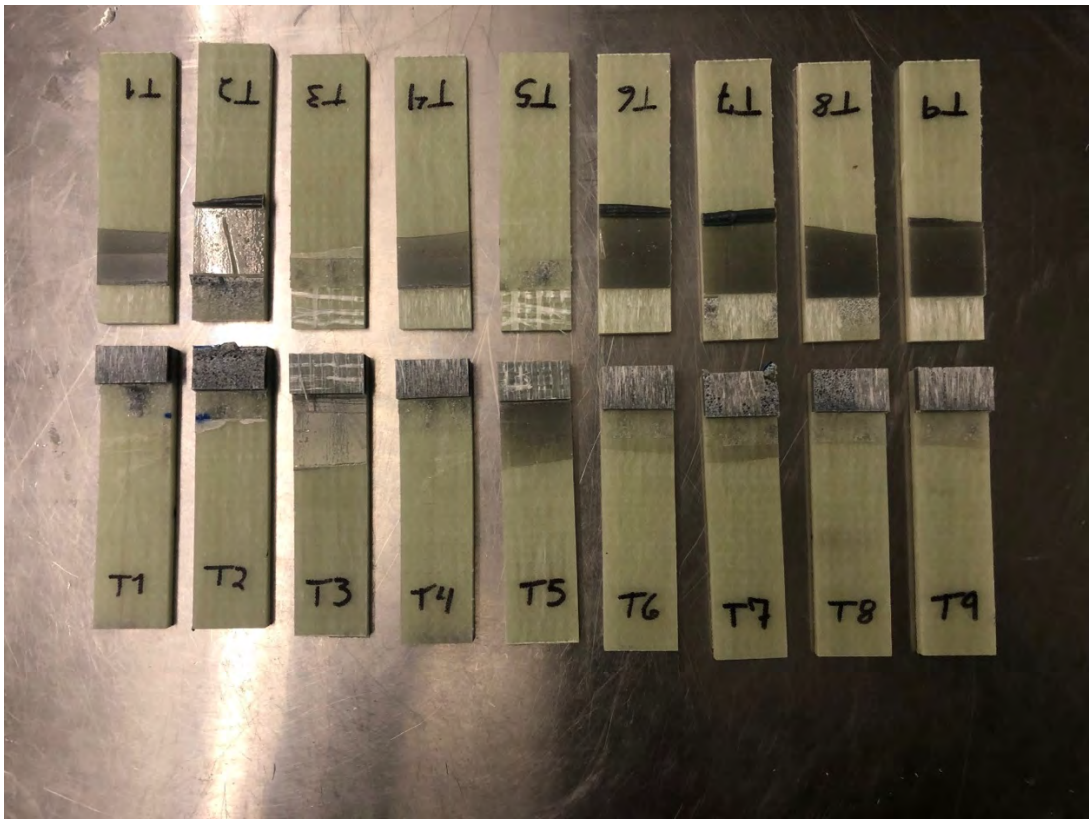

Figure 99. Plexus MA590 3mm samples post-test

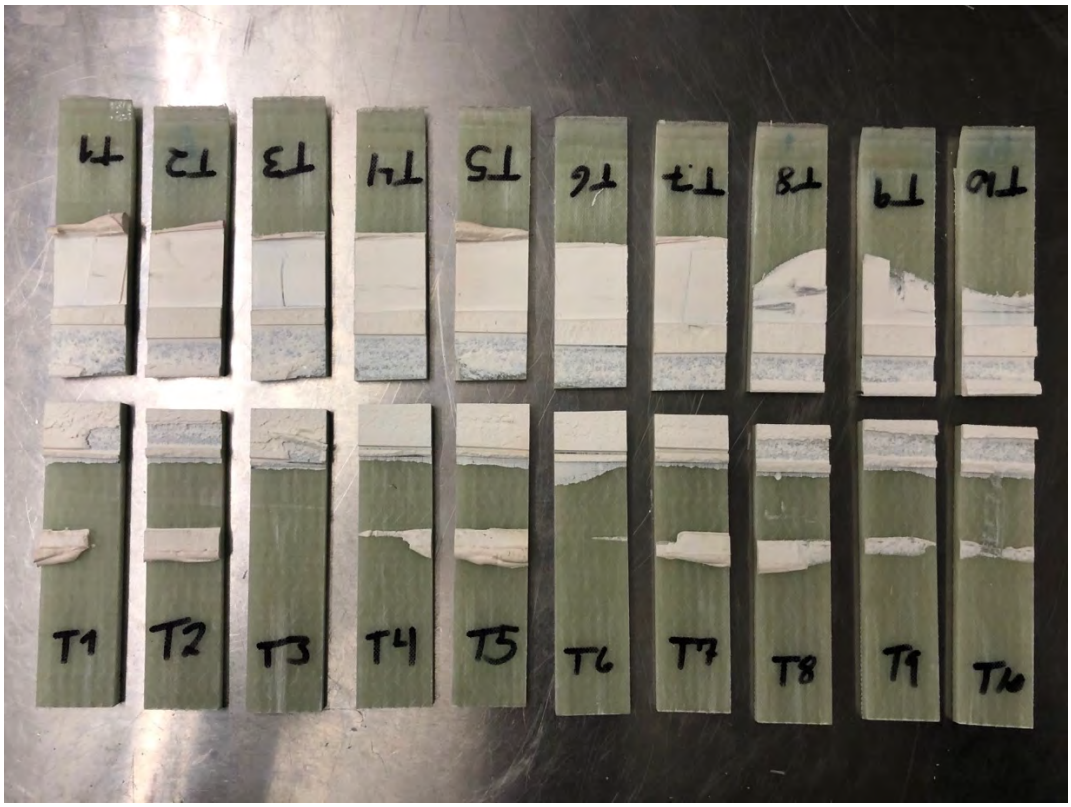

Figure 100. Bostik SAF30 120 3mm samples post-test

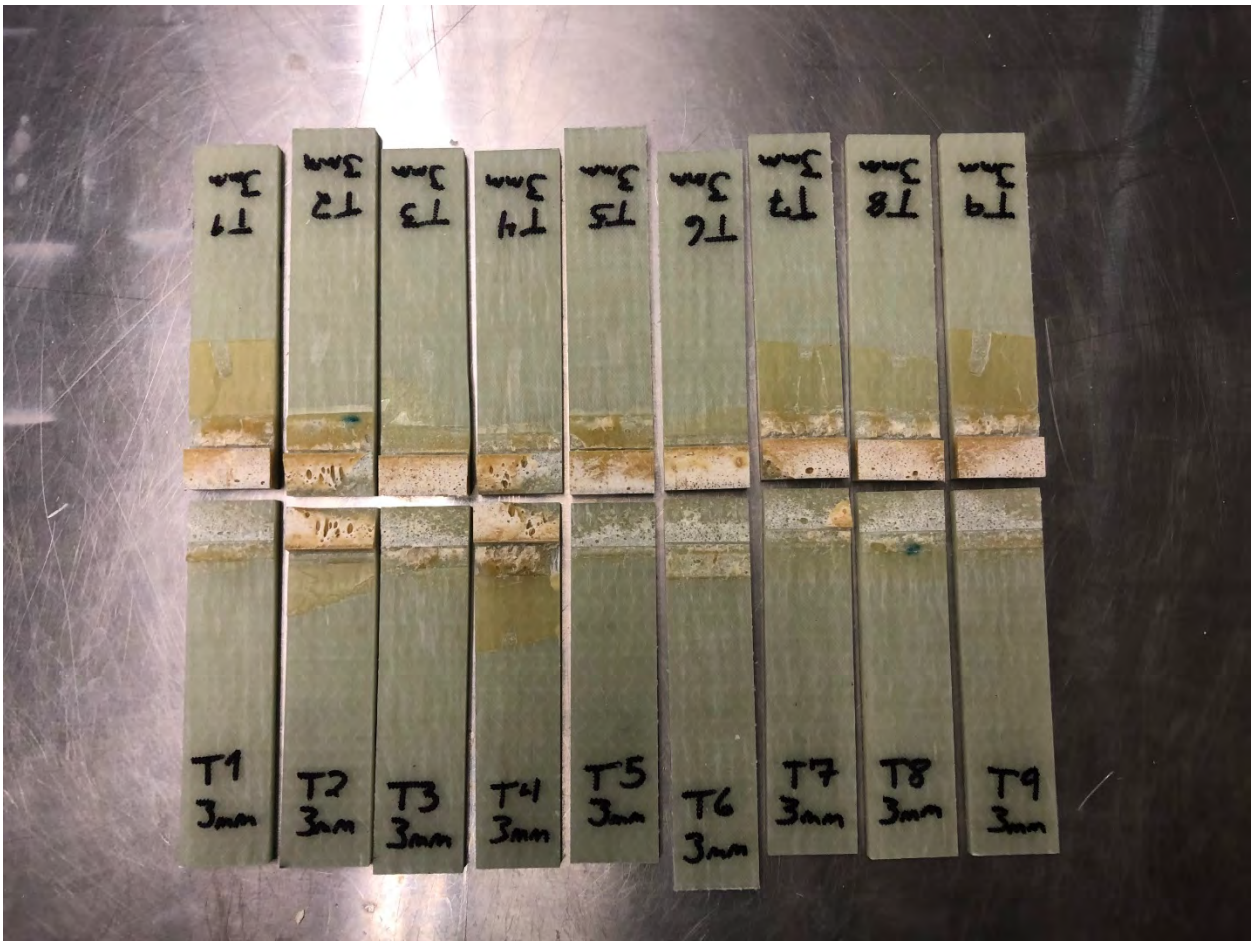

Figure 101. Bostik SAF30 90 3mm samples post-test

Figures 102-104 show the raw test results for the 3mm samples. Once again, the Plexus MA590 and Bostik SAF30 90 adhesives demonstrated similar strength of around 10 MPa. In this case however, the Bostik SAF30 90 adhesive is preferred due to its elongation before failure, demonstrating more ductile behavior. The Bostik SAF30 120 adhesive failed around 7 MPa, lower than the other adhesives.

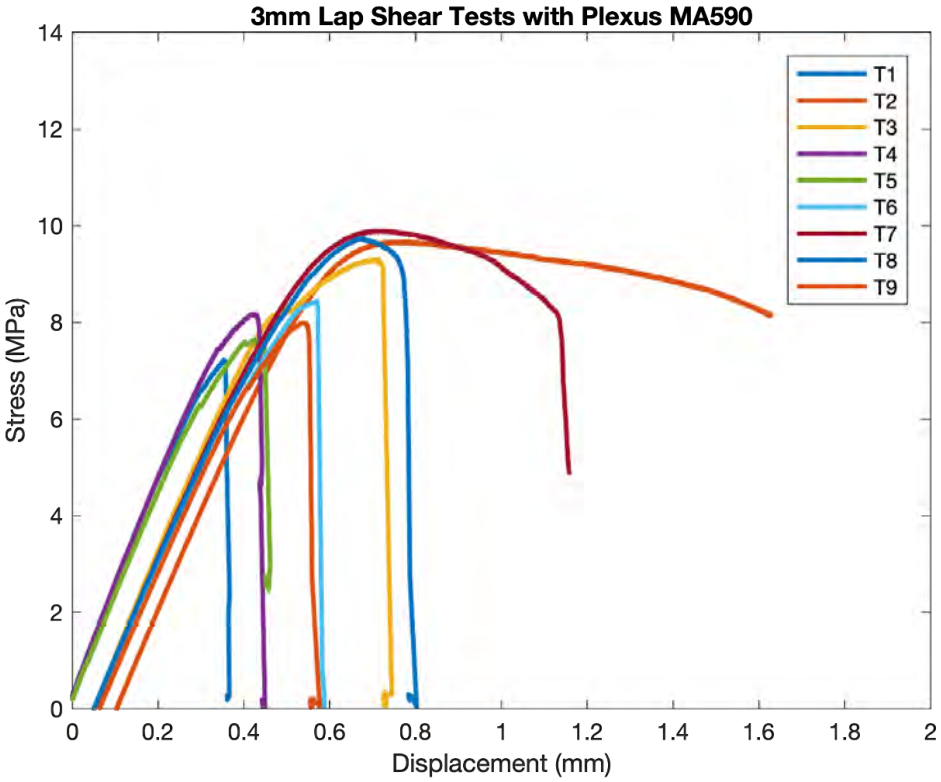

Figure 102. Plexus MA590 3mm lap shear results

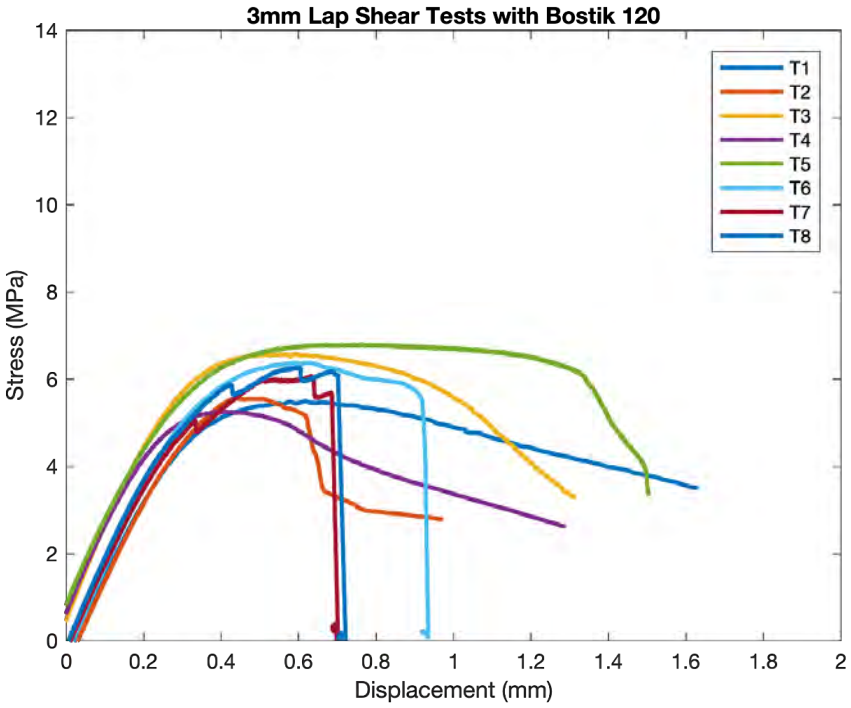

Figure 103. Bostik SAF30 120 3mm lap shear results

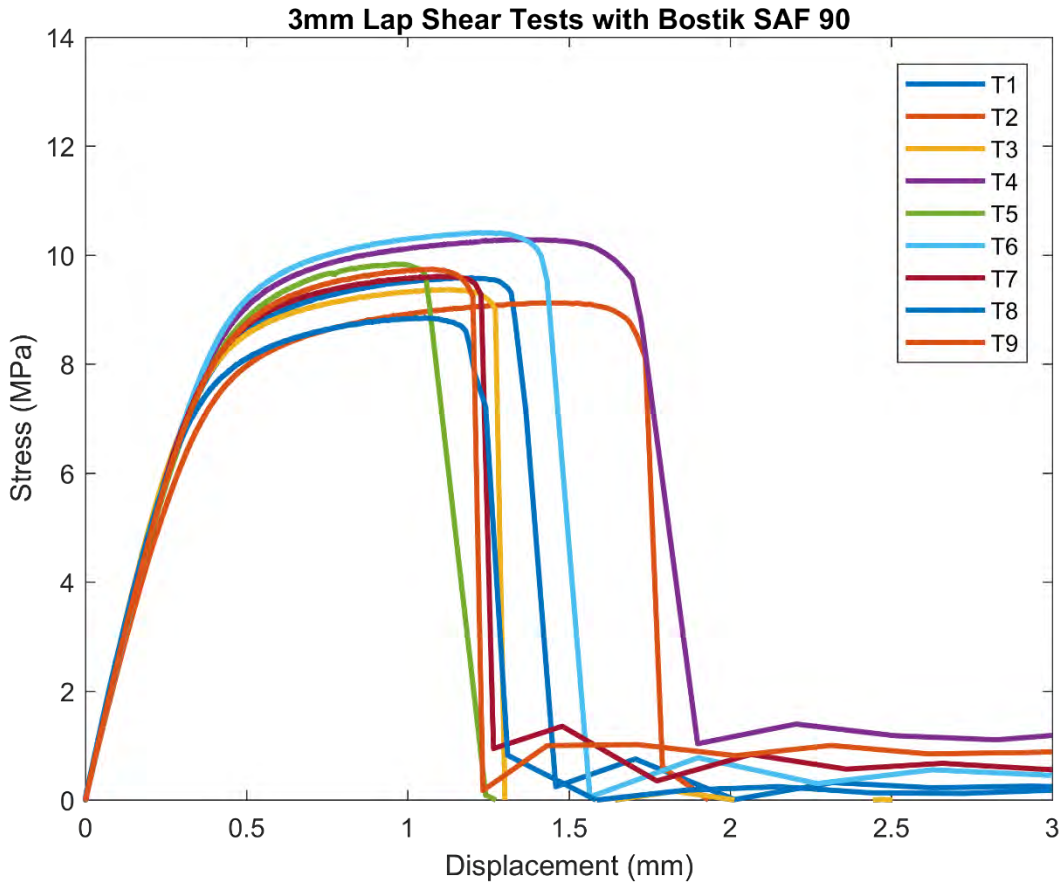

Figure 104. Bostik SAF30 90 3mm lap shear results

Below in Figure 105 is the comparison between the adhesive types. As with the 1mm test results, the Plexus MA590 and Bostik SAF30 90 adhesives failed at similar stresses, while the Bostik SAF30 120 was about 3 MPa lower. It is surprising that the Bostik SAF30 90 adhesive was slightly higher than the Plexus MA590, as the Plexus adhesive failed from ply delamination, whereas the Bostik SAF30 90 adhesive had mainly cohesive failure.

Figure 105. 3mm lap shear test comparison

10mm Lap Shear Tests

Figures 106-108 show the post-test samples for the 10mm lap shear tests. For this adhesive thickness, almost all of the Plexus MA590 and Bostik SAF30 120 samples failed due to ply delamination, whereas the Bostik SAF30 90 had roughly half fail to delamination and half fail due to cohesive failure. The Bostik SAF30 90 adhesives in the 3mm and 10mm samples had substantially less voids that the 1mm samples. As stated above, it is unclear whether this is due to the application process of the adhesive, or a difference in curing due to the adhesive thickness. The Plexus MA590 T3 and Bostik SAF30 90 T1 samples failed prior to testing, thus were not included in the test data.

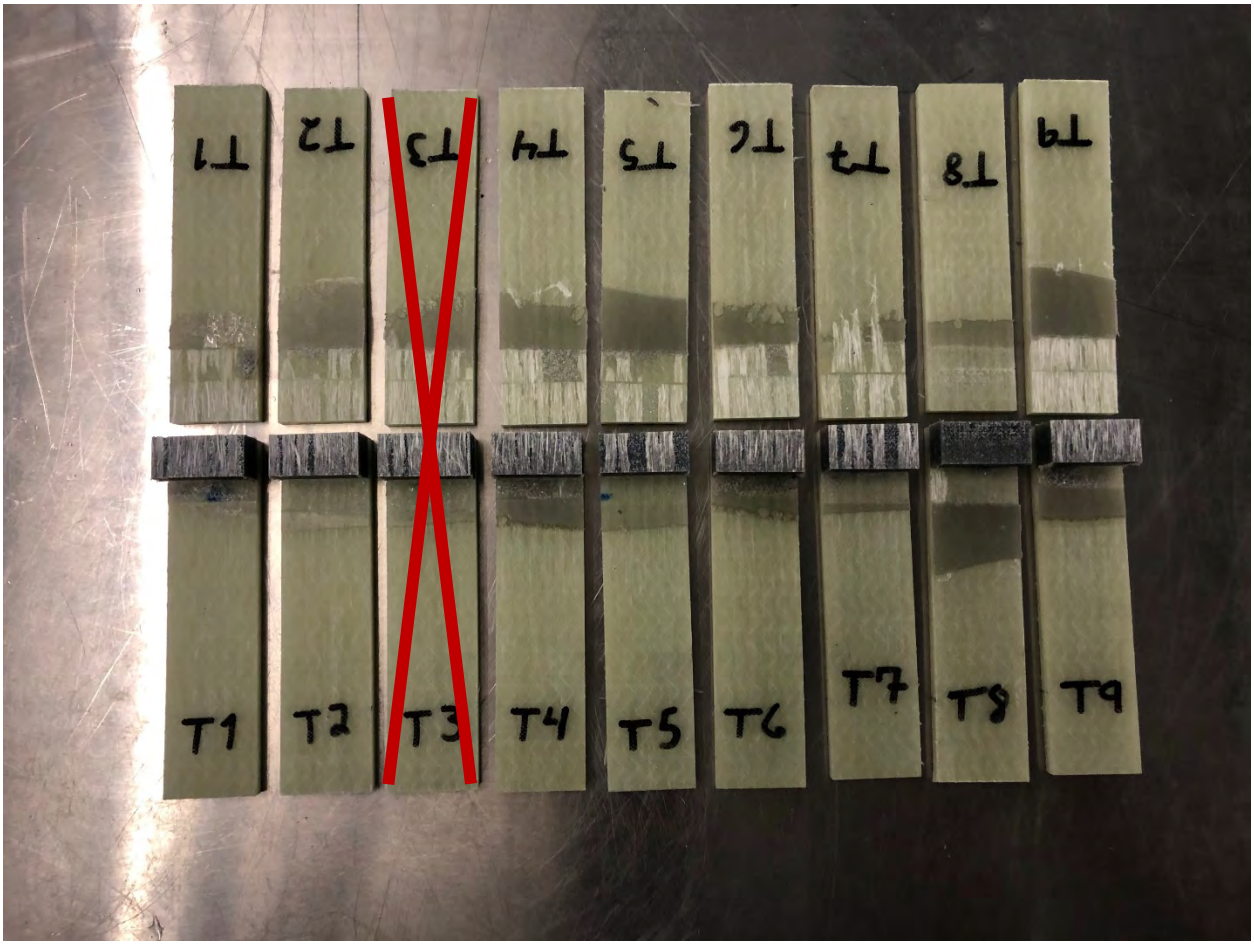

Figure 106. Plexus MA590 10mm samples post-test

Figure 107. Bostik SAF30 120 10mm samples post-test

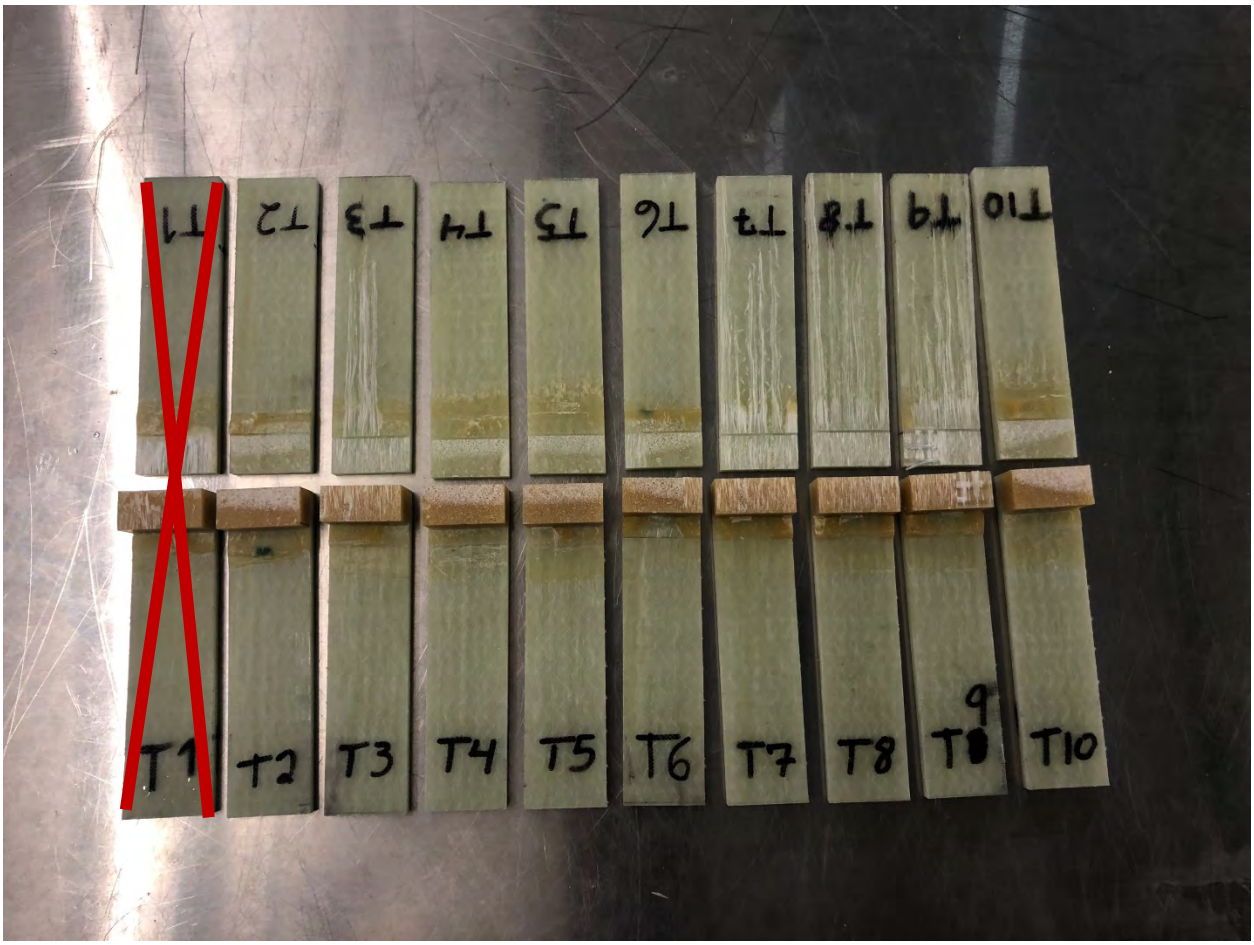

Figure 108. Bostik SAF30 90 10mm samples post-test

The 10mm gap thickness had the least variance in maximum stress at failure between each of the adhesives. The adhesives failed around 3.5-4.0 MPa, with the Bostik SAF30 90 adhesive having the greatest range of values. This is likely due to the different failure types that occurred with that adhesive. Figures 109-112 show the results for the 10mm gap samples.

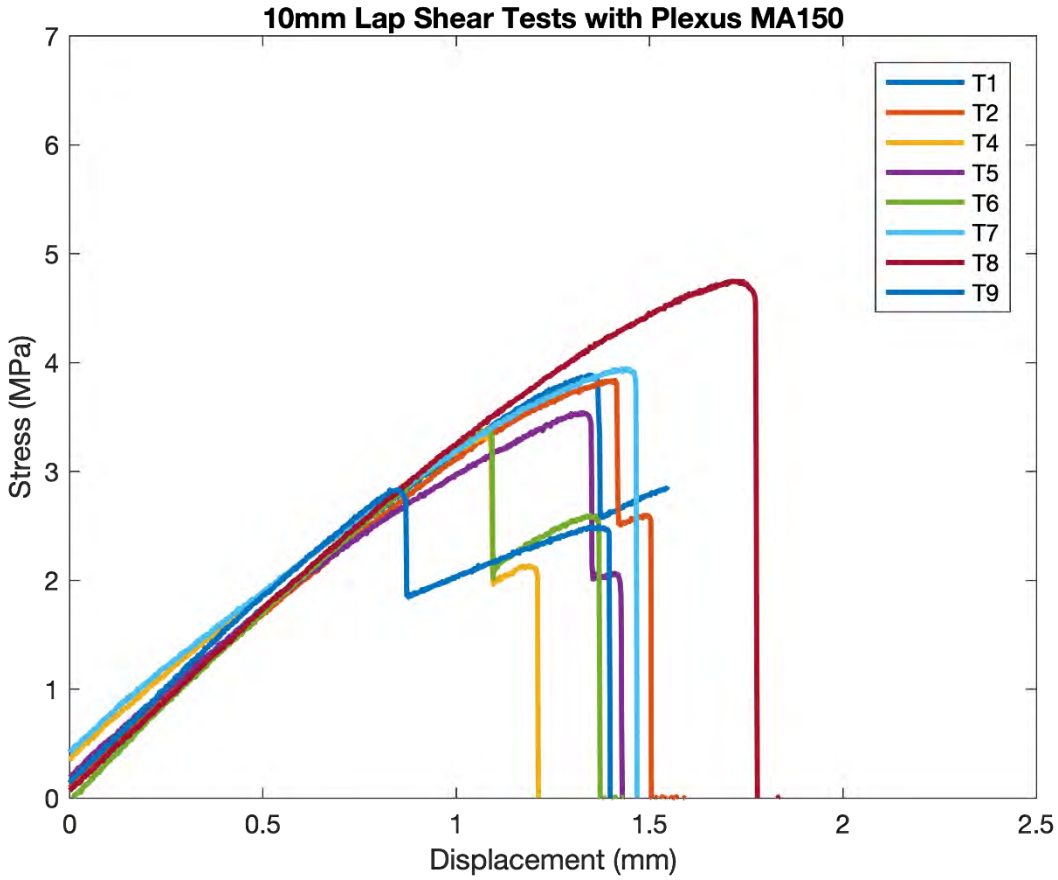

Figure 109. Plexus MA590 10mm lap shear results

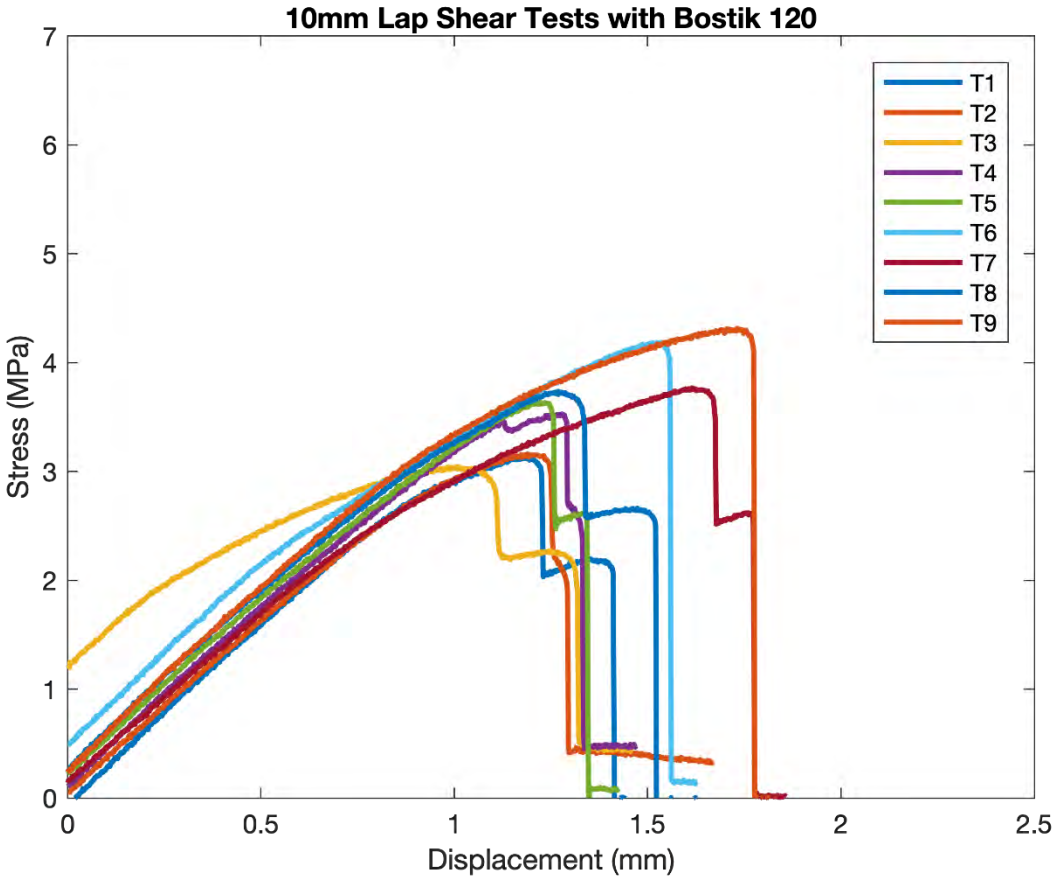

Figure 110. Bostik SAF30 120 10mm lap shear results

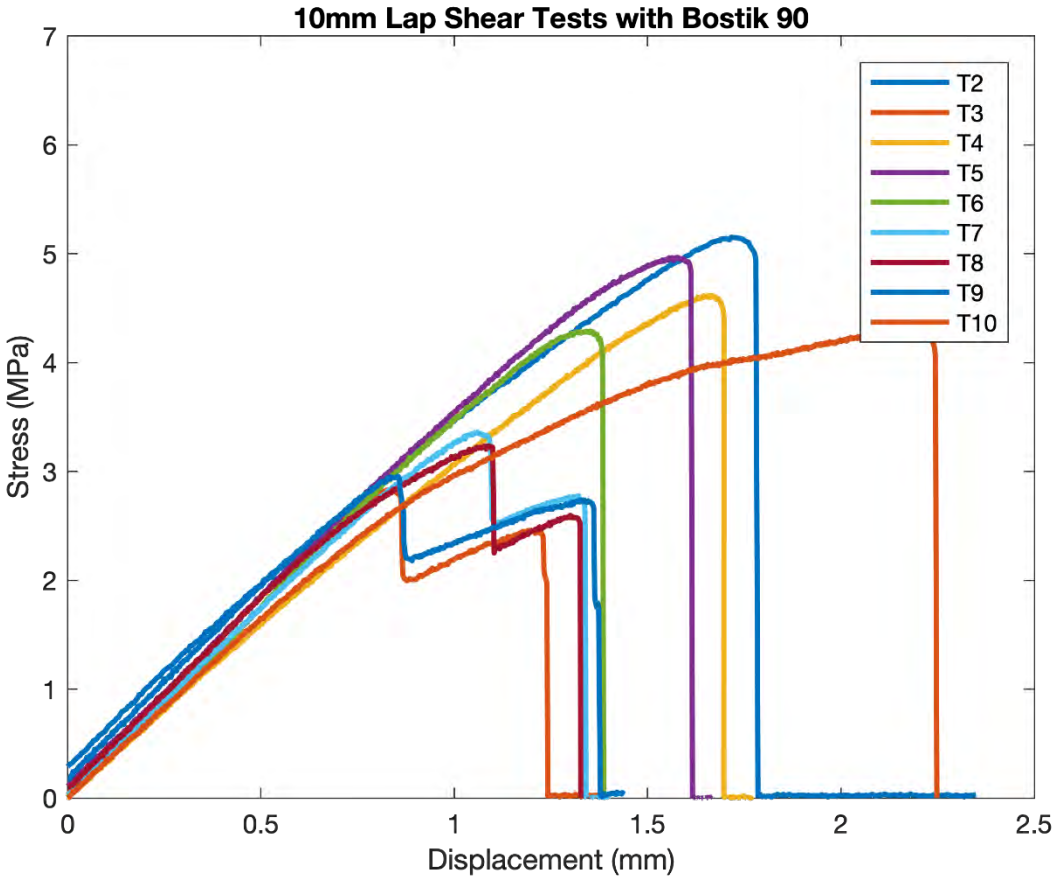

Figure 111. Bostik SAF30 90 10mm lap shear results

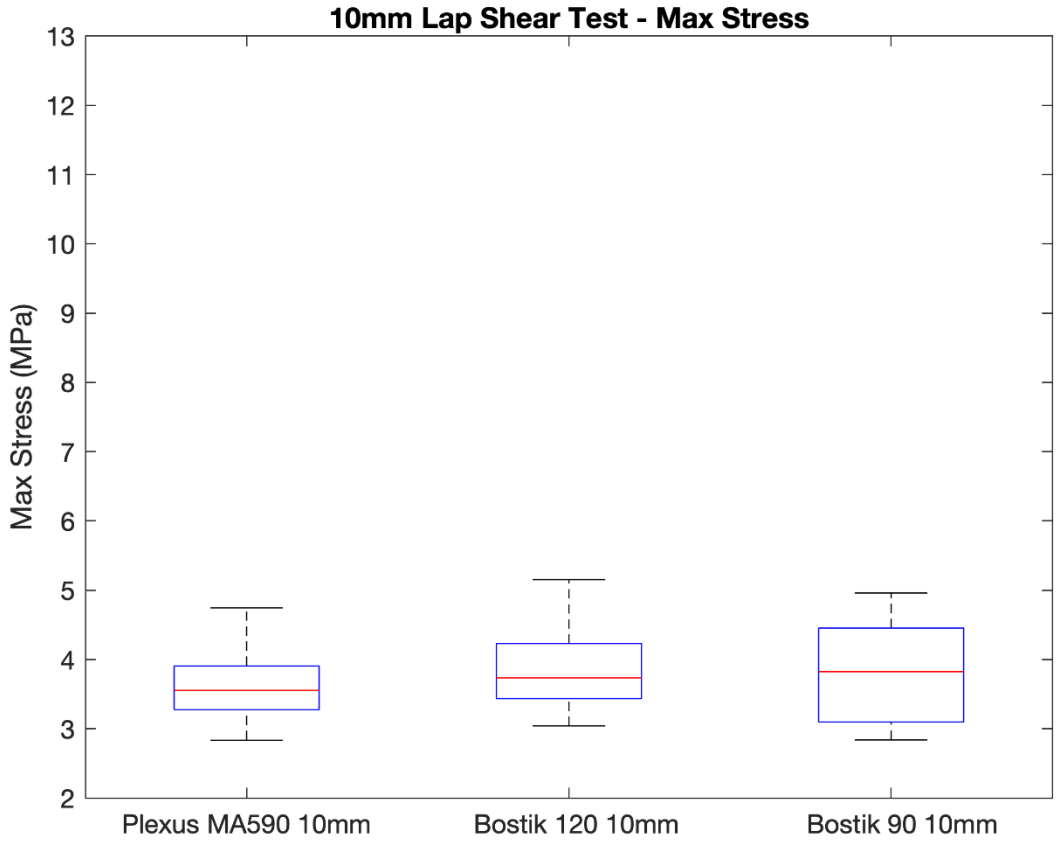

Figure 112. 10mm lap shear test comparison

Data Comparison

The Table 30 below shows the comparison of data for each of the tests. A couple of important things to consider are the mean thicknesses of each group of samples, as well as the mean stress for each of the adhesives. The mean displacement reported in the table is at the maximum stress. In each case, the gap thickness of the adhesive was higher than the desired thickness. In future sample prep, more pressure should be applied to the samples before clamping to ensure all excess adhesive flows past the Teflon spacers.

Table 30. Adhesive Characterization Data Summary

1mm					
	Mean Thickness (mm)	Mean Stress (MPa)	Standard Dev.	Mean Disp. (mm)	Standard Dev.
Plexus MA590	2.131	11.215	0.247	0.434	0.020
Bostik 120	1.694	10.071	0.469	0.712	0.392
Bostik 90	1.291	10.848	1.017	1.218	0.180
3mm					
	Mean Thickness (mm)	Mean Stress (MPa)	Standard Dev.	Mean Disp. (mm)	Standard Dev.
Plexus MA590	3.999	8.679	1.000	0.577	0.151
Bostik 120	3.888	6.859	0.540	0.585	0.113
Bostik 90	3.296	9.656	0.538	1.173	0.176
10mm					
	Mean Thickness (mm)	Mean Stress (MPa)	Standard Dev.	Mean Disp. (mm)	Standard Dev.
Plexus MA590	10.874	3.690	0.563	1.279	0.268
Bostik 120	11.114	3.614	0.454	1.337	0.236
Bostik 90	11.193	3.967	0.881	1.366	0.446

Prediction of Maximum Stress for Varying Thickness

From Figures 113-115 below, it is possible to estimate the maximum stress for a given thickness. In most cases, the Plexus MA590 and Bostik SAF30 90 adhesives failed at very similar stresses, followed by the Bostik SAF30 120 adhesive. As the strength of the sample would decrease more dramatically as the gap increased and this is a linear fit, using this estimation for gaps larger than 10mm is not recommended. As an example, for a gap of 7mm, the Plexus MA590 is expected to fail around 6.75 MPa, the Bostik SAF30 120 is expected to fail around 6.01 MPa, and the Bostik SAF30 90 is expected to fail around 6.94 MPa.

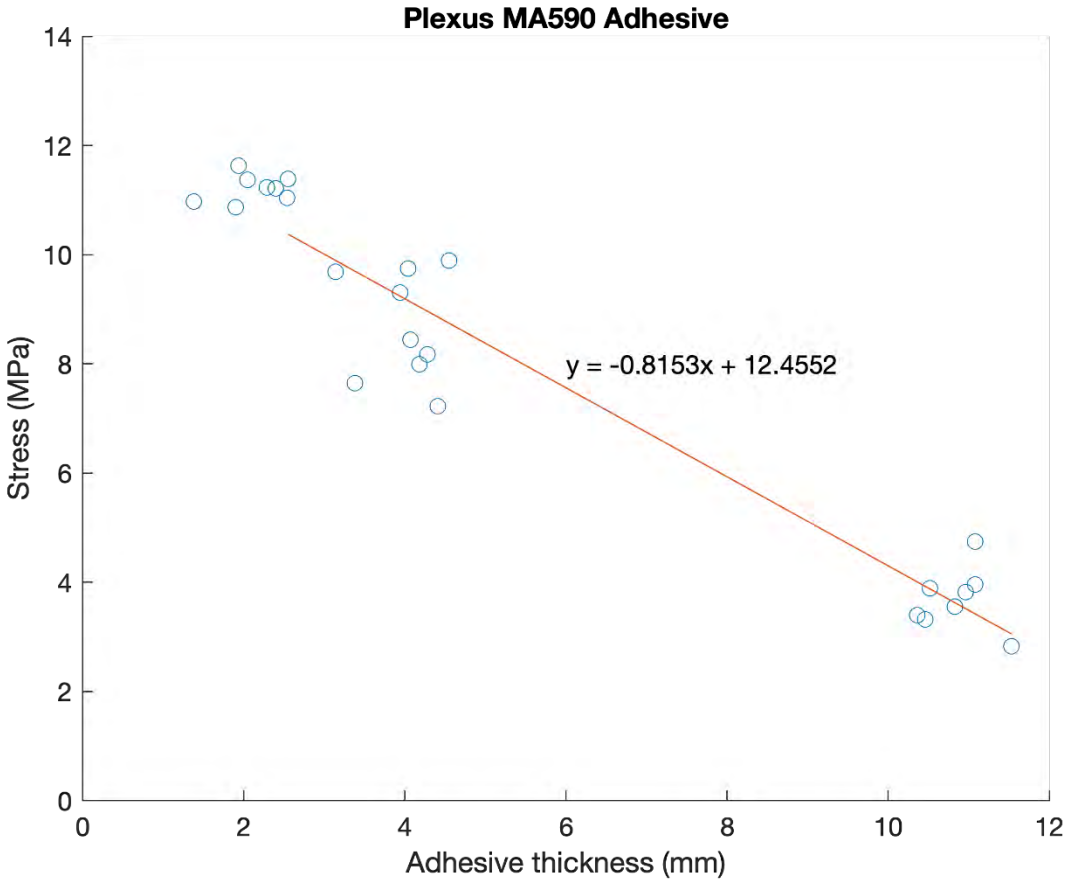

Figure 113. Plexus MA590 data trend to estimate maximum stress

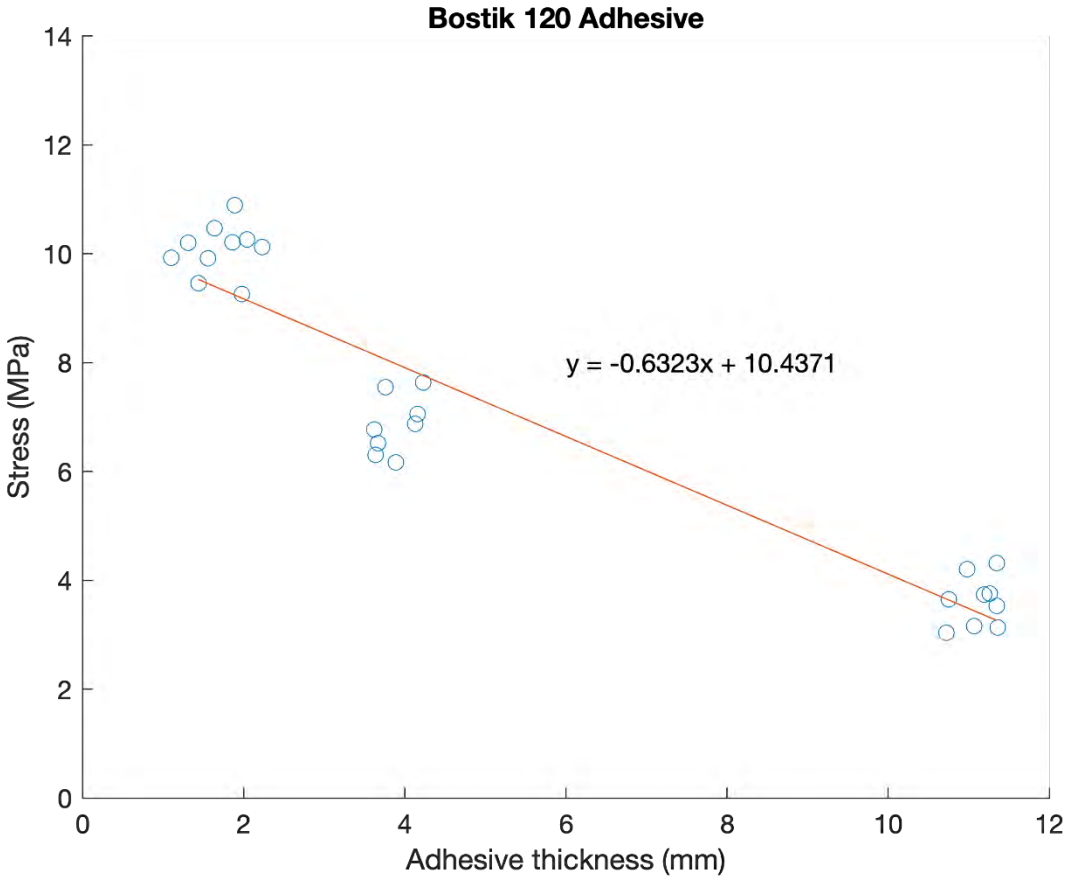

Figure 114. Bostik SAF 120 data trend to estimate maximum stress

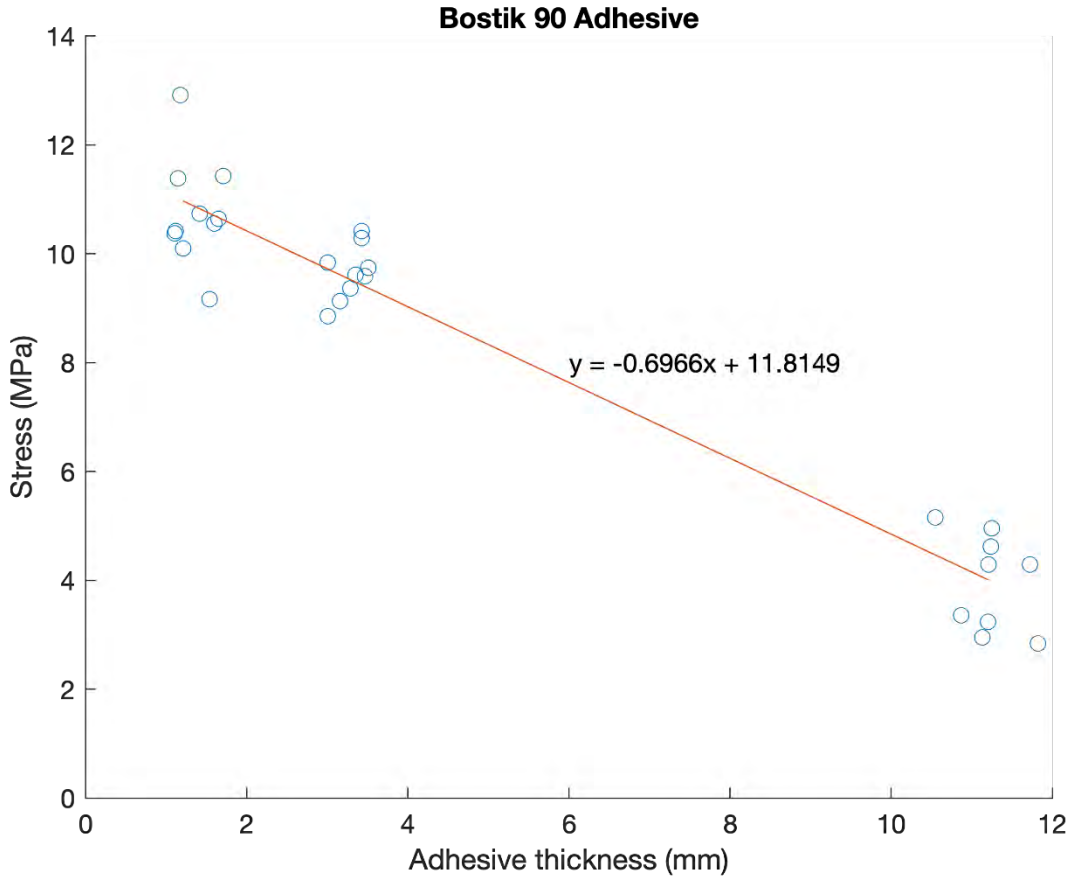

Figure 115. Bostik SAF 90 data trend to estimate maximum stress

5.6 NDE

Temperature monitoring of a composite part using thermocouples and full-field imaging system

The light weight and high strength exhibited by fiber-reinforced polymer (FRP) composites makes them well-suited for high-performance applications (aerospace, high-performance automotive, etc.). However, the expansion of composites into higher volume production industries is currently limited by their cost and a lack of efficient manufacturing techniques. Monitoring the curing process of these composites during manufacturing can potentially help with improving the quality and efficiency of the process and therefore reducing the cost of material waste (i.e., reducing the proportion of parts with unacceptable quality). The research work for this project is aimed at the development of an algorithm to estimate temperatures and degrees of cure inside curing FRP composite parts in real-time. The algorithm fuses the information obtained from surface temperature measurements taken using infrared (IR) thermography with a (physics-based) model of heat conduction to estimate internal temperatures and degrees of cure during the curing process. The non-contact sensing technique (IR thermography) does not interfere with curing or manufacturing operations and is well-suited for implementation in a manufacturing plant. The effectiveness of the methodology is demonstrated by successfully monitoring the key process variables in an FRP composite part manufactured at the National Renewable Energy Lab (NREL) Composites Manufacturing Education and Technology (CoMET) facility. The proposed methodology is a crucial step towards identifying anomalies in the manufacturing process (e.g., non-uniform resin distribution) that negatively impact the quality of FRP composite parts.

The challenges involved in real-time monitoring and estimation of key process states of a composite part as it undergoes the curing process in a mold are addressed using the following:

1. Measure the temperature of a composite part in the manufacturing process using thermocouples and a full-field thermal imaging system

2. Solve the inverse problem by estimating the temperature of a part below the surface of the part (in the bulk) using only the surface temperature measurements in conjunction with a real-time state estimation algorithm

3. Compare the temperature measurements of the part in the mold to those that are predicted using a simulation model to develop a leading indicator of possible sites for flaw formation in composite parts

During the molding process, the temperature of the material is changing due to resin flowing through the layup and the exothermic reaction of the resin. The material properties are also changing through the thickness of the part throughout the polymerization process. To detect and locate manufacturing flaws such as voids and non-uniform resin distribution, which create porosity and non-uniform temperature distribution in the part, the temperature of the part will need to be monitored over a wide area as function of time.

To address objective 1, the M&P team fabricated a VARTM mold at the Vanderbilt University Laboratory for Systems Integrity and Reliability (LASIR) and thermocouples were installed at several locations in the mold. During the molding process, a full-field thermal imaging system was used to measure the temperature of the external surface of the mold over a wide area and thermocouples installed in the mold will be used to measure the internal temperature of the material in the mold at several locations as a function of time. NREL provided the M&P team access to a 9 m blade molds located in their Composites Manufacturing Education and Technology (CoMET) facility. The M&P team deployed a full-field thermal imaging system, which is part of the mobile NDE lab, to NREL and worked with their team members to collect temperature data on the surface of the mold and from thermocouples in the mold as well. Any deviation between the predicted and measured temperatures would indicate an anomaly in the process and/or the material which could drive the formation of flaws in the part.

To address objective 2 the M&P team focused on solving the diagnostic inverse problem by estimating the temperature of a part below the surface of the part (in the bulk) using only the surface temperature measurements in conjunction with a fast system identification algorithm. To accomplish this the team:

- Developed an accurate, efficient and fast system identification algorithm to estimate the thermal and material state throughout the material in the mold during the curing process.
- Used the spatial and temporal temperature data on the surface of the material in the VARTM mold, collected with the full field thermal imaging system and thermocouples, as the input to the fast system identification algorithms.
- Compared the spatial and temporal temperature field data provided by the fast algorithms throughout each of panels to the size, depth and location of the defects identified with ultrasonic technologies to correlate the full field temperature and temperature gradients found in the panels to measured defects in each panel.

The M&P team provided temperature data collected on the 9 m blade section during the VARTM molding process to the Design, Modeling and Simulation (DM&S) team to compare temperature measurements of the part in the mold to those that are predicted using a simulation model.

The work done by the Vanderbilt team was divided into three tasks, corresponding to three milestones. The details of the work done to attain each of the milestones is discussed next.

Internal temperature estimation using a fast (real- or near-real-time) algorithm (Milestone 4.2.5.5)

Fast Algorithm Development

A discretized dynamic system representation of the curing spar cap is being used by considering the part as several smaller layers. Each of these layers conducts heat, stores heat, and also generates heat as a result of the curing of the Elium® resin provided by Arkema. By combining differential equations for each layer, a state-space representation of the dynamics of the heat transfer process was formed to calculate the rates of change of the temperatures for each layer. The temperatures for each layer were then determined through integration. The final result was a model that utilizes the measured surface IR temperature as an input and estimates the layer temperatures as an output.
The implemented model was both digitally and computationally inexpensive.

Fast Algorithm Validation

The M&P team and NREL staff worked together to layup fiberglass material provided by Johns-Manville in a section of a spar cap spar cap mold at the CoMET facility at NREL. Thermocouples were installed between some of the fiberglass layers and on the top fiberglass layer during the layup. A FLIR A8303sc IR camera was mounted above the spar cap mold at CoMET to record the surface temperature of the layup during infusion (See Figure 116).

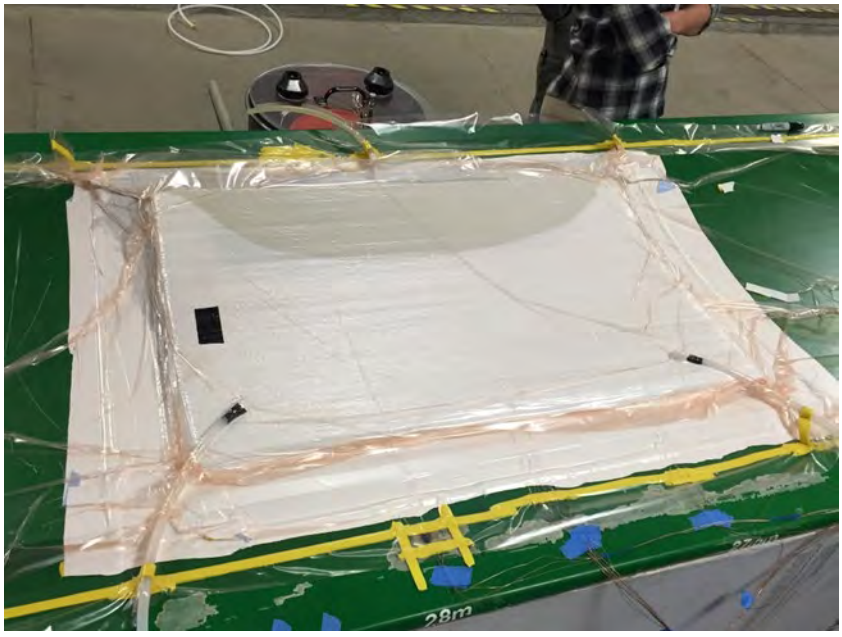

Figure 116. Spar Cap VARTM Layup during infusion at NREL (not pictured: IR camera mounted above layup)

The camera collected IR video of the infusion process, which provided surface temperatures across the spar cap as the resin was infused and cured the mold. A median filter was applied to the measured IR surface temperatures to eliminate dropouts, as well as a low-pass filter to reduce sensor noise. A separate National Instruments data acquisition system was used collect temperature data from the embedded thermocouples in the layup. Figure 117 shows IR video of the main portion of the curing process for the spar cap.

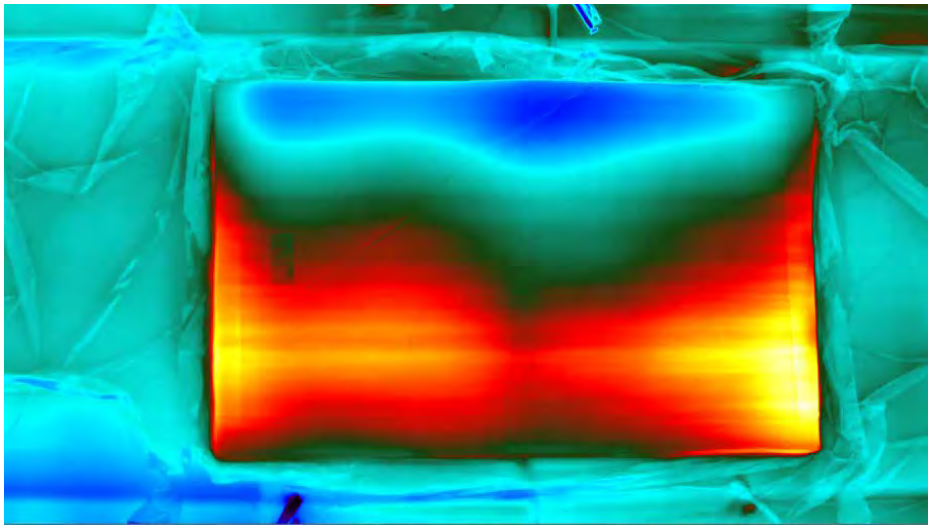

Figure 117. Image of the main portion of the curing process for the spar cap

A section of the spar cap manufactured at NREL that contained the embedded thermocouples was shipped to Vanderbilt LASIR for additional testing. The spar cap section was heated from below using a heating blanket in the lab and temperature data was collected using the embedded thermocouples. The temperature data was used for a lumped material property estimation of the entire spar cap. A finite element (FE) model of the test specimen shown in Figure 118 was created for parameter estimation and validation purposes. The FE Model was used to match predicted and measured temperatures at various depths by adjusting material properties used in the model.

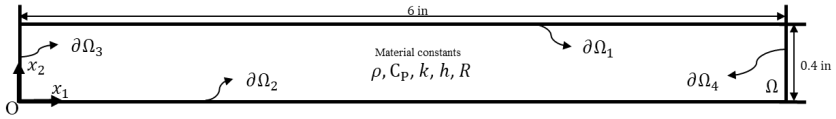

Figure 118. Finite element (FE) model of the test specimen

The governing equation used for the finite element model was:

$$\rho C_P \frac{\partial T}{\partial t} - \nabla \cdot (k \nabla T) = 0 \qquad (1)$$

With the following boundary conditions:

$$(-k\nabla T \cdot \boldsymbol{n}) = h(T - T_{\text{env}}) \quad \text{for } \mathbf{x} \in \partial\Omega_1 \qquad (-k\nabla T \cdot \boldsymbol{n}) = 0 \quad \text{for } \mathbf{x} \in \partial\Omega_3 \cup \partial\Omega_4$$

$$(-k\nabla T \cdot \boldsymbol{n}) = \frac{1}{R}(T - T_{\text{bot}}) \quad \text{for } \mathbf{x} \in \partial\Omega_2 \qquad T(\mathbf{x}, 0) = T_0 \quad \text{for } \mathbf{x} \in \Omega$$

Figure 119 show both the measured and estimated temperature of the spar cap section heated from below with a heat blanket.

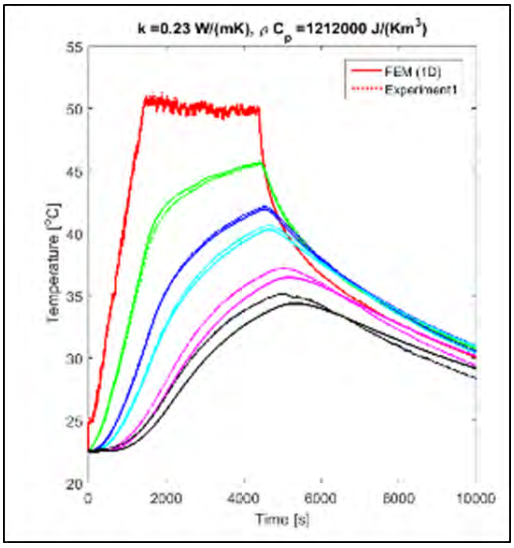

Figure 119. Measured and estimated temperature of the spar cap section heated from below with a heat blanket

The properties which returned the best fit of the FE model to the measured data for these heating experiments were used in our temperature prediction mode;

- Thermal conductivity: 0.23 W/(m*K)
- Specific Heat: 616.25 J/(kg*K)
- Density: 1966.7 kg/m3 (calculated from the total mass of the spar cap divided by its volume)

Lumped Parameter Model

The curing spar cap was modeled as a 9-DOF dynamic system, with 9 discrete elements at respective temperatures as shown in Figure 120. Each element is considered to have a thermal resistance and a thermal capacitance, and the temperature for each element is assumed to be uniform throughout the element. The measured temperature for the surface element is T_1, and the temperature at the bottom element is T_9. Nine (9) elements were chosen to satisfy the condition that the Biot number must be < 0.1 to assume lumped parameters.

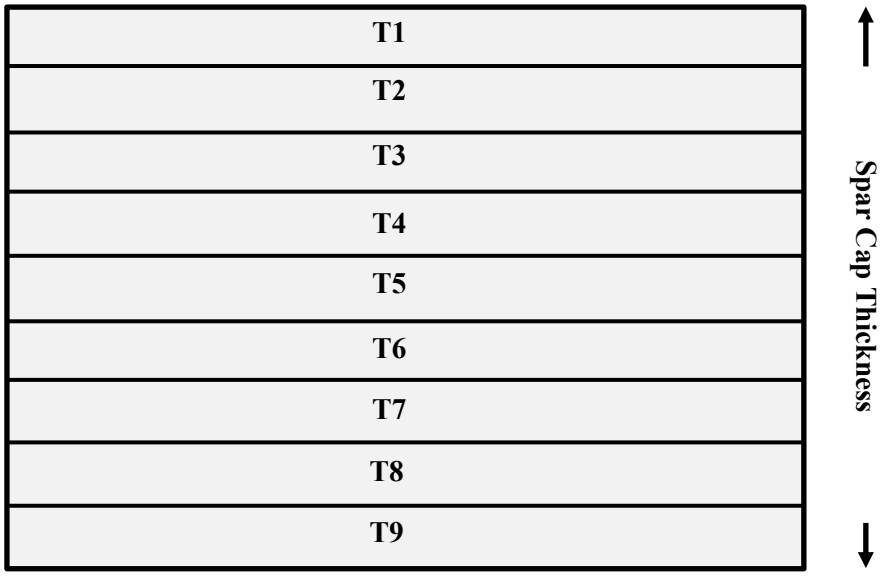

Figure 120. 9-DOF dynamic system used to model the spar cap with 9 discrete elements at respective temperatures

The following state equations were formulated for to represent each element in the model:
The following state equations were formulated for to represent each element in the model:

$$\dot{T_1} = -\left(\frac{1}{RC} + \frac{hA}{C}\right)T_{1,meas} + \frac{1}{RC}T_2 + \frac{\dot{H_{gen,1}}}{C} \quad (2)$$

$$\dot{T_2} = \frac{1}{RC}T_{1,calc} + \frac{1}{RC}T_3 - \frac{2}{RC}T_2 + \frac{\dot{H_{gen,2}}}{C} \quad (3)$$

$$\dot{T_3} = \frac{1}{RC}T_2 + \frac{1}{RC}T_4 - \frac{2}{RC}T_3 + \frac{\dot{H_{gen,3}}}{C} \quad (4)$$

$$\dot{T_4} = \frac{1}{RC}T_3 + \frac{1}{RC}T_5 - \frac{2}{RC}T_4 + \frac{\dot{H_{gen,4}}}{C} \quad (5)$$

$$\dot{T_5} = \frac{1}{RC}T_4 + \frac{1}{RC}T_6 - \frac{2}{RC}T_5 + \frac{\dot{H_{gen,5}}}{C} \quad (6)$$

$$\dot{T_6} = \frac{1}{RC}T_5 + \frac{1}{RC}T_7 - \frac{2}{RC}T_6 + \frac{\dot{H_{gen,6}}}{C} \quad (8)$$

$$\dot{T_7} = \frac{1}{RC}T_6 + \frac{1}{RC}T_8 - \frac{2}{RC}T_7 + \frac{\dot{H_{gen,7}}}{C} \quad (9)$$

$$\dot{T_8} = \frac{1}{RC}T_7 + \frac{1}{RC}T_9 - \frac{2}{RC}T_8 + \frac{\dot{H_{gen,8}}}{C} \quad (10)$$

$$\dot{T_9} = -\left(\frac{1}{RC} + \frac{1}{R_{h,mold}C}\right)T_9 + \frac{1}{RC}T_8 + \frac{\dot{H_{gen,9}}}{C} + \frac{T_{mold}}{R_{h,mold}} \quad (11)$$

The state-space formulation allowed us to use the surface temperature as an input to the model to compute the rates of change of temperatures inside the part, taking into account the heat transfer dynamics of the system. The rates of temperature change were integrated to estimate the temperatures at each layer and those temperatures were then used to compute the rates of temperature change for the next time step. The parameter definitions for the model are as follows:

- R = thermal resistance
- C = thermal capacitance
- h = convection coefficient
- $(H_{\text{gen}})^{\cdot}$ = heat generation
- $R_{h,mold} = \frac{1}{h_{mold}A}$, where h_{mold} = convection coefficient
- A = surface area
- T_{mold}= mold temperature

The heat generation during the reaction was based on the kinetics model for the Elium® resin developed by Colorado School of Mines (CSM) and was integrated into a model-free lookup table based on the format provided by Purdue and Convergent. This kinetics model output a derivative of the estimated extent of reaction based on the current temperature and extent of reaction. The heat generation was proportional to the derivative of the extent of reaction, with the scale factor being the total heat of reaction. The infusion at NREL was carried out using an exotherm control agent in the Elium® resin, which was not accounted for in the kinetics model. The kinetics lookup table was scaled to adjust for this exotherm control agent. Figure 121 shows the plots of the degree of cure estimates for each element of the model using the CSM kinetics model.

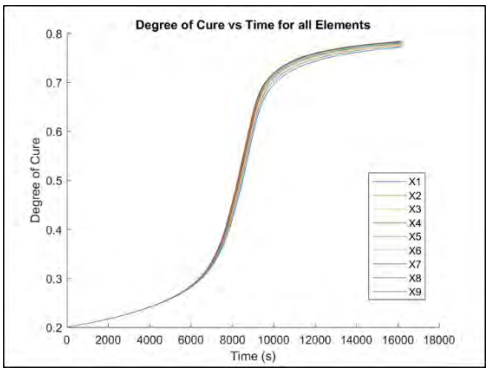

Figure 121. Degree of cure estimates for the Elium® resin for each element of the model

For each time step in the model, T1 was calculated from the state space equations, the ratio between the measured and predicted T1 was computed and this ratio was then used as a proportional gain to scale the predicted T1 value to be equal to the measured temperature.

Results: Internal Temperature Prediction

For each time step, T1 was calculated from the state space equations, the ratio between the measured and predicted T1 was computed and this ratio was then used as a proportional gain to scale the predicted T1 value to be equal to the measured temperature. Figure 122 shows a comparison of the measured and predicted mold surface temperatures.

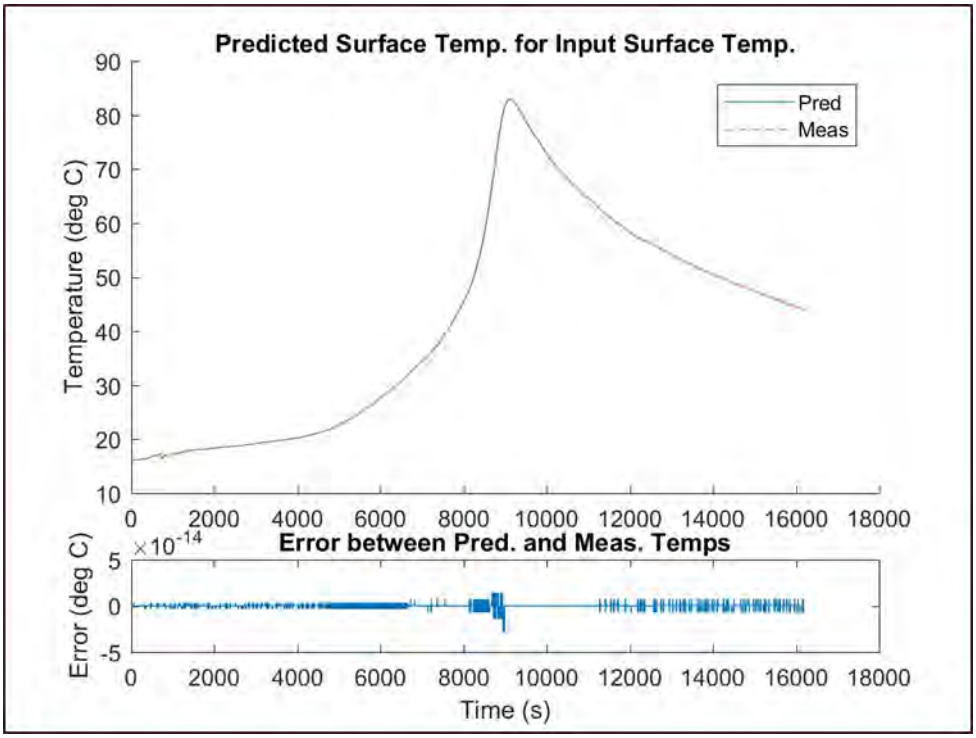

Figure 122. Comparison of the measured and predicted mold surface temperatures during an infusion

As a result, there is essentially no error between the measured and predicted surface temperatures:

- Mean error in the predicted surface temperatures: 5.10e-16 C
- Max error: in the predicted surface temperatures: 2.84e-14 C

The gain computed from the surface temperatures was then applied universally to the other predicted temperatures, and the scaled temperatures were used in the next time step to compute the new rates of temperature change. Figure 123 shows a comparison of the measured and predicted temperatures between the layers during an infusion.

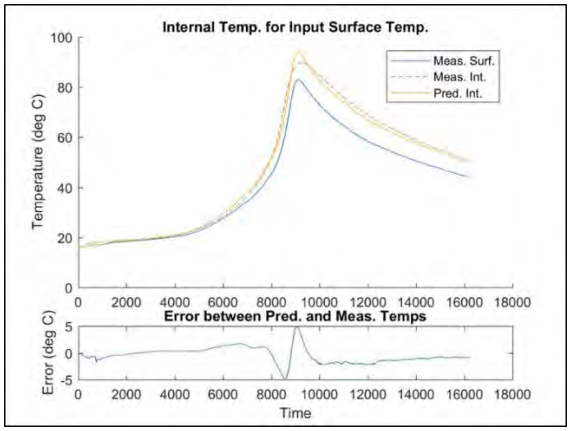

Figure 123: Comparison of the measured and predicted temperatures between the layers during an infusion

The red line in the plot the predicted internal temperature based only on the measured surface temperature (blue). Comparing the predictions with the measured internal temperature at the same depth (yellow), there is very good agreement with our predictions.

- Mean error: 1.18 C
- Max error: 4.94 C

Milestone 4.2.5.5: Estimate the temperature at one location on the surface of the mold and at one location inside the mold using the fast algorithm once per 30 minutes with an accuracy of +/- 5 C.

- The temperatures were estimated using a fast algorithm at rate of once per second.
- There was essentially no error between the measured and predicted surface temperatures.
- The max error magnitude for the internal temperature estimation was less than 5 C, with a mean error of 1.18 C.
- Milestone 4.2.5.5 met.

Additional work has been performed by M&P team to improve-upon this algorithm during the remainder of the 4.2 project. A Kalman filter-based state estimation algorithm was developed and used to estimate internal temperatures in two-dimensional space through the thickness of a curing composite section of a wind turbine blade. The results of this improved estimation algorithm will be included in a journal paper published by the Vanderbilt team and will be available to IACMI.

Flaw Identification in composite molding in the lab using IR temperature measurements (Milestone 4.2.5.8)

Surface temperatures of a curing composite were collected using an IR camera. For 8000 seconds during cure. Temperature is measured at each pixel so each pixel is essentially a temperature sensor. The heat lost per unit area (q) through the surface of the part at a particular pixel through convection (at sample i) is defined by:

$$q_{pix}^{i} = h\left(T_{pix}^{i} - T_{env}\right) \tag{12}$$

where h is the convection coefficient. Total energy lost to the environment from a pixel location is calculated by integrating heat loss over time:

$$E_{pix}^{i} = E_{pix}^{i-1} + \frac{1}{2}\Delta t(q_{pix}^{i} + q_{pix}^{i-1}) \tag{13}$$

Anomalies in the cumulative heat energy loss at a pixel indicate a potential flaw. Surface temperature data was collected during infusion and cure. Surface temperature distribution data was extracted every 10 seconds and cumulative energy loss values were calculated. Pixels with an energy loss value outside either 2 or 3 standard deviations (σ, discussed later) from the mean energy loss of all pixels were identified as outliers for that frame. Figure 124 shows the mean and 3σ statistical bands for the energy loss. An outlier score was calculated for each pixel after each frame:

- Outlier score = Percentage of frames in which a pixel was an outlier

A median filter was applied to the outlier scores to filter out isolated outlier pixels. A higher outlier score indicated a higher flaw potential at that location.

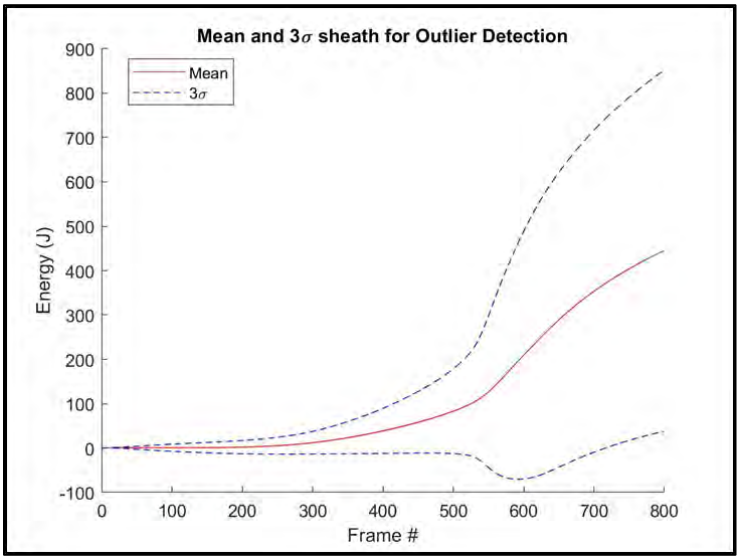

Figure 124. Mean and 3σ statistical bands for the calculated energy loss (Negative energy loss values correspond to energy gained from the environment. This typically occurs during infusion, when the resin temperature is lower than room temperature after the degassing process)

An algorithm was developed to detect flaws and the extent of the flaw formation based on the 2σ and 3σ bands:

- 3σ criteria: Flaw Detection
  - These criteria are stricter and only identify the most significant outliers
  - If pixels have nonzero outlier scores (after application of the median filter) for the 3σ criteria, then those pixels are identified as flaw locations
  - Outliers at pixels within 10% of the top, bottom, and inlet side edges are ignored, since outliers here are typical and do not represent a "characteristic" flaw
- 2σ criteria: Extent of Flaw
  - These criteria are less strict and identify more outliers
  - Once a flaw is detected using the 3σ criteria, the 2σ criteria can be used to determine the extent of the flaw
  - This will be shown later, when the location of a pinhole in the vacuum bag will be detected using 3σ and the effect of the pinhole will be shown using 2σ
  - Outliers within 15% of the inlet edge are ignored to prevent the pixels at the flow front from being identified as outliers during infusion

Two infusions were performed in the lab at Vanderbilt LASIR to demonstrate the flaw detection capability of this algorithm. Figure 125 shows a finished composite with a uniform cure that produced a quality laminate panel and the outlier score after 79998 samples using 3σ criteria. No flaws were detected with the outlier score.

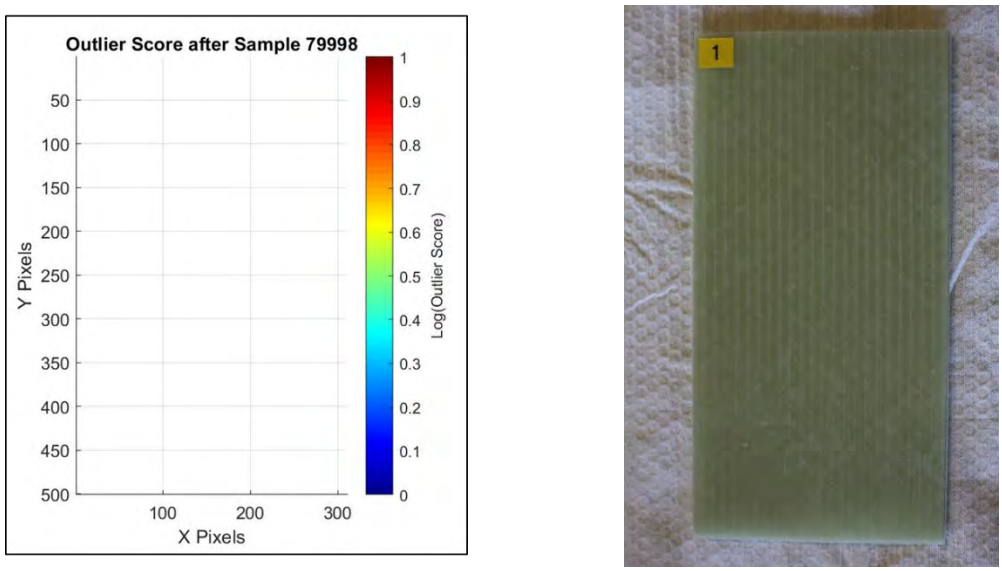

Figure 125. a) Outlier Score using 3σ criteria and b) picture of a "good" composite panel

A panel with a flaw was fabricated by applying pinhole prick in vacuum bag right before infusion which resulted in a laminate panel with dry spots (see Figure 126).

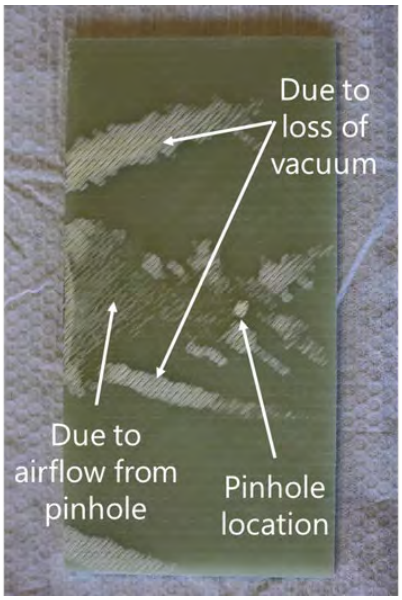

Figure 126. Picture of a "bad" composite panel with dry spots

The 3σ criteria were applied to the temperature data collected with the IR camera for this infusion. Figure 127 shows the Outlier Score for the composite panel with a pinhole flaw applied.

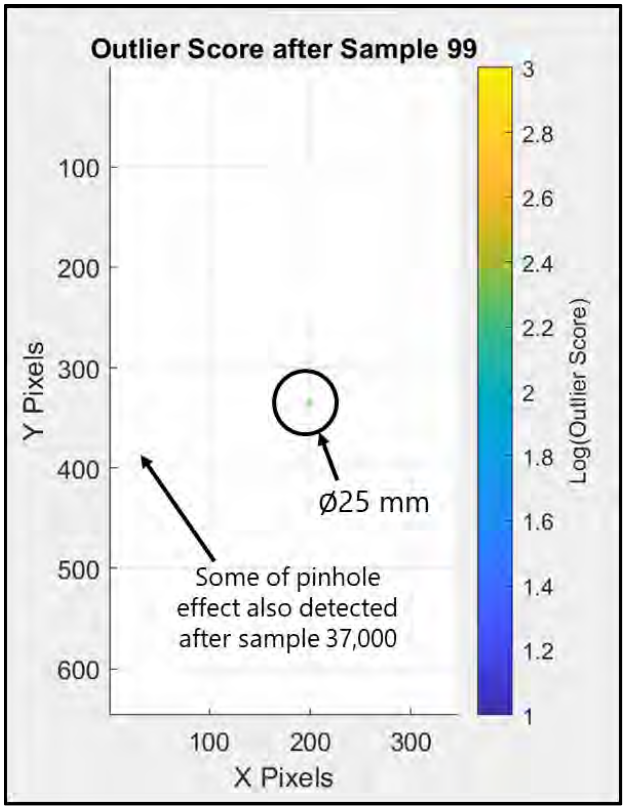

Figure 127. Outlier Score for the 3σ criteria applied for the "bad" composite panel with a pinhole flaw applied

The pinhole was identified after 99 samples. Ideally, this pinhole would be identified by the algorithm and immediately sealed to arrest the damage cause by the leak. The 2σ criteria were applied to the temperature data next. Figure 128 shows the outlier score the 2σ criteria.

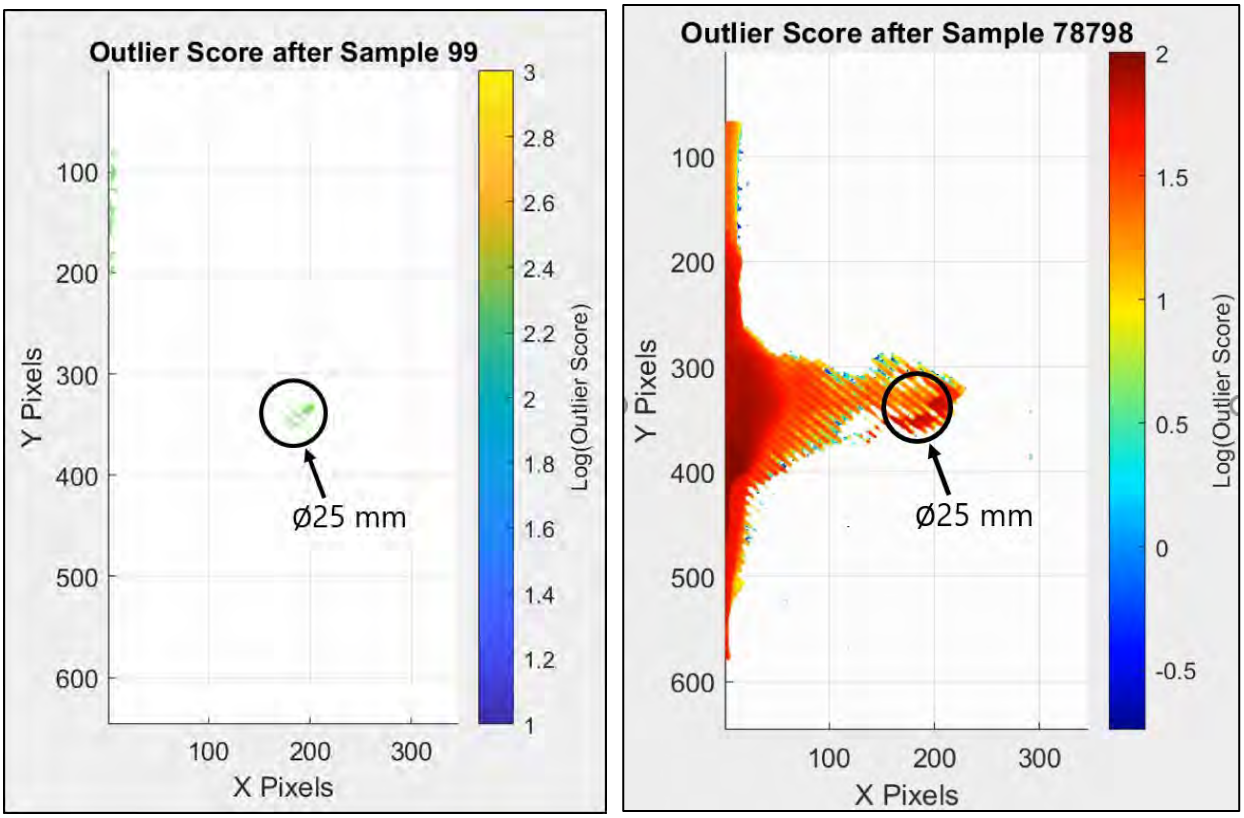

Figure 128. Outlier Score for the 2σ criteria applied for the "bad" composite panel with a pinhole flaw applied

Pixels outside 2σ are now identified as outliers, and the effect of pinhole becomes apparent. Figure 129 shows a comparison of the standard deviation for the good panel with no flaws and the bad panel with a pinhole leak.

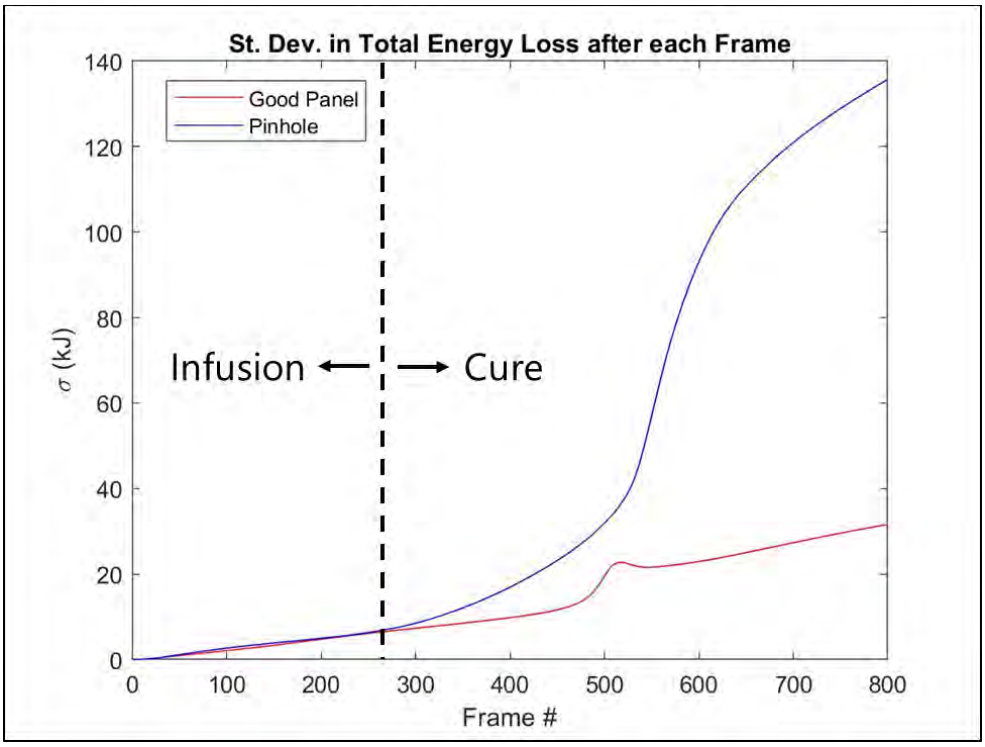

Figure 129. Comparison of the standard deviation for the good panel with no flaws and the bad panel with a pinhole leak

During cure, the panel with the pinhole has a noticeably higher standard deviation for the total energy loss across all pixels as compared to the good panel. The standard deviation in the energy loss seems to be a good indicator of composite part quality during cure.

Milestone 4.2.5.7: Estimate the location of one manufacturing flaw in a molded part in the lab, with a characteristic flaw size of 25 mm diameter or smaller within a diameter of 30 mm using measured mold surface temperature from an IR camera, embedded thermocouples in the mold, temperature estimation algorithms, and data analytics.

- The Heat Energy Loss Outlier algorithm was able to detect and locate a pinhole in the vacuum bag during a VARTM infusion of a composite panel (3σ criteria)
- The algorithm found no flaws in the good panel and is fast enough to run in real time
- The pinhole satisfies the requirement that the characteristic flaw be less than 25 mm in diameter
- Once the pinhole was detected, its effect was highlighted using a relaxed (2σ) criteria
- Milestone 4.2.5.7 met.

Flaw Identification during composite molding in a blade mold using IR temperature measurements

Two max chord sections of a wind turbine blade were manufactured at NREL's CoMET facility. Surface temperatures were measured during before the infusion, during the infusion, and during curing processes using an IR camera. The test setup is shown in Figure 130.

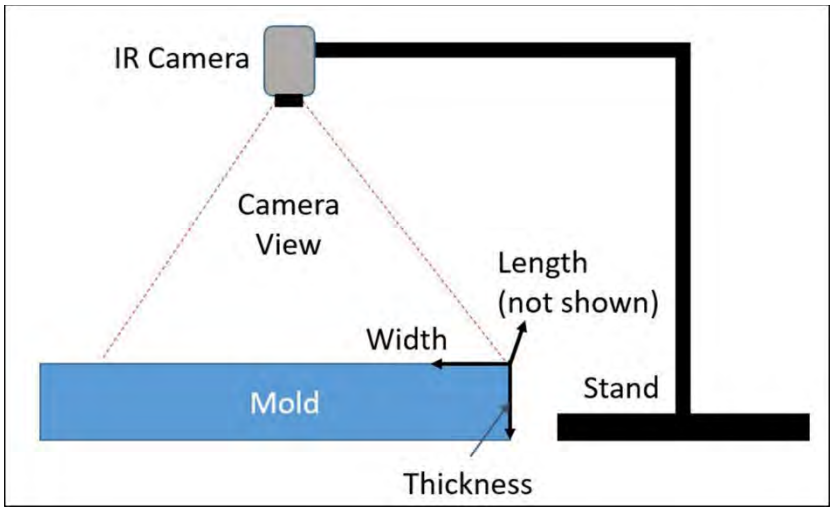

a: side view

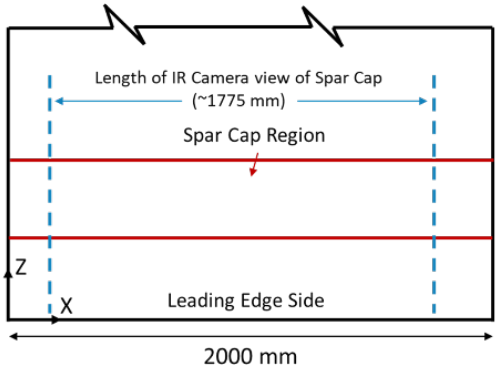

b: top view

Figure 130. Test setup at the CoMET facility for collecting IR temperature data during blade mold infusion

A pinhole was pricked in the vacuum bag of max chord 1 layup to introduce a flaw before infusion, while no flaw was introduced into max chord 2. The pinhole was patched later in the process to simulate the flaw being found and corrected. The surface temperatures measured using IR thermography were used as part of a Heat Energy Loss Outlier algorithm to estimate the location of the pinhole. Other heat anomalies were also indicated by the algorithm. Figure 131 shows IR image of an infusion with the pinhole being detected pre-infusion with the energy loss algorithm.

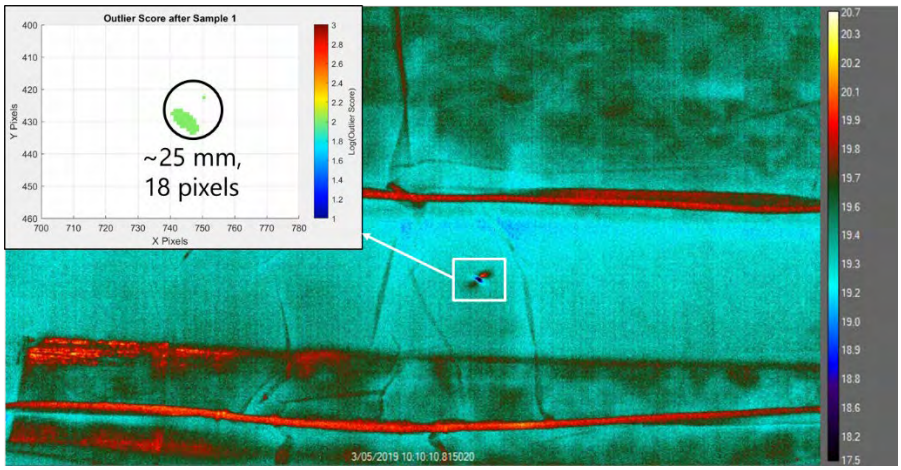

Figure 131. IR image of an infusion with the pinhole being detected pre-infusion with the energy loss algorithm

Figure 132 shows picture of the cured composite that had a pinhole in the bag that was sealed up during the infusion. There was some discoloration in the area where the pin hole was located.

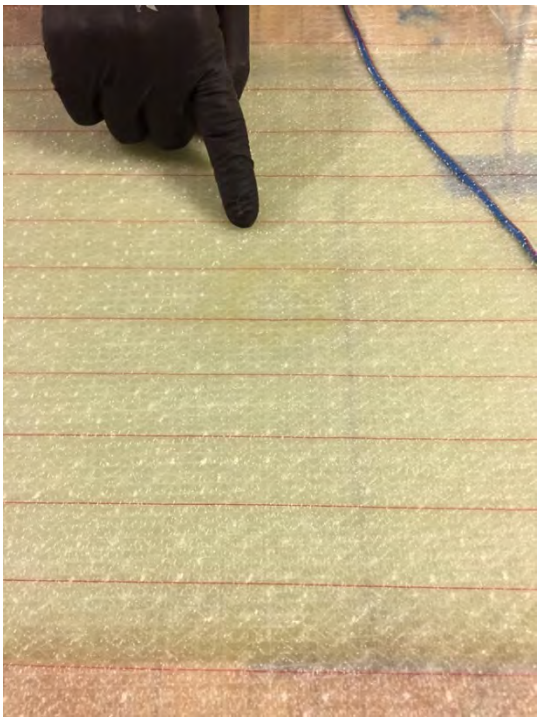

Figure 132. Picture of a cured composite that had a pinhole in the bag that was sealed up during the infusion

Figure 133 shows the outlier score after 87699 IR temperature samples. The energy loss algorithm indicates that there are cold areas, areas where resin has boiled and hot spots in the balsa region along detecting and locating the pinhole in the bag during the infusion.

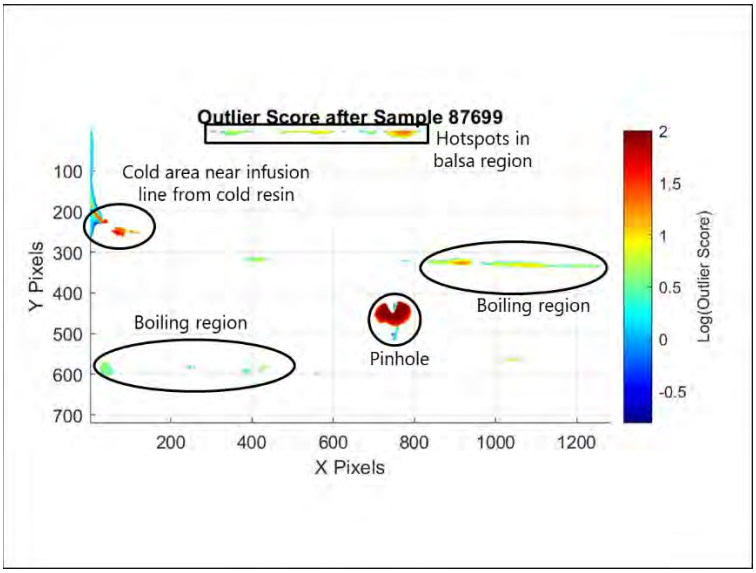

Figure 133. Outlier score after 87699 IR temperature samples

Milestone 4.2.5.8: Estimate the location of one manufacturing flaw in molded part at the CoMET facility, with a characteristic flaw size of 25 mm diameter or smaller within a diameter of 30 mm using measured mold surface temperature from an IR camera, embedded thermocouples in the mold, temperature estimation algorithms and data analytics.

- The Heat Energy Loss Outlier Algorithm was able to detect and locate a pinhole in the vacuum bag during the manufacturing process of a composite part made at NREL's CoMET facility using surface temperature data collected by an IR camera (see Figure 126).
- The pinhole satisfies the requirement that the flaw be less than 25 mm in diameter
- Milestone 4.2.5.8 met.

5.7 Wind Blade Component Manufacturing and Validation

Manufacturing a 13-meter Elium® Composite Wind Turbine Blade

A 13-meter wind turbine blade was produced by the 4.2 project team in the CoMET facility at NREL. Details of this blade manufacturing are contained in Appendix B

Validation Plans for Full-Scale 13-meter Elium® Composite Wind Turbine Blade

Plans were developed for full-scale static and fatigue validation to the 13-meter Elium® composite wind blade. These plans are contained in the following Appendices:

- Appendix C—Static test plan for maximum flapwise loading
- Appendix D—Static test plan for minimum flapwise and maximum and minimum edgewise loading
- Appendix E—Fatigue test plan for flapwise loading

Validation Results for Full-Scale 13-meter Elium® Composite Wind Turbine Blade

The results from the full-scale 13-meter blade validation are contained in Appendix F

5.8 Thermoplastic Composite Recycling

The recycling research from this project was published in the Journal of Cleaner Production in February 2019 (Cousins, Suzuki, Murray, Samaniuk, & Stebner, 2019); it is reprinted in its entirety in Appendix G, with permission from the publisher. A link to this published journal article is available here:

https://www.sciencedirect.com/science/article/pii/S0959652618333195

The abstract for this journal article is copied below:

Thermoplastic resin systems have long been discussed for use in large-scale composite parts but have yet to be exploited by the energy industry. The use of these resins versus their thermosetting counterparts can potentially introduce cost savings due to non-heated tooling, shorter manufacturing cycle times, and recovery of raw materials from the retired part. Because composite parts have high embedded energy, recovery of their constituent materials can provide substantial economic benefit. This study determines the feasibility of recycling composite wind turbine blade components that are fabricated with glass fiber reinforced Elium® thermoplastic resin. Several experiments are conducted to tabulate important material properties that are relevant to recycling, including thermal degradation, grinding, and dissolution of the polymer matrix to recover the constituent materials. Dissolution, which is a process unique to thermoplastic matrices, allows recovery of both the polymer matrix and full-length glass fibers, which maintain their stiffness (190 N/(mm g)) and strength (160 N/g) through the recovery process. Injection molded regrind material is stiffer (12 GPa compared to 10 GPa) and stronger (150 MPa compared to 84 MPa) than virgin material that had shorter fibers. An economic analysis of the technical data shows that recycling thermoplastic–glass fiber composites via dissolution into their constituent parts is commercially feasible under certain conditions. This analysis concludes that 50% of the glass fiber must be recovered and resold for a price of $0.28/kg. Additionally, 90% of the resin must be recovered and resold at a price of $2.50/kg.

6. BENEFITS ASSESSMENT

A primary benefit of this project is the demonstration of a resin system that can be processed in an identical manner to widely used epoxy thermoset resin systems but remains fully thermoplastic after cure. Never before has this been viable. Beyond achieving obligatory mechanical performance, the thermoplastic resin brings many other benefits such as ambient temperature curing and a solution for end-of-life reusability. Ambient temperature curing eliminates the need for a heated mold surface and post-curing, costly required steps for epoxy thermoset systems. The thermoplastic polymer matrix provides an opportunity to recycle and reclaim the separate constituents of the composite material, preventing the blade materials from being discarded into a landfill. Preliminary calculations on recycling of the thermoplastic wind blade indicated a net economic benefit to recyclers. This advantage will have massive implications when this material strategy is adopted in large scale turbines. As wind energy continues to grow, such a future path anticipates a solution to addressing inevitable limitations in end-of-life landfill space requirements.

Results from the early stage techno-economic evaluation indicated an approximately 5% decrease in blade manufacturing costs using the thermoplastic resin compared to a baseline epoxy blade. The calculations do not yet take into account economies of scale cost savings for the thermoplastic resin. Hence, it is anticipated that the material cost will continue to diminish favorably. This anticipated economic benefit paired with the reusability of the blade at end-of-life is expected to incentivize blade manufacturers to adopt the technologies demonstrated in the project.

Furthermore, composites manufacturers with a different application focus can benefit by leveraging data generated during this project; e.g., for VAWTs (vertical axis wind turbines). They will be able apply advantages of the unique characteristics and properties of the liquid thermoplastic composite technology, even to the extent that the advantages can be leveraged in new processes and designs.

7. COMMERCIALIZATION

During the course of the project, we have worked with OEM partners, Tier 1 suppliers, raw materials suppliers, and mentors to enable the evaluation and commercialization of new materials into the commercial production of thermoplastic wind blades for use at large OEMs.

The results of these evaluations highlight that the thermoplastic blade performs mechanically as good as or better than similarly manufactured thermoset blades. Additionally, the techno-economic model has shown that even at the current economy of scale for the thermoplastic resin system, there is an approximately 5% cost advantage of the thermoplastic blade compared to a thermoset blade.

In addition to the initial required coupon level testing, the project took the Technology Readiness Level (TRL) of the project through stage 6/7 by the production and testing of a 13m prototype blade, thereby minimizing the risk for OEM's interest in adopting the technology.

Arkema intends to share applicable performance/cost benefit learnings to respective OEMs and Tier 1 blade suppliers for adoption of the technology in their current blade production. As such, Arkema already commercially supplies liquid thermoplastic resin materials for other composite applications; this project enables expansion of that supply to all wind blade manufacturers.

8. ACCOMPLISHMENTS

Journal Articles

IACMI 4.2 project research was published in the following journal articles—additional pending publications are not listed here:

- **Journal of Applied Polymer Science,** *Infusible Acrylic Thermoplastic Resins: Tailoring of Chemorheological Properties*. Dylan Cousins, Jackson Howell, Yasuhito Suzuki, Joseph Samaniuk, Aaron Stebner, John Dorgan. Published May 2019. https://onlinelibrary.wiley.com/doi/full/10.1002/app.48006
- **Journal of Cleaner Production,** *Recycling glass fiber thermoplastic composites from wind turbine blades*. Dylan Cousins, Yasuhito Suzuki, Robynne Murray, Joseph Samaniuk, Aaron Stebner. Published February 2019. https://www.sciencedirect.com/science/article/pii/S0959652618333195
- **Journal of Renewable Energy**, *Techno-Economic Analysis of a Megawatt-Scale Thermoplastic Resin Wind Turbine Blade***.** Robynne Murray, Scott Jenne, David Snowberg, Derek Berry and Dylan Cousins. Published February 2019. https://www.sciencedirect.com/science/article/pii/S0960148118308292
- **Journal of Applied Composite Materials,** *Manufacturing and Flexural Characterization of Infusion-Reacted Thermoplastic Wind Turbine Blade Subcomponents*. Robynne Murray, Dayakar Penumadu, Dylan Cousins, Ryan Beach, David Snowberg, Derek Berry, Yasuhito Suzuki, Aaron Stebner. Published January 2019. https://link.springer.com/article/10.1007/s10443-019-9760-2
- **Journal of Composite Materials**, *Dual-energy X-ray computed tomography for void detection in fiber-reinforced composites*. Yasuhito Suzuki, Dylan Cousins, John Dorgan, Aaron Stebner, Branden Kappes. Published January 2019. https://journals.sagepub.com/doi/abs/10.1177/0021998319827091

- **Polymer Journal,** *Phase separation during bulk polymerization of methyl methacrylate.* Yasuhito Suzuki, Dylan Cousins, Yuya Shinagawa, Robert Bell, Akikazu Matsumoto and Aaron Stebner. Published November 2018. https://www.nature.com/articles/s41428-018-0142-7
- **Journal of Composites: Part A: Applied Science and Manufacturing,** *Kinetics and temperature evolution during the bulk polymerization of methyl methacrylate for vacuum-assisted resin transfer molding.* Yasuhito Suzuki, Dylan Cousins, Jerred Wassgren, Branden Kappes, John Dorgan, Aaron Stebner. Published January 2018. https://www.sciencedirect.com/science/article/pii/S1359835X17303809
- **Journal of Applied Polymer Science**, *Miscible blends of biobased poly(lactide) with poly(methyl methacrylate): Effects of chopped glass fiber incorporation.* Dylan Cousins, Corinne Lowe, Dana Swan, Robert Barsotti, Mingfu Zhang, Klaus Gleich, Derek Berry, David Snowberg, John Dorgan. Published February 2017. http://onlinelibrary.wiley.com/doi/10.1002/app.44868/full

Conferences

IACMI 4.2 project research was presented at the following conferences:

- **Wind Europe Offshore 2019**, *Structural Validation of a 13m Thermoplastic Wind Turbine Blade.* Ryan Beach, Copenhagen. November 2019
- **Thermoset Resin Formulators Association Conference**, *Real-time resin temperature estimation of a VARTM composite using infrared thermography*. Chris Nash, Ray Bond, Douglas Adams. Nashville, Tennessee. March 2018
- **American Society for Composites, 32nd Technical Conference**, *Manufacturing a 9-meter thermoplastic composite wind turbine blade*. Robynne Murray, Dana Swan, David Snowberg, Derek Berry, Ryan Beach, Sam Rooney. West Lafayette, Indiana. October 2017. http://dpi-proceedings.com/index.php/asc32/article/view/15166 https://www.nrel.gov/docs/fy18osti/68615.pdf

Undergraduate Students, Graduate Students, and Post Docs

IACMI 4.2 project research supported the following students and post docs:

- Dylan Cousins (CSM)
- Peter Caltagirone (CSM)
- Nicole Thomas (CSM)
- Yasuhito Suzuki (CSM)
- Cheikh Cissé (CSM)
- David Briddle (CSM)
- Nicholas Rollman (CSM)
- Jackson Howell (CSM)
- Brandon Hinkle (CSM)
- Nathan Sharp (Purdue)
- Drew Sommer (Purdue)
- Zach Arwood (UTK)
- Stephen Young (UTK)
- Andrew Patchen (UTK)
- Colby Gilbert (UTK)
- James Eun (UTK)
- Sean Lee (UTK)
- Darren Foster (UTK)
- Chris Nash (Vanderbilt)
- Ray Bond (Vanderbilt)

Graduate Theses
IACMI 4.2 project research supported the following graduate theses:

- Dylan Cousins (CSM), PhD in Chemical Engineering: *Advanced Thermoplastic Composites for Wind Turbine Blade Manufacturing*, Colorado School of Mines, December 2018
- Zach Arwood (UTK), partial fulfillment of doctoral study, expected to complete in Spring, 2021

9. CONCLUSIONS

As presented in Section 3 of this report, the overall goals of the IACMI 4.2 project were to identify potential thermoplastic resin systems for wind blade design and production, down select the potential resin systems, develop a material property database through extensive coupon testing, validate resin processing at several scales, and finalize the effort with the production and full-scale structural validation of a 13 meter thermoplastic wind turbine blade. The project team was successful in all of these measures, as well as in other scientific efforts to develop approaches to quantify the material characteristics and processing through the use of NDE and process modeling. While the details of all of these research efforts are presented earlier in this report, this section will summarize the conclusions of the research.

One of the first tasks for the 4.2 project team was to identify potential thermoplastic resin systems that may be candidates for use in the design and production of current utility scale wind turbine blades. These systems, to be utilized as a replacement for the current state-of-the-art technology of thermoset resin systems, had to be evaluated for several key factors that would enable the use of any thermoplastic matrix with current manufacturing practices employed by wind blade manufacturers today. During this initial phase of the research, two potential thermoplastic resins were identified: Nylon-6 and Arkema's Elium® resin system. After preliminary analysis of both systems, the team decided that only the Elium® thermoplastic resin was suitable for use as a 'drop-in' replacement matrix for the currently used thermoset resin systems in wind blade production. The two key issues leading to the elimination of the Nylon-6 thermoplastic system were exotherm temperature and moisture sensitivity. The vast majority of megawatt scale wind blades produced in the US and globally today utilize FRP tooling. These existing molds can handle processing temperatures of up to about 100°C. While Arkema had developed chemistry solutions to limit exotherm during polymerization to somewhere in the range of 80°C, exothermic temperatures during the processing of Nylon-6 reach well above 100°C. In addition, early research identified a potential for Nylon-6 laminates to have an issue with moisture uptake. While no experiments were conducted to assess the level of moisture sensitivity of wind blade laminates in hot/wet environments, this drawback of Nylon-6, in conjunction with the elevated exotherm temperatures, led the team to eliminate this system from consideration. At this point, Elium® became the down-selected thermoplastic resin system to be evaluated during this project.

The next steps in assessing the viability of Arkema's Elium® resin system for use in the design and production of utility scale wind blades included:

- Development of an Elium® material property matrix through coupon testing;
- Comparison of Elium® material properties to current baseline blade matrix properties;
- Development of a comprehensive techno-economic model for the use of Elium® in wind blade production;
- Assessment of Elium® processing characteristics at several scales in the laboratory;
- Final processing and structural validation of the Elium® matrix in a 13-meter wind blade.

As presented earlier in this report, a comprehensive database of material properties for the Elium® thermoplastic resin system was developed through the extensive coupon testing performed by CSM, UTK and other project partners. At the same time, TPI Composites developed a representative baseline of matrix properties for current thermoset resin systems being used in blade production today. While the Elium® composite material properties compared favorably to the baseline thermoset composite properties, the follow-on step of developing a comprehensive TE model comparing both the Elium® and a thermoset epoxy resin system was required to provide detailed metrics to be used in the comparison between the two systems, including an overall metric of final production cost of a blade manufactured with the different systems. The variables included in the TE model included:

- Material costs;
- Material waste percentages and costs;
- Labor costs;
- Capital costs for tooling, fixtures, etc.;
- Potential for recyclability;
- Material properties.

It should be noted that Nylon-6 was also included in early versions of the TE model showing the significant capital investment that would be required to deploy tooling with the capability to handle the elevated processing temperatures of that resin system. The large increase in the cost of tooling for Nylon-6 processing resulted in a manufactured blade cost far higher than for the baseline epoxy blade or the Elium® blade.

While the Elium® material costs were somewhat higher than the baseline epoxy material costs, the TE model also displayed some significant savings in capital equipment costs, labor costs and cycle time for the Elium® blade. Also, it should be noted that the cost for Elium® may be reduced through volume pricing. Overall, the TE model developed during the project showed a slightly lower per blade cost for the Elium® blade compared to the baseline epoxy blade. While the TE model does not take into account all aspects of blade production – such as marketing costs, other overhead costs, etc. – the model does account for the major cost elements of wind blade production and can provide a fairly accurate comparison of final blade cost. Hopefully, the TE model can be a useful tool for our industry partners to make decisions concerning the commercialization of a thermoplastic resin system for use in the design and production of utility scale wind turbine blades.

The research conducted in this project also focused on the processability of the Elium® thermoplastic resin system at various scales: panel (coupon), wind blade element (I-beam), wind blade sub-structure (root, maximum chord, tip, etc.), and full scale wind turbine blade (13 meter blade). The early work consisted of producing many panels varying in length, width and also laminate thickness. The research showed that Elium® could be processed at all panel scales, including very thick laminates in excess of 50 mm. The relatively low viscosity of the Elium® resin system also allowed for efficient wet-out times for panels compared to the epoxy baseline. Finally, evaluations were done at various panel sizes and thicknesses to assess the level of exotherm of the Elium® system. It was shown that, even with very thick laminates, the temperature of the polymerization of the resin could be limited to below about 80°C.

After initial processability trials at the panel level, the team then conducted research at blade element, substructure and full scale. While many processing lessons were learned during this research (e.g., optimal layout of vacuum and feed lines, laminate stacking details to ensure fabric wet-out, etc.), Elium® as well as baseline resin systems in overall processability at all scales of blade production.

The final phase of research for this project was the validation of a full scale Elium® wind turbine blade

with the comparison to an almost identical epoxy blade. A 13-meter Elium® wind blade was validated through full scale structural testing at NREL's Structural Testing Laboratory. The results of this testing were compared to the earlier testing of an epoxy 13-meter blade produced with the same mold and the same structural laminate. The testing consisted of blade properties, modal analysis, static testing and lifetime fatigue testing. As presented earlier in this report, the Elium® wind blade performed exceptionally well throughout the testing, passing all phases of validation compared to the baseline epoxy blade.

Overall, the research conducted during the IACMI 4.2 project demonstrated that the Arkema Elium® thermoplastic resin system is a viable potential drop-in replacement for current epoxy and other thermoset resin systems currently employed by wind turbine OEMs and blade manufacturers in the US and around the world. This research has provided the results and information that can be used in further commercialization activities in conjunction with industry partners.

10. RECOMMENDATIONS

This section of the report will cover two subjects: the recommended steps for the commercialization of the thermoplastic technology that was the subject of this research, and the recommended areas of future research in the area of thermoplastic technology that could expand the knowledge base of this innovative material and increase the viability of the technology across wind industry applications as well as the applicability in many other composite industries. In many ways, the recommendations for steps to commercialization and the recommendations for future research are closely related, as many of the areas of potential follow-on research will serve to overcome some of the challenges to commercialization.

Recommended Steps for Commercialization

The IACMI 4.2 project has brought together a diverse and capable research team consisting of a broad cross-section of IACMI industry partners, universities, and national laboratories. As with all IACMI projects, the foremost goal of this research project was to advance the technology – in this case a thermoplastic resin system suitable for wind turbine blade production – in conjunction with our industry partners to enable commercialization of this innovative material. In this case, the targeted industry for commercialization was the US wind turbine industry; however, the research executed in this project will also enable potential commercialization of the novel composite material in other industries as well. All phases of this research projects - including techno-economic analysis, early composite panel processing, coupon testing, material processing at the sub-component level, process non-destructive evaluation research, manufacturing modeling and analysis, and the production, testing and validation of a full-scale 13-meter thermoplastic wind turbine blade – served to advance the research to augment the viability of this new technology and to ultimately lead to a clear path to commercialization for this thermoplastic resin system in the wind industry with potential future applications in additional composite industries. Our goal is to work closely with our IACMI industry partners at the conclusion of this research project to scale the new technology for viable deployment in current megawatt-scale wind turbine blades for both the onshore and offshore US wind market.

In order to realize the successful commercialization of this novel thermoplastic resin system in the wind turbine blade manufacturing environment, the IACMI 4.2 research team has identified several steps to implement as well as some challenges to overcome. The primary path to commercialization is to demonstrate and validate the new technology at scale. For the US wind industry, this means deploying the thermoplastic resin system in wind turbine blades in the range of 60 to 70 meters in length. This

challenge has been broken down into three categories: the primary steps to achieve this goal, the supporting work required to achieve this goal, and the challenges to achieving this goal. These are presented in the three sections below.

Primary Steps for Commercialization:

- Define a phase-gate process for the potential commercialization of the Elium® thermoplastic resin system, including distinct phases and decision points (gates) with appropriate Go/No-Go criteria to proceed through each gate. Each gate should contain the following elements: inputs, criteria and outputs required to satisfy each step. The tasks, cost, and risks should be identified for each step of the process. Standard wind turbine blade design, validation and certification processes should be taken into account. In addition to the conventional commercialization considerations for wind turbine blades, the decision points for the commercialization of the Elium® thermoplastic resin system should include innovations such as thermal welding and circular economy benefits of the technology. Each phase of the process should identify the key stakeholders to provide input and oversight. For the process of commercialization of a new material for wind turbine blades, this could include such entities as wind turbine OEMs, wind turbine blade designers and manufacturers, blade component and full-scale testing organizations, blade standardization and certification bodies, wind plant financiers, government agencies (such as DOE), etc.
- Identify the supply chain necessary to commercialize the Elium® thermoplastic resin system in the US wind industry;
    - The supply chain should include material suppliers, wind turbine blade manufacturers and wind turbine OEMs;
    - The IACMI industry partners that participated on the 4.2 research project already represent major supply chain elements in this process: Arkema produces the Elium® thermoplastic resin system, Johns Manville produces fiberglass with a sizing that is compatible with the Elium® resin system, and TPI Composites is the world's largest independent supplier of wind turbine blades;
    - Identify additional supply chain entities, such as wind turbine OEMs;
- Review and synthesize the research completed in this IACMI project with the ongoing research in the European based Effiwind 25-meter thermoplastic wind turbine blade project (Chrisophe, 12 March 2020.)(Arkema is an industry partner on both research efforts);
- Analyze the current US wind blade production environment to determine the optimal wind turbine blade length for deployment of the Elium® thermoplastic resin system;
- Working with a wind turbine blade manufacturer and/or a wind turbine OEM, design a new megawatt-scale wind turbine blade in the length range identified above utilizing the Elium® thermoplastic resin system;
- In conjunction with the wind turbine blade supplier and/or a wind turbine OEM partner(s), identify a US blade manufacturing facility that could serve as the initial production site for the wind turbine blade designed with the Elium® thermoplastic resin system;
- In the chosen production environment, manufacture the first full-scale multi-megawatt wind turbine blade – and use this blade as the initial 'cut-up' blade to evaluate the process and quality of the blade structure;
- Once the 'cut-up' blade has been evaluated – and any changes to the manufacturing process updated – produce a second blade to serve as the test blade;
- Perform a full-scale structural validation (similar to the testing program for the 13-meter blade in this project) for the Elium® wind turbine blade;
- If the full-scale structural test results successfully validate a viable Elium® thermoplastic blade design and manufacturing process, continue with the already established steps to ramp up

production of the blade at the selected wind turbine blade manufacturing facility.

Supporting Steps for Commercialization:

- Further refine the IACMI 4.2 project techno-economic model to better capture the value of recyclability of an Elium® thermoplastic blade;
- Convene a workshop consisting of wind turbine OEMs, wind blade manufacturers, composite material suppliers, and other stakeholders to identifying critical supply chain needs;
- Update the IACMI 4.2 project techno-economic model with up-to-date data from real world wind turbine blade production, including in the areas of material cost, capital cost and labor costs;
- Identify and execute additional areas of coupon testing (e.g., creep) to aid in commercialization;
- If a need for intermediate-scale full blade or sub-component production validation is identified by the research team, work with the IACMI 4.2 project industry partners to determine a best path forward to identify partners (industry, national laboratories, academic partners), funding, locations and other logistics to execute this mid-scale research.

Challenges to Commercialization:

- Identifying a wind turbine blade manufacturer and a wind turbine OEM to partner in the commercialization of an Elium® thermoplastic resin wind turbine blade;
- Identify potential supply chain partners to develop secondary sources of Elium® or other thermoplastic resin systems to provide alternate suppliers for wind blade manufacturers and wind turbine OEMs;
- Identifying private and public funding sources to perform any required additional research – some outlined in the section above – to enable the commercialization of this innovative technology at scale;
- Identifying and implementing the proper steps to mitigate any environmental, health and safety (EHS) concerns with respect to the deployment of the Elium® thermoplastic resin system in a production environment.

Recommended Areas of Future Research

In addition and in conjunction with the steps to commercialization identified in the previous section, the IACMI 4.2 project team has also identified areas of research that could further advance the knowledge and deployment of thermoplastic resin systems in full-scale wind turbine blades as well as in other U.S. composite industries.

The first topic for follow on research is in the area of thermal welding. While the research in this project has demonstrated the potential viability of the use of Arkema's Elium® thermoplastic resin system in the production of utility scale wind turbine blades, an additional benefit of this resin system could be realized with the development of thermal welding at scale. Current wind blade production entails the bonding of blade components (high pressure skin, low pressure skin, shear webs, etc.) using adhesive. The use of a thermoplastic resin system in the production of wind blade components could enable the ability to thermally weld these components together during the blade assembly process – potentially eliminating the need for adhesive. As adhesive is often the costliest and the heaviest material in a wind turbine blade, finding a way to eliminate the adhesive as well as potentially improving the reliability of the joint between the blade components could possibly revolutionize how wind blades are produced. While some additional research on this topic has already begun in a follow-on IACMI project (4.3) and also internally at NREL and at Arkema, it is recommended that further research be coordinated to demonstrate the

viability of thermal welding at scale, including utility scale wind turbine blades in the range of 60 to 100 meters in length. Research demonstrating the viability of thermal welding at scale will significantly increase the chances of Elium® thermoplastic resin system being deployed as a matrix in wind turbine blades. The effect of thermal welding on the wind turbine blade lightning protection system (LPS) should be considered. The use of thermal welding media, such as carbon fiber or metal mesh, to enable the thermal welding process could influence the performance of a traditional blade LPS. There is an opportunity to incorporate elements of a thermal welding system into the overall wind turbine blade LPS.

Another critical area recommended for future research is the circular economy of composite materials – specifically in the area of redesign, reuse and recycling of wind turbine blades and other composite structures. Once new materials such as Elium® have been introduced into the potential wind turbine blade material selection process, the design process of future blades can be optimized for end-of-life considerations. This 'recyclable-by-design' approach should be an integral step in enabling a circular economy for wind blades. Future work should also include the research and demonstration of thermoplastic composite recycling at various scales, culminating in the recycling of a full-scale wind turbine blade. Wind turbine blade reuse at the end of functional life should also be considered as an alternative to recycling. Additional areas of research for the circular economy of thermoplastic composite materials should include life cycle analysis (LCA), supply chain analysis, recycling standards development and the continued development of new materials and processes that will augment end-of-life options for wind turbine blades and other composite turbine components in the United States.

In addition to the recommended future research discussed in detail above, the project team also recommends future research in these areas related to thermoplastic resin systems:

- Research to develop repair methods for thermoplastic resin blades, including post-manufacturing repairs in the factory as well as in-service repairs in the field.
    - Repairs, both in the factory and in the field, could take advantage of the ability to depolymerize and repolymerize the Elium® thermoplastic resin system, similar to the process used in thermal welding.
    - Although research is in nascent stages, it is possible that damage to wind turbine blades such as fatigue cracking and delamination could be 'healed' with the application of heat and pressure in the repolymerization process of the Elium® thermoplastic resin system. The current process of repairing damage to traditional thermoset composite wind turbine blade structures generally involves removal of material through grinding and adding of replacement material through hand lay-up or infusion. This process can be difficult and time consuming and can often result in repaired structures that do not have the structural properties of the original laminate. Thermoplastic repair techniques have the potential to reduce the time of repairs, increase the quality of the repairs, and reduce the complexity of the process.
    - Early stage efforts have begun to incorporate repair definitions and requirements in international wind turbine blade design, manufacturing, and maintenance standards. Repair methods for thermoplastic resin systems could be considered.
- Research focused on the creep characteristics of the Elium® thermoplastic resin system – including the range from room temperature up to about 50° Celsius. The typical operating environment temperatures for in-service wind turbine blades should be considered when defining the range of temperatures for creep research.
- Research in the area of thermoplastic resin pultrusion for use in wind turbine blade spar caps and other structural elements. This could also include research into thermal forming of pultruded elements to fit the complex curvature required for wind turbine blade structures. In addition, this research would be widely applicable to other US composite industries.

- Research in the area of high temperature (above 50° Celsius) material properties for the Elium® thermoplastic resin system.
- Continued research in the area of production challenges of thermoplastic resin systems, including the area of identifying and mitigating any EHS concerns with scaling up Elium® processing at blade manufacturing plants.

The recommended areas of future research identified above, as well as other potential research in the area of thermoplastic resin systems for wind turbine blades and other composite applications, will be critical to leveraging and advancing the research already completed in this IACMI project.

11. REFERENCES AND/OR BIBLIOGRAPHY

Arbter, R., Beraud, J., Binetruy, C., Bizet, L., Bréard, J., Comas-Cardona, S., . . . Hasanovic, S. (2011). Experimental determination of the permeability of textiles: a benchmark exercise. *Composites Part A, 42*(9), 1157-1168.

ASTM D2344: Standard Test Method for Short-Beam Strength of Polymer Matrix Composite Materials and Their Laminates . (2016).

ASTM D3410: Standard Test Method for Compressive Properties of Polymer Matrix Composite Materials with Unsupported Gage Section by Shear Loading. (2016).

ASTM D5379: Standard Test Method for Shear Properties of Composite Materials by the V-Notched Beam Method. (2012).

ASTM D6641: Standard Test Method for Compressive Properties of Polymer Matrix Composite Materials Using a Combined Loading Compression (CLC) Test Fixture. (2016).

ASTM D7078: Standard Test Method for Shear Properties of Composite Materials by V-Notched Rail Shear Method. (2012).

ASTM D7264: Standard Test Method for Flexural Properties of Polymer Matrix Composite Materials. (2015).

Chrisophe, M. EFFIWIND: Development of a New Generation of Wind Turbine Blades based on Recyclable Acrylic Materials, *Dismantling and Recycling of Wind Turbines: From Design to End of Life.* Berlin (12 March 2020.).

Cousins, D. S., Suzuki, Y., Murray, R. E., Samaniuk, J. R., & Stebner, A. P. (2019). Recycling glass fiber thermoplastic composites from wind turbine blades. *Journal of Cleaner Production*, 1252-1263.

Davies, W. C. (1994). A test technique for assessing core-skin adhesion in composite sandwich structures. *Journal of Materials Science Letters*, 203-205.

ISO. (2003-03). ISO 4587:2003 2003-03. *Adhesives -- Determination of tensile lap-shear strength of rigid-to-rigid bonded assemblies*.

ISO 527: Plastics — Determination of tensile properties . (2012).

Murray, R. E., Jenne, S., Snowberg, D., Berry, D., & Cousins, D. (2019). Techno-economic analysis of a megawatt-scale thermoplastic resin wind turbine blade. *Renewable Energy, 131*, 111-119.

Parnas, R., Howard, J., Luce, T., & Advani, S. (1995). Permeability characterization. Part 1: A proposed standard reference fabric for permeability. *Polymer Composites, 16*(6), 429-445.

Suzuki, Y., Cousins, D., Wassgren, J., Kappes, B., Dorgan, J., & Stebner, A. (2018). Kinetics and temperature evolution during the bulk polymerization of methyl methacrylate for vacuum-assisted resin transfer molding. *Composites Part A*, 60-67.

12. APPENDIX A
Published Techno-Economic Model

The following techno-economic model was published in the Journal of Renewable Energy in February 2019; it is reprinted here with permission from the publisher and authors. The numbering for tables, figures and references are exclusive to this Appendix and are not integrated into the main body and table of contents of this final report. A link to this published journal article is available here:

https://www.sciencedirect.com/science/article/pii/S0960148118308292

Techno-Economic Analysis of a Megawatt-Scale Thermoplastic Resin Wind Turbine Blade

Robynne E. Murray[$1], Scott Jenne[$], David Snowberg[$], Derek Berry[$], Dylan Cousins[#]
[$]*National Renewable Energy Laboratory, 15013 Denver West Parkway, Golden, CO 80401*
[#]*Colorado School of Mines, 1500 Illinois Street, Golden, CO 80401*
[1]*robynne.murray@nrel.gov*

Abstract—**Two-part, in-situ reactive thermoplastic resin systems for composite wind turbine blades have the potential to lower the blade cost by decreasing cycle times, capital costs of both tooling and equipment, and energy consumption during manufacturing, and enabling recycling at the end of the blade life. This paper describes a techno-economic model used to estimate the cost of a thermoplastic wind turbine blade relative to a baseline thermoset epoxy blade. It was shown that a 61.5-m thermoplastic blade costs 4.7% less than an equivalent epoxy blade. Even though the thermoplastic resin is currently more expensive than epoxy, this cost reduction is primarily driven by the decreased capital costs, faster cycle times, and reduced energy requirements and labor costs. Although thermoplastic technology for resin infusion of wind turbine blades is relatively new, these results suggest that it is economically and technically feasible and warrants further research.**

Keywords—**Techno-Economic Model; Epoxy; Thermoplastic; Composite; Wind Turbine; Manufacturing Blade Cost.**

Introduction

The U.S. Department of Energy has identified blade manufacturing as a key area for cost reduction for wind turbine blades [1]. Advances in blade materials for wind turbines have the potential to enable this manufacturing cost reduction. The vast majority of modern megawatt-scale wind turbine blades are currently manufactured using thermoset resin systems such as polyester, vinyl-ester, or epoxy and an adhesive to bond the blade skins and shear webs. Compared to thermoset materials such as epoxy, which requires extensive heating processes to cure the laminate, in-situ reactive thermoplastic resin systems polymerize (analogous to cure for thermoset resins) at room temperature, eliminating the requirement for heated tooling while significantly reducing the cycle time and embodied energy during blade production. Thermoplastic materials can also be thermally joined, possibly eliminating the need for adhesive bonds at the joints between blade skins and shear webs, and increasing the overall blade strength and reliability. Eliminating the heating requirements during cure may also facilitate on-site blade manufacturing and

assembly, helping to overcome current transportation constraints for large blades. Thermoplastic materials could also increase the ease and reliability of in-field and up-tower composite repairs, and enable end-of-life blade recycling by thermoforming or recovering the constituent materials. With the global market for wind energy rapidly increasing (the United States installed 534 MW of wind capacity during the third quarter of 2017, bringing the nation's total installed wind capacity to 84,944 MW [2]), end-of-life disposal will become an increasingly important consideration in the overall blade design process.

An infusible thermoplastic resin system called Elium®, developed by Arkema Inc, has been shown to have neat resin mechanical properties that are similar to epoxy resin systems. As well, initial investigations into Elium® thermoplastic composite mechanical properties have shown that, for the same fiberglass material, the static tensile and compressive strength of the thermoplastic resin are comparable to epoxy resin systems [3, 4]. With the advantages discussed above, there is potential that thermoplastic resin systems could replace existing thermoset resins as the matrix material in the production of composite wind turbine blades. However, it is critical to quantify the cost benefit of using these new resin systems. To evaluate the cost of replacing a thermoset resin system in a wind turbine blade with a thermoplastic resin system, a comprehensive techno-economic model has been developed to evaluate the manufactured cost of a thermoplastic resin blade with respect to a baseline thermoset epoxy resin blade. The decision to use an epoxy blade as the baseline comparison in the techno-economic model was based on the relative prevalence of the use of epoxy resin systems in the current production of megawatt-scale wind turbine blades compared to the use of polyester and vinyl-ester resin systems, as well as the generally superior mechanical properties of an epoxy matrix in conjunction with fiberglass and/or carbon fiber as compared to polyester and vinyl-ester. Elium® was selected as the thermoplastic resin for this study based on the demonstrated ease of infusion in existing blade manufacturing tooling, as well as the relatively low peak exothermic temperatures recorded during polymerization that will not damage existing blade tooling [5].

To capture all the relevant blade components and subcomponents, the techno-economic model was set up to account for an entire wind turbine blade structure. To represent current turbine and blade technology, the techno-economic model was based on a 5-MW turbine with 61.5-m-long blades developed by the National Renewable Energy Laboratory (NREL) [6], with the structural design by Sandia National Laboratories, given in [7]. The study presented here compares the cost of the 61.5-m blade manufactured with a thermoplastic resin to the cost of a baseline thermoset epoxy blade. This comparison includes the consideration of the blade tooling equipment, manufacturing and labor times, material costs, and end-of-

life disposal. The main objective of this work is to determine if a thermoplastic resin system is an economically feasible replacement option for thermoset resin systems in megawatt-scale wind turbine blades.

Techno-Economic Model

Techno-economic models provide a cost-benefit comparison of different methods or materials and can be used to assess the feasibility of new systems based on both their economic potential as well as their technical viability. Several guidelines and example frameworks for techno-economic analysis were used to guide this work, including [8-10], with modifications to account for the cost factors associated with a wind turbine blade. A combined parametric and process flow method was used, as was done by Schubel et al. [11]. The techno-economic model focuses on the manufactured cost of a wind turbine blade, assuming blades are manufactured using vacuum-assisted resin transfer molding, and was broken down into the categories shown in Figure 1, which are further discussed in Sections 3 through 5.

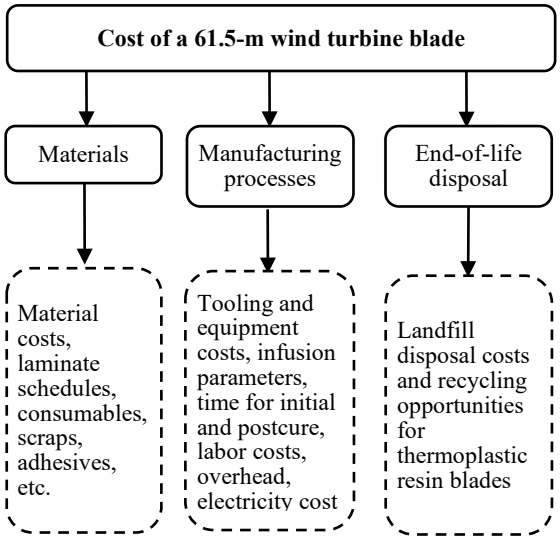

Figure 1. Categories of the techno-economic model.

Materials and manufacturing processes play a significant role in the cost of a wind turbine blades and are therefore important considerations in this work. End-of-life disposal is also considered in this model, although it is not directly part of the manufactured cost of a blade, since it is an important factor in the decision to use thermoplastic resins in wind blades. The techno-economic model was also developed to account for the cost of different structural designs (differing amounts of material in the blades). However, in this case it was assumed that the structural design and laminate schedules were the same since the two resin systems have comparable mechanical properties. Therefore, the three categories in this techno-

economic model are materials, manufacturing processes, and end-of-life disposal.

As mentioned, the basis of this model is the NREL 61.5-m wind turbine blade, which is representative of blades used for modern 5-MW rated land-based turbines. This blade is constructed out of two outer shells (skins), a prefabricated root section, and a box-beam spar section made up of a spar cap in each skin and two shear webs. Figure 2 shows the blade geometry for the 61.5-m blade in the NuMAD [12] user interface.

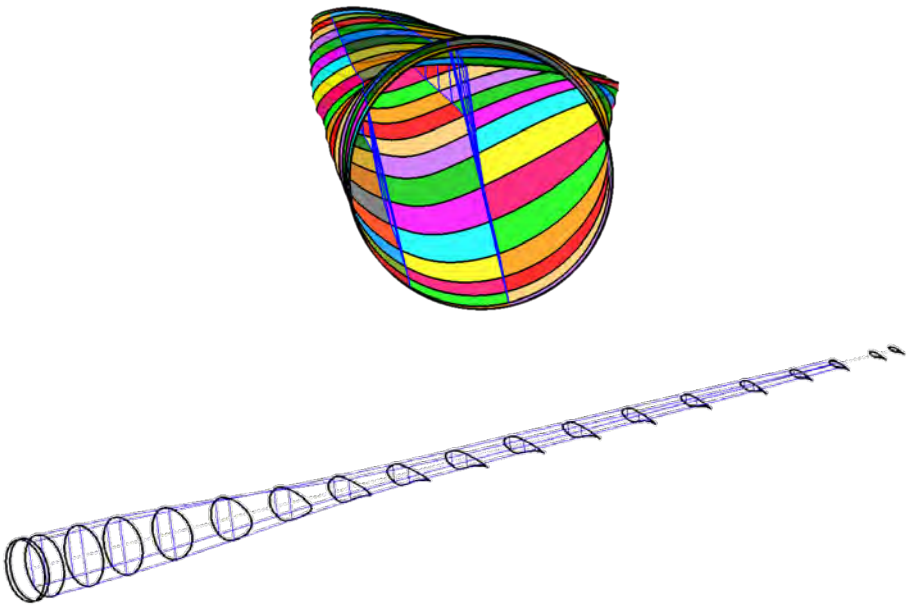

Figure 2. NuMAD three-dimensional model of the 61.5-m wind turbine blade.

Several of the parameters that influence the blade cost are assumed to be the same between different resin systems (for example, root fasteners and bolts, and consumables during manufacturing); however, they are considered in the techno-economic model to facilitate future investigations as well as to ensure that the total blade cost is reasonable. The following assumptions were made during the development of the techno-economic model and do not affect the comparison between the resin types:

- A conservative approach to laminate design was taken to meet the structural requirements for the NREL 61.5-m blade. Because of this approach, the resulting blade weight and cost in this model may be slightly higher than current commercial wind turbine blade weights and costs, making this a more conservative study.
- Like all modern wind turbine blades, the model assumes that a lightning protection system is part of the blade structure. However, because the details of the lightning protection system are not an

essential differentiator of the resin systems, the model was constructed using the estimated cost and weight of a typical multimegawatt blade lightning protection system for both resin systems.

- The model includes a comprehensive analysis of a T-bolt root connection system, including both the T bolts and barrel nuts. Although many modern wind turbine blades employ this style of root connection system, others utilize different systems, such as embedded studs or root inserts.
- The techno-economic model does not include any post-infusion overlay laminate. Most modern megawatt-scale blades include overlay; however, the exclusion of this detail is not expected to alter the comparative results of the model. Future work will investigate the possibility of using thermal welding to bond a thermoplastic blade, potentially eliminating the need for an overlay.
- The techno-economic model includes an educated guess for the bolt circle diameter, the number of T bolts (and barrel nuts), and the size of the T bolts (and barrel nuts).
- The bonding adhesive employed in the techno-economic model is a methacrylate system manufactured by Plexus. Many blades utilize epoxy adhesive systems.
- To simplify the model, the blade shear web geometries were modeled as trapezoids. This approach results in a slightly heavier blade estimate but will not significantly affect the blade cost or the relative comparison between the resin systems.
- The model employs parametric calculations for the consumables to be used during blade production. Consumable estimates could be refined with actual manufacturing statistics.
- The model does not include any material cost or weight for small parts, such as balance boxes, root close-outs, T-nut covers, and so on.
- The model currently does not distinguish between different levels of skill or experience for laborers, and assumes the level of skill required will be equal for the different resin systems.

These assumptions were necessary to develop the techno-economic model and do not impact the cost comparison of the blade with different resin systems.

The key factors, along with the resin cost, that are accounted for in the techno-economic model that differentiate the resin systems include:

- The initial cure time for the thermoplastic blades is assumed to be half compared to the epoxy blades. This timing is based on data that have demonstrated faster cycle times for an Elium® thermoplastic resin system [5].
- The tooling cost for the thermoplastic blades is assumed to be 50% lower than epoxy tooling costs due to the elimination of the requirement for heating elements in the molds. The 50% reduction in cost is based on discussions with TPI Composites [13] and is thought to be conservative as heated tooling can cost up to three times more than nonheated tooling,

depending on the complexity and size of the tooling. The sensitivity of the model to this assumption is investigated in Section 6.

- The power requirements for the cure stage of manufacturing were eliminated for the thermoplastic blades as a result of the room temperature polymerization of the resin. This room temperature polymerization has been demonstrated for a 9-m thermoplastic resin prototype blade [5].
- Postcure is only accounted for with the epoxy blade, hence there is no capital equipment, floor space (the techno-economic model assumes that building costs are equal for all resin systems except for additional floor area required for the postcure oven for the epoxy resin), energy requirements, or labor required for the thermoplastic blade postcure.

These key differences enable the manufacturing cost comparison between thermoplastic and epoxy blades.

Materials

A large part, approximately 30 to 40% based on this study, of the cost of a wind turbine blade is the materials. The initial inputs to the techno-economic model are the materials used to construct the wind turbine blade, including the fiberglass fabric, core material, resin systems, gelcoat, adhesives, root hardware, lightning protection system, leading-edge protection, and blade manufacturing consumables. Typically, material costs are quoted per unit weight, therefore calculating the total weight of each material used in the blade enables a cost estimate of the overall blade materials, as discussed in Section 3.5.

Laminate Schedule

With recent research showing similar mechanical performance between the Elium® thermoplastic resin and epoxy resin systems, it was assumed that both blades had the same laminate schedule. The laminate schedules for the 61.5-m blade were developed based on the original blade structural model given in [7], with small changes to account for the assumption that the blade was constructed entirely of fiberglass with no carbon fiber in the spar caps. A summary of the materials used in the laminate schedule are given in Table 1. The blade skins used for this techno-economic model had two layers of CDB340 triaxial fiberglass on either side of Gurit T600 foam tapering from 40 to 20-mm, the root build up consisted of 128 layers of CDB340 triaxial fiberglass, resulting in a total root thickness of 105 mm, and the spar cap was constructed from 49 layers of 600 mm wide ELT-5500 unidirectional fiberglass, resulting in a 62 mm thick spar cap. Both the leading and trailing edge shear webs had two layers of Seartex biaxial fiberglass on either side of 50 mm thick Gurit T600 foam. The trailing edge reinforcement was constructed of 22 layers of 250 mm wide ELT-5500 unidirectional fiberglass. This layup resulted in a final blade weight of

18.4 tons, including root studs and the lightening protection system. The laminate schedules ultimately drive the amount of fiber reinforcement and resin that are used in the blade components, and by summing all the layer-by-layer fabric areas and weights, the overall fiber usage is calculated (this is summed in the bill of materials calculations shown in Table 1).

Resin

The techno-economic model assumes blades are manufactured using vacuum-assisted resin transfer molding, as this, along with prepreg lamination, accounts for over 90% of blade manufacturing worldwide [14]. To calculate the amount of resin used during the infusion process, the model estimates the overall composite fiber volume based on the laminate schedules and uses the specific gravities of the constituent materials (fiberglass and resin) to calculate the resin per unit of fiberglass. These values are utilized in the model to calculate the overall composite thickness and material usage, and ultimately the cost of the materials.

Blade Bonding and Fasteners

The process of joining the blade components together to manufacture a complete wind turbine blade is referred to as bonding. In a typical multimegawatt size blade, the high-pressure and low-pressure skins are typically bonded together with the shear web or webs in between. The blade bonding analysis section of the techno-economic model uses the geometric specifications of the blade bond lines and parameters, such as bond thickness, flange width, and adhesive density to calculate the total volume and weight of the adhesive in the wind turbine blade. This calculation is assumed to be the same for both resin systems at this time; however, future work will consider thermal welding of the thermoplastic blade components to eliminate adhesives.

As part of the wind turbine blade weight and cost analysis, the techno-economic model calculates the cost associated with the T-bolt root fastening system. In addition to the hardware that is added to the blade, the model also determines the volume and weight of the finished composite (reinforcement and matrix) that is removed from the blade root during the drilling process to allow for the fastening system. Depending on the material properties (particularly the resin density) of the thermoplastic resins, these values can vary between matrix choices.

Consumables and Scrap Materials

Blade geometric and processing specifications, such as material scrap percentages, may vary for different resin systems or reinforcements; however, in this case, the amount of wasted materials was assumed to be

the same for both resin systems. The scrap percentages are given for the different materials in Table 1. Note that these values depend on the type of material and are therefore set for each material independently. For example, there is typically resin left in the resin feedlines using vacuum-assisted resin transfer molding to manufacture the blades, leading to a 15% scrap rate. On the other hand, the scrap rate is only 5% for the unidirectional fiberglass material used in the spar cap because it is assumed that the fabric cutting can be planned based on the blade design to result in less wasted material.

In the wind turbine blade manufacturing process, the consumables are defined as the materials that are used during the manufacturing of the blade but are not part of the blade once the process is complete. These are the items that are discarded after the blade is produced. To be flexible for many blade lengths in the techno-economic model, the approach to calculating consumables is based on a parametric analysis of each material. The amount of each item, such as tacky tape, mold release, tubing or peel ply, is determined based on a definable blade metric, such as blade length, blade perimeter, or blade surface area. Thus, using the blade specifications, the amount of each consumable is estimated, and the cost is summed in the bill of materials.

Bill of Materials

The blade material usage including volumes, weights, and costs of all materials, as well as the wasted materials based on scrap rates, are estimated and totaled based on the data from the preceding sections. The bill of materials tabulates these data and enables a comparison of the relative material costs between the thermoplastic resin and the baseline epoxy resin system. The bill of materials also feeds into the labor and cycle time calculations that are used to determine the total cost to manufacture the 61.5-m blade. Table 1 shows an example of the bill of materials for the thermoplastic blade, including details on some of the key materials used in the 61.5-m blade. Note that the consumables are not shown in this chart, but their cost is calculated similarly. All prices are in U.S. dollars and are based on recent estimates from the wind turbine blade manufacturing industry assuming high-volume use.

Table 1. Example of a bill of materials for the thermoplastic 61.5-m blade (does not include all materials used in blade manufacturing).

Material	*Application*	*Density (kg/m^3)*	*Infused Ply Thickness (mm)*	*Quantity (kg)*	*Mix Ratio*	*Unit Cost ($/kg)*	*Material Cost ($)*	*Scrap (%)*	*Scrap Cost ($)*
CDB340 Triax Fiberglass	Blade skins, root buildup	1,112	0.82	6,540	N/A	$2.86	$18,705	15	$2,806
Saertex Biax Fiberglass	Shear webs	1,210	0.94	989	N/A	$1.85	$4,026	15	$604
ELT-5500 Fiberglass	Spar cap	1,858	1.26	3,753	N/A	$1.87	$7,018	5	$351

Foam, 20 mm	Blade skins	115	20	237	N/A	$2.68	$1,346	20	$269
Foam, 40 mm	Blade skins, shear web	115	40	844	N/A	$2.35	$3,256	20	$651
Foam, 40 mm	Blade skins, shear web	115	50	891	N/A	$3.19	$3,007	20	$601
Huntsman LY1564	Epoxy resin	1,144	N/A	N/A	0.7	$3.63	N/A	N/A	N/A
Huntsman XP3416	Epoxy hardener (medium)	959	N/A	N/A	0.3	$3.63	N/A	N/A	N/A
Arkema Elium® (Part A)	Acrylic based thermoplastic resin	1,036	N/A	4,473	0.97	$6.82	$30,503	15	$4,576
Arkema Elium® (Part B)	Peroxide initiator	1,036	N/A	134	0.03	$6.82	$915	15	$137
Plexus 550 Part A	Adhesive for blade bonding	929	N/A	144	0.815	$109.78	$2,044	15	$307
Plexus 550 Part B	Adhesive for blade bonding	1,714	N/A	27	0.185	$109.78	$204	15	$31

Manufacturing Processes

A manufacturing model previously developed by NREL [1] was adapted to account for the unique attributes of thermoplastic resins compared to thermosets. The manufacturing model uses the material costs and quantities described in Section 3 and applies them to 20 unique process steps, while calculating cycle times and labor hours required to perform each step. Table 2 shows the manufacturing process steps with the number of laborers, tooling costs, power requirements, and capital equipment costs for the epoxy blade (these numbers differ slightly for the thermoplastic blade based on the assumptions discussed in Section 2).

Table 2. Labor and equipment breakdown for the epoxy blade based on process step.

Process Step	Laborers per station	Skin Mold Gating (hrs)	Nongating (hrs)	Equipment Cost per Station	Power Requirement Epoxy Blades [kW]	Tooling Cost per Station Epoxy Blades
Material Cutting	4	0	39	$300,000	145	$0
Root Preform	2.25	0	27	$100,000	164	$350,000
Trailing-Edge Shear Web	3	0	13	$100,000	151	$900,000
Leading-Edge Shear Web	3	0	13	$100,000	151	$900,000
Spar Cap	7.75	0	32	$100,000	153	$350,000
Low-Pressure Skin	7.4	18.25	2.5	$200,000	180	$2,300,000
High-Pressure Skin	7.4	0	20.75	$200,000	180	$2,300,000
Assembly	7.1	6.2	4.75	$1,000,000	145	$0
Demold	5	1.25	0.5	(included in assembly)	(included in assembly)	(included in assembly)
Trim	4	0	18	$1,500,000	145	$0

Overlay	7	0	8.75	$15,000	145	$0
Postcure	2.2	0	11	$1,750,000	145	$0
Root Cut and Drill	3	0	8	$1,250,000	145	$0
Root Hardware Install	3	0	6	$50,000	145	$0
Surface Prep	10	0	16.5	$75,000	145	$0
Paint	4	0	11.5	$3,500,000	145	$0
Surface Inspection and Finish	4	0	12.5	$50,000	145	$0
Weight and Balance	3	0	5	$200,000	145	$0
Inspection	3	0	3	$25,000	145	$0
Shipping Prep	4	0	7.5	$25,000	145	$0

The number of laborers, gating and nongating hours (skin mold gating hours are the mold usage hours which contribute to overall skin mold cycle time), and tooling costs are based on discussions with blade manufacturer TPI Composites [13]. The power requirements shown are the baseline building requirements of 145 kW (assuming the entire facility is powered independent of the process being performed) plus the additional power to run the heated tooling for the epoxy blades, which is based on the cure temperature and heat capacity of the fiberglass-epoxy material. Power requirements for process steps that do not require heated tooling are minimal (for example, the assembly and demolding processes) and were not included. Each process step includes additional operations that quantify the total cost of that step and the impact that the resin selection has on the entire manufacturing process using resin-agnostic inputs, such as the number of blades per year, length of production run, and other exogenous inputs (e.g., wages, working days per year, and price of electricity). Wages are based on the assumption that blades are manufactured in the U.S. The manufacturing model inputs are shown in Table 3.

Table 3. Manufacturing cost inputs for the techno-economic model that affect all processes

Parameter	***Value***	
Annual Production Volume	250	blades/yr
Blade Length	61.5	m
General Labour Direct Wages	$20	/hr
Benefits on Wage and Salary	31.7%	
Average Labour and Equipment Downtime	20%	
Working Days per Year	250	days/yr
Working Hours per Day	24	hrs/day
Capital Recovery Rate	10%	
Equipment Recovery Life	10	years
Building Recovery Life	30	years
Working Capital Period	3	months
Price of Electricity	$0.079	$/kWh

Price of Building Space (to build)	$800	$/m^2
Expected Inflation	0.50%	
Corporate Tax Rate	12.60%	
Research and Development	0.90%	
Installation Costs	10%	

The annual production rate of 250 blades per year was assumed based on the gating hours (cycle time) and labor time per blade. Currently, this is a resin-agnostic input in the techno-economic model; however, as a result of the faster cycle times, this number could potentially be increased for thermoplastic blades. Once all the input parameters are determined for the individual process steps and corresponding stations, the model pulls material data from the bill of materials (discussed in Section 3.5) and calculates variable costs—material, direct labor, and utility—and fixed costs—equipment, tooling, building, maintenance, overhead, and cost of capital.

Results and Sensitivity Analysis

The cost of the 61.5-m wind turbine blade calculated using the techno-economic model was 11.05$/kg (5.02$/lb) for the thermoplastic resin and 11.44$/kg (5.20$/lb) for the epoxy resin, which is similar if not slightly higher than the expected out-of-door cost for current blades manufactured in the USA. These results indicate a 4.7% decrease in blade manufactured cost using the thermoplastic resin when compared to the baseline epoxy blade. Based on sensitivity analysis, this is thought to be within the uncertainty of the model. The breakdown of the blade costs for both resins systems is shown in Figure 3.

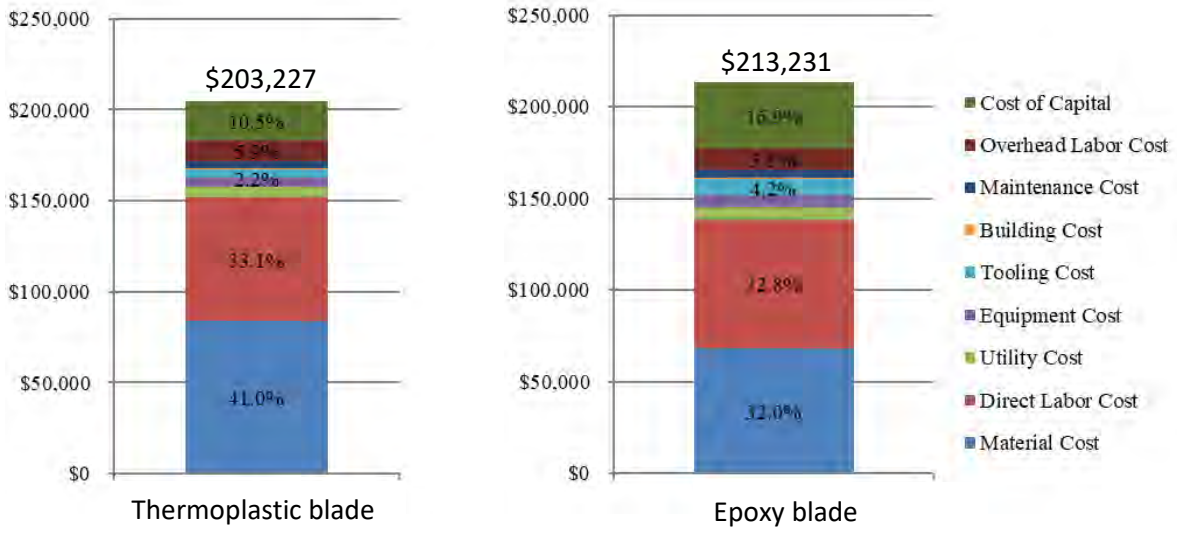

Figure 3. Total blade cost and cost breakdown for the thermoplastic and epoxy blades.

The largest contributors to the blade cost are the materials and the direct labor. This is aligned with the finding of a report by TPI Composites and Sandia National Laboratory [15]. Scrap materials make up 11.4% of the material costs, or 4.2% of the total blade cost. This highlights the significant savings that can come from tighter tolerances and reduced waste, making the case for more automation in blade manufacturing. From Figure 3, the epoxy blade has a higher percentage of the total cost attributed to the tooling, capital, and equipment costs (24% compared to 15%), whereas the thermoplastic blade has higher material costs (41% compared to 32% of the blade cost). The primary drivers for the differences in the blade costs are the Elium® resin cost, which increases the material cost of the thermoplastic blade, and the manufacturing costs, which decrease the cost of the thermoplastic blade. The balance between these two factors results in the overall difference in the blade costs.

A sensitivity analysis informs the level of dependence on the parameters that influence the thermoplastic blade cost. Due to the early stage of the thermoplastic resin technology for wind turbine blades, there is associated uncertainty in the assumptions made in this techno-economic model. By performing a sensitivity analysis, the techno-economic model can be verified by gauging the effect of each parameter on the cost difference between the blade types. This analysis helps identify the parameters that have the highest sensitivity so appropriate levels of uncertainty can be associated with the cost of the blades based on these parameters. The sensitivity of the model input parameters is investigated in the following sections.

Materials

The cost of the fiberglass, scrap materials, and consumables were the same between both blades. However, the thermoplastic resin cost as given by the Elium® manufacturer was almost double the epoxy resin cost, resulting in an overall increase in the cost of materials for the thermoplastic blades. Figure 4 shows the sensitivity of the cost of the overall thermoplastic blade with respect to the Elium® cost, as compared to the epoxy blade cost.

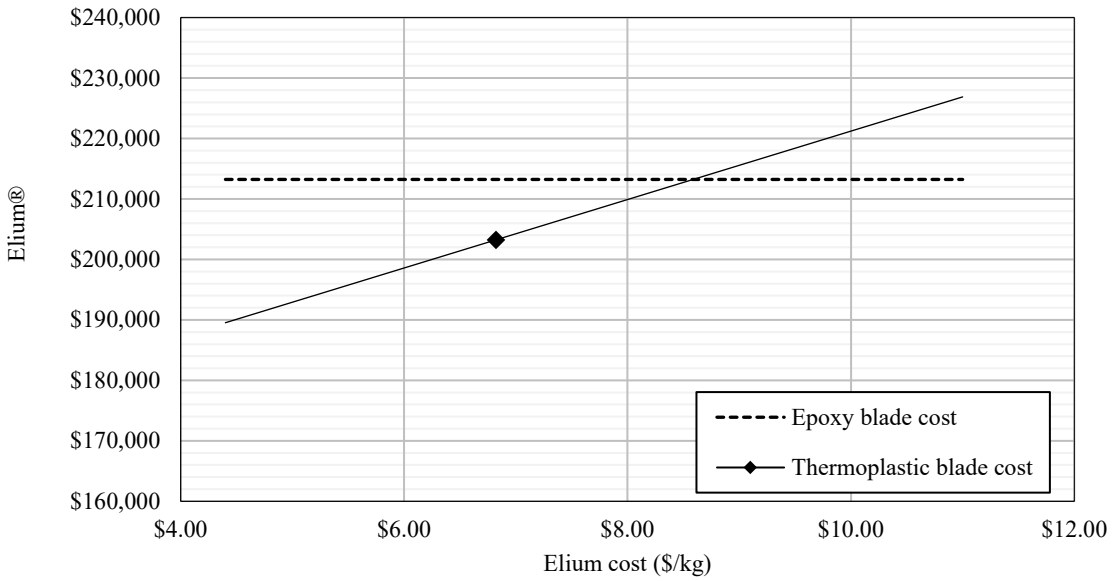

Figure 4. Sensitivity to the cost of the Elium® thermoplastic resin.

The cost of the Elium® thermoplastic resin would have to increase to over 8.50$/kg for the cost difference to be such that the thermoplastic blade cost is the same as the epoxy blade, based on the manufacturing assumptions for the thermoplastic blades. This means that the error bands on the Elium® cost could as large as 25% while still maintaining a lower overall blade cost and illustrates the significance of the reduced capital tooling costs, shorter cycle times, and lower energy requirements on the cost of the thermoplastic blade.

The current cost of the Elium® resin is projected to decrease to $5.50/kg [16], as the manufacturer sets up manufacturing facilities in the U.S and increases production volumes. Using the projected lower Elium® resin cost results in a 3.7% decrease in the thermoplastic blade cost estimated previously using the techno-economic model, making it 8.2% less expensive than an epoxy blade, based on the thermoplastic blade manufacturing assumptions. However, there is uncertainty in the market on the price of the base Elium® material methyl-methacrylate because of recent material shortages. Currently, it is not in the scope of this work to predict the future cost of the resin, however, this material shortage is an important consideration for future cost estimates.

Manufacturing Processes

The main drivers of the cost reduction for manufacturing the thermoplastic blades are the lower cost of tooling (no heating elements), the reduction in labor associated with the faster curing cycle of thermoplastics compared to the thermoset resin, and the elimination of the capital equipment and labor

costs for postcure ovens. By eliminating the need for oven curing, not only are the equipment and labor costs reduced but the energy costs associated with the curing operation are eliminated. In addition, if no equipment is required for postcure, there are small savings in the required facility floor space.

The reduction in the tooling costs for manufacturing the thermoplastic blades compared to the epoxy blades was found to have the most significant effect on the overall thermoplastic blade cost. Figure 5 shows the percent reduction in the cost of the thermoplastic blades relative to the epoxy blades as a function of the percent reduction in the thermoplastic blade tooling cost relative to the epoxy blade tooling cost, with the assumed 50% tooling cost reduction given by the diamond marker.

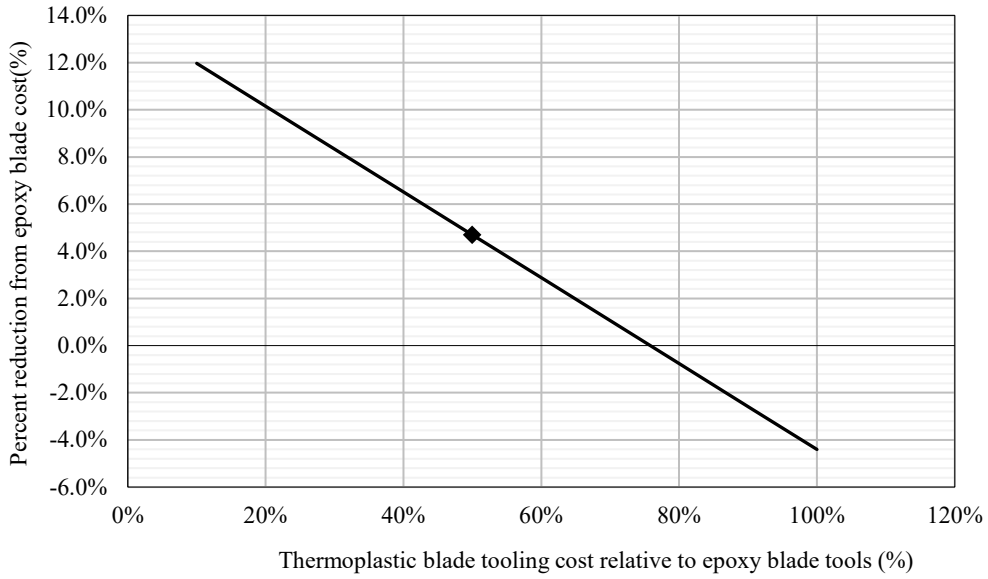

Figure 5. Sensitivity to percent reduction in tooling costs for thermoplastic blades.

From Figure 5, for the thermoplastic blades to be the same or less expensive than the epoxy blades they must have at least a 25% reduction in the tooling cost (in other words, the tooling for thermoplastic blades can be no more than 75% of the cost of equivalent epoxy tooling). With the significant cost savings from the lack of heating elements in the thermoplastic blade tooling, this is expected to be easily achievable.

Additional outcomes from the manufacturing process sensitivity analysis include:

- The postcure required for the epoxy blades accounts for approximately 1.2% of the blade cost, hence the lack of this stage in manufacturing the thermoplastic resin blades has associated cost savings as a result of capital and labor costs and floor space.
- The shorter cure time of the thermoplastic resin blades was found to result in less than a 1% difference in the thermoplastic blade costs due to decreased labour hours. However, this does not consider an increase in annual production volume that may be possible with thermoplastic resins.

The annual production volume is an important consideration in the overall blade manufacturing cost. In

this study it was assumed that both the thermoplastic and epoxy blades have the same annual production volume and that the blade tooling has the same lifespan. In this case, it was assumed that 1,000 blades could be made from each mold. Figure 6 shows the sensitivity of the blade cost to the annual production volume.

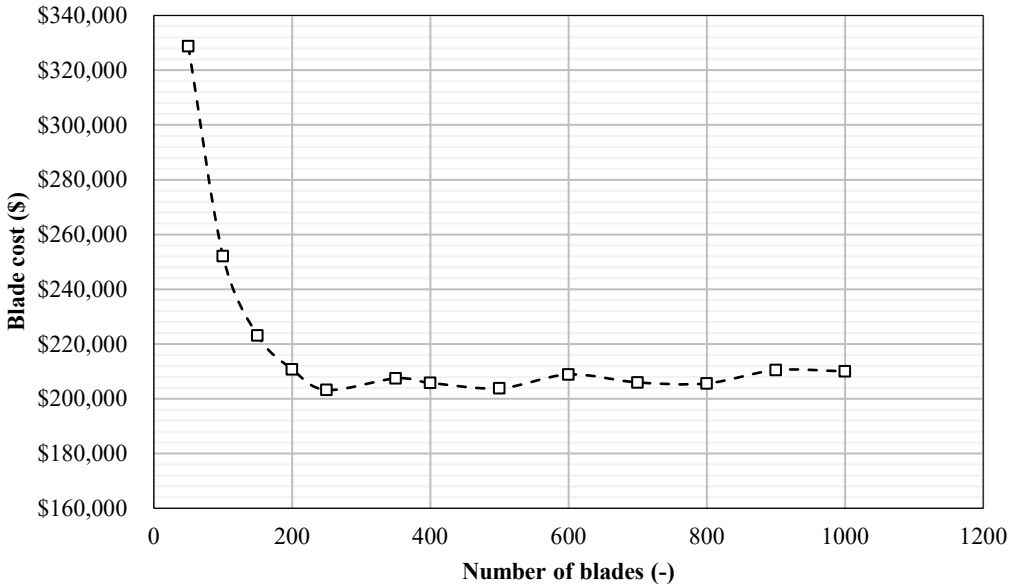

Figure 6. Sensitivity to the annual production volume.

The effects of economies of scale are realized with similar trends down to approximately 200 blades per year. Between 200 and 1000 blades the total cost decreases minimally. However, at small production runs of only 100 blades, there is a 24% increase in blade cost over the baseline scenario of 250 blades per year. This finding implies that the model does not have a bias to large-volume production runs and therefore should not grossly under or overpredict the impact that material cost has on total blade cost. These results are similar to the outcomes found by Schubel et al. [11].

End-of-Life Disposal

End-of-life disposal is an important consideration when looking at the overall life cycle costs of blades because of the large amount of material that will have to be disposed. One reference suggests there will be nearly 50,000 tons of blade waste in 2020 and 200,000 tons by 2034, worldwide [17], whereas another reference states there could be as much as 705,000 tons of blade waste by 2030 in the United States alone [18]. There are currently three options for disposing of wind turbine blades at the end of their lives: landfill, incineration, and recycling [19]. Currently, landfill is the cheapest option; however, legislation may become a driver toward recycling. For example, in Germany composites were banned from landfills in 2005, and Cherrington et al. [20] showed using a review of European waste management policy that landfill bans implemented by government effectively divert waste from landfills and drive incineration or

recycling. Incineration involves burning the composite materials and extracting energy from the burning polymers. Because there are existing incineration facilities, this may be done at a lower cost. However, no large parts can be incinerated and the ash content needs to be distributed to the landfill afterward [21]. Recycling blades means recovering materials that can be used as secondary raw materials in other products. The advantage of recycling is that some materials have economic value, but challenges arise for nonhomogeneous thermoset blades with different materials in various quantities. A preliminary study at the Colorado School of Mines demonstrates that recycling has the potential to be a more feasible option for thermoplastic blades [22]. One method of recycling thermoplastic blades is pyrolysis, which uses heat to melt or burn the resin away from the fibers, thereby enabling the fibers to be recovered. However, this process is currently expensive at a large scale. For thermoplastic blades, dissolution offers another method of separating the resin and fiberglass materials. Another end-of-life option is repairing and reusing the blades in other wind markets.

This techno-economic model assumes the lowest cost feasible option for both resin types:

- Epoxy blades are transported, using the average cost of transportation given in [23], to a landfill and disposed of at a cost of $49/ton [24],
- Thermoplastic blades are sent to a recycling facility at only the cost of transportation to the facility (using the average cost of transportation given in [23]).

Although end-of-life disposal is not part of the manufactured blade cost, the end-of-life costs were added to the total blade cost to enable a cost comparison between the two blade types. Because these costs are in today's dollars, the current value is added to the total blade cost with an adjustment for assumed inflation of 2.5%, assuming a 20-year blade lifespan. For the epoxy blade, the total end-of-life cost is $4,1035 per blade, which makes up 1.9% of the total blade cost. For the thermoplastic blade, transportation to the recycling facility costs $3,115, making recycling 1.5% of the total cost of the blade. It is likely that there will be costs associated with cutting or demolishing the blade into smaller pieces. However, we did not consider these costs because the process is resin-agnostic, meaning the blades will need to be processed for both landfill disposal and recycling. This analysis demonstrates a minimal difference in the end-of-life disposal costs, however, this does not consider the resale value of the recycled materials. Continued work will further explore the cost benefit of recycling thermoplastic blades. Without additional cost benefits of reselling the recycled materials, it is likely that recycling of blades will be driven by customer demand and government legislation.

Conclusions

Results of the techno-economic model show that a thermoplastic resin wind turbine blade has the potential to reduce the overall blade cost by 4.7% compared to a thermoset epoxy baseline blade. With the

consideration of uncertainty in the techno-economic model due to the early stage of the thermoplastic resin technology for wind turbine blades, this reduction in cost demonstrates the economic feasibility of thermoplastic resin blades, but should not be used as a definite cost estimate for a thermoplastic blade. The main driver for the cost difference between the epoxy and thermoplastic resin blades is the difference in manufacturing processes, such as reduced capital costs of tooling due to the elimination of heating elements, the reduced cure time, and elimination of the post cure stage for thermoplastic blades. A sensitivity analysis indicated that even with variations in the model assumptions, the thermoplastic resin blades warrant further investigation. The techno-economic model results showed that:

- The 50% reduction in the tooling cost for the thermoplastic blade had a significant effect on the cost, however, a reduction of only 25% of the cost of existing tooling still results in thermoplastic blades being the same or less expensive than epoxy thermoset blades,
- The reduced cure time leads to less than 1% difference in the thermoplastic blade cost due to reduced labor time. The model does not account for increase annual production capacity due to faster cycle times,
- The postcure required for the epoxy blades accounts for approximately 1.2% of the blade cost, hence eliminating this stage results in cost savings for the thermoplastic blades,
- The thermoplastic resin would have to cost over $8.50/kg (compared to the current $6.82 cost) for the resin price increase to outweigh the manufacturing cost reductions associated with the thermoplastic blade.

Another advantage of the thermoplastic resin blades is the potential to be repaired by applying heat and reforming the materials without grinding and damaging the laminate. The cost of operating and maintaining blades was not considered in this model, however, future work could investigate the life cycle cost benefits of thermoplastic resins by considering the savings associated with maintenance and repair. Replacing adhesives using thermal welding of thermoplastic blades was also neglected in this study and may have significant cost advantages due to decreased in-mold cycle times. Future work includes further refinement of the model assumptions through discussions with other blade manufacturers and turbine original equipment manufacturers, and investigation of the blade cost for other blade sizes and geometries.

Acknowledgments

This material is based upon work supported by the U.S. Department of Energy's Office of Energy Efficiency and Renewable Energy (EERE) under the support of the Task 4.2 of Institute for Advanced Composites Manufacturing and Innovation (IACMI), Award Number DE-EE006926 managed by John Winkel from DOE and John Unser from IACMI. Academic and National Laboratory partners for this project are: Derek Berry and David Snowberg (National Renewable Energy Lab), Aaron Stebner (Colorado School of Mines), Nathan Sharpe (Purdue University), Dayakar Penumadu (University of

Tennessee), Douglas Adams (Vanderbilt). Industrial consortium was led by Dana Swan (Arkema), Mingfu Zhang (Johns Manville), and Stephen Nolet (TPI Composites). The views and opinions of authors expressed in this paper or referenced documents do not necessarily state or reflect those of the United States Government or the identified collaborating partners. Authors also acknowledge that important insight and ideas were obtained from academic and industrial collaborators during the project activities who are not being formally acknowledged in this manuscript as co-authors. Materials supplied, and manufacturing methods developed by the industrial collaborators is gratefully acknowledged.

References

1. James, T. and A. Goodrich, *Supply chain and blade manufacturing considerations in the global wind industry*. 2013, US Department of Energy National Renewable Energy Laboratory
2. *U.S. Wind Industry Third Quarter 2017 Market Report*. 2017, American Wind Energy Association
3. Dylan Cousins, A.S., Dayakar Penumadu, Stephen Young, David Snowberg *Elium® and Epoxy Composite Structural Comparison* in *IACMI 4.2 Project Deliverable* 2018.
4. Davies, P., P.Y. Le Gac, and M. Le Gall, *Influence of Sea Water Aging on the Mechanical Behaviour of Acrylic Matrix Composites.* Applied Composite Materials, 2016. **24**(1): p. 97-111.
5. Murray, R.E., et al. *Manufacturing a 9-Meter Thermoplastic Composite Wind Turbine Blade*. in *ASC 32nd Technical Conference*. 2017. Purdue University, USA.
6. Jonkman, J., et al., *Definition of a 5-MW Reference Wind Turbine for Offshore System Development*. 2009, National Renewable Energy Laboratory, U.S.
7. Resor, B.R., *Definition of a 5MW/61.5m Wind Turbine Blade Reference Model*. 2013: Sandia National Laboratories.
8. James.C.Fisher II., *Introduction to Performing a Techno‐Economic Analysis for Power Generation Systems*. 2015, U.S. Department of Energy: National Energy Technology Laboratory.
9. L. Fingersh, M.Hand, and A. Laxson *Wind Turbine Design Cost and Scaling Model* 2006, U.S. Department of Energy, National Renewable Energy Laboratory.
10. Swanson, R.M., et al., *Techno-Economic Analysis of Biofuels Production Based on Gasification* 2010, U.S. Department of Energy, National Renewable Energy Laboratory.
11. Schubel, P.J., *Cost modelling in polymer composite applications: Case study – Analysis of existing and automated manufacturing processes for a large wind turbine blade.* Composites Part B: Engineering, 2012. **43**(3): p. 953-960.
12. Berg, J.C. and B.R. Resor, *Numerical Manufacturing And Design Tool (NuMAD v2.0) for Wind Turbine Blades: User's Guide*. 2012: Sandia National Laboratories.
13. Nolet, S., *TPI Composites: Manufacturing wind turbine blade specifications,* Internal Communication with S. Jenne, D. Berry, and D. Snowberg, 2017.
14. Schubel, P.J., *Technical cost modelling for a generic 45-m wind turbine blade producedby vacuum infusion (VI).* Renewable Energy, 2010. **35**(1): p. 183-189.
15. Berry, D., et al., *Cost Study for Large Wind Turbine Blades*, in *WindPACT Blade System Design Studies*. 2003, Sandia National Laboratories and TPI Composites, Inc.
16. Swan, D., *Arkema Inc, Elium® Cost*, Internal Communication with S. Jenne and D. Snowberg, 2017.
17. H. Albers, S.G., H. Seifert, U. Kühne, *Recycling of Wind Turbine Rotor Blades - Fact or Fiction?*, in *DEWI MAGAZIN* 2009.
18. Arias, F., *Assessment of Present/Future Decommissioned Wind Blade Fiber-Reinforced Composite Material in the United States*. 2016, Department of Civil Engineering: City College of New York.
19. Larsen, K. *Recycling wind turbine blades.* 2009; Available from: Larsen, Kari (2009, January/February) 71-73.
20. Cherrington, R., et al., *Producer responsibility: Defining the incentive for recycling composite wind turbine blades in Europe.* Energy Policy, 2012. **47**: p. 13-21.
21. *Research note outline on recycling wind turbines blades,* EWEA.
22. Cousins, D., *Recycling of Elium® Composite Components*. 2017, Budget Period 3 IACMI 4.2 Project Deliverable Colorado School of Mines.
23. Fox, T.R., *Recycling wind turbine blade composite material as aggregate in concrete*. 2016, Iowa State University.
24. Thompson, J. *Landfill Waste Costs Continued to Rise in 2016*. 2017; Available from: https://nrra.net/sweep/cost-to-landfill-waste-continues-to-rise-through-2016/.

13. APPENDIX B
Manufacturing a 13-m Elium® Composite Wind Blade

This Appendix contains results from the fabrication of 13-meter Elium® composite wind turbine blade (Milestone 4.2.6.5). The numbering for pages, tables, figures and references are exclusive to this Appendix and are not integrated into the main body and table of contents of this final report.

Fabrication of thermoplastic wind blade for IACMI Milestone 4.2.6.5 April 30, 2019

This report outlines the fabrication of the 13m thermoplastic wind blade at NREL's CoMET facility.

Milestone 4.2.6.5 *Design and fabricate thermoplastic wind blade(s) and/or other OEM relevant components.*

Figure 1. 13m thermoplastic wind blade

A 13m wind blade has been fabricated at NREL's CoMET facility for the IACMI 4.2 project. This blade was produced on a 3D printed mold-set donated by TPI Composites. Construction materials for this blade were primarily fiberglass provided by Johns Manville, Elium-188O thermoplastic resin provided by Arkema, and balsa core purchased commercially. Initial material quantities for this blade build can be found in Table 1.

Table 1. Blade material estimates

Blade Component	*Materials*	*Material Use (excluding scrap)*
Suction Skin	Elium 188-0 Resin Johns Manville Fiberglass Balsa Core	58kg 143kg 12.5kg
Pressure Skin	Elium 188-0 Resin Johns Manville Fiberglass Balsa Core	73.5kg 150.5kg 11.5kg
Main Shearweb	Elium 188-0 Resin Johns Manville Fiberglass Balsa Core	14.5kg 18.5kg 4kg
Aft Shearweb	Elium 188-0 Resin Johns Manville Fiberglass Balsa Core	1.5kg 2.5kg 0.5kg

The blade was fabricated in four components using the vacuum infusion method. Dry materials were placed in the mold according to the design drawings (Arkema, NREL, TPI, 2018); see Figure 2 for material layup. Once material placement was complete vacuum infusion consumables, consisting of release films, peel plies, flow media, flow lines, vacuum lines, etc., were placed on top of the dry materials. Finally, a vacuum bag was placed over the entire part to remove air and consolidate the part.

Figure 2. Dry material placement in the mold

Vacuum infusion for the blade skins was performed in 5 zones: 3 zones in the root, a "trailing edge" zone that included the sparcap, and a "leading edge" zone. Overall infusion time for the skins was approximately 2hours per skin. The infusion layout for the Suction Skin (SS) can be seen in Figure 3.

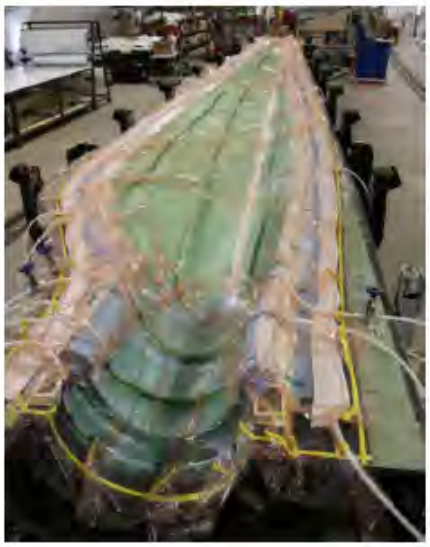

Figure 3. SS under vacuum bag during infusion

Following individual component fabrication, the blade was assembled with Bostick SAF30-90CP adhesive. The bonding process took place in 2 steps:

1) Bonding the main and aft shearwebs into the SS
2) Bonding the blade halves together.

Prior to bonding, multiple rounds of fit checks were performed to measure the bond gaps and make minor adjustments to the components to achieve proper mating alignment; see Figure 4 for fit check layout.

Figure 4. Bond gap measurements

The bond paste was packaged in 825mL, 10:1 cartridges. During bonding, paste as applied using pneumatic mixers. A total of fifty-five 825mL cartridges were used; see Figure 5 for bond paste laydown.

Figure 5. Bond paste application

After the blade components were bonded, an overlamination was applied to the root according to the design documents that accompanied the mold set. This deviated slightly from the design (Arkema, NREL, TPI, 2018) and added an extra three overlamination plies (16 total vs. 13 from design). See Figure 6 for overlamination details.

Figure 6. TE Overlamination (top: under bag, bottom: after cure)

Once overlamination was complete, the blade was placed into the root finishing machine. The root face was cut using a serrated diamond blade saw to create a clean, smooth face. Following the face cut operation a total of thirty holes, dimensioned 40mmØ x 205mm deep, were drilled into the root on a 508mm Ø bolt circle pattern. See Figure 7 for the blade positioned in the root finishing machine during the hole drill operation. Both cutting and drilling operations were done "wet", with water sprayed on the saw blade and pushed through the drill bit to ensure tooling and the blade stayed cool to avoid melting the thermoplastic resin.

Figure 7. Root finishing

Root inserts were bonded into the blade root using the root finishing machine. The inserts were secured to the root insert plate with custom injection bolts containing a center-bored hole for paste application. Inserts were potted into the blade using the same Bostik SAF30-90CP; approximately six 825mL cartridges were used. See Figure 8 for root inserts prior to bond.

Figure 8. Root insert prep

A final trim of the LE and TE flashing followed by sanding was performed finish the blade manufacturing. Final weight and blade of the blade can be found in Table 2.

Table 2. Final Blade properties

	Weight (kg)	*C.G. (dist from root face)*
13m Thermoplastic Wind Blade	493.5 kg 1,088 lb	4,006 mm 13ft-8"

References

Arkema, NREL, TPI. (2018). *4.2 Milestone 4.2.2.5 - TE model blade parts - RevA.*

14. APPENDIX C
Static Test Plan for Maximum Flapwise Loading to a 13-m Elium® Composite Blade

This Appendix contains the maximum flapwise test plan for the 13-meter Elium® composite wind turbine blade. The numbering for pages, tables, figures and references are exclusive to this Appendix and are not integrated into the main body and table of contents of this final report.

NREL
NATIONAL RENEWABLE ENERGY LABORATORY

STATIC TEST PLAN

LABORATORY MAXIMUM FLAPWISE STATIC TESTING OF THE THERMOPLASTIC 13-METER WIND TURBINE BLADE

Conducted by:
National Renewable Energy Laboratory
National Wind Technology Center
15013 Denver West Parkway
Golden, CO 80401

Conducted for:
IACMI 4.2 Project Team

February 28, 2019

Approval By: _____ Feb 28, 2019
David Snowberg, IACMI 4.2 Project Manager — Date

Approval By: _____ Feb 28, 2019
Ryan Beach, NREL Test Engineer — Date

Approval By: _____ Feb 28, 2019
Scott Hughes, NREL Test Engineer — Date

TABLE OF CONTENTS

LIST OF ABBREVIATIONS

Phrase	Abb.	Phrase	Abb.
National Wind Technology Center	NWTC	Department of Energy	DOE
National Renewable Energy Laboratory	NREL	National Rotor Testbed	NRT
Sandia National Laboratories	SNL	Scaled Wind Farm Technology	SWiFT
Ethercat Data Acquisition System	EDAS	Thermoplastic	TP
National Instruments	NI	Institute for Advanced Composite Manufacturing Innovation	IACMI

DOCUMENT HISTORY AND DOCUMENT MANAGEMENT

Revision	Date (yy/mm/dd)	Description	Author(s)	Communication of Change
RevA	190227	Internal Draft	Ryan Beach, Scott Hughes, David Snowberg	NREL
RevB	190228	updated plan per NREL team input	Ryan Beach, Scott Hughes David Snowberg	DOE, IACMI 4.2, and NREL

1-DISCLAIMER

This test plan shall not be reproduced, except in full, without the written approval of NREL.

2-CONTACTS

Table 1.1 – List of Contacts

Name	Title	Email	Phone
National Renewable Energy Laboratory			
Ryan Beach	Test Engineer	Ryan.beach@nrel.gov	303-384-6949
Scott Hughes	Test Engineer	scott.hughes@nrel.gov	303-384-7054
Dave Snowberg	Test Engineer	david.snowberg@nrel.gov	303-384-6920
Robynne Murray	Engineer	Robynne.murray@nrel.gov	303-384-7191
Derek Berry	IACMI Wind TA Director	Derek.berry@nrel.gov	303-384-7372
David Barnes	Technician	David.barnes@nrel.gov	303-275-4796
Mike Jenks	Technician	mike.jenks@nrel.gov	303-384-6994
Bill Gage	Technician	bill.gage@nrel.gov	303-384-7071
Troy Boro	Technician	troy.boro@nrel.gov	303-384-7065
Sara Fairchild	Technician	Sara.fairchild@nrel.gov	303-384-7114
Jim Ringwall	EHS POC	Jim.Ringwall@nrel.gov	303-384-7256

3-BACKGROUND

A 13m thermoplastic (TP) blade was produced at NREL's CoMET facility using the same blade skin molds that were previously used to produce epoxy blades for SNL's SWiFT facility. New shear web molds were produced at NREL to replicate the molds used for the previously tested epoxy blades.

4-SCOPE

This test plan describes the test setup, instrumentation, and load matrix for the maximum flapwise static test of the 13m TP blade.

Testing will be performed in the Structural Testing Laboratory (STL) at NREL's National Wind Technology Center (NWTC) near Boulder, Colorado. Single-point static loads will be applied to the blade using a bridge crane and a ballast weight.

This test is not for certification purposes. The NREL Quality Management system and guidance from the IEC 61400-23 blade test standard will be used where appropriate [1].

Work is being performed as part of the IACMI 4.2 project.

During active program work, files will be kept in the following location on the NREL certification server:

> *Y:\Wind\Confidential\Projects\Cert\A-C\Certification Projects\Blade Testing\2-Current Tests\2019 thermoplastic 13m blade*

A log book will be maintained for the test.

5-OBJECTIVES

The objectives of the structural test are as to:

1. Validate the blade is able to sustain the factored extreme positive flapwise bending moment.
2. Measure deflections and strains resulting from the applied test loads.
3. Compare results from thermoplastic blade to previously tested epoxy blade

6-TEST ARTICLE DESCRIPTION

The 13m TP blade was made from materials that include Johns Manville fiberglass, balsa wood, Bostik SAF30 90 CP adhesive, and Arkema's Elium 188 resin. The 13m TP blade was designed with a fiberglass layup to be structurally equivalent to the previously tested epoxy blade. The blade root bolt pattern is (30) M20 bolts on a 508-mm bolt pattern. The nominal maximum chord is 1.473 m. The blade includes pre-bend in the flapwise, upwind direction.

The blade was fabricated by NREL at the CoMET facility at the NWTC. This blade production was for Milestone 4.2.6.5 from the IACM 4.2 project.

7-LOADS

7.1-Design Loads

Maximum flapwise design bending moment distribution given in Table 7.1 was provided by SNL [2]. Spanwise stations are given as the length along the blade from the blade root. The maximum static flapwise load case is also referred to as 'Load 90'.

Table 7.1 – Design Maximum Flapwise Moment

Spanwise Station [m]	Design Flap Moment [kN-m]
0.00	204.4
0.87	179.3
1.82	156.1
2.60	136.2
3.48	115.0
4.44	93.0
5.46	70.9
5.98	62.0
7.02	44.2
8.05	29.7
9.05	19.1
9.52	14.0
10.40	8.0
11.53	2.9
12.37	0.3
12.99	0.0

7.2-Test Load Factors

The design loads provided do not include test load factors. Target test loads include a test load factor for blade to blade variation as shown in Table 7.2 as defined in the IEC 61400-23 standard.

Table 7.2 – Test Load Factors

Test Load Factor		Multiplier
ysu	Blade to Blade Variation	1.10

7.3-Target Test Load

The target test loads are determined by multiplying the design loads by the test load factors as prescribed in Equation 7.1, and are shown in Table 7.3.

Equation 7.1 – $M_{target} = M_{design} \times \gamma_{su}$

Table 7.3 – Target Test Loads

Spanwise Station [m]	Target Test Flap Moment [kN-m]
0.00	224.9
0.87	197.2
1.82	171.7
2.60	149.9
3.48	126.5
4.44	102.3
5.46	77.9
5.98	68.2
7.02	48.6
8.05	32.6
9.05	21.0
9.52	15.5
10.40	8.7
11.53	3.2
12.37	0.3
12.99	0.0

7.4-Tare Moment

Tare moment is the moment along the blade span created by the weight of the blade and load fixtures mounted on or between the blade and load cell. The calculated root

bending moment based on property testing to the epoxy blade is 18.45 kN-m (to be recalculated for the thermoplastic blade). The measured tare load of saddles and rigging equipment is provided in Table 7.4.

Table 7.4 – Tare Weights

Load Application Station Number	Blade Span [m]	Weight [kN]
1	4.60	1.96
2	7.55	1.95
3	10.85	1.66

Measured tare loads include wooden saddle forms, steel saddle frames, beam clamps and load cells. The 7.55m and 10.85m tare weight also includes the distributed weight of the spreader bar. As minor modifications of the tare loads may be necessary between load cases, the test loads will be modified as necessary.

7.4-Applied Test Load

To achieve the target test load from the root of the blade to the 70% span (9.1 m station), external forces are applied to the load saddles. Table 7.5 provides the external forces necessary to load the epoxy blade to the target test moment in addition to the moment created by the blade weight and test load equipment; these values will be recalculated based on actual property measurements to the 13m TP blade.

Table 7.5 – External Test Loads (Epoxy Blade)

Load application Station Number	Spanwise Station [m]	Load [kN]
1	4.6	4.45
2	7.55	5.15
3	10.85	9.64

Figure 7.1 compares the target test moment distribution with the tare moment and target applied bending moment.

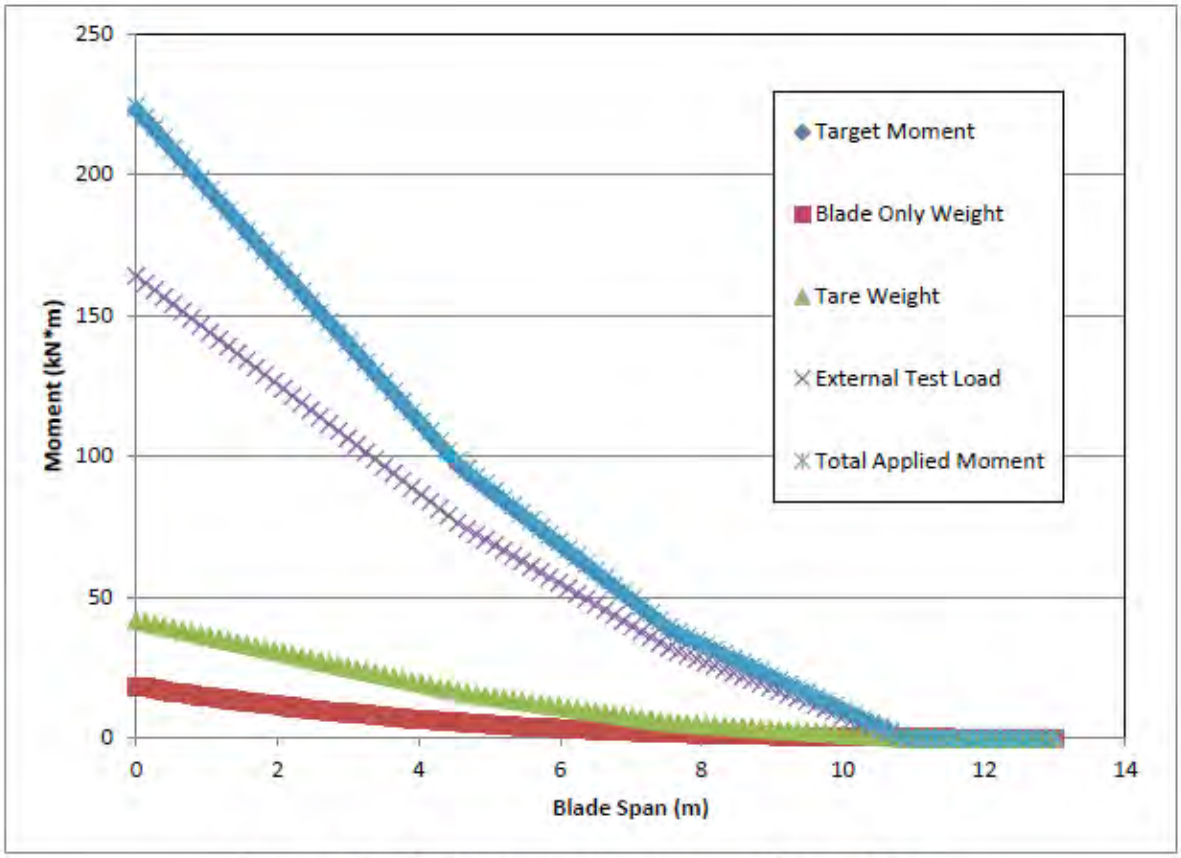

Figure 7.1 – Test Moment Distributions (Epoxy Blade)

7.5-Estimated Blade Deflections

Deflections resulting from the application of the tare load and at the maximum applied test bending moment are estimated from analytical models, estimates are provided in Table. Deflections are provided relative to the blade in an unloaded (zero moment) condition. Predicted deflections from ANSYS of the TP 13m blade are within 10% of the epoxy blade.

Table 7.6 – Estimated Deflections (for Epoxy Blade)

Station [m]	Deflection at Tare Load [m]	Deflection at the Target Test Load [m]
4.6	0.02	0.11
7.55	0.06	0.40
10.85	0.13	1.03
13 (Blade Tip)	0.22	1.49

8-TEST SETUP

8.1-Quality and Safe Operating Procedures

All testing will be conducted in accordance with NREL Safe Operating Procedure (SOP) #515009412 – Conducting Structural Tests at the NWTC [3]. A Readiness Verification (RV) will be performed prior to the start of testing that will demonstrate that the test is in compliance with NREL SOP's and all systems are working according to specification.

All NREL staff and visiting professionals shall comply with the SOP and RV while working at the NWTC. Visiting professionals will be required to participate in an NREL EHS orientation before being allowed to participate in testing activities at the NWTC.

Safe Work Permits and Lift Permits will be issued by NREL EHS where work is out of the scope of the structural testing SOP.

Test equipment will be reviewed following the NWTC TEDVP.

8.2-Test Location

Structural testing will be conducted at NREL's NWTC located near Boulder, CO. Structural testing will be performed at the Structural Testing Laboratory (STL), with the blade cantilevered to the 5.4 MN-m test stand for structural tests.

8.3-Property Testing

Weight and CG measurements of the blade will be performed prior to installing test instrumentation—either with a 2-point lift or if a single-point lift is used then the inclination of the root face will be measured. The sling(s) will be used in a basket configuration. The lift will be conducted with the blade positioned such that the trailing edge (TE) is up, towards the laboratory ceiling, and the leading edge (LE) is down, towards the laboratory floor. For single point lifts, the sling position will be adjusted until the root face of the blade is vertical. The weight will be measured with load cell(s) and the CG distance will be measured with a tape measure from the root plane to the center of the sling along the low-pressure (LP) surface. The results from the epoxy blade are presented in Table 8.1 (this will be updated with results from the TP 13m blade).

Table 8.1 – Weight and CG (Epoxy Blade)

Property	Measured Values
Weight (kN)	5.08
CG Location (m)	3.630

Modal parameters were measured with the epoxy blade using free-decay and impact methods. The blade was cantilevered to the test stand in Building A-60 for modal characterization. Summary information from modal characterization is provided in Table 8.2 for the epoxy blade, which will be repeated in the STL for the 13m TP blade.

Table 8.2 – Modal Parameters (Epoxy Blade)

Mode Shape	Frequency [Hz]	Damping [% Critical]
1st Flat	2.19	0.12
1st Edge	4.92	0.2
2nd Flat	7.06	0.14
3rd Flat	14.5	0.15
2nd Edge	18.1	0.23
Flap / Torsion	24	0.2
1st Torsion	26.6	0.18
Flap / Edge / Torsion	35.7	
3rd Edge	42	
2nd Torsion	46.2	

Airfoil profile measurements were taken on the epoxy blade using a laser tracker. Profile measurements were made in Building A-60 with the blade cantilevered to the A-60 test stand.

Select airfoil profile measurements may be taken on the TP blade in the STL, as time permits.

8.4-Facility Configuration

The test stand will be tilted back to 5 degrees to allow clearance for rigging equipment between the blade and t-slot base plate.

T-slot base plates will be mounted to the floor to react the external loads applied to the blade.

8.5-Blade Pre-twist Orientation

The blade will be mounted to the test stand with the HP surface up. The 10.85 m station airfoil inclination will be 6.3 degrees relative to the laboratory floor, with the trailing edge lower than the leading edge. The as-tested inclination is 1.7 degrees from the ideal design condition of a 4.6 degree airfoil pre-twist at the 10.85 m station. Given the discrete inclination increments available from the existing adapter plate bolt pattern, 1.7 degrees is the closest possible test configuration.

8.6-Adapter Plate and Root Fixturing

The blade will mount to the test stand through an adapter plate. The adapter plate is 3" (~75-mm) thick steel. The blade bolts to the adapter plate through the (30) root bolts. The blade bolt pattern is milled into the blade such that two bolts are at top-dead-center relative to the laboratory frame of reference.

A 1" (~25mm) thick steel spacer ring will be placed between the bolt heads and the adapter plate to match the grip length of the SWiFT turbine pitch bearing and crank plate. This will allow the same length root bolts to be used during laboratory fatigue testing and in-field turbine operation.

The blade is secured to the adapter plate using (30) 160 mm, M20 Class 10.9 bolts equally spaced on a 508 mm bolt circle diameter. Blade bolts will be torqued to 305 N-m (225 ft-lb), using TS-70 molypaste. The bolt torque sequence includes (1) seating the bolts to 150 N-m in a star pattern, (2) torque bolts to 305 N-m in a star pattern, (3) torque to 305 N-m in a circular pattern.

The adapter plate is secured to the test stand using (24), 18 in length, 1-8 UNC grade B7 all threads equally spaced on a 30-in bolt circle diameter. Adapter plate to test stand bolts will be torqued to 450 ft-lb (dry threads).

8.7-Load Introduction Method and Hardware

Three load introduction stations at 4.6 m, 7.55 m and 10.85 m will be used for testing. The external loads applied at these stations combined with the tare moment introduce the target test loads in the positive flapwise direction. A ballast weight will be suspended from the blade at the 4.6 m station. Test loads at the 7.55 m and 10.85 m station will be applied by a test operator controlling the STL's 35 ton overhead bridge crane. A spreader bar will be positioned between the 7.55 m and 10.85 m load introduction stations. This spreader bar will attach to the load line from the overhead crane. Turning blocks mounted to the t-slot base plates will react and redirect the force from the overhead bridge crane to a force applied to the spreader bar pulling downwards towards the laboratory floor. Figure 8.1 provides a photograph of a representative test system from a previous test campaign.

Figure 8.1 – Photograph of a representative test system (from different blade test)

Load saddles are constructed using wood forms surrounded by steel frames. The wood forms consist of epoxied plywood cut to the station airfoil profile and fitted to the blade surface with rubber and thickened epoxy. The epoxy when fitted conforms the blade airfoil profile to the wood form. The wood forms are 5.25 in (133.4 mm) thick in the spanwise direction and are centered at the nominal blade station. Steel frames are fabricated around the wood forms and secure the load saddle to the blade using four ½-13 grade B7 threaded rods that are torqued to 20 ft-lb (dry threads) to prevent the load saddle from slipping. The torque applied to the threaded rod creates a preload on the

blade of 2400 lb [10.7 kN]. The preload from the saddle clamping force is approximately three times the force of the applied test load. Loads will be applied to the saddles in the chordwise direction at the 30% chord of the local airfoil section.

The spreader beam was designed specifically for this test and is constructed from aluminum c-channel bolted together with aluminum plates and shackles for loading points.

A 5/8-in Dyneema synthetic rope will be connected to the spreader bar and run through the turning block to the overhead crane.

8.8-Controls and Safety Interlocks

The test is configured with controls and interlocks designed to ensure safety of test personnel, minimize hazards to facilities and equipment, and prevent overloading of the test article during test operation. This test will be conducted as an attended-only test.

- Restricted access to test area– A perimeter is established around the blade, preventing access by non-testing staff and other contracted workers. The restricted access area will be defined in the RV document.

9-INSTRUMENTATION

The actual instrumentation used during this test may change with agreement from the test plan approvers. These changes will consider time/budget constraints balanced with value of each measurement.

9.1-Load

Two 50-kN capacity load cells will be used to measure the applied test loads. One load cell will be positioned at the 4.6 m station and the second load cell will be positioned under the spreader beam connecting to the 7.55 m and 10.85 m station saddles.

9.2-Displacement

Three string potentiometers will be used to measure blade displacements at the 4 m, 7 m, and 11.25 m stations. String potentiometers will be attached to the blade at the center of the spar cap.

Optionally, a laser distance transducer may be positioned to measure blade displacements at the trailing edge of the 7 m station.

9.3-Strain Gages

Resistance strain gages will be installed on the blade for strain measurement and applied moment derivation. The single-axis strain gages are Measurements Group WK-06-250BG-350 and the rosettes are Measurements Group WK-06-250RA-350. All the strain gages have a nominal 350 Ohm resistance and are connected in a three-wire configuration. External single-axis strain gages will be orientated at 0 degree (parallel with the spanwise axis and perpendicular to the chordwise axis) and will be mounted on the center of the spar caps on both the high and low pressure sides of the blade. Rosettes will be oriented such that one gage is 0 degree, one gage is 45 degree, and one gage is 90 degree (parallel with the chordwise axis and perpendicular to the spanwise axis). Table 9.1 provides the location of the strain gages.

Table 9.1 – Strain Gage Locations

Name	Span	Surface	Chord Position	Type
SG01-200-LP0	0.2	LP	0°	Uni
SG02-200-LP45	0.2	LP	45°	Uni
SG03-200-LP90	0.2	LP	90°	Uni
SG04-200-LP135	0.2	LP	135°	Uni
SG05-200-HP180	0.2	HP	180°	Uni
SG06-200-HP225	0.2	HP	225°	Uni
SG07-200-HP270	0.2	HP	270°	Uni
SG08-200-HP315	0.2	HP	315°	Uni
SG09-1900-HP-AP-0	1.9	HP	Aft Panel at Spar Interface	Rosette
SG10-1900-HP-AP-45	1.9	HP	Aft Panel at Spar Interface	Rosette
SG11-1900-HP-AP-90	1.9	HP	Aft Panel at Spar Interface	Rosette
SG12-2500-HP-AP-0	2.5	HP	Aft Panel at Spar Interface	Rosette
SG13-2500-HP-AP-45	2.5	HP	Aft Panel at Spar Interface	Rosette
SG14-2500-HP-AP-90	2.5	HP	Aft Panel at Spar Interface	Rosette
SG15-2750-HP-TE	2.75	HP	TE	Uni
SG16-2750-TE	2.75		TE	Uni
SG17-2900-LP-SC-0	2.9	LP	Center of Sparcap	Rosette
SG18-2900-LP-SC-45	2.9	LP	Center of Sparcap	Rosette

Name	Span	Surface	Chord Position	Type
SG19-2900-LP-SC-90	2.9	LP	Center of Sparcap	Rosette
SG20-2900-LP-FP-0	2.9	LP	Mid Fore Panel	Rosette
SG21-2900-LP-FP-45	2.9	LP	Mid Fore Panel	Rosette
SG22-2900-LP-FP-90	2.9	LP	Mid Fore Panel	Rosette
SG23-3250-HP-SC	3.25	HP	Center of Sparcap	Uni
SG24-3250-LP-SC	3.25	LP	Center of Sparcap	Uni
SG25-3250-LE	3.25		LE	Uni
SG26-3250-TE	3.25		TE	Uni
SG27-3250-LP-TE	3.25	LP	TE	Uni
SG28-6300-LP-AP-0	6.3	LP	Mid Aft Panel	Rosette
SG29-6300-LP-AP-45	6.3	LP	Mid Aft Panel	Rosette
SG30-6300-LP-AP-90	6.3	LP	Mid Aft Panel	Rosette
SG31-6300-HP-LE-0	6.3	HP	LE	Rosette
SG32-6300-HP-LE-45	6.3	HP	LE	Rosette
SG33-6300-HP-LE-90	6.3	HP	LE	Rosette
SG34-6500-HP-SC	6.5	HP	Center of Sparcap	Uni
SG35-6500-LP-SC	6.5	LP	Center of Sparcap	Uni
SG36-6500-LE	6.5		LE	Uni
SG37-6500-TE	6.5		TE	Uni
SG38-9000-LP-AP-0	9.0	LP	Mid Aft Panel	Rosette
SG39-9000-LP-AP-45	9.0	LP	Mid Aft Panel	Rosette
SG40-9000-LP-AP-90	9.0	LP	Mid Aft Panel	Rosette
SG41-9750-HP-SC	9.75	HP	Center of Sparcap	Uni
SG42-9750-LP-SC	9.75	LP	Center of Sparcap	Uni
SG43-9750-LE	9.75		LE	Uni
SG44-9750-TE	9.75		TE	Uni
SG45-3250-HP-TE	3.25	HP	Center of Sparcap	Uni
SG46-2750-LP-TE	2.75	LP	Center of Sparcap	Uni

9.4-Temperature

Ambient temperature and relative humidity will be measured near the blade root.

9.5- Data Acquisition

The Ethercat Data Acquisition System (EDAS) will be employed for this test which is based on National Instruments (NI) Ethercat PXI technology combined with custom NREL developed LabVIEW coded software. All channels will be scanned at 1000 Hz

and time series data will be recorded at 100 Hz in 'fast' data files and 10 Hz in 'slow' data files.

9.6-Photos and Videos

Still photographs will be taken throughout the test program from various angles. Video will be recorded from the root to the tip, and a second camera viewing tip to root.

10-MAXIMUM FLAPWISE STATIC TESTING

10.1-Test Matrix

Loads will be applied in 25% load levels starting at 50% load to the 100% load. Load application from tare to target load will take approximately 20 seconds. Each load plateau will be held for at least 30 seconds, and then gradually released back to tare before moving to the next load level. Strain and displacement from each applied load level will be evaluated prior to proceeding to the next load level. Figure 10.1 provides a schematic of the load profile.

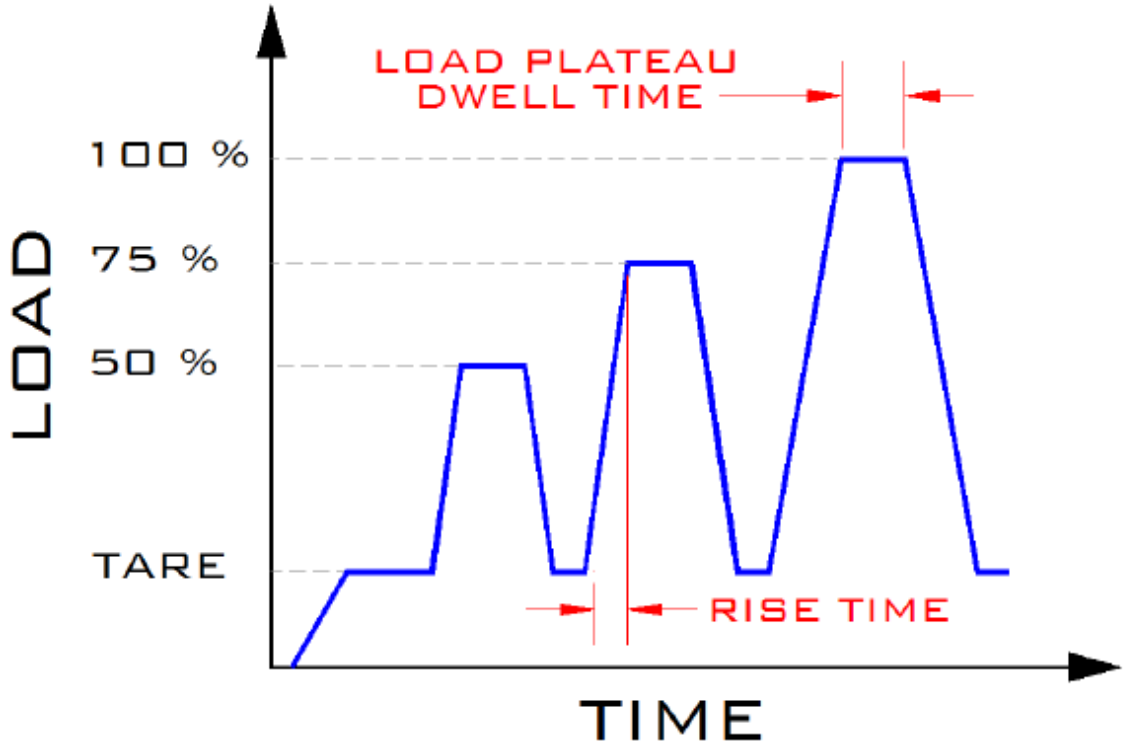

Figure 10.1 – Load Introduction Profile

Table 10.1 provides the target applied external loads for each load level.

Table 10.1 – Test Matrix Load Levels (Epoxy Blade)

Applied Load Level (% of Maximum Target Load)	Applied Test Root Bending Moment [kN-m]	External Load at 4.6 m [kN]	External Load at 7.55 m [kN]	External Load at 10.85 m [kN]
50	114	0	1.94	3.62
75	169	2.07	3.57	6.67
100	224	4.45	5.15	9.64

10.2-Test Procedure

1. Measure weight of all hardware attached to blade
2. Secure blade to test stand and attach load introduction hardware
3. Ensure load cell/crane is directly above pull point
4. Ensure function and readout of data acquisition and sensors
5. Ensure access restriction of highbay
6. Apply negative flap tare load with overhead crane for each strain gage location. Zero strain at each load.
7. Start Video
8. Start DAQ
9. 50% load
    a. Test operator load blade to 50% load
    b. Hold load for 30-seconds
    c. Return to tare
    d. Review data as necessary
    e. Maintain tare load for 30-seconds
10. 75% load
    a. Test operator load blade to 75% load
    b. Hold load for 30-seconds
    c. Return to tare
    d. Review data as necessary
    e. Maintain tare load for 30-seconds
11. 100% load
    a. Test operator load blade to 100% load
    b. Hold load for 30-seconds
    c. Return to tare
    d. Review data as necessary
    e. Maintain tare load for 30-seconds
12. Verify data collection and backup data

11-REPORTING

NREL will provide a test report after the completion of testing, per Milestone 4.2.6.7.

12-EXCEPTIONS FROM STANDARD PRACTICE

- None.

13-UNRESOLVED ISSUES

- None

14-REFERENCES

1. IEC 61400-23, Full-scale Structural Testing of Rotor Blades, 2014.
2. Load Document. Received June 6, 2017 from Joshua Paquette. File: 'NRT Test Loads.xlsx'.
3. NREL Safe Operating Procedure (SOP) #515009412 – Conducting Structural Tests at the NWTC

15. APPENDIX D
Static Test Plan for Minimum Flapwise, Maximum Edgewise and Minimum Edgewise Loading to a 13-m Elium® Composite Blade

This Appendix contains the minimum flapwise, maximum edgewise and minimum edgewise loading test plan for the 13-meter Elium® composite wind turbine blade. The numbering for pages, tables, figures and references are exclusive to this Appendix and are not integrated into the main body and table of contents of this final report.

NREL
NATIONAL RENEWABLE ENERGY LABORATORY

STATIC TEST PLAN

LABORATORY MINIMUM FLAPWISE, AND MAXIMUM AND MINIMUM EDGEWISE, STATIC TESTING OF THE THERMOPLASTIC 13-METER WIND TURBINE BLADE

Conducted by:
National Renewable Energy Laboratory
National Wind Technology Center
15013 Denver West Parkway
Golden, CO 80401

Conducted for:
IACMI 4.2 Project Team

February 28, 2019

Approval By: _____ Feb 28, 2019
David Snowberg, IACMI 4.2 Project Manager — Date

Approval By: _____ Feb 28, 2019
Ryan Beach, NREL Test Engineer — Date

Approval By: _____ Feb 28, 2019
Scott Hughes, NREL Test Engineer — Date

TABLE OF CONTENTS

LIST OF ABBREVIATIONS

Phrase	Abb.	Phrase	Abb.
National Wind Technology Center	NWTC	Department of Energy	DOE
National Renewable Energy Laboratory	NREL	National Rotor Testbed	NRT
Sandia National Laboratories	SNL	Scaled Wind Farm Technology	SWiFT
Ethercat Data Acquisition System	EDAS	Thermoplastic	TP
National Instruments	NI	Institute for Advanced Composite Manufacturing Innovation	IACMI

DOCUMENT HISTORY AND DOCUMENT MANAGEMENT

Revision	Date (yy/mm/dd)	Description	Author(s)	Communication of Change
RevA	190227	Internal Draft	Ryan Beach, Scott Hughes David Snowberg	NREL
RevB	190228	updated plan per NREL team input	Ryan Beach, Scott Hughes David Snowberg	DOE, IACMI 4.2, and NREL

1-DISCLAIMER

This test plan shall not be reproduced, except in full, without the written approval of NREL.

2-CONTACTS

Table 1.1 – List of Contacts

Name	Title	Email	Phone
National Renewable Energy Laboratory			
Ryan Beach	Test Engineer	Ryan.beach@nrel.gov	303-384-6949
Scott Hughes	Test Engineer	scott.hughes@nrel.gov	303-384-7054
Dave Snowberg	Test Engineer	david.snowberg@nrel.gov	303-384-6920
Robynne Murray	Engineer	Robynne.murray@nrel.gov	303-384-7191
Derek Berry	IACMI Wind TA Director	Derek.berry@nrel.gov	303-384-7372
David Barnes	Technician	David.barnes@nrel.gov	303-275-4796
Mike Jenks	Technician	mike.jenks@nrel.gov	303-384-6994
Bill Gage	Technician	bill.gage@nrel.gov	303-384-7071
Troy Boro	Technician	troy.boro@nrel.gov	303-384-7065
Sara Fairchild	Technician	Sara.fairchild@nrel.gov	303-384-7114
Jim Ringwall	EHS POC	Jim.Ringwall@nrel.gov	303-384-7256

3-BACKGROUND

A 13m thermoplastic (TP) blade was produced at NREL's CoMET facility using the same blade skin molds that were previously used to produce epoxy blades for SNL's SWiFT facility. New shear web molds were produced at NREL to replicate the molds used for the previously tested epoxy blades.

Static load testing in the maximum flapwise direction is planned under a separate test plan.

4-SCOPE

This test plan describes the test setup, instrumentation, and load matrix for the minimum flapwise static test and edgewise static tests of the 13m TP blade.

Testing will be performed in the Structural Testing Laboratory (STL) at NREL's National Wind Technology Center (NWTC) near Boulder, Colorado. Single-point static loads will be applied to the blade using a bridge crane and a ballast weight.

This test is not for certification purposes. The NREL Quality Management system and guidance from the IEC 61400-23 blade test standard will be used where appropriate [1].

Work is being performed as part of the IACMI 4.2 project.

During active program work, files will be kept in the following location on the NREL certification server:

> *Y:\Wind\Confidential\Projects\Cert\A-C\Certification Projects\Blade Testing\2-Current Tests\2019 thermoplastic 13m blade*

A log book will be maintained for the test.

5-OBJECTIVES

The objectives of the structural test are as to:

1. Validate the blade can sustain the factored extreme negative flapwise bending and static edgewise bending moments.
2. Measure deflections and strains resulting from the applied test loads.
3. Compare results from thermoplastic blade to previously tested epoxy blade.

6-TEST ARTICLE DESCRIPTION

The 13m TP blade was made from materials that include Johns Manville fiberglass, balsa wood, Bostik SAF30 90 CP adhesive, and Arkema's Elium 188 resin. The 13m TP blade was designed with a fiberglass layup to be structurally equivalent to the previously tested epoxy blade. The blade root bolt pattern is (30) M20 bolts on a 508-mm bolt pattern. The nominal maximum chord is 1.473 m. The blade includes pre-bend in the flapwise, upwind direction.

The blade was fabricated by NREL at the CoMET facility at the NWTC. This blade production was for Milestone 4.2.6.5 from the IACM 4.2 project.

7-LOADS

7.1-Design Loads

Design bending moment distributions provided by SNL are given in Table 7.1 [2]. Spanwise stations are given as the length along the blade from the blade root. The design moments include both flap and edge components from the design load document [2].

Table 7.1 – Design Moments

Spanwise Station [m]	Design Min Flap Moment [kN-m]	Design Max Edge Moment [kN-m]	Design Min Edge Moment [kN-m]
0.00	178.0	151.7	144.9
0.87	152.7	132.0	124.1
1.82	126.6	112.9	102.3
2.60	106.4	96.7	86.4
3.48	85.4	79.5	70.2
4.44	66.3	62.7	53.7
5.46	48.3	47.4	39.3
5.98	40.2	40.2	32.9
7.02	27.4	28.0	22.5
8.05	17.6	18.5	14.2
9.05	10.4	11.5	8.3
9.52	7.7	8.8	6.2
10.40	4.1	4.6	3.4
11.53	1.1	1.3	0.9
12.37	0.1	0.2	0.1
12.99	0.0	0.0	0.0

Figure 7.1 provides the inclination of the 12.96 m station as mounted to the test stand for each load case.

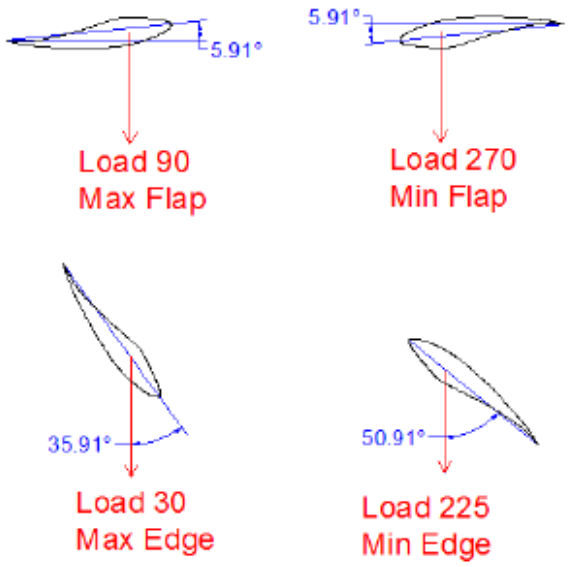

Figure 7.1 – As mounted Inclination of the Blade at the 12.96 m station

7.2-Test Load Factors

The design loads provided do not include test load factors. Target test loads include a test load factor for blade to blade variation as shown in Table 7.2 as defined in the IEC 61400-23 standard.

Table 7.2 – Test Load Factors

Test Load Factor		Multiplier
γsu	Blade to Blade Variation	1.10

7.3-Target Test Load

The target test loads are determined by multiplying the design loads by the test load factors as prescribed in Equation 7.1, and are shown in Table 7.3.

Equation 7.1. $M_{target} = M_{design} \times \gamma_s$

Table 7.3 – Target Test Loads

Spanwise Station [m]	Target Test Min Flap Moment [kN-m]	Target Test Max Edge Moment [kN-m]	Target Test Min Edge Moment [kN-m]
0.00	195.8	166.8	159.4
0.87	168.0	145.2	136.5
1.82	139.3	124.2	112.6
2.60	117.0	106.4	95.1
3.48	93.9	87.5	77.2
4.44	72.9	69.0	59.1
5.46	53.1	52.1	43.3
5.98	44.3	44.2	36.2
7.02	30.2	30.8	24.7
8.05	19.3	20.4	15.6
9.05	11.4	12.6	9.1
9.52	8.5	9.7	6.8
10.40	4.5	5.0	3.7
11.53	1.2	1.4	1.0
12.37	0.2	0.2	0.1
12.99	0.0	0.0	0.0

7.4-Tare Moment

Tare moment is the moment along the blade span created by the weight of the blade and load fixtures mounted on or between the blade and load cell. The calculated root bending moment based on property testing to the epoxy blade is 18.45 kN-m (to be recalculated for the thermoplastic blade). The measured tare load of saddles and rigging equipment is provided in Table 7.4.

Table 7.4 – Tare Weights

Load Application Station Number	Blade Span [m]	Weight [kN]
1	4.60	1.96
2	7.55	1.95
3	10.85	1.66

Measured tare loads include wooden saddle forms, steel saddle frames, beam clamps and load cells. The 7.55m and 10.85m tare weight also includes the distributed weight of the spreader bar. As minor modifications of the tare loads may be necessary between load cases, the test loads will be modified as necessary.

7.4-Applied Test Load

To achieve the target test load from the root of the blade to the 70% span (9.1 m station), external forces are applied to the load saddles. Table 7.5 provides the external forces necessary to load the epoxy blade to the target test moment in addition to the moment created by the blade weight and test load equipment; these values will be recalculated based on actual property measurements to the 13m TP blade.

Table 7.5 – External Test Loads (Epoxy Blade)

Load application Station Number	Spanwise Station [m]	Minimum Flap Load [kN]	Maximum Edge Load [kN]	Minimum Edge Load [kN]
1	4.6	8.90	8.90	6.52
2	7.55	5.37	3.13	2.87
3	10.85	4.75	3.54	5.36

Figure 7.2 through 7.4 compare the target test moment distribution with the tare moment and target applied bending moment for each load case.

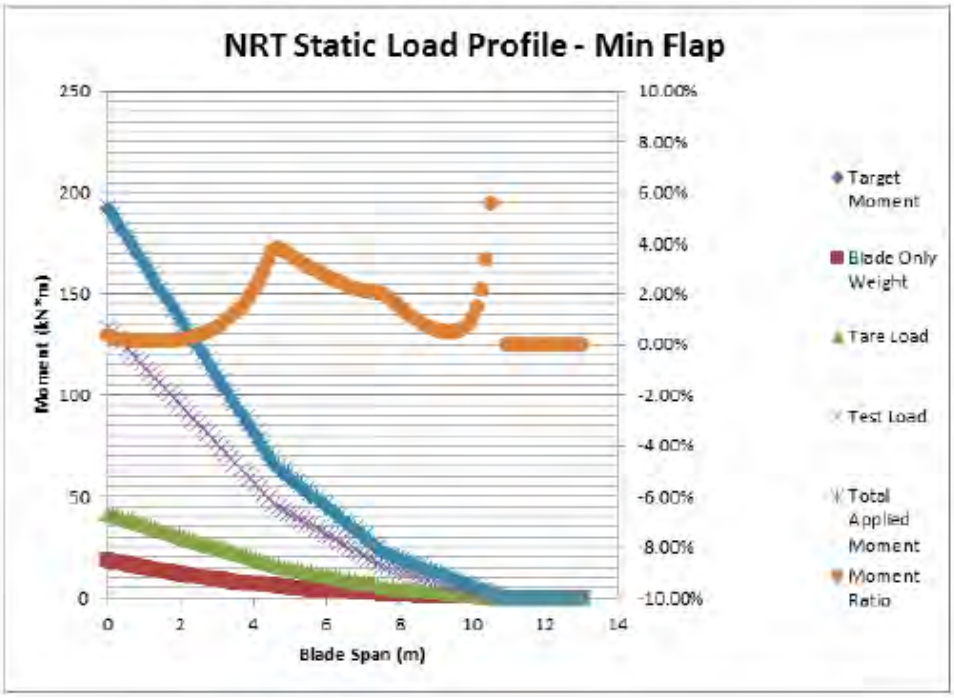

Figure 7.2 – Minimum Flap Test Moment Distributions (Epoxy Blade)

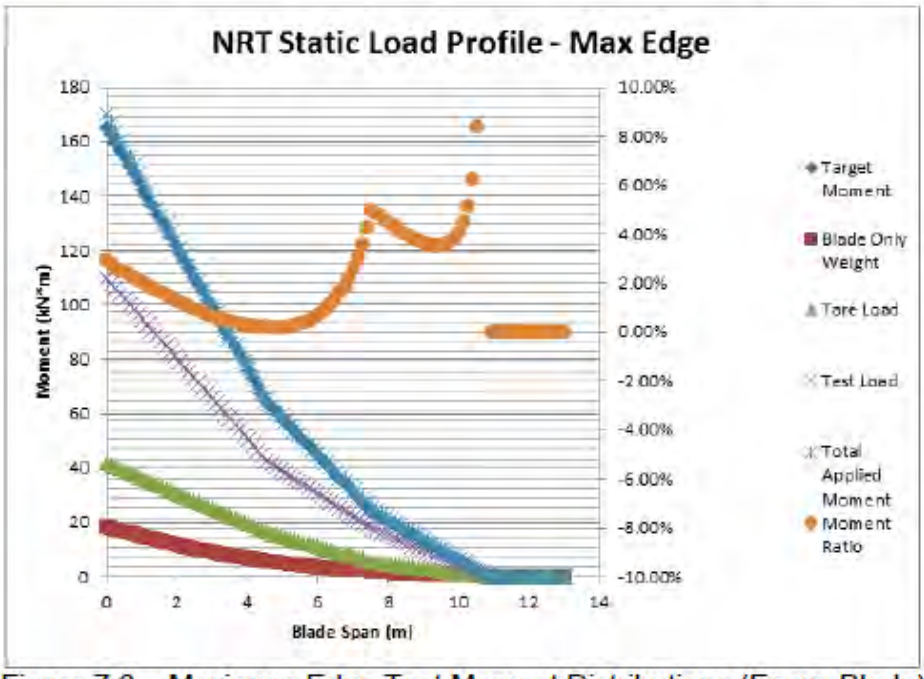

Figure 7.3 – Maximum Edge Test Moment Distributions (Epoxy Blade)

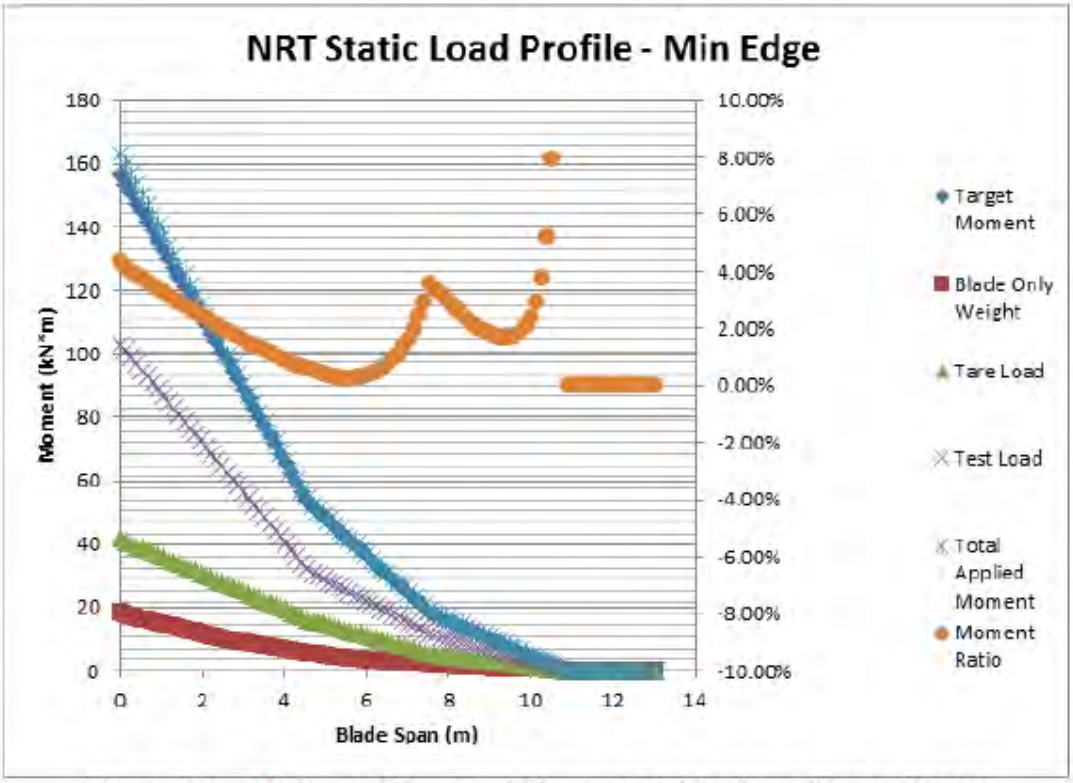

Figure 7.4 – Minimum Edge Test Moment Distributions (Epoxy Blade)

7.5-Estimated Blade Deflections

The blade tip displacement due to the application of the external loads for the minimum flapwise is estimated as 0.8 m. The blade tip displacement for the edge load cases is estimated to be less than 0.2 m.

8-TEST SETUP

8.1-Quality and Safe Operating Procedures

All testing will be conducted in accordance with NREL Safe Operating Procedure (SOP) #515009412 – Conducting Structural Tests at the NWTC [3]. A Readiness Verification (RV) will be performed prior to the start of testing that will demonstrate that the test is in compliance with NREL SOP's and all systems are working according to specification.

All NREL staff and visiting professionals shall comply with the SOP and RV while working at the NWTC. Visiting professionals will be required to participate in an NREL EHS orientation before being allowed to participate in testing activities at the NWTC.

Safe Work Permits and Lift Permits will be issued by NREL EHS where work is out of the scope of the structural testing SOP.

Test equipment will be reviewed following the NWTC TEDVP.

8.2-Test Location

Structural testing will be conducted at NREL's NWTC located near Boulder, CO. Structural testing will be performed at the Structural Testing Laboratory (STL), with the blade cantilevered to the 5.4 MN-m test stand for structural tests.

8.3-Property Testing

Weight and CG measurements of the blade will be performed prior to installing test instrumentation—either with a 2-point lift or if a single-point lift is used then the inclination of the root face will be measured. The sling(s) will be used in a basket configuration. The lift will be conducted with the blade positioned such that the trailing edge (TE) is up, towards the laboratory ceiling, and the leading edge (LE) is down, towards the laboratory floor. For single point lifts, the sling position will be adjusted until the root face of the blade is vertical. The weight will be measured with load cell(s) and the CG distance will be measured with a tape measure from the root plane to the center of the sling along the low-pressure (LP) surface. The results from the epoxy blade are presented in Table 8.1 (this will be updated with results from the TP 13m blade).

Table 8.1 – Weight and CG (Epoxy Blade)

Property	Measured Values
Weight (kN)	5.08
CG Location (m)	3.630

Modal parameters were measured with the epoxy blade using free-decay and impact methods. The blade was cantilevered to the test stand in Building A-60 for modal characterization. Summary information from modal characterization is provided in Table 8.2 for the epoxy blade, which will be repeated in the STL for the 13m TP blade.

Table 8.2 – Modal Parameters (Epoxy Blade)

Mode Shape	Frequency [Hz]	Damping [% Critical]
1st Flat	2.19	0.12
1st Edge	4.92	0.2
2nd Flat	7.06	0.14
3rd Flat	14.5	0.15
2nd Edge	18.1	0.23
Flap / Torsion	24	0.2
1st Torsion	26.6	0.18
Flap / Edge / Torsion	35.7	
3rd Edge	42	
2nd Torsion	46.2	

Airfoil profile measurements were taken on the epoxy blade using a laser tracker. Profile measurements were made in Building A-60 with the blade cantilevered to the A-60 test stand.

Select airfoil profile measurements may be taken on the TP blade in the STL, as time permits.

8.4-Facility Configuration

The test stand will be tilted back to 5 degrees to allow clearance for rigging equipment between the blade and t-slot base plate.

T-slot base plates will be mounted to the floor to react the external loads applied to the blade.

8.5-Blade Pre-twist Orientation

Figure 7.1 above provides pre-twist orientations for each of the load cases.

8.6-Adapter Plate and Root Fixturing

The blade will mount to the test stand through an adapter plate. The adapter plate is 3" (~75-mm) thick steel. The blade bolts to the adapter plate through the (30) root bolts.

The blade bolt pattern is milled into the blade such that two bolts are at top-dead-center relative to the laboratory frame of reference.

A 1" (~25mm) thick steel spacer ring will be placed between the bolt heads and the adapter plate to match the grip length of the SWiFT turbine pitch bearing and crank plate. This will allow the same length root bolts to be used during laboratory fatigue testing and in-field turbine operation.

The blade is secured to the adapter plate using (30) 160 mm, M20 Class 10.9 bolts equally spaced on a 508 mm bolt circle diameter. Blade bolts will be torqued to 305 N-m (225 ft-lb), using TS-70 molypaste. The bolt torque sequence includes (1) seating the bolts to 150 N-m in a star pattern, (2) torque bolts to 305 N-m in a star pattern, (3) torque to 305 N-m in a circular pattern.

The adapter plate is secured to the test stand using (24), 18 in length, 1-8 UNC grade B7 all threads equally spaced on a 30-in bolt circle diameter. Adapter plate to test stand bolts will be torqued to 450 ft-lb (dry threads).

Between each load case, the blade will be rotated by rotating the adapter plate relative to the test stand.

8.7-Load Introduction Method and Hardware

Three load introduction stations at 4.6 m, 7.55 m and 10.85 m will be used for testing. The external loads applied at these stations combined with the tare moment introduce the target test loads in the positive flapwise direction. A ballast weight will be suspended from the blade at the 4.6 m station. Test loads at the 7.55 m and 10.85 m station will be applied by a test operator controlling the STL's 35-ton overhead bridge crane. A spreader bar will be positioned between the 7.55 m and 10.85 m load introduction stations. This spreader bar will attach to the load line from the overhead crane. Turning blocks mounted to the t-slot base plates will react and redirect the force from the overhead bridge crane to a force applied to the spreader bar pulling downwards towards the laboratory floor. Figure 8.1 provides a photograph of a representative test system from a previous test campaign.

Figure 8.1 – Photograph of a representative test system (from different blade test)

Load saddles are constructed using wood forms surrounded by steel frames. The wood forms consist of epoxied plywood cut to the station airfoil profile and fitted to the blade surface with rubber and thickened epoxy. The epoxy when fitted conforms the blade airfoil profile to the wood form. The wood forms are 5.25 in (133.4 mm) thick in the spanwise direction and are centered at the nominal blade station. Steel frames are fabricated around the wood forms and secure the load saddle to the blade using four ½-13 grade B7 threaded rods that are torqued to 20 ft-lb (dry threads) to prevent the load saddle from slipping. The torque applied to the threaded rod creates a preload on the blade of 2400 lb [10.7 kN]. The preload from the saddle clamping force is approximately three times the force of the applied test load. Loads will be applied to the saddles in the chordwise direction at the 30% chord of the local airfoil section. Lifting straps may be placed around the saddle for the edge load cases.

The spreader beam was designed specifically for this test and is constructed from aluminum c-channel bolted together with aluminum plates and shackles for loading points.

A 5/8-in Dyneema synthetic rope will be connected to the spreader bar and run through the turning block to the overhead crane.

8.8-Controls and Safety Interlocks

The test is configured with controls and interlocks designed to ensure safety of test personnel, minimize hazards to facilities and equipment, and prevent overloading of the test article during test operation. This test will be conducted as an attended-only test.

- Restricted access to test area– A perimeter is established around the blade, preventing access by non-testing staff and other contracted workers. The restricted access area will be defined in the RV document.

9-INSTRUMENTATION

The actual instrumentation used during this test may change with agreement from the test plan approvers. These changes will consider time/budget constraints balanced with value of each measurement.

9.1-Load

Two 50-kN capacity load cells will be used to measure the applied test loads. One load cell will be positioned at the 4.6 m station and the second load cell will be positioned under the spreader beam connecting to the 7.55 m and 10.85 m station saddles.

9.2-Displacement

Three string potentiometers will be used to measure blade displacements at the 4 m, 7 m, and 11.25 m stations. String potentiometers will be attached to the blade at the center of the spar cap.

Optionally, a laser distance transducer may be positioned to measure blade displacements at the trailing edge of the 7 m station for the minimum flapwise test. The laser distance transducer is not used for the edgewise load cases.

9.3-Strain Gages

Resistance strain gages will be installed on the blade for strain measurement and applied moment derivation. The single-axis strain gages are Measurements Group WK-06-250BG-350 and the rosettes are Measurements Group WK-06-250RA-350. All the strain gages have a nominal 350 Ohm resistance and are connected in a three-wire configuration. External single-axis strain gages will be orientated at 0 degree (parallel

with the spanwise axis and perpendicular to the chordwise axis) and will be mounted on the center of the spar caps on both the high and low pressure sides of the blade. Rosettes will be oriented such that one gage is 0 degree, one gage is 45 degree, and one gage is 90 degree (parallel with the chordwise axis and perpendicular to the spanwise axis). Table 9.1 provides the location of the strain gages.

Table 9.1 – Strain Gage Locations

Name	Span	Surface	Chord Position	Type
SG01-200-LP0	0.2	LP	0°	Uni
SG02-200-LP45	0.2	LP	45°	Uni
SG03-200-LP90	0.2	LP	90°	Uni
SG04-200-LP135	0.2	LP	135°	Uni
SG05-200-HP180	0.2	HP	180°	Uni
SG06-200-HP225	0.2	HP	225°	Uni
SG07-200-HP270	0.2	HP	270°	Uni
SG08-200-HP315	0.2	HP	315°	Uni
SG09-1900-HP-AP-0	1.9	HP	Aft Panel at Spar Interface	Rosette
SG10-1900-HP-AP-45	1.9	HP	Aft Panel at Spar Interface	Rosette
SG11-1900-HP-AP-90	1.9	HP	Aft Panel at Spar Interface	Rosette
SG12-2500-HP-AP-0	2.5	HP	Aft Panel at Spar Interface	Rosette
SG13-2500-HP-AP-45	2.5	HP	Aft Panel at Spar Interface	Rosette
SG14-2500-HP-AP-90	2.5	HP	Aft Panel at Spar Interface	Rosette
SG15-2750-HP-TE	2.75	HP	TE	Uni
SG16-2750-TE	2.75		TE	Uni
SG17-2900-LP-SC-0	2.9	LP	Center of Sparcap	Rosette
SG18-2900-LP-SC-45	2.9	LP	Center of Sparcap	Rosette
SG19-2900-LP-SC-90	2.9	LP	Center of Sparcap	Rosette
SG20-2900-LP-FP-0	2.9	LP	Mid Fore Panel	Rosette
SG21-2900-LP-FP-45	2.9	LP	Mid Fore Panel	Rosette
SG22-2900-LP-FP-90	2.9	LP	Mid Fore Panel	Rosette
SG23-3250-HP-SC	3.25	HP	Center of Sparcap	Uni
SG24-3250-LP-SC	3.25	LP	Center of Sparcap	Uni
SG25-3250-LE	3.25		LE	Uni
SG26-3250-TE	3.25		TE	Uni
SG27-3250-LP-TE	3.25	LP	TE	Uni
SG28-6300-LP-AP-0	6.3	LP	Mid Aft Panel	Rosette

Name	Span	Surface	Chord Position	Type
SG29-6300-LP-AP-45	6.3	LP	Mid Aft Panel	Rosette
SG30-6300-LP-AP-90	6.3	LP	Mid Aft Panel	Rosette
SG31-6300-HP-LE-0	6.3	HP	LE	Rosette
SG32-6300-HP-LE-45	6.3	HP	LE	Rosette
SG33-6300-HP-LE-90	6.3	HP	LE	Rosette
SG34-6500-HP-SC	6.5	HP	Center of Sparcap	Uni
SG35-6500-LP-SC	6.5	LP	Center of Sparcap	Uni
SG36-6500-LE	6.5		LE	Uni
SG37-6500-TE	6.5		TE	Uni
SG38-9000-LP-AP-0	9.0	LP	Mid Aft Panel	Rosette
SG39-9000-LP-AP-45	9.0	LP	Mid Aft Panel	Rosette
SG40-9000-LP-AP-90	9.0	LP	Mid Aft Panel	Rosette
SG41-9750-HP-SC	9.75	HP	Center of Sparcap	Uni
SG42-9750-LP-SC	9.75	LP	Center of Sparcap	Uni
SG43-9750-LE	9.75		LE	Uni
SG44-9750-TE	9.75		TE	Uni
SG45-3250-HP-TE	3.25	HP	Center of Sparcap	Uni
SG46-2750-LP-TE	2.75	LP	Center of Sparcap	Uni

9.4-Temperature

Ambient temperature and relative humidity will be measured near the blade root.

9.5- Data Acquisition

The Ethercat Data Acquisition System (EDAS) will be employed for this test which is based on National Instruments (NI) Ethercat PXI technology combined with custom NREL developed LabVIEW coded software. All channels will be scanned at 1000 Hz and time series data will be recorded at 100 Hz in 'fast' data files and 10 Hz in 'slow' data files.

9.6-Photos and Videos

Still photographs will be taken throughout the test program from various angles. Video will be recorded from the root to the tip, and a second camera viewing tip to root.

10-STATIC TESTING

10.1-Test Matrix

Loads will be applied in 25% load levels starting at 50% load to the 100% load. Load application from tare to target load will take approximately 20 seconds. Each load plateau will be held for at least 30 seconds, and then gradually released back to tare before moving to the next load level. Strain and displacement from each applied load level will be evaluated prior to proceeding to the next load level. Figure 10.1 provides a schematic of the load profile.

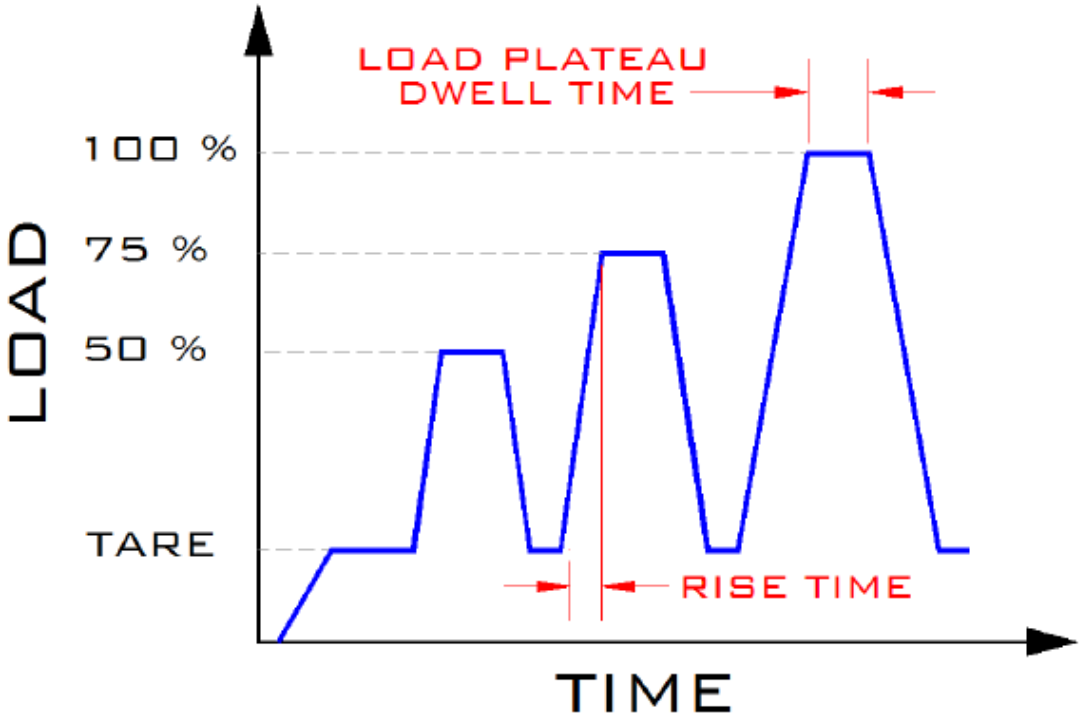

Figure 10.1 – Load Introduction Profile

Table 10.1 provides the target applied external loads for each load level for the minimum flap test. Tables 10.2 and 10.3 provide the same information for the maximum and minimum edge load cases.

Table 10.1 – Test Matrix Load Levels for Minimum Flap (Epoxy Blade)

Applied Load Level (% of Maximum Target Load)	Applied Test Root Bending Moment [kN-m]	External Load at 4.6 m [kN]	External Load at 7.55 m [kN]	External Load at 10.85 m [kN]
50	97.0	2.07	1.59	1.41
75	148.8	6.52	3.42	3.03
100	193.2	8.90	5.37	4.75

Table 10.2 – Test Matrix Load Levels for Maximum Edge (Epoxy Blade)

Applied Load Level (% of Maximum Target Load)	Applied Test Root Bending Moment [kN-m]	External Load at 4.6 m [kN]	External Load at 7.55 m [kN]	External Load at 10.85 m [kN]
50	82.1	2.07	0.63	0.71
75	118.9	4.45	1.93	2.18
100	163.2	8.90	3.13	3.54

Table 10.3 – Test Matrix Load Levels for Minimum Edge (Epoxy Blade)

Applied Load Level (% of Maximum Target Load)	Applied Test Root Bending Moment [kN-m]	External Load at 4.6 m [kN]	External Load at 7.55 m [kN]	External Load at 10.85 m [kN]
50	84.0	0	0.85	1.59
75	130.3	4.45	1.78	3.33
100	170.1	6.52	2.87	5.36

10.2-Test Procedure

1. Measure weight of all hardware attached to blade
2. Secure blade to test stand and attach load introduction hardware

3. Ensure load cell/crane is directly above pull point
4. Ensure function and readout of data acquisition and sensors
5. Ensure access restriction of highbay
6. Apply negative flap tare load with overhead crane for each strain gage location. Zero strain at each load.
7. Start Video
8. Start DAQ
9. 50% load
    a. Test operator load blade to 50% load
    b. Hold load for 30-seconds
    c. Return to tare
    d. Review data as necessary
    e. Maintain tare load for 30-seconds
10. 75% load
    a. Test operator load blade to 75% load
    b. Hold load for 30-seconds
    c. Return to tare
    d. Review data as necessary
    e. Maintain tare load for 30-seconds
11. 100% load
    a. Test operator load blade to 100% load
    b. Hold load for 30-seconds
    c. Return to tare
    d. Review data as necessary
    e. Maintain tare load for 30-seconds
12. Verify data collection and backup data

11-REPORTING

NREL will provide a test report after the completion of testing, per Milestone 4.2.6.7.

12-EXCEPTIONS FROM STANDARD PRACTICE

- None.

13-UNRESOLVED ISSUES

- None

14-REFERENCES

1. IEC 61400-23, Full-scale Structural Testing of Rotor Blades, 2014.
2. Load Document. Received June 6, 2017 from Joshua Paquette. File: 'NRT Test Loads.xlsx'.
3. NREL Safe Operating Procedure (SOP) #515009412 – Conducting Structural Tests at the NWTC

16. APPENDIX E
Fatigue Test Plan for Flapwise Loading to a 13-m Elium® Composite Blade

This Appendix contains the flapwise fatigue loading test plan for the 13-meter Elium® composite wind turbine blade. The numbering for pages, tables, figures and references are exclusive to this Appendix and are not integrated into the main body and table of contents of this final report.

NREL
NATIONAL RENEWABLE ENERGY LABORATORY

FATIGUE TEST PLAN

LABORATORY FLAPWISE FATIGUE TESTING OF THE THERMOPLASTIC 13-METER WIND TURBINE BLADE

Conducted by

National Renewable Energy Laboratory
National Wind Technology Center
15013 Denver West Parkway
Golden, CO 80401

Conducted for

IACMI 4.2 Project Team

February 28, 2019

Approval by: _____ Feb 28, 2019
David Snowberg Date
IACMI 4.2 Project Manager

Approval by: _____ FEB 28, 2019
Scott Hughes Date
NREL Test Engineer

Approval by: _____ Feb 28, 2019
Ryan Beach Date
NREL Test Engineer

Table of Contents

List of Figures

List of Tables

Document History and Document Management

Table 1. Document Revision History

Revision	Date (yy/mm/dd)	Description	Author(s)	Communication of Change
RevA	190227	Draft for internal review	R. Beach, D. Snowberg	NREL
RevB	190228	updated plan per NREL team input	R. Beach D. Snowberg	DOE, IACMI 4.2, and NREL

Nomenclature or List of Acronyms & Initialisms

AE	acoustic emission
DOE	Department of Energy
EDAS	EtherCAT Data Acquisition System
EHS&Q	NREL's Environment, Safety, Health & Quality office
HP	high-pressure blade surface
HPU	hydraulic power unit
IACMI	Institute for Advanced Composite Manufacturing Innovation
IEC	International Electrotechnical Commission
LE	leading edge of airfoil section
LP	low-pressure blade surface

MTS	manufacturer of actuators and hydraulic controller
NA	not applicable
NI	National Instruments
NREL	National Renewable Energy Laboratory
NRT	National Rotor Testbed
NWTC	National Wind Technology Center
POP	period of performance
RR	readiness review
RV	readiness verification
SDI	Silicon Designs Inc.
SNL	Sandia National Laboratory
SOP	safe operating procedure
SWiFT	Sandia Scaled Wind Farm Technology facility
TBD	to be determined
TE	trailing edge of airfoil section
TEDVP	test equipment design verification process
TP	thermoplastic
UREX	Universal Resonant EXcitation system

1 Contact Information

Table 2. Contact Information

NAME	TITLE	EMAIL	PHONE / CELL
NREL			
Dave Simms	NWTC Research Operations Director	david.simms@nrel.gov	303-384-6942
Scott Hughes	Test Engineer	scott.hughes@nrel.gov	303-384-7054 720-234-1923
Ryan Beach	Engineer	ryan.beach@nrel.gov	303-384-6949
Dave Snowberg	Engineer	david.snowberg@nrel.gov	303-384-6920
Robynne Murray	Engineer	Robynne.murray@nrel.gov	303-384-7191
Derek Berry	IACMI Wind TA Director	Derek.berry@nrel.gov	303-384-7372
David Barnes	Technician	David.barnes@nrel.gov	303-275-4796
Mike Jenks	Technician	mike.jenks@nrel.gov	303-384-6994
Bill Gage	Technician	bill.gage@nrel.gov	303-384-7071
Troy Boro	Technician	troy.boro@nrel.gov	303-384-7065
Sara Fairchild	Technician	sara.fairchild@nrel.gov	303-384-7114
Jim Ringwall	EHS&Q POC	jim.ringwall@nrel.gov	303-384-7256 303-503-8889
Don Young	EHS&Q POC	don.young@nrel.gov	303-384-7144 303-598-2821

2 Disclaimer

This test plan shall not be reproduced, except in full, without the written approval of NREL.

3 Background

A 13m thermoplastic (TP) blade was produced at NREL's CoMET facility using the same blade skin molds that were previously used to produce epoxy blades for SNL's SWiFT facility. New shear web molds were produced at NREL to replicate the molds used for the previously tested epoxy blades.

A series of structural validation tests including property testing, static strength testing, and fatigue testing will be performed at the National Renewable Energy Laboratory (NREL). The first test performed at NREL will be to validate that the blade has enough strength to react a maximum extreme static load in the flapwise direction. Static load testing in the maximum flapwise, minimum flapwise, maximum edgewise, and minimum edgewise direction will be completed under separate test plans [1,2].

4 Scope

Work is being performed through the IACMI project 4.2 project agreement [3].

This test plan covers the fatigue testing for the 13m thermoplastic blade (test article). The test purpose is to observe test article response from test load inputs. Information stated in this test plan supersedes other test specification documents.

NREL will use existing hydraulic equipment and existing facilities to apply a fatigue test load to the test article.

This test is not for certification purposes. The NREL Quality Management system and guidance from the IEC 61400-23 blade test standard will be used where appropriate [4].

During active program work, files will be kept in the following location on the NREL certification server:

> *Y:\Wind\Confidential\Projects\Cert\A-C\Certification Projects\Blade Testing\2-Current Tests\2019 thermoplastic 13m blade*

A log book will be maintained for the test.

5 Objectives

The objectives of the structural test are as to:

1. Apply a laboratory flapwise fatigue test load to the test article.
2. Measure strains and accelerations resulting from the applied test loads.
3. Compare results from test article to previously tested epoxy blade.

6 Test Article Description

The 13m TP blade was made from materials that include Johns Manville fiberglass, balsa wood, Bostik SAF30 90 CP adhesive, and Arkema's Elium 188 resin. The 13m TP blade was designed with a fiberglass layup to be structurally equivalent to the previously tested epoxy blade. The blade root bolt pattern is (30) M20 bolts on a 508-mm bolt pattern. The nominal maximum chord is 1.473 m. The blade includes pre-bend in the flapwise, upwind direction.

The blade was fabricated by NREL at the CoMET facility at the NWTC. This blade production was for Milestone 4.2.6.5 from the IACM 4.2 project.

The test article will be subjected to maximum flapwise, minimum flapwise, maximum edgewise, and minimum edgewise bending test loads—before the commencement of this fatigue test.

In addition to the previously subjected static loading, the blade weight, center of gravity, and modal properties will also be measured. Blade weight and CG will be measured using a 2-point (or single point) lift, and modal parameters will be measured using free-decay and impact methods. Measured blade properties for the epoxy blade can be found in Table 3 and Table 4; these will be updated for the thermoplastic test article.

Table 3. Blade Weight and CG (Epoxy Blade)

Blade Property	Measured Value	Note
Weight (kN)	5.08	
Center of Gravity (m)	3.630	Measured from root face of blade

Table 4. Modal Parameters (Epoxy Blade)

Mode Shape	Frequency [Hz]	Damping [% Critical]
1st Flat	2.19	0.12
1st Edge	4.92	0.2

Mode Shape	Frequency [Hz]	Damping [% Critical]
2nd Flat	7.06	0.14
3rd Flat	14.5	0.15
2nd Edge	18.1	0.23
Flap / Torsion	24	0.2
1st Torsion	26.6	0.18
Flap / Edge / Torsion	35.7	
3rd Edge	42	

Figure 1. Blade test article and test setup (epoxy blade shown)

7 Loads

The flapwise target test load distribution and number of test cycles from SNL are shown in 5 [5]. Loads provided by SNL are factored loads, applying a total test load factor of 1.328 to the fatigue equivalent loads. The mean moment is from the combination of the estimated distributed epoxy blade weight and the measured weight of test equipment attached to the blade—the mean moment will be adjusted for the actual property measurements from the thermoplastic test article.

The target number of test cycles is 1,000,000. The test load input will be controlled to maintain target loads at a station near the root.

Table 5. Flapwise Fatigue Target Test Loads

Distance from root plane z (m)	Mean moment (epoxy blade) M_{mean} (kN-m)	Moment Amplitude Mamp (kN-m)	r-ratio (min / max)
0	100.39	83.24	0.09
1.3	74.81	61.17	0.10
2.86	45.46	45.55	0.00
3.9	26.58	31.11	-0.08
5.46	10.62	19.32	-0.29
7.02	4.87	11.15	-0.39
8.06	2.48	7.50	-0.50
9.62	1.01	2.84	-0.48
11.18	0.13	1.65	-0.85
12.22	0.02	1.97	-0.98

8 Test Setup—Mechanical

8.1 Quality and Safe Operating Procedures

The test article and test equipment will be regularly inspected. A procedure and checklist will be developed for this purpose.

Testing will be conducted in accordance with NREL Safe Operating Procedure (SOP) #515009412 – Conducting Structural Tests at the NWTC [6], and this test plan.

All critical or specialized crane or transportation lifts and operations will be covered by lift permits as deemed necessary by the test manager and EHS&Q point of contact.

A job walk will be conducted prior to starting this test. This job walk will cover unique aspects of the test setup and illustrate facility restrictions.

All NREL staff and visiting professionals with onsite activities shall comply with the SOP and RV/RR document. Visiting professional may be required to participate in an EHS&Q orientation.

Safe Work Permits and Lift Permits will be issued by NREL EHS&Q where work is out of the scope of the structural testing SOP [6].

Equipment used for this test is provided with nameplate ratings from manufacturers or has been designed and reviewed through the NREL Test Equipment Design Verification Process (TEDVP).

8.2 Facility Configuration

All testing is planned for the STL fatigue test stand (5.4 MN-m rated) located on the west side of the Structural Testing Laboratory (STL) highbay at the NWTC in Boulder, CO. The test stand will be tilted back to 3 degrees to allow clearance during fatigue test operation.

8.3 Blade Pre-twist orientation

The 12.96m station of the blade will be inclined to 5.91 degrees as indicated in Figure 2. The pre-twist orientation is the same as was used for the maximum flapwise static test [1].

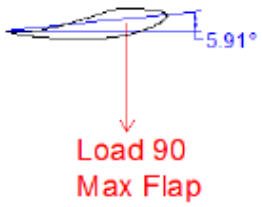

Figure 2. As mounted inclination of the blade at the 12.96m station

8.4 Adapter Plate and Root Fixturing

The blade will mount to the test stand through an adapter plate. The adapter plate is 3" (~75-mm) thick steel. The blade bolts to the adapter plate through the (30) root bolts. The blade bolt pattern is milled into the blade such that two bolts are at top-dead-center relative to the laboratory frame of reference.

A 1" (~25mm) thick steel spacer ring will be placed between the bolt heads and the adapter plate to match the grip length of the SWiFT turbine pitch bearing and crank plate. This will allow the same length root bolts to be used during laboratory fatigue testing and in-field turbine operation.

The adapter plate assembly is secured to the test stand using (24), 18-in length, 1-8 UNC grade B7 all threads equally spaced on a 30-in bolt circle diameter.

Section 8.7 of this test plan provides torque specifications.

Figure 3. Adapter plate assembly

8.5 Fatigue Load Input (UREX)

The fatigue load input will result from resonant excitation of the blade using a hydraulically controlled Universal Resonant EXcitation (UREX) test system. The UREX connects directly to the blade saddle with no other facility interface for load reaction. The oscillating mass from each UREX ranges from 70 kg to approximately 200 kg, in approximately 5 kg increments. One UREX is planned for this test on the south side (LE) of the 4.6-m saddle for flapwise loading with an oscillating mass of 170 kg; this setup repeats what was previously completed to the epoxy blade.

Figure 4. UREX test frame

8.6 Blade Saddles

A load introduction saddle at the 4.6-m station is planned for this test. The saddle is composed of a wood insert with rubber sheets contacting the blade and structural steel assembly around the wood insert. The two UREXs will connect to this saddle for flapwise loading. Additional ballast load saddles at the 7.55-m and 10.85-m stations are also planned. Table 6 contains the saddle span-wise location, mass, and span-wise thickness for the baseline test system. Saddle mass may be adjusted during testing to better match the target load distribution. Saddle mass includes the UREXs configuration with 225kg of oscillating mass. The additional mass of hydraulic hoses and cables will be noted and included in the final report.

Table 6. Blade Test Article Saddles

Saddle station (w.r.t) blade station (m)	Load configuration	Saddle Mass (kg)	Span-wise Saddle thickness (mm)
4.60	Load input	1352	133
7.55	Ballast	204	133
10.85	Ballast	35	133

With this configuration, it is estimated that the blade first flap natural frequency will be 1.48Hz, have a static tip deflection (blade and saddle weight only) of 0.308m and a dynamic tip displacement of ±0.52m.

8.7 Fastener Torque

See Table 7 for fastener torque specifications for this test.

The blade is secured to the adapter plate using (30) 180 mm, M20 Class 10.9 bolts equally spaced on a 508 mm bolt circle diameter. Blade bolts will be torqued to 305 N-m, using TS-70 Moly Paste. TS-70 will be applied to the bolt thread and bolt head to washer interface. The bolt torque sequence includes:

(1) hand tighten all bolts
(2) torque bolts to 150 N-m in a star pattern
(3) torque bolts to 305 N-m in a star pattern
(4) torque bolts to 305 N-m in a circular pattern

The adapter plate is secured to the test stand using (24), 18 in length, 1-8 UNC grade B7 all threads equally spaced on a 30-in bolt circle diameter. Adapter plate to test stand bolts will be torqued to 450 ft-lb (dry threads).

Table 7. Fastener Torque

Location	Fastener	Torque (all with TS-70 Moly Paste, unless stated otherwise)
Blade root bolts	M20-2.5, Class 10.9	286 N*m (lubricated)
Adapter plate to test stand	1-8 threaded rod, B7	610 N*m (lubricated)
4.60-m saddle	Vertical wood form compression, ½-13, B7	4 @ 27 N*m (dry)
7.55-m saddle	Vertical wood form compression, ½-13, B7	4 @ 27 N*M (dry)
10.85-m saddle	Vertical wood form compression, ½-13, B7	4 @ 27 N*M (dry)
UREX	Various	See UREX specification
Moment-calibration system	Various	See Verification Checklist from TEDVP

9 Test Setup—Instrumentation

The actual instrumentation used during this test may change with agreement from the test plan approvers. These changes will consider time/budget constraints balanced with value of each measurement.

9.1 Strain Gages

Table 9 contains the strain gages planned for this test. This set of strain gages is the same as was used for static testing [1]. Strain gage failure is common during a fatigue test. Testing may

continue with broken gages if the test engineer determines there are enough functional gages to adequately derive the applied test load distribution. Gages may be replaced during this test, but this is not explicitly required.

Table 8. Strain Gage Specifications

Strain Gage No:	Mfg.	Type:	Gage Factor:	Gage Type*
WK-06-250BG-350	Vishay Micro-Measurements	Uni-axial	2.03	1
WK-06-250RA-350	Vishay Micro-Measurements	Rosette	2.02	2

* Cross-reference between

Table 8 & Table 9

Table 9. Strain Gage Names and Locations

EDAS Channel Name	Span Location (m)	Surface	Chord Position	Gage Type*
SG01-200-LP0	0.2	LP	0°	1
SG02-200-LP45	0.2	LP	45°	1
SG03-200-LP90	0.2	LP	90°	1
SG04-200-LP135	0.2	LP	135°	1
SG05-200-HP180	0.2	HP	180°	1
SG06-200-HP225	0.2	HP	225°	1
SG07-200-HP270	0.2	HP	270°	1
SG08-200-HP315	0.2	HP	315°	1
SG09-1900-HP-AP-0	1.9	HP	Aft Panel at Spar Interface	2
SG10-1900-HP-AP-45	1.9	HP	Aft Panel at Spar Interface	2
SG11-1900-HP-AP-90	1.9	HP	Aft Panel at Spar Interface	2
SG12-2500-HP-AP-0	2.5	HP	Aft Panel at Spar Interface	2
SG13-2500-HP-AP-45	2.5	HP	Aft Panel at Spar Interface	2
SG14-2500-HP-AP-90	2.5	HP	Aft Panel at Spar Interface	2
SG15-2750-HP-TE	2.75	HP	TE	1
SG16-2750-TE	2.75		TE	1
SG17-2900-LP-SC-0	2.9	LP	Center of Sparcap	2
SG18-2900-LP-SC-45	2.9	LP	Center of Sparcap	2
SG19-2900-LP-SC-90	2.9	LP	Center of Sparcap	2
SG20-2900-LP-FP-0	2.9	LP	Mid Fore Panel	2

EDAS Channel Name	Span Location (m)	Surface	Chord Position	Gage Type*
SG21-2900-LP-FP-45	2.9	LP	Mid Fore Panel	2
SG22-2900-LP-FP-90	2.9	LP	Mid Fore Panel	2
SG23-3250-HP-SC	3.25	HP	Center of Sparcap	1
SG24-3250-LP-SC	3.25	LP	Center of Sparcap	1
SG25-3250-LE	3.25		LE	1
SG26-3250-TE	3.25		TE	1
SG27-3250-LP-TE	3.25	LP	TE	1
SG28-6300-LP-AP-0	6.3	LP	Mid Aft Panel	2
SG29-6300-LP-AP-45	6.3	LP	Mid Aft Panel	2
SG30-6300-LP-AP-90	6.3	LP	Mid Aft Panel	2
SG31-6300-HP-LE-0	6.3	HP	LE	2
SG32-6300-HP-LE-45	6.3	HP	LE	2
SG33-6300-HP-LE-90	6.3	HP	LE	2
SG34-6500-HP-SC	6.5	HP	Center of Sparcap	1
SG35-6500-LP-SC	6.5	LP	Center of Sparcap	1
SG36-6500-LE	6.5		LE	1
SG37-6500-TE	6.5		TE	1
SG38-9000-LP-AP-0	9.0	LP	Mid Aft Panel	2
SG39-9000-LP-AP-45	9.0	LP	Mid Aft Panel	2
SG40-9000-LP-AP-90	9.0	LP	Mid Aft Panel	2
SG41-9750-HP-SC	9.75	HP	Center of Sparcap	1
SG42-9750-LP-SC	9.75	LP	Center of Sparcap	1
SG43-9750-LE	9.75		LE	1
SG44-9750-TE	9.75		TE	1
SG45-3250-HP-TE	3.25	HP	Center of Sparcap	1
SG46-2750-LP-TE	2.75	LP	Center of Sparcap	1

9.2 Transducer list (non-strain gage)

Table 10 contains the non-strain gage transducers for this test. Equivalent transducers or modules may be used in place of those shown in this table. Final channel names may deviate from that

shown in this table. There may be periods during the test when measurements from some of these transducers are not recorded during normal test operation.

The NREL acoustic emission (AE) measurement system may be used at the root area; this may be added to the test setup after the test begins. The AE system is not required for this test.

Table 10. Non-Strain Gage Transducers

EDAS Channel Name	Transducer	Manufacturer	Model	Position	Required NI Module
Accel1Flap	Accelerometer	SDI	2470-002	Root HP	9239
Accel1LeadLag	Accelerometer	SDI	2470-002	Root HP	9239
Accel2Flap	Accelerometer	SDI	2460-005	4.6 m UREX N	9239
Accel2LeadLag	Accelerometer	SDI	2460-005	4.6 m UREX N	9239
Accel3Flap	Accelerometer	SDI	2470-005	4.6 m UREX S	9239
Accel3LeadLag	Accelerometer	SDI	2470-005	4.6 m UREX S	9239
Accel4Flap	Accelerometer	SDI	2460-005	4.7 m TE	9239
Accel4LeadLag	Accelerometer	SDI	2460-005	4.7 m TE	9239
Accel5Flap	Accelerometer	SDI	2470-005	4.7 m LE	9239
Accel5LeadLag	Accelerometer	SDI	2470-005	4.7 m LE	9239
Accel6Flap	Accelerometer	SDI	2460-010	9.75 m TE	9239
Accel6LeadLag	Accelerometer	SDI	2460-010	9.75 m TE	9239
Accel7Flap	Accelerometer	SDI	2470-005	9.75 m LE	9239
Accel7LeadLag	Accelerometer	SDI	2470-005	9.75 m LE	9239
Accel8Flap	Accelerometer	SDI	2470-010	Tip	9239
Accel8LeadLag	Accelerometer	SDI	2470-010	Tip	9239
NorthUREX	Linear position	MTS	LVDT	UREX 4.6-m north saddle flap LVDT	9239
SouthUREX	Linear position	MTS	LVDT	UREX 4.6-m south saddle flap LVDT	9239
Temperature	Temperature	Omega	HX93BV2	Root	9237
Humidity	Humidity	Omega	HX93BV2	Root	9237
LDT	Laser Distance Transducer	Baluff	BOD 63M-LA04-S115	TBD	9239
String Pot 4m	String Potentiometer	UniMeasure	HX-PA-30	4m spar cap	9239
String Pot 7m	String Potentiometer	UniMeasure	PA-80	7m spar cap	9239
String Pot 11.25m	String Potentiometer	UniMeasure	HX-PA-150	11.25m spar cap	9239
TT LC Outboard	Load Cell	Transducer	10-kip	Varies	9237
MTS LC Inboard	Load Cell	Transducer	6.61E+00	Varies	9237

9.3 Data Acquisition

The EtherCAT Data Acquisition System (EDAS) will be used for this test. This system uses National Instruments PXI hardware technology and custom NREL developed LabVIEW software. All transducer signals are wired to one of the NI-9144 chassis. The NI-9144 chassis are connected in series with the PXI chassis via Ethernet cables.

All signals will be recorded throughout the fatigue test as peak-valley data. Peak-valley data collection is defined as the recording of the maximum and minimum values of each channel during each cycle. Short snapshots of time series data will be recorded a few times during this test. Time series data at a sample rate of at least 100 Hz may be substituted for the real-time peak-valley data collection.

9.4 Photos and Video

Digital photos and video will be taken throughout the test project—including test setup and execution.

9.5 Hydraulic controller

The MTS Flextest 60 hydraulic controller located in the STL control room will be used for this test. The UREX systems are controlled using the Flextest 60. The MTS resonant tracking software will be used to maintain the fatigue load input from the UREXs at the flapwise resonant frequency of the test article.

9.6 Test Interlock Plan

Table 11 contains the plan for automatic test interlocks. These test interlocks are designed to automatically stop the test if the signal goes outside the preset range. The set point values for these interlock signals will be tuned throughout the test, as necessary. Additional test interlocks and/or changes to this interlock plan may be implemented during this test project.

A manual E-stop button will be positioned near the MTS hydraulic controller station.

Table 11. Automatic Test Interlocks

Signal	Required for Attended Testing?	Required for Unattended Testing?	Description
UREX frequency	Yes	Yes	Stop test if UREX frequency goes above or below expected frequency range—configured in MTS controller. Limits TBD during test tuning.
UREX displacement limit	Yes	Yes	Stop test if UREX displacement goes outside expected range—configured in MTS controller. Actual limits will be set during test tuning. This protects the UREX from going outside its available range and it protects the test article by limiting the available stroke for load input.

Signal	Required for Attended Testing?	Required for Unattended Testing?	Description
Strain (load) limit	Yes	Yes	Stop test if strain signal (for load control) at MTS controller goes outside of its expected value. This is the single signal used for test load control. The strain signal originates at the EDAS and is sent to the MTS controller via the 9263 module, or equivalent.
Strain peak limits	Yes	Yes	Stop test if a strain gage peak-to-peak limit goes outside its expected range. This interlock system is configured in the EDAS and outputted to the MTS controller via the 9401 module, or equivalent.
Accelerometer (tip)	No	Yes	Stop test if accelerometer signal at test article tip goes outside expected value.
Accelerometer (UREX mass)	No	Yes	Stop test if accelerometer signal on UREX moving mass goes outside expected value (one accelerometer per UREX).
Watchdog	No	Yes	Stop test if some EDAS functionality stops. This feature configured in EDAS and sent to MTS controller via the 9401 module, or equivalent.
HPU hydraulic oil level & temperature	No	Yes	Stop test if HPU oil level drops below expected reservoir level or oil temperature exceeds limit.
Test article displacement limit	No	Yes	Stop test if test article displacement during test goes outside of expected range (downwind direction). This system is configured with a string potentiometer tripwire (or laser curtain) configured below the test apparatus.
Acoustic emission	No	No	Stop test if AE microphone measures signal outside TBD expected range.

10 Test Procedure

1. Perform stiffness check (i.e. determine strain gage-to-moment sensitivity) by pulling on the blade with an in-line load cell, while measuring blade deflection. The saddle on the 10.85-m station will be used for the flapwise load input. See Section 10.1 for details.
2. Tune fatigue test setup to reach the fatigue test load distribution. The tuning will be completed to the satisfaction of NREL.
3. Daily—assuming test cycles added since previous day (frequency may change at the discretion of NREL):
    - NREL will complete test setup inspection.

- Test operation according to Table 5 loads.

4. At least one stiffness check and blade inspection during flap loading.
5. Test will conclude after the Table 5 loads are completed or a blade failure occurs that makes it impractical or unsafe to continue testing, as determined by NREL.

10.1 Static Calibration Pulls and Stiffness Checks

A single-point static calibration pull will be conducted in the negative flapwise direction to calibrate the strain gages by deriving the strain versus applied bending moment relationship. These calibrations will be used to determine the applied fatigue loads for resonant testing. The target static calibration load will be 4 kN and will be applied at the 10.85-m saddle, which will apply a root bending moment of 43-kN-m, which is approximately 25% of the target root fatigue test load. This static calibration pull will be conducted prior to the beginning of the start of the fatigue test.

The procedure for the flapwise static calibration pull is as follows:

1. Prepare rigging to load blade at the 10.85-m station.
2. Attach load cell to saddle.
3. Attach string pot to 11.25m station.
4. Start data collection at 10-Hz.
5. Gradually apply a load of 4-kN using the overhead bridge crane, holding for 30 seconds at load, and then slowly release back to zero.
6. Hold at zero for at least 30 seconds.
7. Stop data collection.
8. Remove load cell, string pot, and rigging.
9. Calculate strain gage sensitivities (moment vs strain).

Stiffness checks will be performed in the flapwise direction periodically. The static calibration pulls may need to be repeated if non-linearities are observed in the data, or when strain gages have been replaced.

11 Analysis and Reporting

NREL will provide a report covering test setup, test execution, and summary data. All raw data, photos, and video will be provided, as requested.

12 Exceptions from Standard Practice

- None

13 Unresolved Issues

- none

14 References

1. NREL Static Test Plan. Laboratory Maximum Flapwise Static Testing of the Thermoplastic 13-meter Wind Turbine Blade. February 28, 2019.
2. NREL Static Test Plan. Laboratory Minimum Flapwise, and Maximum and Minimum Edgewise, Static Testing of the Thermoplastic 13-meter Wind Turbine Blade. February 28, 2019.
3. IACMI Project Agreement Number 4, PA16-0349-4.2-01.
4. IEC 61400-23, Full-scale structural testing of rotor blades, 2014
5. Load Document. Received June 6, 2017 from Joshua Paquette. File: "NRT Test Loads.xlsx".
6. Safe Operating Procedure, SOP-515009412, Conducting Structural Tests at the National Wind Technology Center.

17. APPENDIX F
Test Report for Static and Fatigue Loading to a 13-m Elium® Composite Blade

This Appendix contains the report from the static and fatigue test loading to the 13-meter Elium® composite wind turbine blade. The numbering for pages, tables, figures and references are exclusive to this Appendix and are not integrated into the main body and table of contents of this final report.

NREL	Issued by: National Renewable Energy Laboratory National Wind Technology Center 15013 Denver West Parkway Golden, CO 80401

Test type:		Approved Use:		
Structural Static	☒	Accredited Report	☒	A2LA ACCREDITED Acoustics and Vibration CERT #1239.01
Structural Fatigue	☒	Internal Only	☐	
Structural Property	☐	Other:_____	☐	
Other:	☐			

Test Identifier: 13m thermoplastic	Test Report	Date: November 22, 2019

Report Title:
LABORATORY WIND TURBINE BLADE STATIC AND FATIGUE TESTING OF THE IACMI 4.2 13m THERMOPLASTIC WIND TURBINE BLADE

Test Client:	Test Article(s):
IACMI Project 4.2 Team 2360 Cherahala Blvd. Knoxville, TN 37932	13m THERMOPLASTIC WIND BLADE

Statements and Declarations:

This Test Report may not be reproduced, except in full, without written approval of NREL

Prepared by:	Ryan Beach	Engineer	
Checked by:	Derek Berry	Engineer	
Reviewed by:	Scott Hughes	Engineer	
Approved by:	David Snowberg	QA Technical Manager	

Table of Contents

List of Figures

List of Tables

ACROYNMS and INITIALISMS

Phrase	Abb.	Phrase	Abb.
National Wind Technology Center	NWTC	Department of Energy	DOE
National Renewable Energy Laboratory	NREL	Institute for Advanced Composites Manufacturing and Innovation	IACMI
Ethercat Data Acquisition System	EDAS	Center of Gravity	CG
National Instruments	NI	Damage Equivalent Load	DEL
Trailing Edge	TE	High Pressure side	HP
Low Pressure side	LP	Leading Edge	LE

Document Management

Table 1. Document Revision History

Revision Date (yymmdd)	Description	Author(s)	Communication of Change
191122	Static and fatigue test report	R. Beach	NREL & IACMI

1 DISCLAIMER

This report was prepared by the National Renewable Energy Laboratory (NREL), operated for the United States Department of Energy (DOE) by the Alliance for Sustainable Energy, LLC (Alliance), as an account of work sponsored by the United States government. The test results documented in this report define the characteristics of the test article as configured and under the conditions tested.

THIS REPORT IS PROVIDED "AS IS" AND NEITHER THE GOVERNMENT, ALLIANCE, NREL NOR ANY OF THEIR EMPLOYEES, MAKES ANY WARRANTY, EXPRESS OR IMPLIED, INCLUDING THE WARRANTIES OF MERCHANTABILITY AND FITNESS FOR A PARTICULAR PURPOSE, OR ASSUMES ANY LEGAL LIABILITY OR RESPONSIBILITY FOR THE ACCURACY, COMPLETENESS, OR USEFULNESS OF ANY SUCH INFORMATION DISCLOSED IN THE REPORT, OR OF ANY APPARATUS, PRODUCT, OR PROCESS DISCLOSED, OR REPRESENTS THAT ITS USE WOULD NOT INFRINGE PRIVATELY OWNED RIGHTS.

Neither Alliance nor the U. S. Government shall be liable for special, consequential or incidental damages. Reference herein to any specific commercial product, process, or service by trade name, trademark, manufacturer, or otherwise does not necessarily constitute or imply its endorsement, recommendation, or favoring by the United States government or any agency thereof. The views and opinions of the authors expressed herein do not necessarily state or reflect those of the United States government or any agency thereof or Alliance. NREL is a DOE Laboratory, and as an adjunct of the United States government, cannot certify wind turbines. The information in this report is limited to NREL's knowledge and understanding as of this date.

NREL is ISO 17025 accredited by the American Association for Laboratory Accreditation (A2LA) (certificate number 1239.02). The results shown in this test report that include the A2LA logo have been determined in accordance with the NREL's terms of accreditation unless stated otherwise in the report. The certificate and scope of accreditation can be found at https://portal.a2la.org/scopepdf/1239-01.pdf.

This report shall not be reproduced, except in full, without the written approval of Alliance or successor operator of NREL. Information supplied by the customer is clearly identified in the report and may affect the validity of the reported results. The reported results relate only to the items tested. NREL seeks feedback from the customer—please send feedback to the NREL personnel listed on the test report.

2 EXECUTIVE SUMMARY

The IACMI 4.2 project fabricated a 13m thermoplastic (TP) wind turbine research blade that was made using Arkema's Elium® thermoplastic resin system. The purpose of this project was to design, manufacture, and structurally validate a thermoplastic wind turbine blade. This blade was manufactured in a mold set that was previously used to produce thermoset (epoxy) blades; one of those blades underwent the same structural validation process as the TP blade [1]. A series of structural validation tests including property testing, static strength testing, and fatigue testing were performed at the National Renewable Energy Laboratory (NREL). This report documents the static and fatigue load cases applied to the 13m TP blade.

Figure 1.– Maximum Edgewise Static Test Setup

Figure 2 – Fatigue Test Setup

3 SCOPE

This test report provides information on the test setup, instrumentation, and load matrix used for laboratory testing of the 13m TP blade. This report covers the following load cases:

- Maximum Flapwise Proof Load
- Minimum Flapwise Proof Load
- Maximum Edgewise Proof Load
- Minimum Edgewise Proof Load
- Flapwise Fatigue Load

4 BACKGROUND

Static and fatigue laboratory test loading was performed on the 13m TP blade. Throughout the program, modal surveying was also performed. Following the static proof loading described in this report a flapwise fatigue test was performed. Table 2 provides information and references on each of the experiments and tests performed on the blade.

Table 2. Sequence of Property and Structural Testing of the 13m TP blade

Event	Date(s)
Blade arrive in STL	Aril 26, 2019
Maximum Flap Static Proof Load	May 15, 2019
Minimum Flap Static Proof Load	May 22, 2019
Minimum Edge Static Proof Load	June 4, 2019
Maximum Edge Static Proof Load	June 11, 2019
Flapwise Fatigue Testing	June 18, 2019 – July 24, 2019

Work was performed through the IACMI 4.2 charge code: AMFG>--10230 - 02.00.02

Testing was performed according to NREL's Quality Assurance Program. NREL is accredited by A2LA for blade testing in accordance with the IEC 61400-23 standard [2], A2LA Certificate Number 1239-01 [3]. Testing operations complied with the NWTC Structural Testing Safe Operating Procedure and were conducted within the scope of the Job Walk [4]. Structural validation testing was performed according to the test plans for static and fatigue testing [5, 6, 7].

5 TEST OBJECTIVE

The objectives of the static proof loading of the blade were to:

1. Validate the blade can sustain the factored extreme flapwise bending and static edgewise bending moments.
2. Measure deflections and strains resulting from the applied test loads.

The objectives of the flapwise fatigue test were to:

1. Apply a cyclic fatigue load to the blade to an equivalent 20-year damage equivalent load
2. Measure strains and accelerations during fatigue loading

6 TEST ARTICLE

The 13m TP blade was a wind turbine blade 13 meters in length, with construction materials that include fiberglass, balsa wood, and Elium® resin. Fabrication was done using the vacuum infusion process. The blade was fabricated in 4 components: high pressure (HP) shell, low pressure (LP) shell, main shearweb, and aft shearweb. Following component fabrication, the blade was assembled using Bostick SAF90 adhesive. After assembly, a final blade trimming and root finishing was performed. The blade root is connected to the turbine rotor, or laboratory test stand, through a bolt pattern consisting of (30) M20 bolts on a 508-mm bolt pattern. The

nominal maximum chord is 1.473 m. The blade includes pre-bend in the flapwise, upwind direction.

The blade was fabricated between December, 2018 and April, 2019 by the IACMI 4.2 team at the NWTC CoMET facility from blade tooling supplied by TPI Composites.

7 TEST SETUP

7.1 Test Location

Testing was performed inside of the highbay of the Structural Testing Laboratory (STL) at NREL's National Wind Technology Center (NWTC), in Boulder, CO.

7.2 Facility Configuration

The blade was cantilevered to the 5.4 MN m test stand in the STL highbay. The 5.4 MN m test stand was secured to t-slot base plates on the west end of the highbay.

The test stand was tilted back at several angles between load cases to allow adequate clearance for test equipment while keeping the blade relatively close to the laboratory floor. Test stand inclination angles are provided in the test plans.

A T-slot base plate blade was mounted to the highbay floor to react the external load applied by the overhead crane for both static load cases and calibration pulls during the fatigue test.

7.3 Blade to Test Stand Connection

The blade was mounted to the test stand through an adapter plate. The adapter plate is a 3" (~75-mm) thick, A-36 steel plate. Bolt torque and mounting configurations we followed according to the test plans.

7.4 Blade Pre-twist Orientation

For all static load cases the test loads were applied vertically with respect to the laboratory. For each load case the blade and attached adapter plate was removed from the test stand, keeping the blade mounted to the adapter plate. The blade was rotated and remounted to the test stand for each load case.

Figure 3 provides the inclination of the 12.96 m airfoil as mounted to the test stand for each static load case. These inclinations were not measured, but assumed to match a previously measured blade of the same geometry.

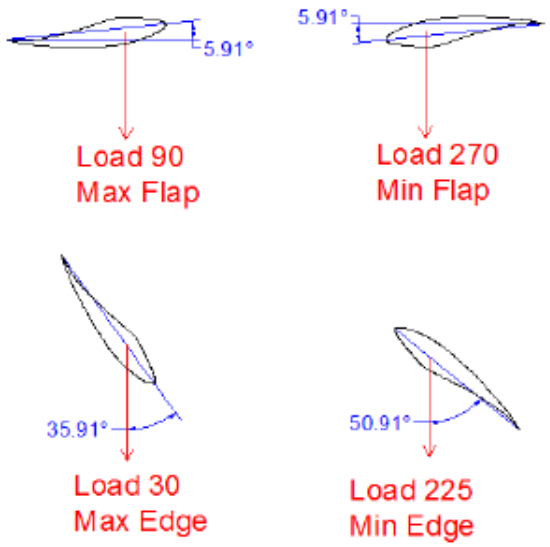

Figure 3 – Blade Mounting Orientation (view is from root to tip)

The mounting orientation for the flapwise fatigue test was the same as the maximum flapwise proof load, with the inclination of the 12.96 m airfoil at 5.91 degrees.

7.5 Load Introduction Method and Hardware

7.5.1 Static Proof Load Cases

The applied test bending moment includes blade self-weight, tare load from the weight of the load saddles, and the external loads applied via the overhead crane and ballast weights.

Three load introduction stations at 4.6 m, 7.55 m and 10.85 m were used to apply external loads. A ballast weight was suspended from the blade at the 4.6 m station. External test loads were applied at the 7.55 m and 10.85 m stations by a test operator controlling the STL's 35-ton overhead bridge crane. A spreader bar was positioned between the 7.55 m and 10.85 m load introduction stations to carry the load applied by the crane to the saddles. Turning blocks mounted to the t-slot base plates reacted and redirected the force from the overhead bridge crane to a force applied to the spreader bar pulling downwards towards the laboratory floor. A 5/8-in Dyneema synthetic rope was used to connect to the spreader bar and run through turning blocks to the overhead crane.

Load saddles were used to apply the external loads to the blade. Load saddles are comprised of wood forms which are shaped to match the airfoil profile; steel frames are built around the wood forms to transfer the test load from the overhead crane to the wood forms. The wood forms are constructed from microlam beams that are cut to the station airfoil profile and fitted to the blade surface with rubber and structural putty, this ensures good surface contact that distributes to point load from the load point across the station chord. The load saddle wood forms were 5.25 in (133.4 mm) thick in the spanwise direction, centered at the nominal blade station. The steel frames are fabricated around the wood forms and secure the load saddle to the blade using four ½-13 grade B7 threaded rods that were torqued to 20 ft-lbf. The torque applied to the threaded rods created a preload of approximately 10.7 kN on the blade. Saddles were designed to apply loads to the blade at the center of a line between the centers of the high-pressure and low-pressure spar caps.

For edge load static cases, chain bridles were attached to the saddles. Unequal length bridles provided the ability to adjust the external load to center through the center of the spar. For all load cases the geometry of the saddle was designed for load to pass through the center of the spar.

7.5.2 Fatigue Testing

For fatigue load input, the UREX exciter was mounted to the 4.6 m saddle. Additional ballast mass was attached to the 4.6 m and 7.55 m saddles. A metal frame of the 10.85 m station saddle that was used for blade mounting was removed for the test. Saddles were ballasted according to the test plan to provide the appropriate mean load and fatigue load amplitude. The amplitude of the applied moment was controlled by adjusting the displacement amplitude of the UREX actuator. Table 3 provides the saddle mass and total oscillating mass as configured and for fatigue test.

Table 3. Fatigue Test Saddle and UREX Weights

Property	Test Configuration
Total 4.6 m Saddle Mass [kg]	1197
Total Oscillating mass [kg]	170
Test Operating Frequency [Hz]	1.62
Total 7.55 m Saddle Mass [kg]	204
Total 10.85 m Saddle Mass [kg]	21

8 INSTRUMENTATION

The channel map for the sensors used during the test is provided in the test plans [5, 6, 7]. Several strain gages listed in the test plans were omitted, See Table 7 for a list of strain gages used and Section 12.1 for a list of omissions. Instrumentation records and calibration certificates are available upon request.

8.1 Load

8.1.1 Static Proof Load

Two load cells were used to measure the applied test loads during static proof load testing. One load cell was positioned at the 4.6 m station and the second load cell was positioned under the spreader beam connecting to the 7.55 m and 10.85 m station saddles. Table 4 provides the specifications for the load cells. Load cells were zeroed without rigging attached beneath the load cell.

Table 4. Static Proof Load Cell Specifications

Type	Manufacturer	Model	Serial
Load Cell 1	MTS	661.20E-03	04859C
Load Cell 2	Transducer Techniques	SW-10K	4718C

8.1.2 Fatigue

A load cell was used for calibration pulls to enable correlation of moment to strain. Table 5 provides specifications for the load cell used for moment calibration during fatigue testing.

Table 5. Fatigue Calibration Pull Load Cell

Type	Manufacturer	Model	Serial
Load Cell	Transducer Techniques	SW-10K	4718C

8.2 Displacement

8.2.1 Static Proof Loading

Three string potentiometers were used to measure blade displacements at the 4 m, 7 m, and 11.25 m stations for static testing. String potentiometers were attached to the blade along the center of the spar cap and ran vertically with respect to the lab to the ground. String pot specifications are provided in Table 6.

Table 6. String Potentiometer Specifications

Location	Manufacturer	Model	Serial
4m Static	UniMeasure	HX-PA-30	48050140
7m Static	UniMeasure	HX-PA-50	32060222
11.25m Static	UniMeasure	HX-PA-80	48050142
Fatigue Calibration Pull – Flap (11.25m)	UniMeasure	HX-PA-80	48050142
Fatigue Calibration Pull – Edge (11.13m)	UniMeasure	HX-PA-50	32060222

8.2.2 *Fatigue Loading*

Calibration pulls were performed periodically during fatigue testing. String pot specifications for these calibration pulls are provided in Table 6.

8.3 Strain

Resistance strain gages were installed on the blade for strain measurement. The single-axis strain gages are Measurements Group WK-06-250BG-350 and the rosettes are Measurements Group WK-06-250RA-350. All the strain gages have a nominal 350 Ohm resistance and were connected in a three-wire configuration. Single-axis strain gages were orientated at 0 degree (parallel with the spanwise axis and perpendicular to the chordwise axis). Rosettes were oriented such that one gage is 0 degrees, one gage is 45 degrees, and one gage is 90 degrees (parallel with the chordwise axis and perpendicular to the spanwise axis). Table 7 provides the location of the strain gages.

Table 7. Strain Gage Locations

Strain Gage Name	Span	Surface	Chord Position	Type
SG01-200-LP0	0.2	LP	0°	Uni
SG02-200-LP45	0.2	LP	45°	Uni
SG03-200-LP90	0.2	LP	90°	Uni
SG04-200-LP135	0.2	LP	135°	Uni
SG05-200-HP180	0.2	HP	180°	Uni
SG06-200-HP225	0.2	HP	225°	Uni
SG07-200-HP270	0.2	HP	270°	Uni
SG08-200-HP315	0.2	HP	315°	Uni
SG12-2500-HP-AP-0	2.5	HP	Aft Panel at Spar Interface	Rosette
SG13-2500-HP-AP-45	2.5	HP	Aft Panel at Spar Interface	Rosette

Strain Gage Name	Span	Surface	Chord Position	Type
SG14-2500-HP-AP-90	2.5	HP	Aft Panel at Spar Interface	Rosette
SG17-2900-LP-SC-0	2.9	LP	Center of Sparcap	Rosette
SG18-2900-LP-SC-45	2.9	LP	Center of Sparcap	Rosette
SG19-2900-LP-SC-90	2.9	LP	Center of Sparcap	Rosette
SG23-3250-HP-SC	3.25	HP	Center of Sparcap	Uni
SG24-3250-LP-SC	3.25	LP	Center of Sparcap	Uni
SG25-3250-LE	3.25	LP	LE	Uni
SG26-3250-TE	3.25	LP	TE	Uni
SG34-6500-HP-SC	6.5	HP	Center of Sparcap	Uni
SG35-6500-LP-SC	6.5	LP	Center of Sparcap	Uni
SG36-6500-LE	6.5	LP	LE	Uni
SG37-6500-TE	6.5	LP	TE	Uni
SG41-9750-HP-SC	9.75	HP	Center of Sparcap	Uni
SG42-9750-LP-SC	9.75	LP	Center of Sparcap	Uni
SG43-9750-LE	9.75	LP	LE	Uni
SG44-9750-TE	9.75	LP	TE	Uni

Table 8 provides specifications for the strain gages. For static testing, strain gage channels were zeroed before application of the first load step of the first static loading, but after all hardware and rigging was installed on the blade (i.e. zeroed with tare weight). For fatigue testing, gages were periodically zeroed at mean load during calibration pulls (blade with load saddles and UREX installed) and at the startup of testing each day.

Table 8. Strain Gage Specifications

Type	Manufacturer	Model
Single element Strain Gage	Vishay	WK-06-250BG-350
Rosette Strain Gage	Vishay	WK-06-250RA-350

8.4 Temperature and Humidity

Ambient temperature and relative humidity were measured during the test. Measurements were taken near the blade root.

Table 9 provides specifications for the temperature and relative humidity sensor.

Table 9. Temperature and Humidity Sensor Specifications

Type	Manufacturer	Model	Serial
Temperature and Humidity	Omega	HX93BV2	1506023

8.5 Accelerometers

Accelerometers were mounted to the blade during fatigue testing. Each accelerometer measured acceleration in both flap and edge (lead-lag) directions. Table 10 provides a list of the accelerometers locations used during fatigue testing. Accelerometers were mounted to the top surface of the blade.

Table 10. Accelerometer Specifications

EDAS Channel Name	Manufacturer	Model	Serial	Position
A-Tip-Flap	SDI	2460-010	1340	Tip
A-Tip-LeadLag	SDI	2460-010	1340	Tip
A-9750LE-Flap	SDI	2460-005	1337	9.75 m LE
A-9750LE-LeadLag	SDI	2460-005	1337	9.75 m LE
A-9750TE-Flap	SDI	2460-010	1341	9.75 m TE
A-9750TE-LeadLag	SDI	2460-010	1341	9.75 m TE
A-4700LE-Flap	SDI	2470-005	3106	4.7 m LE
A-4700LE-LeadLag	SDI	2470-005	3106	4.7 m LE
A-4700TE-Flap	SDI	2470-005	3105	4.7 m TE
A-4700TE-LeadLag	SDI	2470-005	3105	4.7 m TE
A-Root-Flap	SDI	2460-002	1678	Root
A-Root-LeadLag	SDI	2460-002	1678	Root
A-UREX-Flap	SDI	2470-010	3172	4.6 m UREX S

8.6 Data Acquisition

The Ethercat Data Acquisition System (EDAS) was used for static and fatigue testing. The EDAS is based on National Instruments (NI) Ethercat PXI technology combined with custom NREL developed LabVIEW coded software (software version v4.00.00.00). All channels were scanned at 1000 Hz and recorded as time series data at 200 Hz. For fatigue testing, data was also collected as peak/valley data pairs, recording the maximum and minimum values for each cycle of every channel.

8.7 Property Testing Instrumentation

A Chatillon crane scale was used to measure weight for the mass and CG balance. A round poly sling was used to lift the blade. The lift position was adjusted until the root face of the blade was vertical during the mass and CG balance. Table 11 provides specifications on the instruments used for weight and balance measurements.

Table 11. Property Testing Instrumentation Specifications

Type	Manufacturer	Model	Serial
Crane Scale	Chatillon	RDWT-5000	42168
Tape Measure	Lufkin	33'	33257

Accelerometers listed in Table 10 were used for free decay modal testing.

9 APPLIED TEST LOADING

9.1 Static Proof Load Cases

Each proof load case was performed by applying the external loads of ballast weight and crane load. For each load case the loads were applied in three load ramps, at approximately 50%, 75%, and 100% of the target load.

9.2 Fatigue Test Loading

Fatigue test moments were applied by operating the UREX actuator at the system's natural frequency. The mean test moment was created by the static weight of the blade and saddles, including the weight of the UREX system. Moment amplitude was maintained by using dual-mode feedback for UREX actuator amplitude control.

Periodically, a static calibration pull was performed on the blade at the 10.85 m saddle. The overhead crane was used to increasingly apply load, hold load at 1,000lbs (4.448kN), then gradually release the load. See Figure 4 for loading zone example. The data from these three load zones were averaged. The transition period between each zone is ignored to eliminate noise from these times of the pull. The median value of the calibration pulls (typically 3) for the control gage is the data used for DEL calculation. Strain to moment sensitivities of select strain gages were then be used to calculate the applied bending moment under dynamic cycling through strain gage measurements.

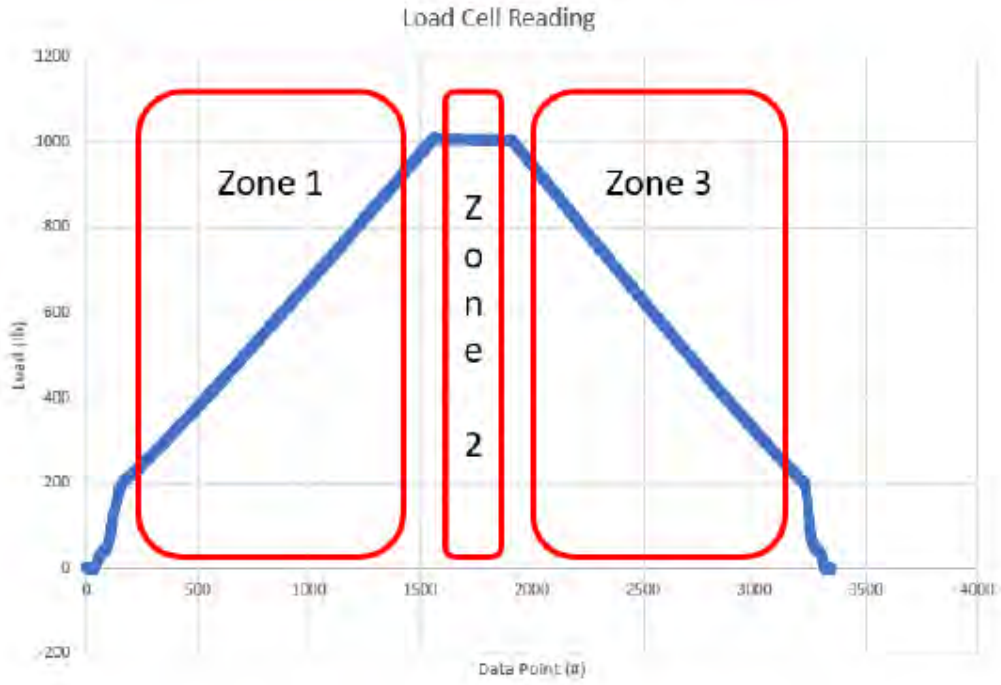

Figure 4 – Calibration loading zones

10 TESTING AND RESULTS

10.1 Property Testing

Weight and CG measurements of the blade were performed with a single point lift prior to installing test instrumentation. A polyester lifting sling was basketed around the blade at the center of gravity location. The lift was conducted with the blade positioned flat such that the HP surface was up, towards the laboratory ceiling, and the LP was down, towards the laboratory floor. The sling position was adjusted along the span of the blade until the root face of the blade was vertical. The weight was measured with crane scale and the CG distance was measured with a tape measure from the root face of the blade to the center of the sling along the low-pressure (LP) surface. The results are presented in Table 12.

Table 12. Weight and CG

Property	Measured Values
Weight (kN)	4.84
CG Location (m)	4.006

Modal parameters were measured using free-decay methods. Simple modal surveys were performed throughout the fatigue test, in approximately 250k cycle intervals. Modal surveys were performed with the blade configured in the fatigue setup: blade saddles, UREX actuator, and cable wiring were attached to the blade. Summary information of modal survey frequency results are provided in Table 13. Summary information of modal survey damping results for July 29, 2019 modal survey are provided in Table 14.

Table 13. Modal Survey Frequency Results

Date [Approx. Cycle Count]	Temp [°C]	Frequency [Hz]		
		1st Flap	1st Edge	2nd Flap
19.June, 2019 [0]	22.3	1.611	2.970	3.908
27 June, 2019 [250k]	25.8	1.607	2.939	3.887
8 July, 2019 [500k]	26.0	1.605	2.930	3.881
16 July, 2019 [750k]	26.9	1.604	2.932	3.883
29 July, 2019 [1M]	26.8	1.610	2.937	3.883

Table 14. 29 July, 2019 Modal Survey Damping Results

Mode Shape	Frequency [Hz]	Damping [% of Critical Damping]
1st Flat	1.611	0.70
1st Edge	2.970	1.34

10.2 Static Proof Testing

Blade static proof load testing followed the test plan. Table 15 provides the 100% applied test moments for each of the static proof load cases. Appendix A provides information on how the applied loads are calculated. Figure 5 provides the ratio between the applied test moment to the target test moment. The applied test moment exceeded the target test moment for ratios greater than 1.

Table 15. Applied Test Loads for Static Proof Load Cases

Spanwise Station [m]	Maximum Flapwise Moment		Minimum Flapwise Moment		Maximum Edgewise Moment		Minimum Edgewise Moment	
	Target [kN-m]	Applied [kN-m]	Target [kN-m]	Applied [kN-m]	Target [kN-m]	Applied [kN-m]	Target [kN-m]	Applied [kN-m]
0	224.9	228.0	195.8	196.9	166.8	175.0	159.4	167.7
0.87	197.2	200.8	168	170.0	145.2	151.5	136.5	143.6
1.82	171.7	174.4	139.3	143.8	124.2	129.2	112.6	120.6
2.6	149.9	151.9	117	121.5	106.4	109.9	95.1	100.8
3.48	126.5	127.6	93.9	97.5	87.5	89.4	77.2	79.6
4.44	102.3	101.6	72.9	71.8	69.0	67.6	59.1	57.0
5.46	77.9	80.7	53.1	54.9	52.1	52.9	43.3	43.6
5.98	68.2	70.1	44.3	46.8	44.2	45.8	36.2	37.3
7.02	48.6	50.1	30.2	31.5	30.8	32.5	24.7	25.7
8.05	32.6	33.4	19.3	19.7	20.4	21.5	15.6	16.3
9.05	21	21.5	11.4	12.7	12.6	13.8	9.1	10.5
9.52	15.5	15.7	8.5	9.2	9.7	10.1	6.8	7.6
10.4	8.7	5.4	4.5	3.2	5.0	3.4	3.7	2.6
11.53	3.2	0.0	1.2	0.0	1.4	0.0	1	0.0
12.37	0.3	0.0	0.2	0.0	0.2	0.0	0.1	0.0
12.99	0	0.0	0	0.0	0.0	0.0	0	0.0

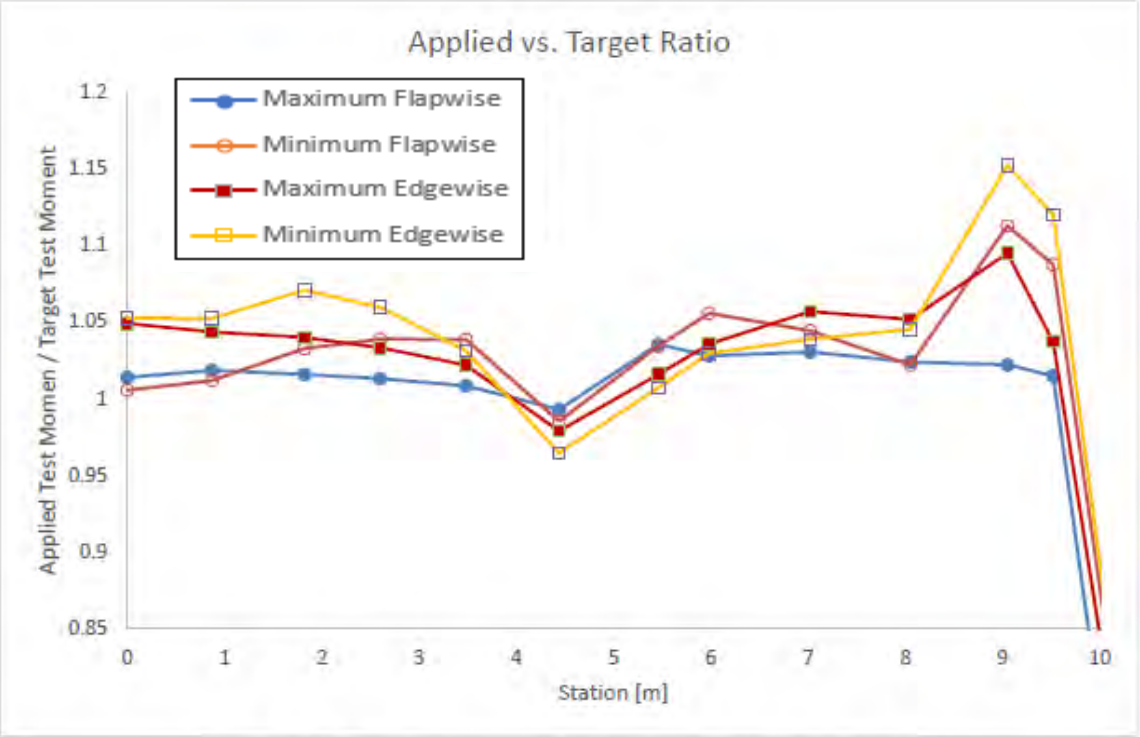

Figure 5 – Static Proof Load Testing Applied to Target Load Ratio

Appendix B through Appendix E provide data charts for the 100% load ramps for each of the static proof load cases.

The blade sustained each of the proof load cases without evidence of damage or apparent changes in physical shape.

10.3 Flapwise Fatigue Loading

Testing was performed in attended operation, where staff was present during loading. The test was stopped in the evening and restarted in the morning.

Table 16 provides the strain to moment sensitivities of gages located on the spar caps or root that were used to monitor applied moment. These sensitivities were calculated during calibration pulls performed periodically during testing. The sensitivity is the linear curve-fit slope of the strain versus applied moment curve.

Table 16. Strain to Moment Sensitivities

Strain Gage Information		Strain Gage Sensitivity [kN-m / ue] for Pull Date [approximate cycle count]			
Strain Gage Name	Strain Gage Span Location [m]	19.June, 2019 [0]	27 June, 2019 [250k]	8 July, 2019 [500k]	17 July, 2019 [750k]
SG03-200-LP90	0.2	0.1880	0.1811	0.1828	0.1852
SG07-200-HP270	0.2	0.2321	0.1999	0.1947	0.1990
SG23-3250-HP-SC	3.25	0.0206	0.0205	0.0204	0.0206
SG24-3250-LP-SC	3.25	0.0225	0.0224	0.0222	0.0225
SG34-6500-HP-SC	6.5	0.0106	0.0106	0.0106	0.0106
SG35-6500-LP-SC	6.5	0.0112	0.0112	0.0111	0.0112
SG41-9750-HP-SC	9.75	0.0036	0.0036	0.0036	0.0036
SG42-9750-LP-SC	9.75	0.0033	0.0033	0.0033	0.0033

Figure 6 compares the target 1 million cycle DEL with DELs calculated from the applied fatigue test load. Appendix F provides the equations used to calculate the applied test DEL. An inverse slope parameter of 11 is used for this calculation. The low-pressure surface gages provided higher estimates of applied DEL, with an excepting being at the 0.2 m station. The DEL at the 0.2 m station is approximately 15% below the target DEL.

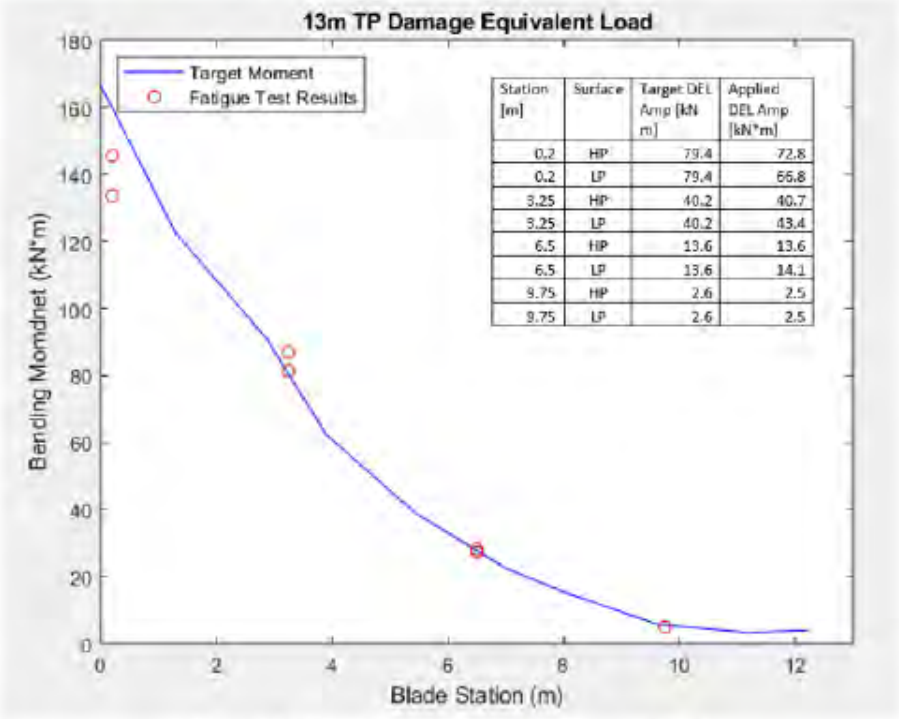

Station [m]	Surface	Target DEL Amp [kN m]	Applied DEL Amp [kN*m]
0.2	HP	79.4	72.8
0.2	LP	79.4	66.8
3.25	HP	40.2	40.7
3.25	LP	40.2	43.4
6.5	HP	13.6	13.6
6.5	LP	13.6	14.1
9.75	HP	2.6	2.5
9.75	LP	2.6	2.5

Figure 6 –Target and Applied Flapwise DEL's

Damage Equivalent Loads were calculated using single direction calibration pulls in the 0° direction (vertically down towards laboratory floor).

Appendix G provides data charts for the flapwise fatigue test. Taking a snapshot of operating data, Table 17 provides data ranges (peak-to-peak) at a cycle count of 1 million cycles.

Table 17. Data Ranges At The 1-Million Cycle Mark

Channel Name	Range @ 1e6 Cycles	Units	Channel Name	Range @ 1e6 Cycles	Units
LVDT	147.17	mm	SG34-6500-HP-SC	1290	ue
Temperature (Average Value)	25.93	C	SG35-6500-LP-SC	1266	ue
Humidity (Average Value)	31.5	% RH	SG36-6500-LE	18	ue
SG01-200-LP0	64.22	ue	SG37-6500-TE	694	ue
SG02-200-LP45	324	ue	SG41-9750-HP-SC	684	ue
SG03-200-LP90	360	ue	SG42-9750-LP-SC	770	ue
SG04-200-LP135	198	ue	SG43-9750-LE	65	ue
SG05-200-HP180	53	ue	SG44-9750-TE	317	ue
SG06-200-HP225	343	ue	A-Tip-Flap	9.512	g
SG07-200-HP270	352	ue	A-Tip-LeadLag	2.216	g
SG08-200-HP315	191	ue	A-9750LE-Flap	4.937	g
SG12-2500-HP-AP-0	569	ue	A-9750LE-LeadLag	1.594	g
SG13-2500-HP-AP-45	187	ue	A-9750TE-Flap	4.911	g
SG14-2500-HP-AP-90	392	ue	A-9750TE-LeadLag	1.634	g
SG17-2900-LP-SC-0	2040	ue	A-4700LE-Flap	0.956	g
SG18-2900-LP-SC-45	748	ue	A-4700LE-LeadLag	0.302	g
SG19-2900-LP-SC-90	492	ue	A-4700TE-Flap	0.927	g
SG23-3250-HP-SC	1987	ue	A-4700TE-LeadLag	0.302	g
SG24-3250-LP-SC	1948	ue	A-Root-Flap	0.005	g
SG25-3250-LE	276	ue	A-Root-LeadLag	0.004	g
SG26-3250-TE	813	ue	A-UREX-Flap	1.654	g

10.4 Blade Inspections

Visual inspections of the blade's exterior were performed at approximated 250k cycle intervals throughout the fatigue test program. No visible defects were observed. No internal inspections were performed.

11 MEASUREMENT UNCERTAINTY

The uncertainty budget for measurements and calculations contained in this report are shown in Table 18; the traceable uncertainty values calculated for reported measurands in this report do not exceed the values contained in this uncertainty budget.

Table 18. Uncertainty Budget

Application/equipment/purpose	Units	Effective d.o.f.	Expanded uncertainty (k=2, unless noted otherwise)
NI 9239, ±10VDC input	V	>1E+03	0.05% reading
NI 9237, half/full-bridge analog input	V/V	>1E+03	0.1% reading
NI 9236, quarter-bridge analog input	microstrain	>1E+03	0.05% reading
string potentiometers & NI 9239, displacements	mm	>1E+03	0.5% reading
DC accelerometers & NI 9239, acceleration	g	>1E+03	0.5% reading
Omega HX93 & NI 9239, temperature	°C	>1E+03	1 °C
Load cell, MTS 1020AFF, load	lb	>1E+03	0.04 %RD
Load cell, Transducer Technique SW-10k, load	lb	>1E+03	0.05 %RD
Crane Scale, load	lb	>1E+03	0.5 %RD
Omega HX93 & NI 9239, % relative humidity (RH)	%RH	5.70E+01	8 %RH
Torque wrenches, torque	N-m or ft-lbs	>1E+03	10% reading
blade strain (range)	microstrain	>1E+03	2% (max-min reading)
blade stiffness	N/mm	4.47E+02	2% reading
strain gage sensitivites	kN-m/microstrain	>1E+03	2% reading
applied fatigue damage equivalent load (DEL)	kN-m	>1E+03	3% reading
static bending moment	kN-m	>1E+03	2% reading

* = various manufacturers/models
%RD = percent reading
%RH = percent relative humidity

12 EXCEPTIONS FROM STANDARD PRACTICE

12.1 Deviations from the Test Plans

1. Several strain gages listed in the test plan were not installed for any of the testing. They were: SG09-1900-HP-AP-0, SG10-1900-HP-AP-45, SG11-1900-HP-AP-90, SG15-2750-

HP-TE 2.75 HP TE, SG16-2750-TE 2.75 TE, SG20-2900-LP-FP-0, SG21-2900-LP-FP-45, SG22-2900-LP-FP-90, SG27-3250-LP-TE 3.25 LP TE, SG28-6300-LP-AP-0, SG29-6300-LP-AP-45, SG30-6300-LP-AP-90, SG31-6300-HP-LE-0, SG32-6300-HP-LE-45, SG33-6300-HP-LE-90, SG38-9000-LP-AP-0, SG39-9000-LP-AP-45, SG40-9000-LP-AP-90, SG45-3250-HP-TE, and SG46-2750-LP-TE

12.2 Deviations from the IEC 61400-23 Standard

1. The inside of the blade was not inspected between static and fatigue test programs

12.3 Deviations from the NREL Quality Assurance Program

1. None

13 References

[1] NREL, "Laboratory wind turbine blade static testing of the Sandia National Rotor Testbed 13-meter wind turbine blade," 2018.

[2] IEC, *Wind turbines--Part 23: Full-scale structural testing of rotor blades,* IEC, 2014.

[3] A2LA, 11 2020. [Online]. Available: http://www.a2la.org/scopepdf/1239-01.pdf.

[4] NREL/NWTC, *Safe Operating Procedure, SOP-515009412, Conducting Structural Tests at the National Wind Turbine Technology Center.*

[5] NREL, "Laboratory minimum flapwise, and maximum and minimm edgewise, static testing of the thermoplastic 13-meter wind turbine blade," 2019.

[6] NREL, "Laboratory maximum flapwise static testing of the thermoplastic 13-meter wind turbine blade," 2019.

[7] NREL, "Laboratory flapwise fatigue testing of the thermoplastic 13-meter wind turbine blade".

14 LIST OF APPENDICIES

Appendix A. – Applied Test Moment Calculation
Appendix B – Data Charts for Maximum Flapwise Proof Loading
Appendix C – Data Charts for Minimum Flapwise Proof Loading
Appendix D – Data Charts for Maximum Edge Proof Loading
Appendix E – Data Charts for Minimum Edge Proof Loading
Appendix F – Fatigue Damage Equivalent Load Calculation
Appendix G – Data Charts for Flapwise Fatigue Loading
Appendix H – Test Photographs

Appendix A – Applied Test Moment Calculation

This appendix provides parameters and equations used to calculate the Applied Test Moment (ATM). The ATM includes tare loads and external loads. For all static test load cases, the applied test loads were acting with gravity, being applied downward toward the laboratory floor. Tare load at each load station includes all weight suspended by the blade from load saddle to load cell. This includes saddles, rigging hardware like chains, shackles, spreader bar, and the weight of the load cell. In addition to the tare loads from rigging equipment and the external loads, the self-weight of the blade creates an additional bending moment. External loads were applied by hanging ballast weights or applying loads with the overhead crane. External loads were measured by the inboard and outboard load cells. The ATM is calculated by summing the contributions from rigging tare, blade self-weight tare, and the external load. Figure A-1 provides a schematic of the dimension used to calculate the ATM.

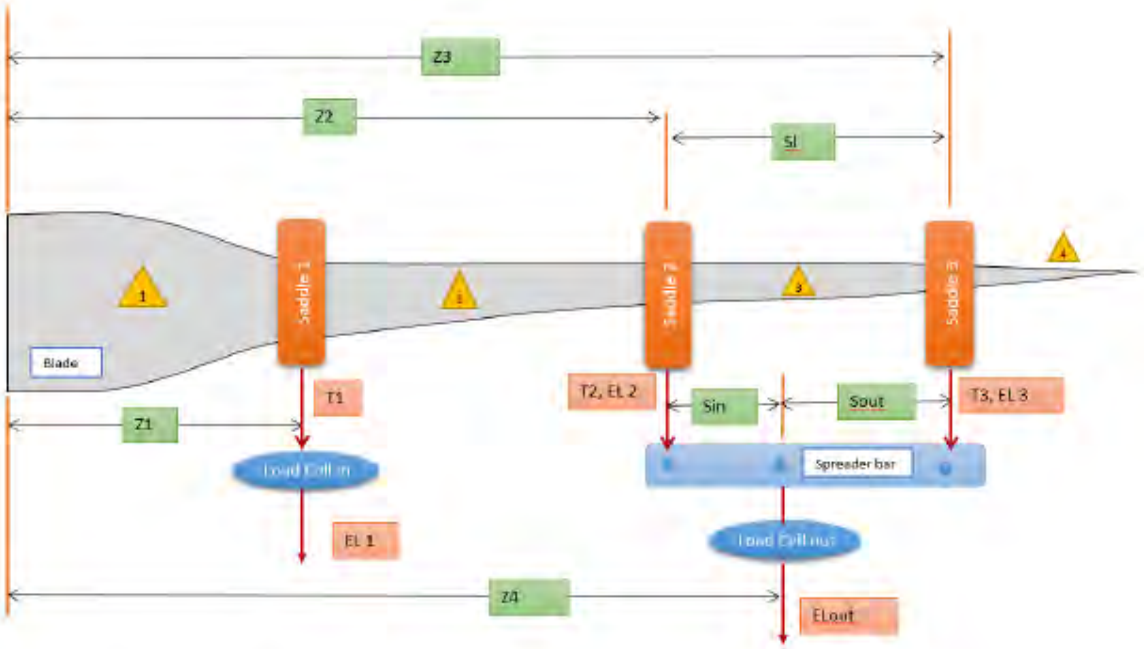

Figure A-1 – Dimensions used for calculating the Applied Test Moment

In addition to the load saddles, a spreader bar was used to apply loads at the 7.55 m and 10.85 m stations by dividing the outboard external load of the overhead crane (reacted through turning blocks to pull down towards the laboratory floor). The tare weight of the spreader bar was taken to be evenly distributed between the 7.55 m and 10.85 m stations. The center of gravity of the spreader bar is offset from the center of the beam as the reaction point hardware connecting to the external winch line was not always positioned at the center of the beam. This difference in the center of gravity of the spreader bar is considered negligible. The weight of instrumentation and cables placed on the blade for strain gages and accelerometers was not included in tare weight values. Table A-1 provides dimensions and rigging tare weights.

Table A-1 – Test setup geometry and rigging tare weights

Load Case	Z1 [m]	Z2 [m]	Z3 [m]	Z4 [m]	T1 [N]	T2 [N]	T3 [N]	Sl [m]	Sin [m]	Sout [m]	EL 2 [fraction of EL out]	EL 3 [Fraction of EL out]
Maximum Flap	4.6	7.55	10.85	9.679	1899.4	1783	1858.9	3.299	2.129	1.170	0.355	0.645
Minimum Flap				9.120	1899.4	1797.9	1854.1		1.570	1.729	0.524	0.476
Maximum Edge				9.679	2177.4	1793	1858.9		2.129	1.170	0.355	0.645
Minimum Edge				9.279	2177.4	1796.3	1855.7		1.729	1.570	0.476	0.524

Variable Description	
Z1	Distance from root to Saddle 1
Z2	Distance from root to Saddle 2
Z3	Distance from root to Saddle 3
Z4	Distance from root to effective outboard load station
T1	Tare load at Saddle 1
T2	Tare load at Saddle 2
T3	Tare load at Saddle 3
Sl	Spreader length
Sin	Distance between Saddle 2 and external outboard load station
Sout	Distance between external outboard load station and Saddle 3
EL 2	Fraction of external outboard load applied at Saddle 2
EL 3	Fraction of external outboard load applied at Saddle 3

The tare moment created by the self-weight of the blade was estimated based on mass per unit length data provided in the design document and then scaled by the root bending moment calculated by laboratory mass balance measurements performed prior to structural testing. To calculate self-weight bending moment, the blade was discretized into sections between the stations given in the design information document. The CG of each of these sections was calculated as the center of a trapezoid with lengths equal to the design mass per unit at the section end points. For most sections, the sectional CG calculated as a trapezoid is very close to taking the section CG as the midpoint of the section. As the design mass per unit length did not include the weight of the steel root inserts, a mass of 22 kg was added at the z=0.1 m station, where (z) is the distance from the root face of the blade. For a measured blade weight of 4.84 kN and CG 4.006m from root, the calculated root bending moment due to blade self-weight is 19.38 kN m. Table A-2 provides the bending moment from blade self-weight based on design information and the estimated bending moment based from blade self-weight scaled to the as-measured CG and mass of the blade. Values for estimated self-weight bending moment (M_z^{SW}) are used for reporting.

Table A-2 – Design and estimated as-built blade self-weight bending moment.

Spanwise Station [m]	Self-weight Bending Moment from Design Information [N m]	Estimated Self-weight Bending Moment based on measured Weight and CG [N m]
0	20657.9	19854.1
0.125	20000.8	19296.8
0.25	19406.8	17560.8
0.67	17654.3	16915.0
0.85	16958.8	14547.3
1.525	14492.6	12384.8
2.2	12254.0	11217.3
2.605	11023.9	8859.1
3.482	8647.7	6665.0
4.443	6472.7	4764.3
5.458	4616.0	3785.8
6.115	3627.8	2632.9
7.023	2507.3	2115.7
7.542	1982.9	1677.7
8.054	1540.9	1026.4
8.95	929.8	727.4
9.518	638.1	360.6
10.402	311.6	153.0
11.184	132.4	79.5
11.65	65.8	29.8
12.125	23.8	10.2
12.46	7.5	1.7
12.738	1.2	0.3
12.865	0.2	0.0
12.947	0.0	0.0
13	0.0	0.0

Creating a spline fit of the information in Table A-2, Table A-3 provides the estimated blade self-weight bending moment at saddle and strain gage locations. These values are used for reporting moment versus strain.

Table A-3 – Estimated as-built blade self-weight bending moment at select blade stations.

Station [m]	Estimated Self-Weight Bending Moment based on Measured Weight and CG [N m]
0	19854.1
0.2	18203.5
1.9	12232.2
2.5	9451.2
2.75	8208.0
2.9	7717.2
3.25	7020.5
4	5604.2
4.6	4570.1
6.3	2432.0
6.5	2303.8
7	2126.3
9	703.9
9.7	273.1
9.75	255.0
11.25	71.8

Given the geometry and values of rigging tare and blade self-weight moments provided above, the ATM can be calculated by including the external loads measured during testing. The external loads applied to Saddle 2 and Saddle 3 by the outboard external load is calculated with the following equations.

$$EL_2 = EL_{out}\left(\frac{S_L - S_{in}}{S_L}\right)$$

$$EL_3 = EL_{out}\left(\frac{S_{in}}{S_L}\right)$$

Between the root of the blade and Saddle 1 (Section 1) the Applied Test Moment is then calculated as:

$$ATM_{Section\ 1} = M_z^{SW} + \{(T_1 + EL_1) * (Z_1 - z)\} + \{(T_2 + EL_2) * (Z_2 - z)\} + \{(T_3 + EL_3) * (Z_3 - z)\}$$

Again, (z) is the distance from the root of the blade where the ATM is calculated. Between Saddle 1 and Saddle 2 (Section 2) the Applied Test Moment is calculated as:

$$ATM_{Section\ 2} = M_z^{SW} + \{(T_2 + EL_2) * (Z_2 - z)\} + \{(T_3 + EL_3) * (Z_3 - z)\}$$

Between Saddle 2 and Saddle 3 (Section 3) the Applied Test Moment is calculated as:

$$ATM_{Section\ 3} = M_z^{SW} + \{(T_3 + EL_3) * (Z_3 - z)\}$$

Outboard of Saddle 3 (Section 4) the Applied Test Moment is simply the moment due to blade self-weight, given as:

$$ATM_{Section\ 4} = M_z^{SW}$$

Appendix B – Data Charts for Maximum Flapwise Proof Loading

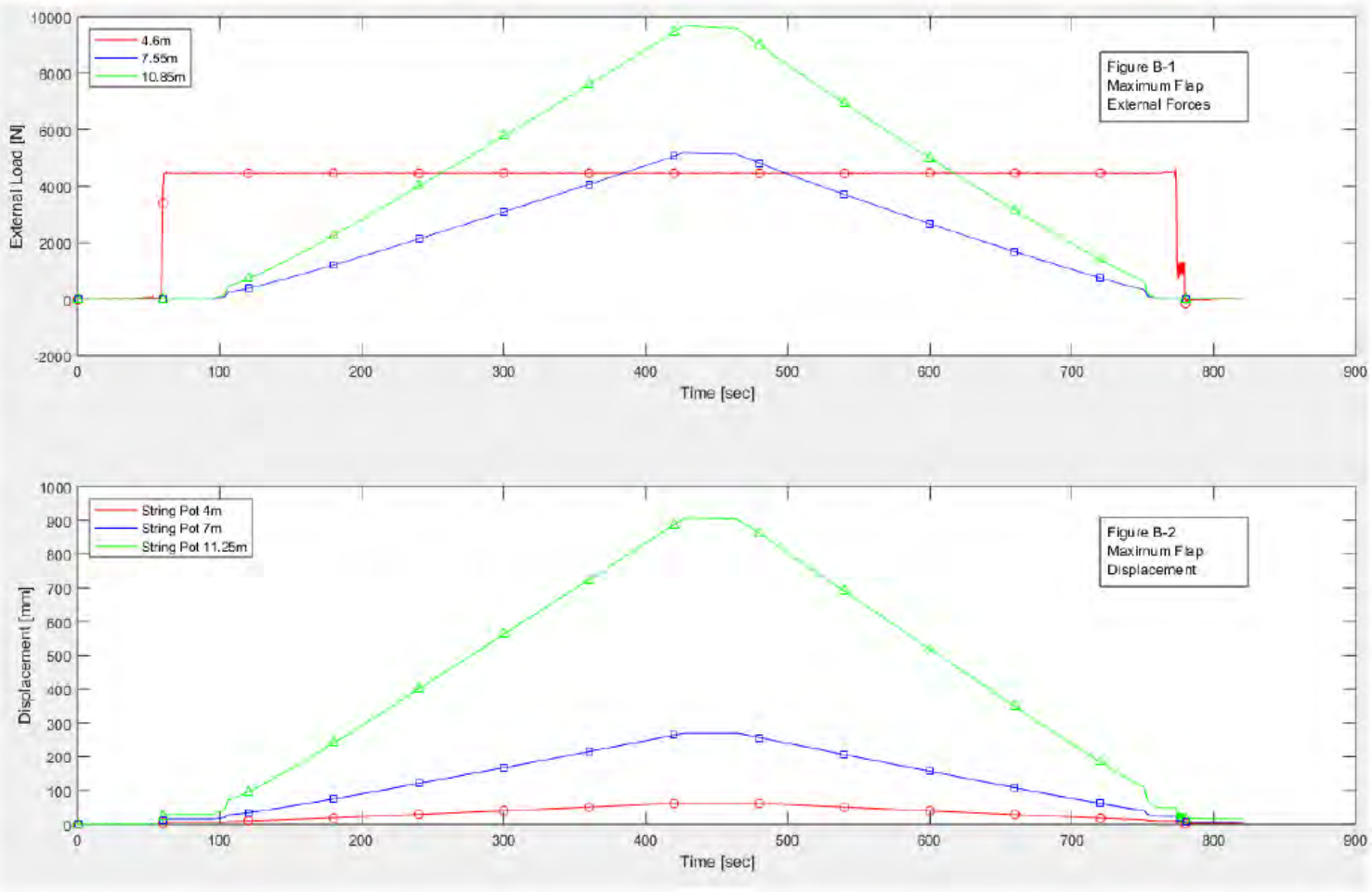

Figure B1-2 – Maximum Flap Static Load and Displacement

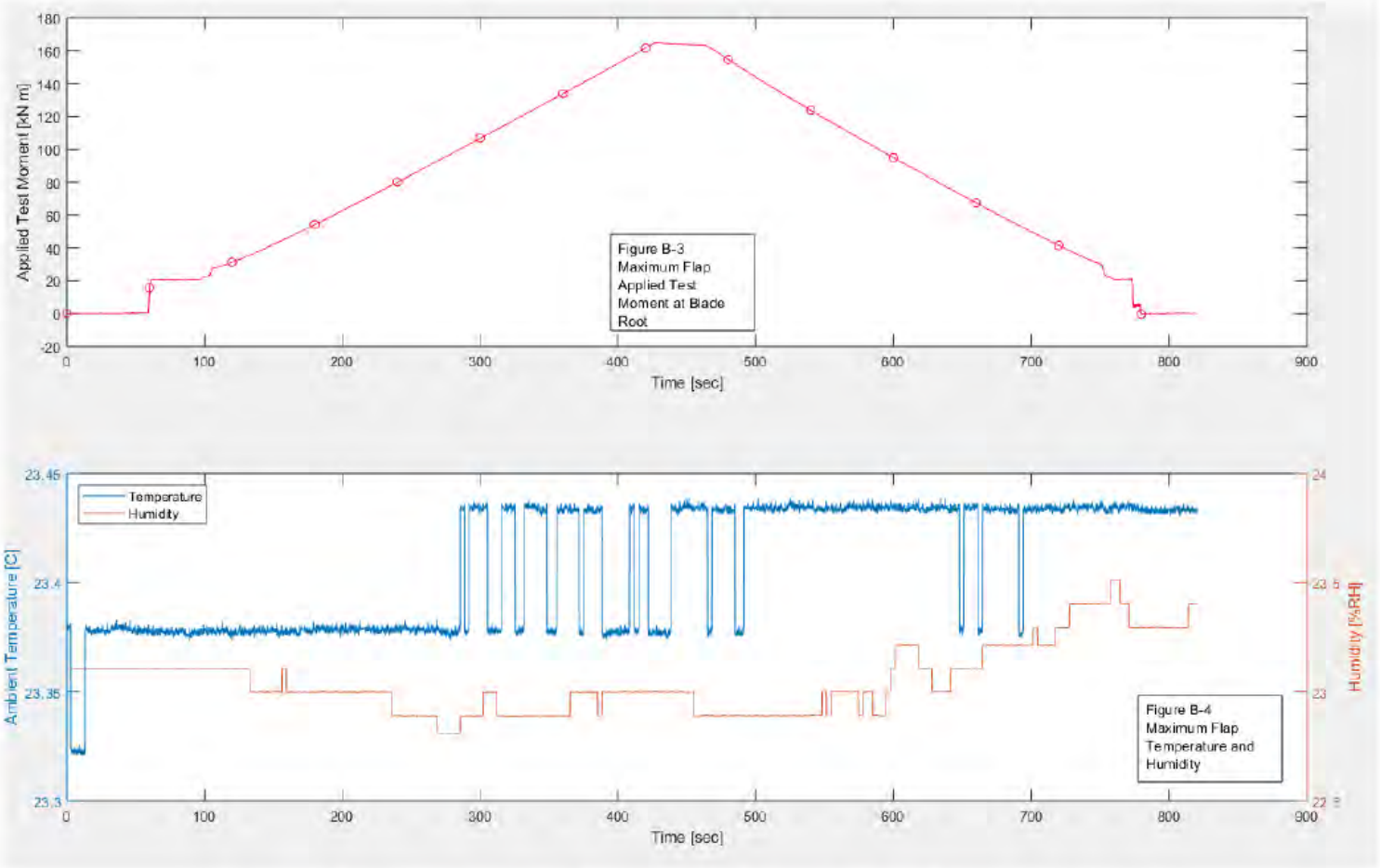

Figure B3-4 – Maximum Flap Root Moment, Temperature and Relative Humidity

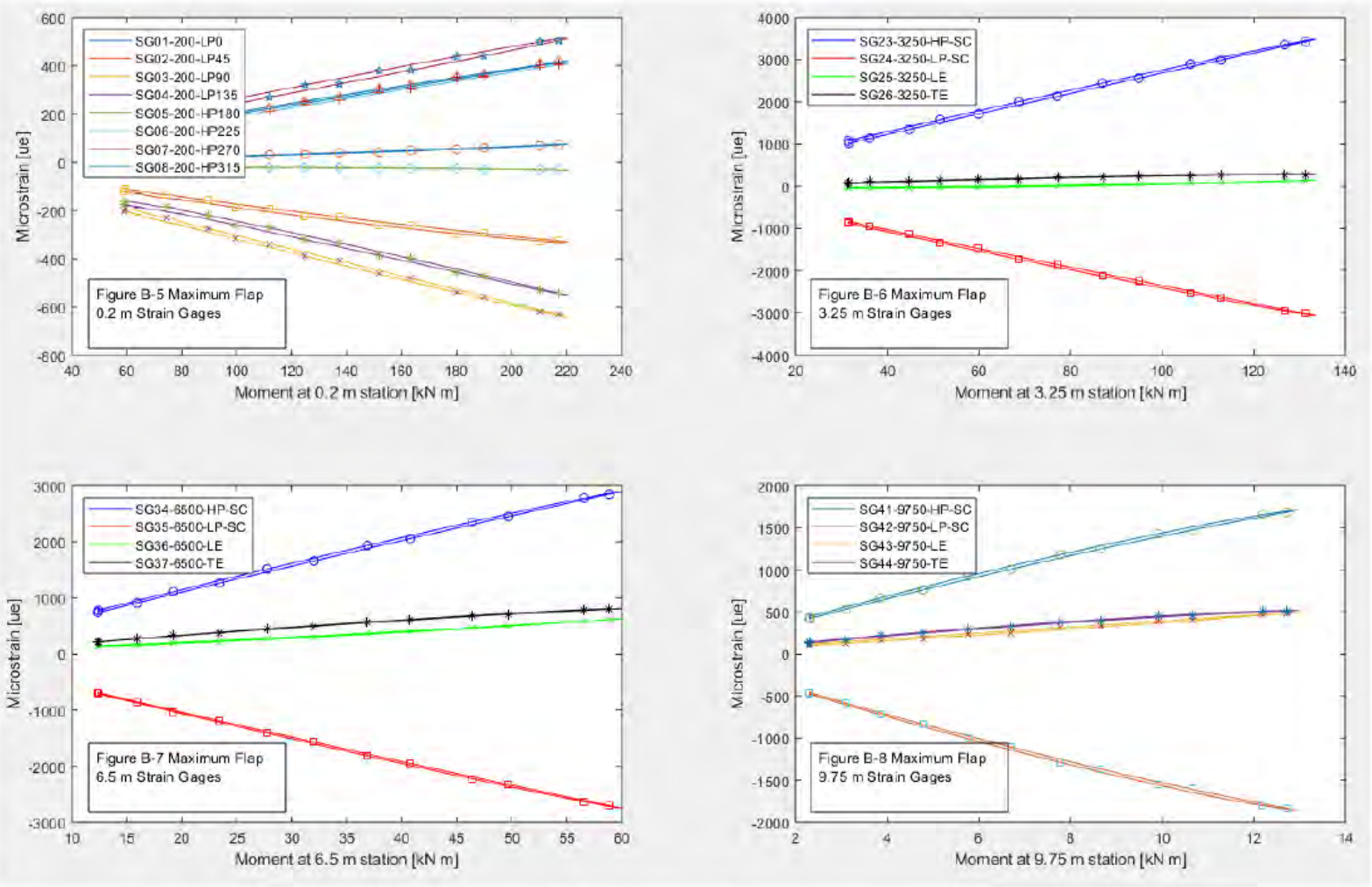

Figure B5-8 – Maximum Flap Static Strain

Appendix C – Data Charts for Minimum Flapwise Proof Loading

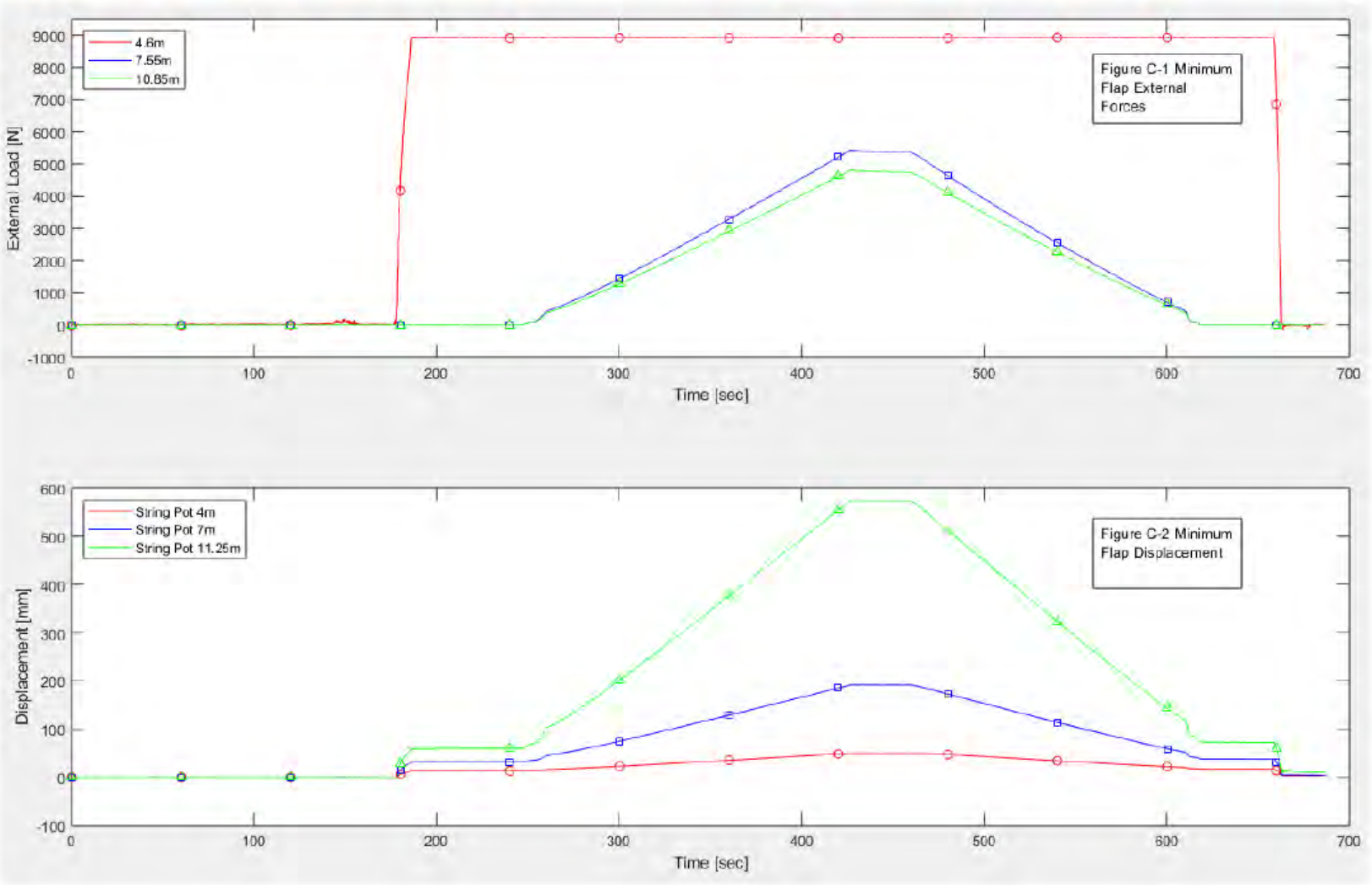

Figure C1-2 – Minimum Flap Static Load and Displacement

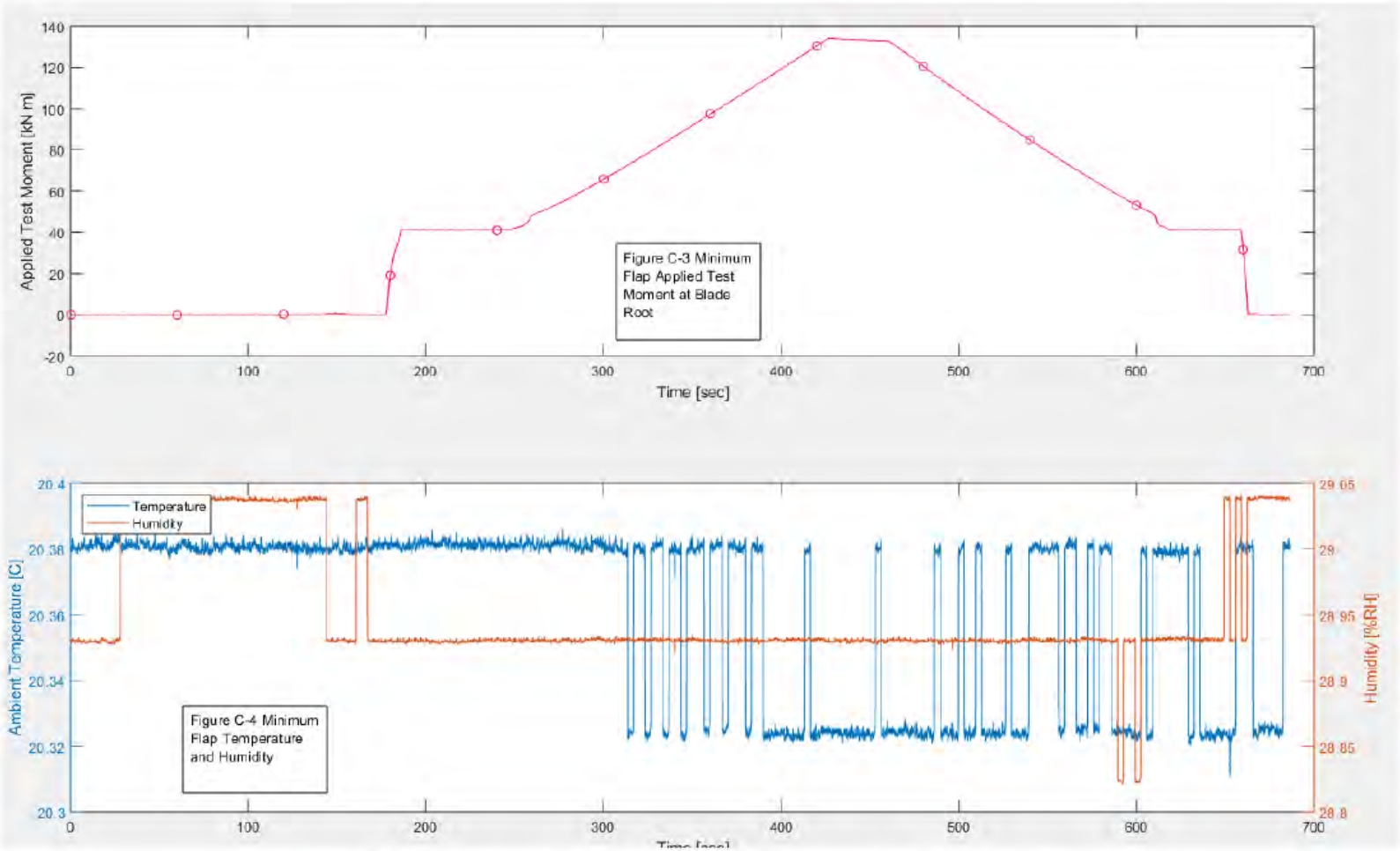

Figure C3-4 – Minimum Flap Root Moment, Temperature and Relative Humidity

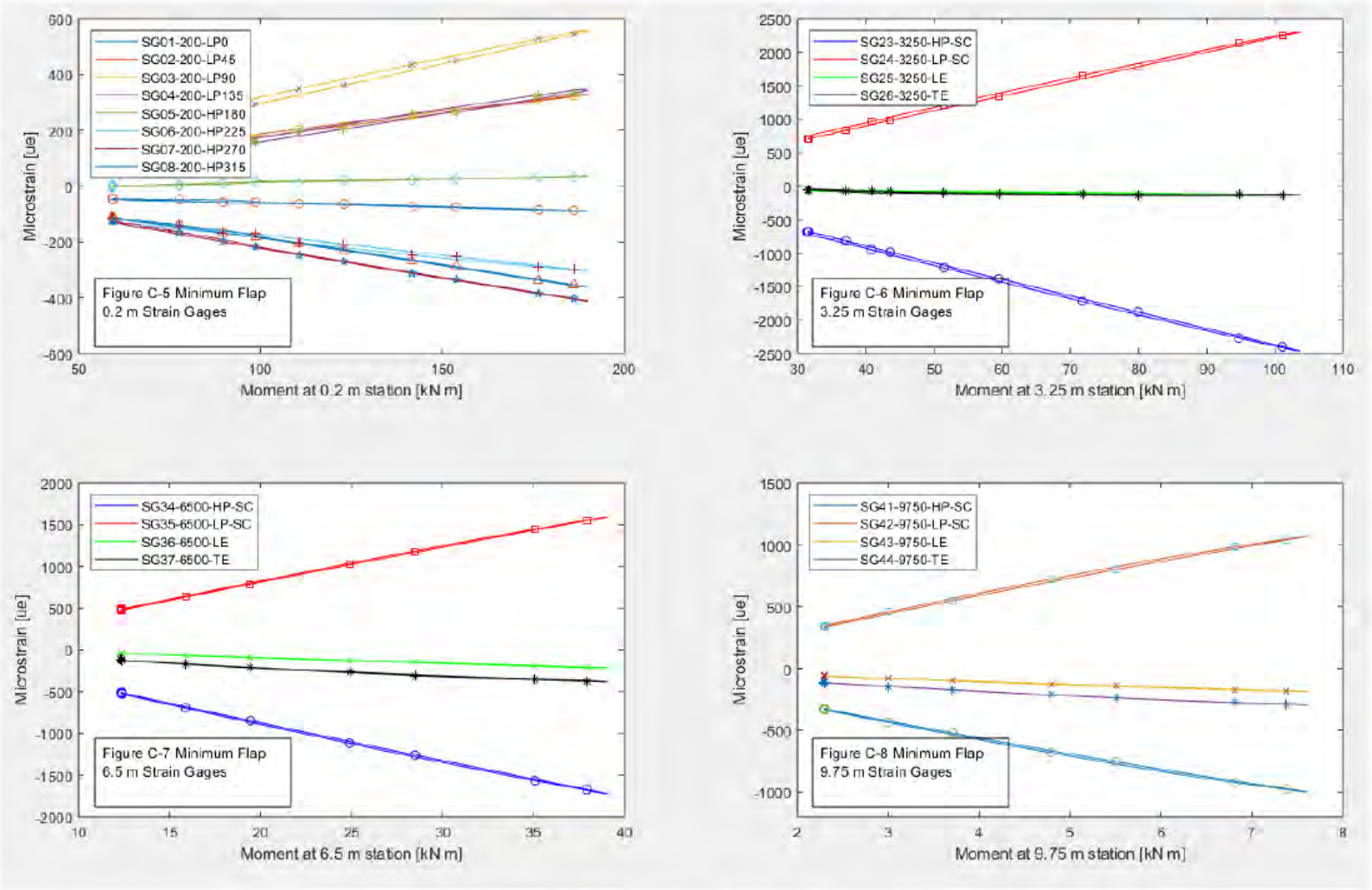

Figure C5-8 – Minimum Flap Static Strain

Appendix D – Data Charts for Maximum Edge Proof Loading

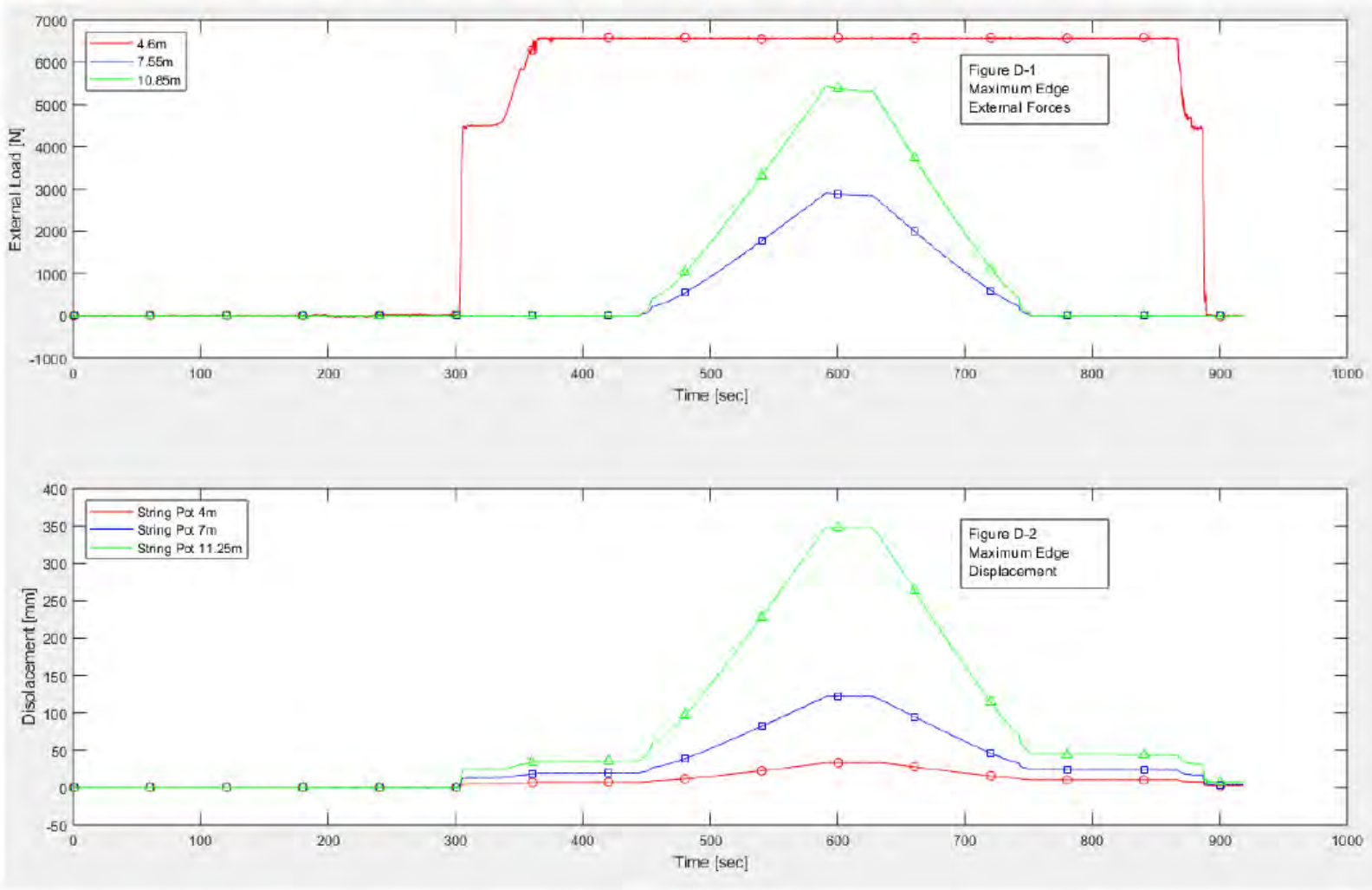

Figure D1-2 – Maximum Edge Static Load and Displacement

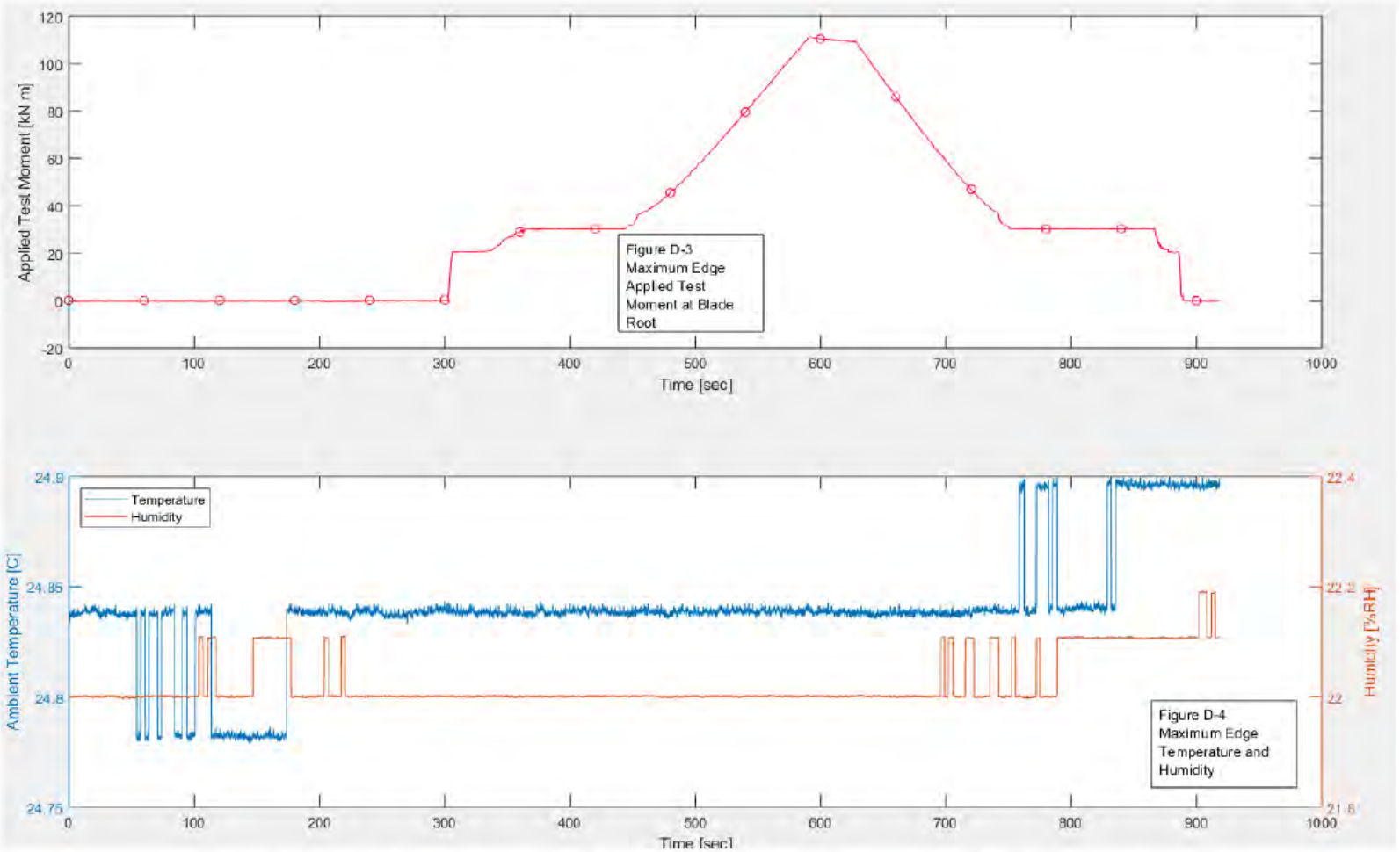

Figure D3-4 – Maximum Edge Root Moment, Temperature and Relative Humidity

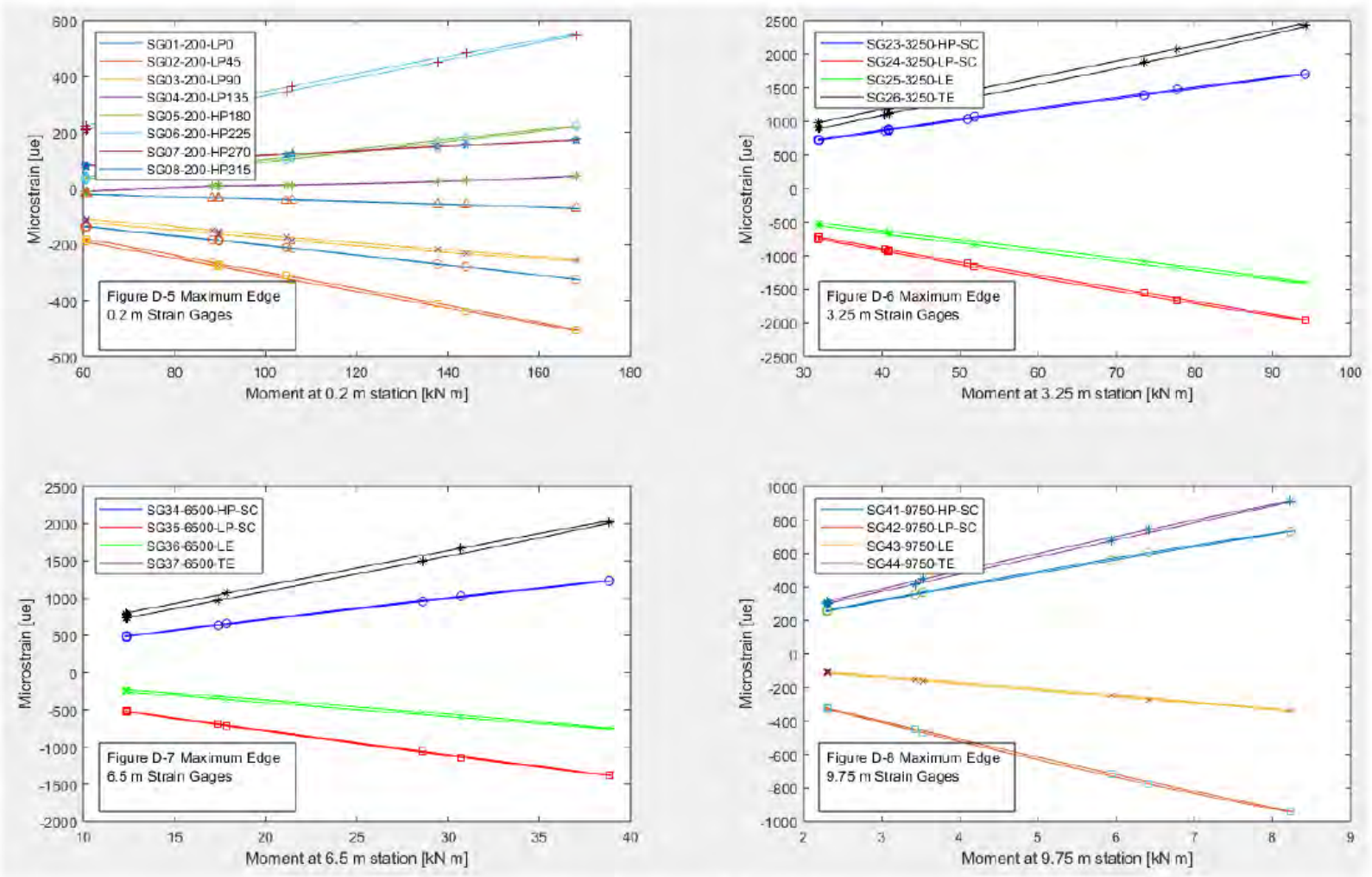

Figure D5-8 – Maximum Edge Static Strain

Appendix E – Data Charts for Minimum Edge Proof Loading

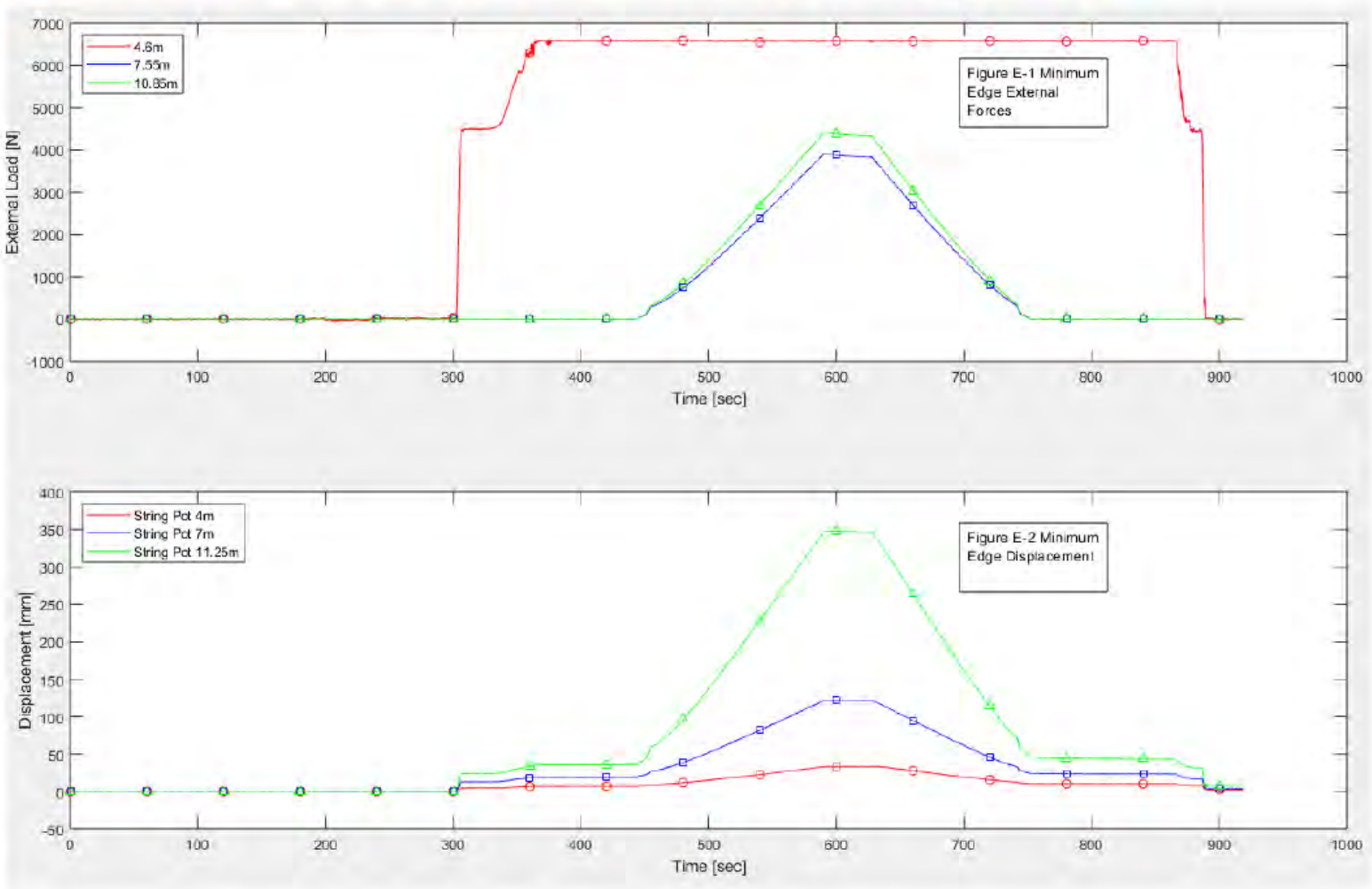

Figure E1-2 – Minimum Edge Static Load and Displacement

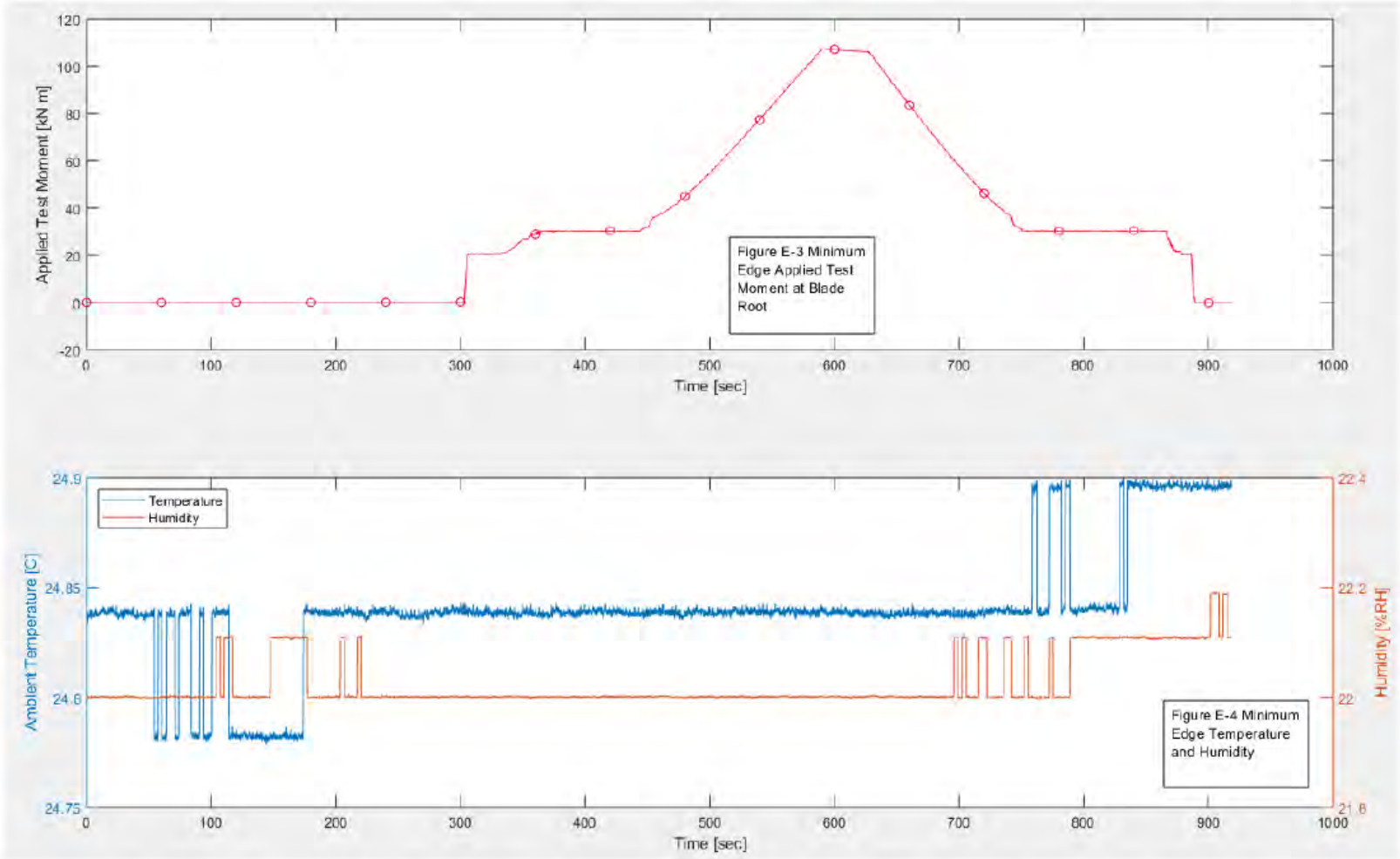

Figure E3-4 – Minimum Edge Root Moment, Temperature and Relative Humidity

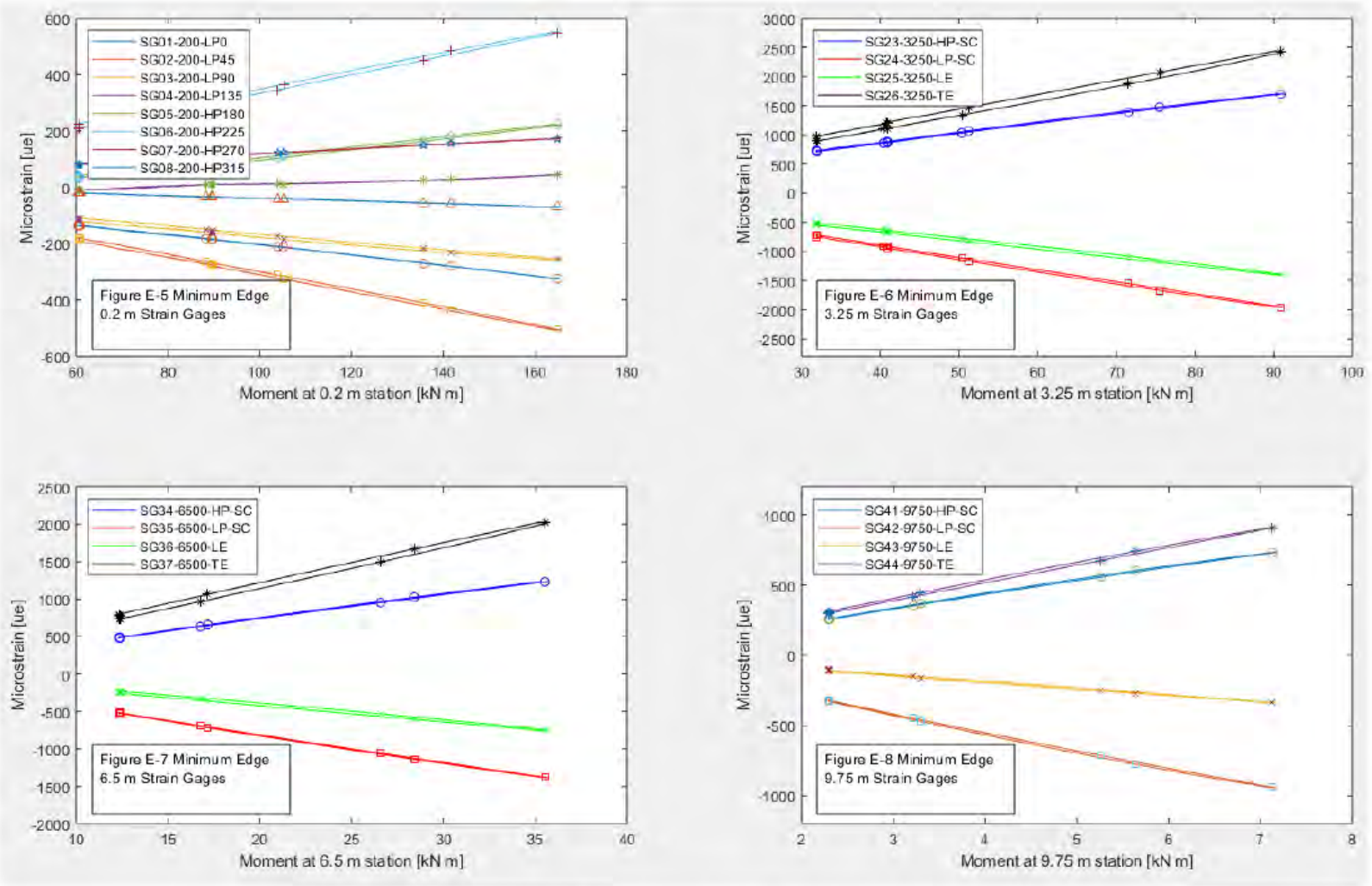

Figure E5-8 – Minimum Edge Static Strain

Appendix F – Fatigue Damage Equivalent Load Calculation

The equations used to estimate the damage equivalent load (DEL) are provided below. The DEL's were computed at four spanwise stations using the strain gages calibrated for bending moment. The DEL's are based on peak to peak strains and moments, mean effects were ignored. The equivalent damage was based on the target test cycles and target test bending moments. The complete peak-valley record of strains was used to estimate the DEL's. For reporting purposes, an inverse slope parameter (m) of 11 was used.

$$Eq.1 \quad d_i = \left(\frac{M_a}{M_u}\right)^m * \frac{N_a}{N_{eq}}$$

$$Eq.2 \quad D = \sum d_i$$

$$Eq.3 \quad DEL = M_u * D^{\frac{1}{m}}$$

Definitions for the variables in Equations 1 through 3 include:

- di – damage from binned moment range
- D – damage from all binned moment ranges
- Ma – binned moment range
- Mu – target test moment range
- Na – number of cycles in a bin
- Neq – damage equivalent cycles (Neq=1e6 used in this analysis)
- M – inverse slope parameter (m=10 used in this analysis)

Appendix G – Data Charts for Flapwise Fatigue Loading

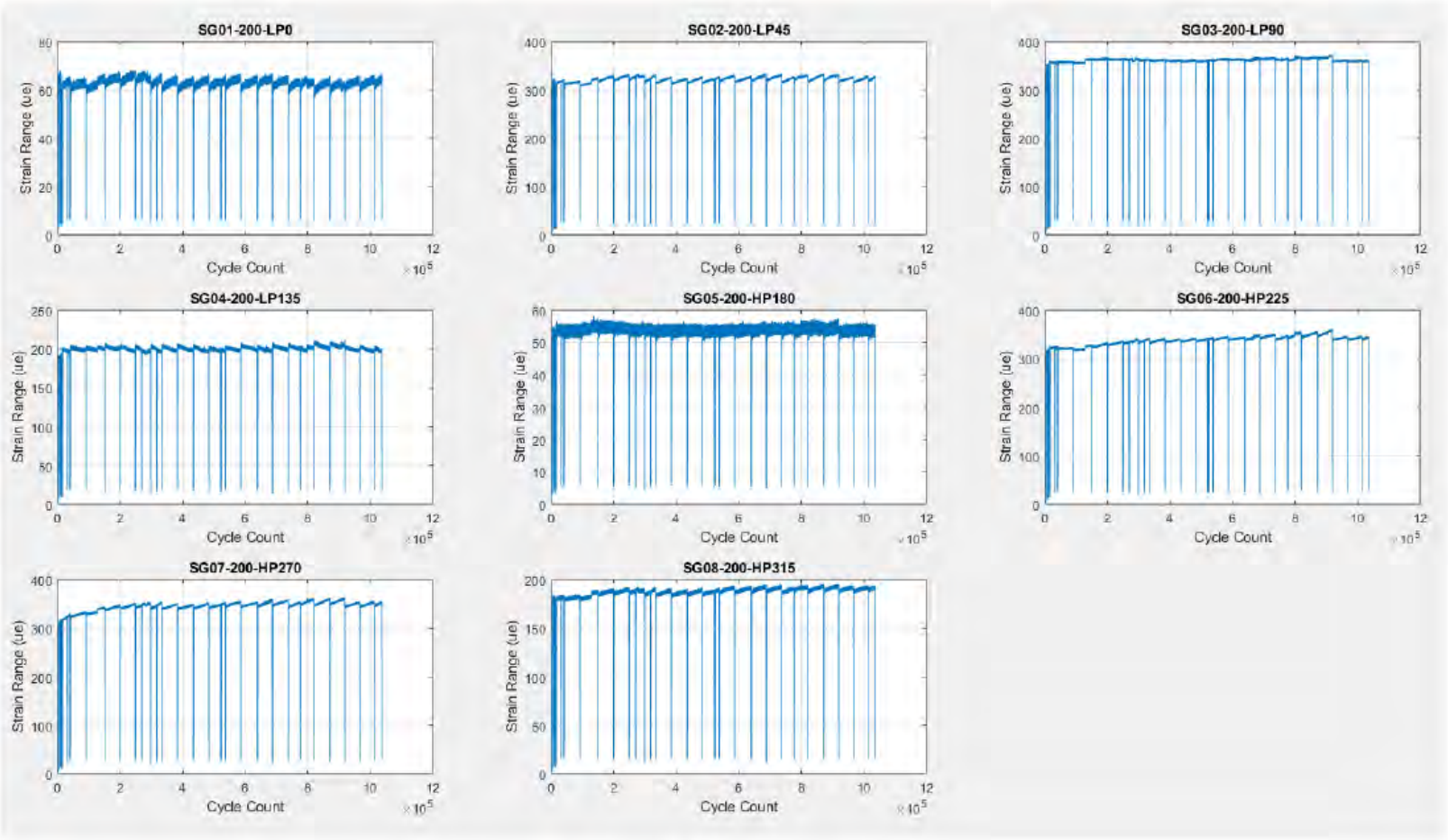

Figure G-1. Root Strain Gages

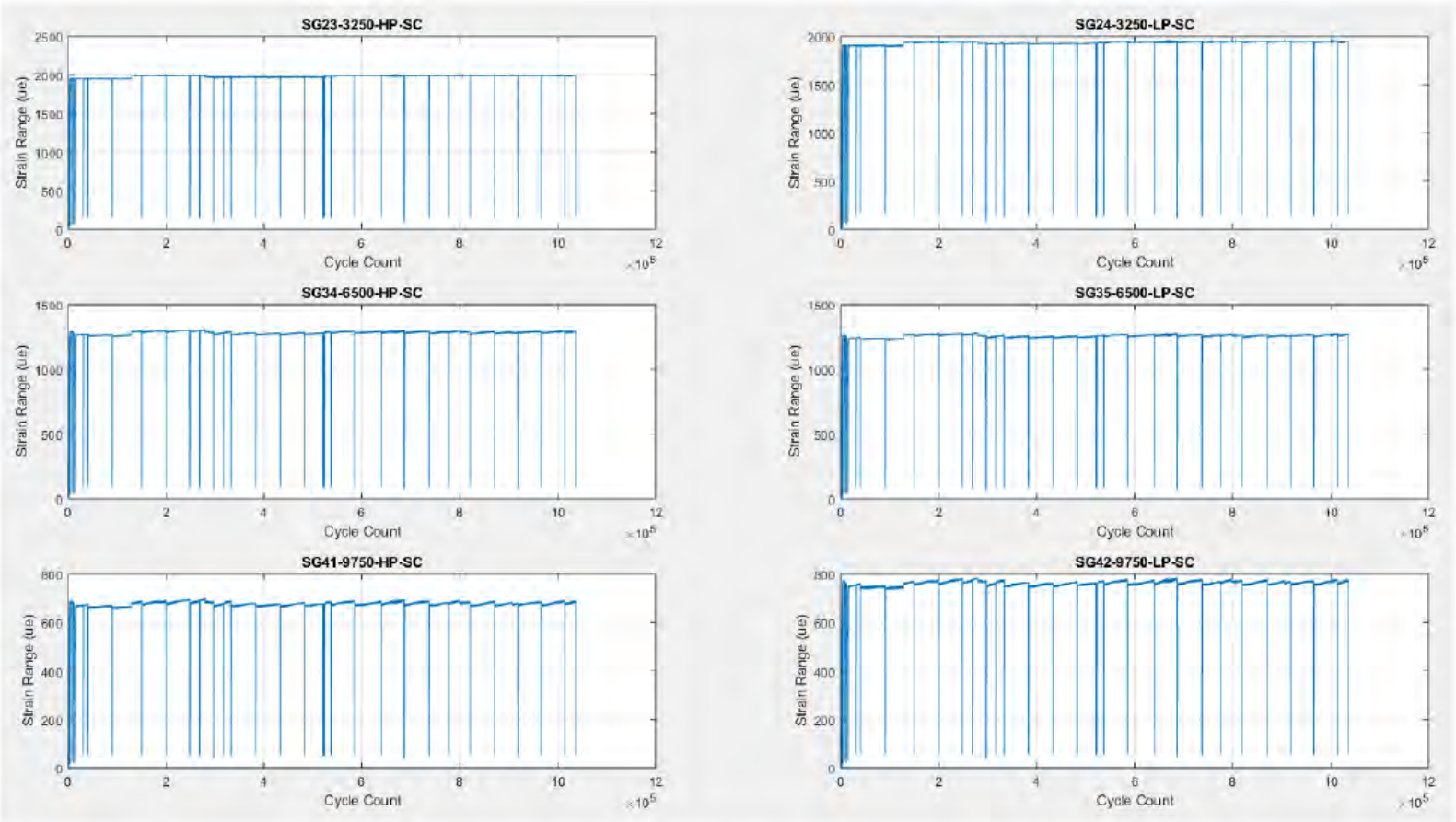

Figure G-2. Flap Strain Gages

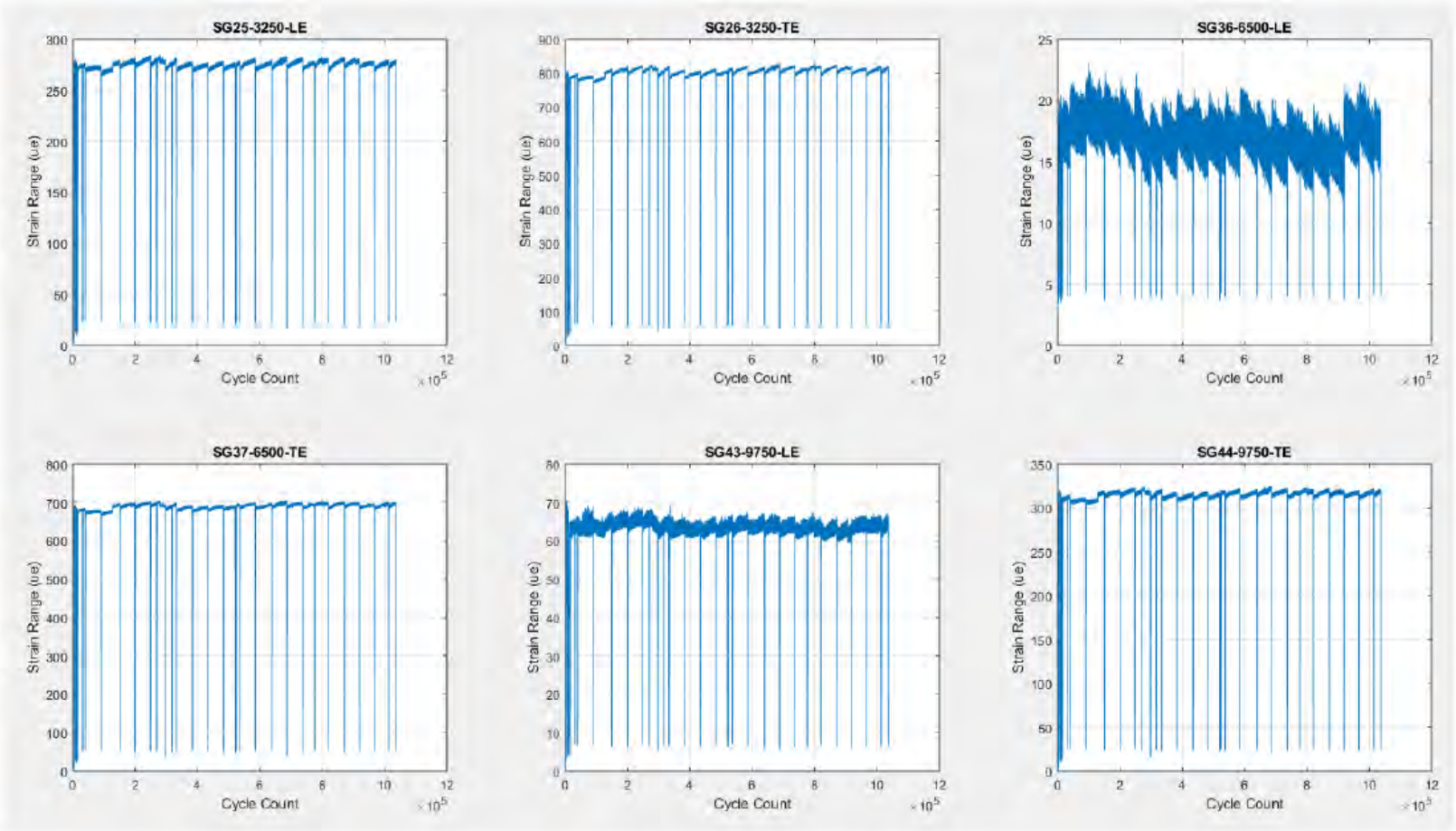

Figure G-3. Edge Strain Gages

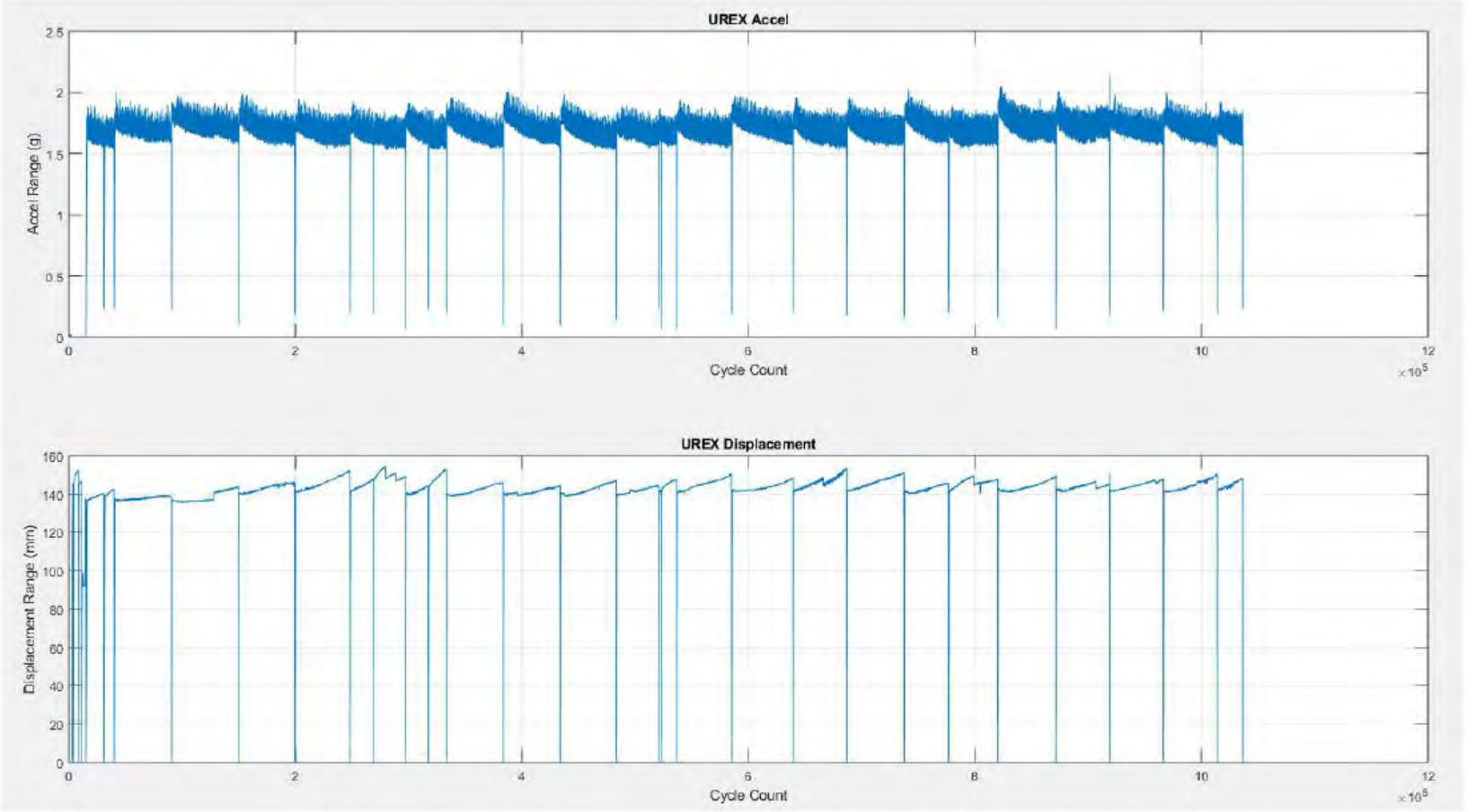

Figure G-4. UREX Displacement and Acceleration

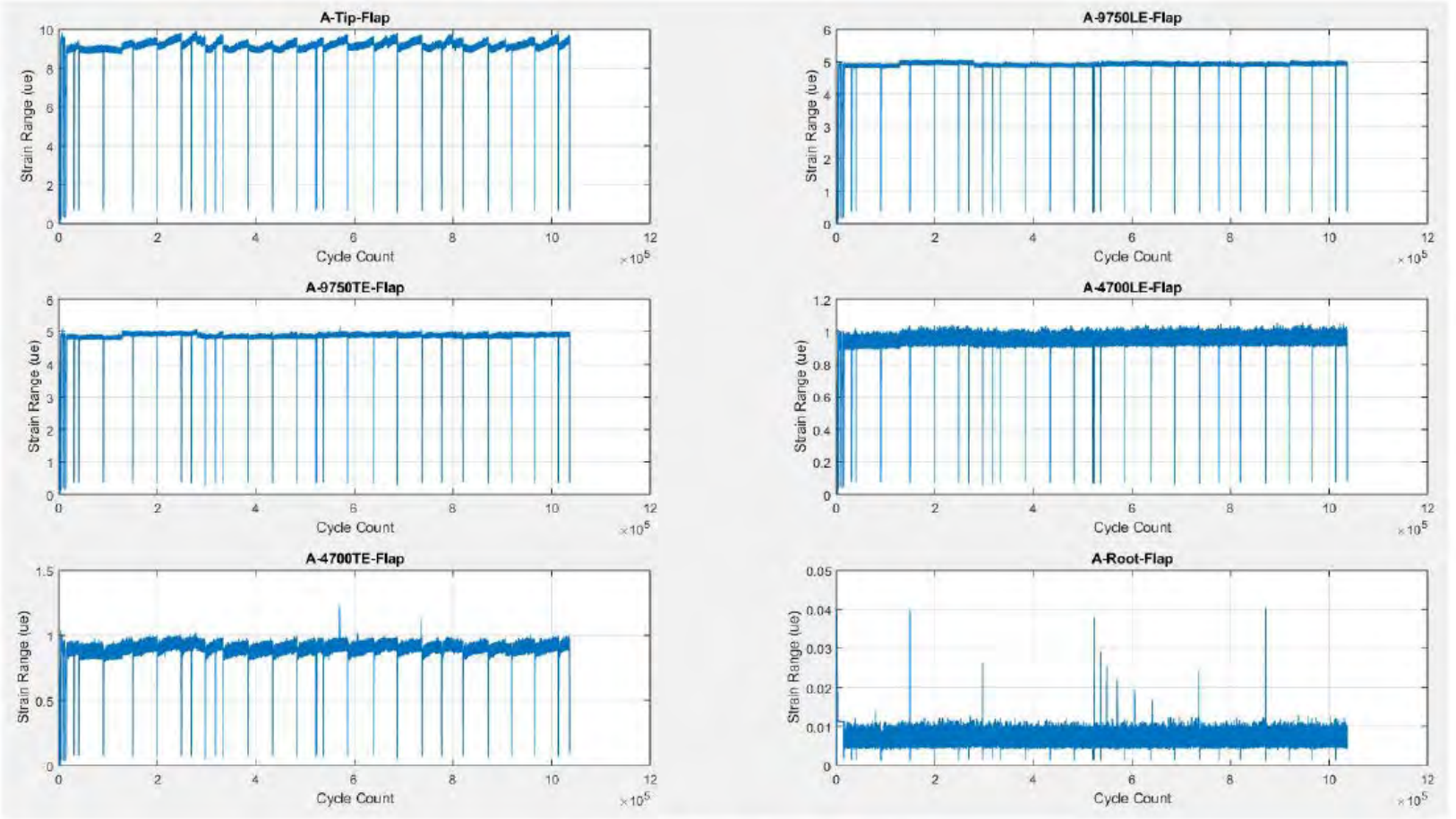

Figure G-5. Flap Accelerometers

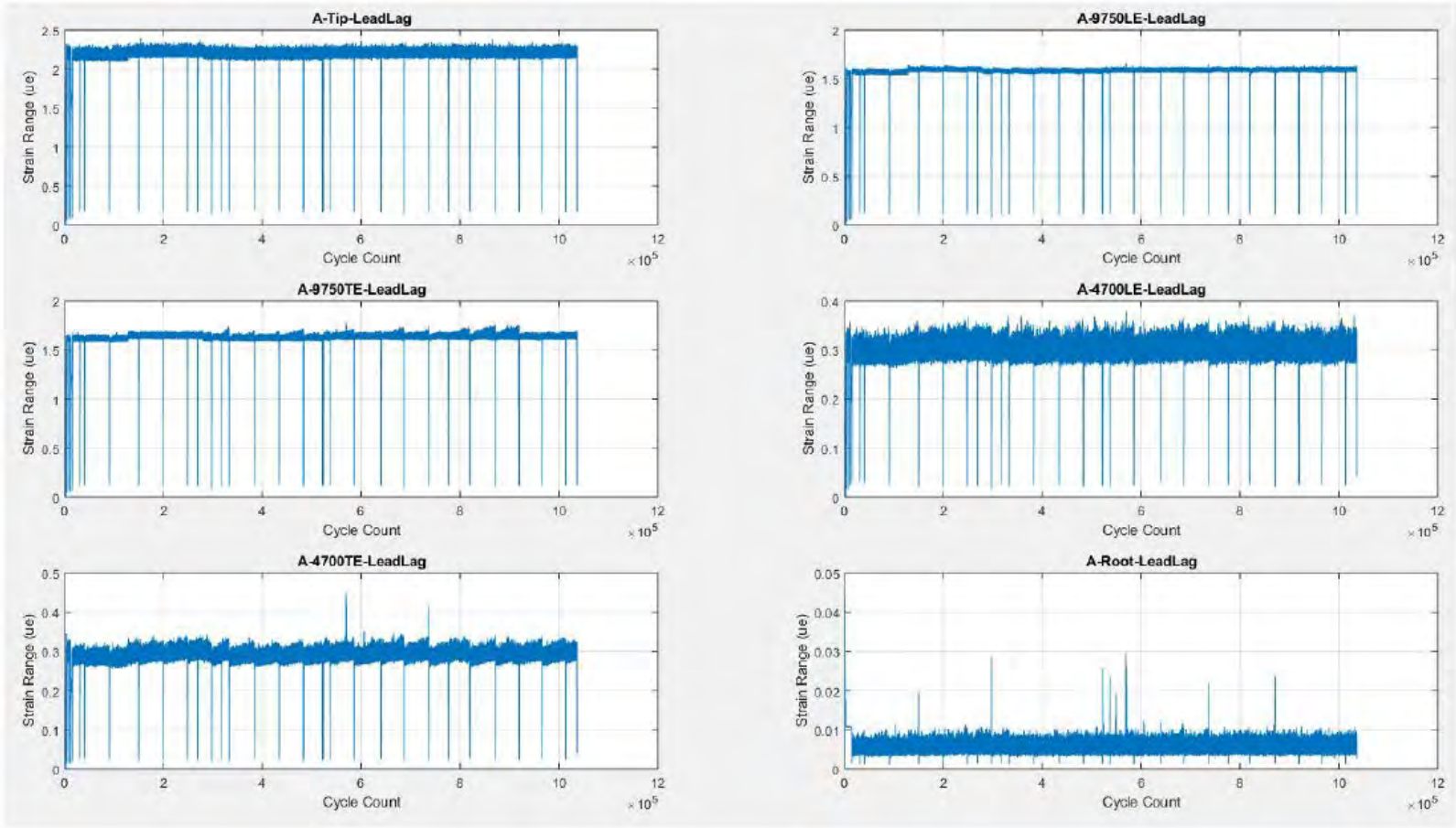

Figure G-6. Edge Accelerometers

Appendix H – Test Photographs

Figure H-1. Adapter Plate Mounting Configuration for Static Proof Load Tests

Figure H-2. Maximum Flap Test Setup

Figure H-3. Max Flap setup showing rigging line from spreader bar to overhead crane

Figure H-4. Minimum Flap Test Setup

Figure H-5. Minimum Flap Removal from Test Stand

Figure H-6. Maximum Edge setup

Figure H-7. Minimum Edge Setup

Figure H-8. Maximum Edge, Saddle to Spreader Bar Connection

Figure H-9. Flapwise Calibration Pull for Fatigue Test Setup

Figure H-10. Fatigue Test Setup. Single UREX on South, or Leading Edge side

18. APPENDIX G
Published Research on Thermoplastic Wind Blade Recycling

The following recycling research was published in the Journal of Cleaner Production in February 2019 (Volume 209, pages 1252-1263); it is reprinted here with permission from the publisher and authors. The numbering for tables, figures and references are exclusive to this Appendix and are not integrated into the main body and table of contents of this final report. A link to this published journal article is available here:

https://www.sciencedirect.com/science/article/pii/S0959652618333195

Recycling glass fiber thermoplastic composites from wind turbine blades

Dylan S. Cousins[a], Yasuhito Suzuki[b,1], Robynne E. Murray[c], Joseph R. Samaniuk[a], Aaron P. Stebner[b]

[a]Chemical and Biological Engineering, Colorado School of Mines, 1500 Illinois Street, Golden, CO 80401, USA
[b]Mechanical Engineering, Colorado School of Mines, 1500 Illinois Street, Golden, CO 80401, USA
[c]National Renewable Energy Laboratory, 15013 Denver West Parkway, Golden, CO 80401, USA

Abstract

Thermoplastic resin systems have long been discussed for use in large-scale composite parts but have yet to be exploited by the energy industry. The use of these resins versus their thermosetting counterparts can potentially introduce cost savings due to non-heated tooling, shorter manufacturing cycle times, and recovery of raw materials from the retired part. Because composite parts have high embedded energy, recovery of their constituent materials can provide substantial economic benefit. This study determines the feasibility of recycling composite wind turbine blade components that are fabricated with glass fiber reinforced Elium® thermoplastic resin. Several experiments are conducted to tabulate important material properties that are relevant to recycling, including thermal degradation, grinding, and dissolution of the polymer matrix to recover the constituent materials. Dissolution, which is a process unique to thermoplastic matrices, allows recovery of both the polymer matrix and full-length glass fibers, which maintain their stiffness (190 N/(mm g)) and strength (160 N/g) through the recovery process. Injection molded regrind material is stiffer (12 GPa compared to 10 GPa) and stronger (150 MPa compared to 84 MPa) than virgin material that had shorter fibers. An economic analysis of the technical data shows that recycling thermoplastic–glass fiber composites via dissolution into their constituent parts is commercially feasible under certain conditions. This analysis concludes that 50% of the glass fiber must be recovered and resold for a price of $0.28/kg. Additionally, 90% of the resin must be recovered and resold at a price of $2.50/kg.

[1] Present address: Department of Applied Chemistry, Graduate School of Engineering, Osaka Prefecture University, 1-1 Gakuen-cho, Naka-ku, Sakai, Osaka, 599-8531, Japan

Keywords
thermoplastic, recycling, composite, wind turbine blade, dissolution

Introduction

Fiber-reinforced polymer composites are a desirable class of structural engineering materials due to their high specific mechanical properties. They are increasingly used in the construction, automotive, aerospace, and energy sectors (Mazumdar et al., 2017). Electricity generated from wind turbines has grown consistently by approximately 7.3 GW of installed capacity every year for the last decade in the United States (American Wind Energy Association, 2017). Wind turbine blades are constructed with fiber reinforced polymer and balsa or foam core; landfilling turbine blades contributes a massive amount of composite material to the waste stream. One study estimates 9.6 metric tons of composite per megawatt of installed capacity (Arias, 2016). Such waste of highly engineered material represents not only an environmental issue, but also a loss of potentially recoverable capital. Thermoplastic resins, which are inherently recyclable (Jacob, 2011), are potentially a better design choice due to increasing regulation of composite waste landfilling. The European Union Directive on Landfill Waste has enacted legislation that prohibits disposal of large composite parts such as wind turbine blades (1999/31/EC). It is prudent to anticipate the potential for similar legislation in the United States; therefore, it is a primary objective of the Institute of Advanced Composites Manufacturing Innovation to qualify composite technologies of which 80% of the constituent materials can be reused or recycled (IACMI, 2018).

Thermosetting resins such as epoxy, vinyl ester, and poly(urethane) dominate the composites market; the wind industry exclusively uses these resins for vacuum infusion of blades. However, there is an increasing trend toward using thermoplastic resins in long fiber composites outside of the wind industry and a growing interest for using these resins for blade fabrication (Yao et al., 2018). Presently, there are several options for wind turbine blades at the end of their service lives: direct deposit in a landfill, grind for use as aggregate in concrete, or incineration with energy recovery (Correia et al., 2011; Fox, 2016; Larsen, 2009; Papadakis et al., 2010; Ribeiro et al., 2015). Additionally, a recent study has shown that thermoset blades can be recycled via grinding to be used for construction materials (Mamanpush et al., 2018). That these recycling techniques are not commercially exploited on a large scale demonstrates the small margins on which they operate. Thermoplastics can potentially limit the extent of down-cycling that thermoset composites require. Still, the viability of composite recycling is heavily dependent upon reintroduction of recovered materials into the supply chain to displace virgin materials (Li et al., 2016; Witik et al., 2013).

The current investigation quantifies and demonstrates the methods by which the Elium thermoplastic resin system (Arkema, 2018) can facilitate recycling of large-scale composite parts by recovering and reusing material from a component of a wind turbine blade. A portion of a spar cap, which acts as the end of the I-beam structure in the interior of the blade, was used for this study. Four recycling techniques are considered, including thermal decomposition of the polymer matrix, mechanical grinding, thermoforming, and dissolution. The decomposition energy of a commercial epoxy and Elium are compared via simultaneous thermal analysis (STA), which combines thermogravimetric analysis (TGA) and differential scanning calorimetry (DSC). The tensile properties of recycled thermoplastic regrind are compared to those of similar virgin material. Thermoforming is demonstrated on a thermoplastic spar cap, and test panels are thermoformed to make a prototypical skateboard. Energy requirements for dissolution of thermoplastic components and separation into their constituent materials are estimated. Further, the tensile mechanical properties of glass fibers recovered from the dissolution experiment are compared to those of virgin glass fibers. Dissolution of thermosets is not possible, and therefore only the thermoplastic system is investigated using this recycling technique. Finally, the technical results from the investigation of the dissolution technique are used in an economic analysis to assess the commercial viability of

recycling.

Review of relevant recycling methods

Thermal degradation

Pyrolysis allows recovery of fiber from either thermoset or thermoplastic polymer composites. Previous studies thoroughly characterize pyrolysis of composite materials but primarily investigate thermoset composites with carbon fiber reinforcement (López et al., 2012, 2013; Oliveux et al., 2015; Rybicka et al., 2016). Pyrolysis can be detrimental to the mechanical performance of the recovered glass fibers because the process is typically carried out at temperatures above 450 °C (Oliveux et al., 2015). It has been shown that composites fabricated with glass fiber recovered from pyrolysis suffer severe degradation of mechanical properties compared to composites fabricated with virgin materials (Cunliffe and Williams, 2003). An advantage of pyrolysis is that the oil recovered from the process can potentially be used to sustain the reaction so that no outside energy is required (Torres et al., 2000). Additionally, poly(methyl methacrylate) (PMMA) can be pyrolyzed under conditions such that monomer can be recovered (Kaminsky and Franck, 1991).

Polymer composites can be combusted on an industrial scale to supply energy for cement kilns, and the recovered fibers can be used in the cement (Pickering, 2006). In either the case of pyrolysis or combustion, the polymer matrix is lost at the expense of recovering pyrolysis oil or energy. This is of concern because of the high embedded energy of synthetic polymers, which is 50 MJ/kg for poly(vinyl chloride), 70 MJ/kg for poly(ester) and epoxy, and 200 MJ/kg for PMMA (Howarth et al., 2014; Keoleian et al., 2000; Song et al., 2009). Some of this energy can be recovered in combustion; the heat of combustion of PMMA is 25 MJ/kg (Walters et al., 2000). Similarly, pyrolysis oils typically have a lower heating value (LHV) of 15 to 20 MJ/kg (Bridgwater, 2012; Oasmaa and Czernik, 1999). In the present work, pyrolysis of thermoplastic Elium and thermoset epoxy resins is conducted to estimate the energy required for thermal degradation. This energy requirement is used as a reference for comparison to other recycling techniques in the ensuing presentation of results.

Mechanical grinding

Grinding of composites has been extensively investigated and is considered a mature technology for recovery of raw materials (Howarth et al., 2014; Kouparitsas et al., 2002; Li et al., 2016; Shuaib and Mativenga, 2016a, 2016b). For thermoset composites, the primary objective is to isolate the fibers from the polymer by cyclone or another resin-fiber separation technique since the reclaimed thermoset matrix is of little use. Isolated fibers could be further ground for production of thermal and acoustic insulating foams (D'Amore et al., 2017). While it is possible to compound thermoset regrind into a virgin thermoplastic for injection molding, thermoplastic regrind is desirable because less virgin material is required for effective injection molding (Kouparitsas et al., 2002; Pickering, 2006; Zia et al., 2007). Another use for regrind is sheet molded compound (SMC) or bulk mold compound (BMC), which rely on discontinuous fibers as their reinforcement (Palmer et al., 2010). Recovering and reusing composite manufacturing waste is also of great interest; thermoplastic scrap material could potentially be used for BMC or SMC mats (Rybicka et al., 2015). While it is a relatively simple and mature technology, a significant disadvantage of grinding composite parts is the loss of high–aspect ratio fibers that can contribute to greater modulus, strength, and toughness (Fu and Lauke, 1996; Petersen and Liu, 2016). In fact, the economic feasibility of reusing ground carbon fibers is reduced after two rounds of recycling due to fiber length degradation (Longana et al., 2016). However, to preserve fiber length and therefore mechanical properties, composites may also be chipped rather than fully ground. The present study grinds long-fiber composites to short fiber regrind and uses this material for injection molding tensile test bars. The estimated energy requirements for this process are presented and compared to the other recycling techniques investigated in this study.

Recent work has shown that the efficiency of mechanical grinding increases with throughput; the specific energy requirements decay as a power law (Howarth et al., 2014; Shuaib and Mativenga, 2016a, 2016b) up to a throughput of 150 $kg_{composite}$/h. Therefore, at a throughput of 150 $kg_{composite}$/h, the specific energy consumption (SEC) required for grinding is 0.16 MJ/$kg_{composite}$, assuming a screen size of 5 mm. This value is consistent with values reported by another recent grinding study (Asmatulu et al., 2013). Because the material in the present study is further ground to pass through a 7 standard mesh screen with 2.8 mm holes, the SEC for grinding will be higher than 0.16 MJ/$kg_{composite}$. In fact, screen size is the most significant processing parameter affecting SEC for grinding (Shuaib and Mativenga, 2016a). Accordingly, the estimated energy required for grinding is assumed to be nearly double the value of that correlation, or 0.29 MJ/ $kg_{composite}$, since the screen size used in the present study is 44% smaller than that used in the study by Shuaib and Mativenga (Shuaib and Mativenga, 2016a).

Thermoforming

Continuous fiber-reinforced thermoplastics became commonplace in the mid-1980s, and the thermoforming process is now considered mature (Offringa, 1996). In this process, thermoplastic composite sheets are heated above the glass transition of the polymer so that the material can be formed to a three-dimensional shape in a heated mold. Upon cooling, the composite retains this shape. While thermoforming granulated thermoplastic material has been well documented, recycling of large continuous-fiber thermoplastics by thermoforming has garnered little attention in the literature. Large-scale thermoplastic parts such as wind turbine blades could be cut into sections, straightened by heated pressing, and then planed into segments that are suitable for construction materials, such as building flooring. The feasibility of this straightening technique is demonstrated on a section of a spar cap in this work. Additionally, thermoplastic test panels are fully down-cycled into a skateboard by thermoforming.

Solvolysis and dissolution

Processing via solvolysis or dissolution enables recovery of full-length fibers from the composite part (Pimenta and Pinho, 2011). Confusion exists in some studies as to what constitutes dissolution versus solvolysis (Liu et al., 2017; Yang et al., 2012). In these works, the term dissolution is used to describe a reaction that breaks the chemical bonds of a polymer matrix. In this work, dissolution is more appropriately defined as dissolving thermoplastic polymer chains into a solvent, which is a purely physical process. The term solvolysis implies a technique to use a reactive solvent to break the covalent bonds of a polymer matrix. Solvolysis typically requires elevated temperatures and pressures, which could incur significant energy expenditures on an industrial scale (Bai et al., 2010; Liu et al., 2012; Piñero-Hernanz et al., 2008). Furthermore, these elevated temperatures can compromise the mechanical properties of the recovered fibers (Cunliffe and Williams, 2003). However, a recent study shows promise of a low-energy process via cleavable thermoset resin (La Rosa et al., 2016). Thermoplastic materials enable the possibility of recovering both the polymer matrix and full-length fibers at the end of the blade life by dissolution of the polymer matrix at low temperatures. This recycling technique is makes thermoplastic resins highly advantageous; it is an especially intriguing aspect of this class of materials (Yang et al., 2012). While recycling different chemical species of comingled thermoplastic polymers by dissolution has been studied for several decades (Nauman and Lynch, 1989; Subramanian, 1995), relatively little work has investigated dissolution of thermoplastic composite parts (Knappich et al., 2017; Ramakrishna et al., 1998). Feasibility of reselling materials recovered via dissolution is investigated in this work via an economic model.

Methods

Materials

Part A Elium liquid thermoplastic resin, which is a resin in the family of methacrylates, and Luperox AFR40, a peroxide initiator, were used to fabricate the spar cap component used for this study. The Elium resin is a viscous liquid that is suitable for infusion, after which it cures into a solid thermoplastic

polymer. All fiberglass used for the work conducted in this study was Johns Manville StarRov 086-1200. The epoxy system for thermal decomposition comparison was Hexion Epikote Resin MGS RIMR 135 with Epikure Curing Agent MGS RIMH blend of 134/137 (1366) at a ratio of 80:20. Chloroform for the dissolution study was ACS grade from Fisher Scientific. Methanol for precipitation was ACS grade from Pharmco-AAPER.

Fabrication of spar cap component

A section of a spar cap was fabricated at the National Wind Technology Center (NWTC) in Boulder, Colorado, using the Elium resin system in a VARTM infusion process. The peroxide initiator was added to the Elium liquid thermoplastic resin at 2 wt% and manually mixed for 5 min. The resin was degassed under vacuum for an additional 5 min prior to infusion. The layup of the spar cap was 50 plies of StarRov 086-1200 fiberglass. Figure 1 shows the part under the vacuum bag prior to infusion, and Figure 2 shows the part after de-molding. The part took approximately 20 min to infuse. Fifteen thermocouples embedded in the part detected peak exotherm temperatures between 77 °C and 90 °C approximately 2.5 h after infusion.

Fabrication and thermoforming of thermoplastic test panels

Thermoplastic composite panels with glass fiber reinforcement were used to demonstrate the viability of recycling via thermoforming. The flash material from the edge of the panels was also used for simultaneous thermal analysis of the two different resin systems. The panels were fabricated in a mold from Composite Integration (Cornwall, UK). Both thermoplastic Elium and thermoset Hexion epoxy panels were fabricated with four plies of Johns Manville 086-1200 fiberglass. Elium was initiated with 3 parts per hundred resin (PPHR) Luperox AFR 40. Hexion epoxy panels were made by mixing RIMR 135 resin with RIMH 1366 hardener at a ratio of 100:30. In both cases, the reactive resin was pulled into the mold cavity with 50 kPa vacuum below atmospheric pressure. Once the mold had filled, the vacuum line was clamped and 200 kPa pressure was provided by compressed argon to the feed side. Panels cured overnight before being removed from the mold. Mold cavity was set to produce panels with a thickness of 3.2 mm.

To demonstrate the plausibility of thermoforming, a 2.1 kg curved section of the thermoplastic spar cap was straightened by heating the specimen at 120 °C for 8 h under metal plates, which provided 5.4 kPa of pressure. Furthermore, a thin thermoplastic composite panel was used as reinforcement for constructing a thermoformed skateboard deck. To make the finished skateboard deck, the thermoplastic panel was sectioned into strips 25 cm wide and positioned with 4 plies of poly(vinyl acetate) (PVA) monomer-coated wood on a skateboard mold. This composite stack was then transferred to a radio-frequency press that used dielectric heating to cure the PVA resin. This heat was also sufficient to allow the thermoplastic panel to be molded to the shape of the skateboard.

Simultaneous thermal analysis

Simultaneous thermal analysis (STA) uses differential scanning calorimetry (DSC) and thermogravimetric analysis (TGA) to probe decomposition kinetics. Approximately 10 mg samples were cut from Thermoplastic Elium and Hexion epoxy test panel flash material. The instrument used was a Labsys Evo TGA-DSC 1600C. The total enthalpy required for decomposition can be elucidated from this experiment. The heating protocol under nitrogen was as follows: heat from ambient temperature to 90 °C at 10 °C/min, hold at 90 °C for 30 min for controller stabilization, then heat to 800 °C at 10 °C/min. The gas was then switched to dry air (79% N_2, 21% O_2) to combust any residual material.

Mechanical testing of injection molded samples

A section of the same spar cap fabricated at the NWTC was used for a study of the feasibility of using regrind material for injection molded parts. A Foremost A2 granulator was used to grind the spar cap

component. To grind the component down, it had to be cut into strips and then pre-cracked using a hammer and chisel to not jam the grinder. Figure 3 shows the strips before being fed into the grinder (left) and the subsequent ground material (right). The composite was ground using a 3.5 standard mesh screen and then re-fed into the grinder with a 7 standard mesh screen to obtain a size suitable for injection molding.

The material was then injection molded into ASTM type IV dog bones using a Morgan-Press G-55T injection molding machine with a barrel temperature of 245 °C (ASTM D 638, 1941). The ground material initially contained a fiber content that was too high to be effectively injection molded; therefore, a weight equivalent of the polymer precipitated from the dissolution experiment was added to the ground material. This mixture was still too viscous to be effectively molded, so an additional weight equivalent of Altuglas V920 PMMA was added to the mixture. This addition of preformed polymer allowed the material to be effectively injection molded into dog bones for tensile testing, as depicted in Figure 4. Tensile testing of the dog bones fabricated from the ground material was conducted on an MTS 370.10 uniaxial servohydraulic load frame according to ASTM D 638. After tensile testing, the fiber volume fraction of the specimens was determined by dissolution to be 0.128 ± 0.005 (mass fraction of 0.221 ± 0.007). For comparison to other recycling techniques, the energy required for injection molding is estimated to be 19 MJ/kg (Song et al., 2009).

Dissolution of spar cap component

A specimen was cut from the spar cap component using a diamond blade tile saw. The initial weight of the piece used for the dissolution experiment was 0.924 kg. The component was placed in a glass pan, immersed in chloroform, covered with aluminum foil, and allowed to soak for 48 h. After 48 h, the outer plies of fiberglass were able to be removed and rinsed (about 10 plies on either side), while most of the 50 inner plies were still adhered and were unable to be pulled apart by hand. Therefore, the polymer-laden chloroform was removed from the pan and fresh chloroform was added to increase the chemical potential for dissolution of the polymer matrix from the composite to the solvent. After 24 h of further dissolution, the rest of the plies of the composite part were able to be separated. Prior to drying, the plies were further rinsed in fresh chloroform to remove any residual polymer. As such, the chloroform used for rinsing had only a dilute concentration of polymer.

After dissolution, the polymer was precipitated from the chloroform into methanol. The polymer was dried on a foil sheet for 24 h and then under vacuum (78 kPa below atmospheric pressure) at 60 °C for an additional 12 h. Figure 5 shows the polymer and glass fiber plies that were separated from the original composite part. The mass recovery of the fibers and polymer totaled 91% of the initial mass of the composite part. The mass loss is attributed to incomplete precipitation and manual removal of the polymer from the beaker. As such, it is assumed that the mass loss was completely polymer. In total, 4 L (5.96 kg) of chloroform was used to dissolve and rinse the polymer from the material. Of this, 2.44 kg (41 wt%) was used in primary dissolution while 3.52 kg (59 wt%) was used for rinsing. Additionally, 8 L of methanol was needed for precipitation of the polymer out of solution.

Tensile testing of recovered glass fiber rovings

Tensile properties of the recycled fibers from the dissolution experiment were determined by preparing rovings from the plies of recovered glass fiber with tabs using Loctite 401 and G10 epoxy tabbing material. Tabs were applied to virgin fibers from a roll of Johns Manville StarRov 086 in the same manner. Figure 6 shows the seven specimens of each sample type prior to testing. All of the rovings were cut to the same length of 107 ± 1 mm and weighed. The gauge length on all samples was 31.5 ± 0.5 mm. The mass of the roving was used for normalization of the mechanical properties because the cross-sectional area of the rovings could not be accurately measured. This is unusual for tensile testing because properties are typically normalized by the cross-sectional area. The force at break was normalized by the

mass of the fibers as $\sigma_{max} = P_{max}/m$ where σ_{max} (N/g) is the mass-normalized force, P_{max} (N) is the maximum load borne by the specimen during the test, and m (g) is the mass of the roving in the gauge region. The stiffness of the specimens was compared by calculating the mass-normalized load-displacement curve as $\delta = d/m$ where δ (N/(mm g)) is the mass-normalized slope of the load-displacement curve, d (N/mm) is the slope of the load-displacement curve, and m is again the mass of the specimen in the gauge region. Tensile testing was conducted on an MTS 370.10 uniaxial servohydraulic load frame at a crosshead rate of 0.5 mm/min.

Thermogravimetric analysis of recovered fibers

Thermogravimetric analysis (TGA) was conducted on fibers recovered from the dissolution experiment to quantify the amount of polymer remaining on the fibers after dissolution. Specimens of about 20 mg were heated under nitrogen from ambient temperature to 850 °C at a heating rate of 10 °C/min. At 800 °C, air was introduced as the flow gas to combust any residual material in the cell.

Results and Discussion

Simultaneous thermal analysis

Typical plots of the heat flow as a function of temperature for both the Elium and epoxy systems are presented in Figure 7 with their corresponding mass loss profiles and derivatives. Elium shows a clear endothermic peak where heat is flowing into the sample as the material pyrolyzes around 350 °C to 400 °C. The epoxy sample shows a peak that yields a slight exotherm over the mass loss region; therefore, less heat is needed from the instrument to pyrolyze the material. Of particular interest is the heat required to decompose the material. To determine this, the heating due to the heat capacity of the material is not subtracted as it would be to obtain the heat of pyrolysis. In the case of the Elium system, this coincided with zero mass, but in the case of the epoxy system, around 10 wt% mass remained, which is a typical char content for epoxy resins (Liu et al., 1997; Rwei et al., 2003). The total heat of decomposition is calculated by integrating the heat flow from ambient temperature to the point that the mass loss profile derivative became zero (Hirschler, 1986; Beyler and Hirschler, 2016). This gives the total heat needed to decompose the material, which can then be normalized by the mass of the specimen. The total heat required to decompose the Elium sample is 1,080 J/g, while for the Hexion epoxy it is 243 J/g. That is, the epoxy requires 78% less energy for thermal decomposition.

The mass loss profile for epoxy displays char left in the epoxy system after the primary decomposition. About 10% of the mass remains, even to 800 °C. The char is then combusted when air is introduced into the system. From a practical standpoint, this char may hinder recovery of fiberglass from epoxy matrix composites; the thermoplastic resin system may be advantageous for large-scale parts that are meant to be pyrolyzed.

Thermal decomposition of Elium resin is found to require 1.1 $MJ/kg_{polymer}$ in this study. However, the heat capacity of the glass must be taken into account if the polymer matrix in the composite part is going to decompose, leaving only the glass. To heat the glass from 25 °C to 800 °C requires 0.81 MJ/kg_{glass} (NIST Webbook, 2018a). Therefore, on a mass basis for decomposition of a composite with 30 wt% resin and 70 wt% glass, the energy required is 1.0 $MJ/kg_{composite}$. This is similar to the values for various types of biomass, which range from 0.8 to 1.6 MJ/kg (Daugaard and Brown, 2003).

Injection molded samples: tensile properties

The results of the tensile tests are presented in Figure 8 with comparisons to virgin Altuglas V920 PMMA and also Altuglas V920 PMMA blended with StarStran glass fiber (Type 718) from Johns Manville fabricated in a previous study (Cousins et al., 2017). The values presented in Figure 8 for the composite parts are normalized to a fiber volume fraction (FVF) of 0.22 as

$$E_{norm} = \frac{0.22E_{exp}}{\phi} \quad (1)$$

where E_{norm} is the normalized property (modulus or ultimate tensile strength), E_{exp} is the experimentally determined property, and ϕ is the FVF in the part (U.S. Department of Defense, 2000). The FVF from the recycled dog bones was determined by dissolution of the polymer matrix, whereas the value for the virgin material was determined by TGA in the previous study to be 0.22. The recycled dog bones have an average mass fraction of 0.221 ± 0.007 that corresponds to an average volume fraction of 0.112 ± 0.005.

When compared to the other fiber-reinforced plastic, the FVF normalized modulus of the recycled material is 12.1 GPa, which is 21% higher than that of the virgin Altuglas V920 reinforced with short glass fiber (StarStran 718 from Johns Manville). The FVF normalized ultimate tensile strength of the recycled material is 150 MPa, which is 79% higher than that of the virgin Altuglas V920 reinforced with short glass fiber. The higher FVF values of the recycled dog bones compared to those of the short fiber virgin material dog bones is most likely due to the fact that the fibers in the recycled specimens were longer (200 to 2,500 μm) compared to the fibers of the compounded specimens from the previous study (50 to 500 μm) as determined by optical microscopy. A melt compounded system has more homogeneous morphology, and stress is more evenly carried throughout the part; however, the shorter fiber length yields lower tensile properties.

Thermoforming thermoplastic spar cap and test panels

Figure 9 shows a curved section of the thermoplastic spar cap that has been straightened by thermoforming. This component is now easier to plane into thinner sheets that can be used for construction. If these thick parts are planed into thinner sheets, discontinuous fibers will be made because it is impossible to cut precisely between fiber bundles. Therefore, non-critical applications for which these recycled materials could be employed include flooring, building siding, or recreational goods. Figure 10 shows a prototypical skateboard deck constructed using thermoplastic test panels, which demonstrates the plausibility of using thin thermoplastic composite sheets for construction.

Dissolution of spar cap component

The separation of the composite into its constituent parts is one of the primary features that makes thermoplastic matrices for composites attractive. Chloroform and methanol are not inexpensive solvents, and need to be recycled for this process to be cost-effective. For this reason it is of interest to estimate the energy requirements needed to distill these two solvents. The chloroform-methanol system has a minimum boiling azeotrope at a composition of 67 mol% chloroform. This means that the composition cannot be distilled to a higher purity at this pressure. Because the azeotrope exists at different compositions at different pressures, however, pressure swing distillation may be used to effectively separate these two solvents.

Aspen Plus was used to simulate this distillation to estimate the energy requirements needed for separation. The process flow diagram is shown in Figure 11. In the pressure swing distillation simulation, the mixture was distilled in two different columns: one at 1 atm and the other at 10 atm. The simulation used an input feed stream of 50 wt% chloroform/50 wt% methanol, which is close to the ratio used in the dissolution experiment. The UNIQUAC activity coefficient model was chosen as the phase equilibria equation of state because it accurately predicts thermophysical properties of polar/nonpolar mixtures (Wankat, 2012). The boiler duty for the columns and the electricity for the pump total 1.43 $MJ/kg_{solvent}$. This value is consistent with the heat-integrated pressure swing distillation energy requirments found by another study of 1.62 $MJ/kg_{solvent}$, although the feed composition of that study was 3.7:1 chloroform:methanol by mass (Hosgor et al., 2014). Based on the ratio of the solvent to the estimated amount of polymer in the initial composite part from the dissolution experiment, the energy requirement for distillation is 87 $MJ/kg_{polymer}$.

Another method for separation of the polymer matrix from chloroform is to evaporate and then recondense the solvent. The recovered chloroform can then be reused for dissolution. An additional simulation was conducted in Aspen Plus to determine the primary energy requirements for this process. For this simulation, PMMA was chosen as a surrogate for the acrylic-based Elium since these materials are in the same chemical family. While chloroform is the solvent used in this study, acetone is also a good solvent for PMMA; it is cheaper, more environmentally benign, and less hazardous to human health (Alder et al., 2016). Therefore, two sub-studies were carried out: (1) separate a stream of 19:1 chloroform:PMMA by mass and (2) separate a stream 19:1 acetone:PMMA by mass. The 19:1 ratio is roughly the proportion of chloroform used to dissolve the Elium in this study. The temperature of the evaporator (Flash2 separator in Aspen Plus) was set to 200 °C. At this temperature, the equilibrium amount of PMMA left in the chloroform was 5 wt% and in the acetone, 2.3%. The evaporation simulation calculated that the energy required to conduct this separation was 6.6 $MJ/kg_{polymer}$ for the chloroform solution and 15.3 $MJ/kg_{polymer}$ for the acetone solution. Calculating the energy requirement from the enthalpy of vaporization yields 5.0 $MJ/kg_{polymer}$ for chloroform and 10.2 $MJ/kg_{polymer}$ for acetone; so the results seem plausible based on thermophysical material properties (NIST Webbook 2018b, 2018c).

After sufficient evaporation, diffusional limitations will prevent transport of the solvent out of the polymer. Past this point, devolatilization extrusion is needed to further dry the polymer. Therefore, the energy required for this process must also be accounted for in the economic analysis. Specific energy consumption to run the motor of an extruder varies between 0.3 and 2.6 MJ/kg and depends on screw speed and design (Abeykoon et al., 2014). For the purpose of the analysis here, it is assumed that the extruder would require 2.6 MJ/kg.

Tensile properties of recovered fiberglass rovings

The physical properties determined from tensile testing rely on normalizing the force applied to the specimen by the linear density of the fibers rather than the cross-sectional area. The slope of the load-displacement curve is determined between displacement values of 0.1 and 0.3 mm by least-squares linear regression. Figure 12 depicts the tensile properties of the recovered fiber rovings compared to those of the virgin StarRov 086 rovings that are described by the equations given in 2.6.1 for mass-normalized force and mass-normalized load-displacement slope. The mass-normalized force at break is within the combined inter-quartile range of both sample types. The recycled fibers showed a 12% reduction in mass-normalized load-displacement slope. The slight loss of stiffness may be due to several factors. Foremost is that during the dissolution and recovery process, the fibers were pulled apart from the composite by hand, during which misalignment or slight degradation may have occurred. The misalignment will manifest itself in lower stiffness, but once the fibers are pulled into alignment during the test, the final force at break will be governed by the strength of the glass itself. Since the glass fibers were not heated during recovery, their properties remain uncompromised. It should be noted that the properties of fibers recovered from in-service composite parts will be diminished, but the recovery process itself does not incur any additional damage that compromises mechanical properties.

Thermogravimetric analysis of recovered fibers from dissolution

TGA was conducted to elucidate the efficacy of dissolution of the polymer matrix from the glass fibers. This technique allows determination of the amount of polymer left on the glass fibers. TGA showed a 1.9 wt% mass loss from the total initial weight of the recovered fibers. Virgin StarRov 086-1200 has a sizing content of 0.6 wt%. Here, it is assumed that none of the sizing was dissolved because it is covalently bonded to the glass fibers. However, the sizing mass was lost during the TGA heating because the covalent bonds were broken during pyrolysis. Accordingly, the mass fraction of polymer left on the fibers is estimated to be 1.3 wt% of the total recovered fiber weight. Of the original 924 g composite part, it is estimated that 9 g of polymer is left on the recovered fibers. This represents 4 wt% of the original 204 g

of polymer matrix.

Economic analysis and recycling facility model

To investigate the feasibility of thermoplastic Elium resin for large-scale composite production, it is important to consider the economic impact of recycling the composite materials. Therefore, an economic analysis was conducted that models the cost of operating a recycling facility. Table 1 shows the primary energy requirements from the various recycling processes investigated in this work. The primary energy consumption for grinding is determined from previous studies (Shuaib and Mativenga, 2016a, 2016b). The primary energy consumption values for all other processes are determined in this work. Note that the figures for dissolution have been corrected to a mass-of-composite basis. Although grinding and thermal decomposition have lower energy requirements, the investigation here focuses on dissolution coupled with evaporation of the solvent, which has not been significantly analyzed to date. It is assumed that the evaporative technique is used to separate the polymer and solvent after dissolution because it is much less energy-intensive than the solvent distillation process.

Table 1.Primary energy costs for various recycling methods for acrylic-based composites.

Recycling process	Primary Energy Consumption ($MJ/kg_{composite}$)
Grinding	0.29
Thermal decomposition	1.0
Dissolution/distillation/extrusion	20.0
Dissolution/evaporation/extrusion	4.0

Elium is an acrylic-based polymer, so for approximation, it is important to consider the energy required to manufacture PMMA—the most common thermoplastic acrylic polymer. PMMA is very energy-intensive to produce, with a primary production energy cost of 207.3 MJ/kg (Keoleian et al., 2000). In the same study, only aluminum was found to require more production energy (207.8 MJ/kg). Another study reports a primary energy required for manufacturing PMMA of 116 MJ/kg (Boustead, 2005). The energy intensity of its production causes PMMA to be a costly commodity polymer with a price of about $2.50/kg. The energy costs associated with PMMA production represent a valuable market opportunity for recycled materials. In this way, not only could turbine owners recuperate some of the capital costs of blade production, but the embedded energy of other acrylic products could be reduced by using recycled material.

Table 2 shows the parameters of an economic analysis conducted using the proposed model. This analysis assumes a 61.5 m blade length with a mass of 21,106 kg/blade. The primary equipment for the recycling facility are a vessel for dissolution and evaporation, condensers for solvent recapture, and a devolatilization extruder for removing residual solvent from the polymer after evaporation. This equipment capital cost is estimated at $3,000,000. This figure accounts for an extruder and post-processing equipment, which are estimated at $1,000,000, and the dissolution vessel with associated condensers, which is estimated at $500,000. A contingency factor of 2 is then applied to cover tubing, pumps, and other minor equipment. Landfill, labor, electricity, and building costs were assumed to be the same as those for a wind turbine blade manufacturing facility estimated in a recent study (Murray et al., 2018). It is assumed that the recycling facility can charge 60% of the landfill cost of the blade to the decommissioning service.

A recovery rate of 90 wt% of the resin was chosen based on only 4 wt% of the polymer left adhered to the fibers from the dissolution experiment; most of the resin lost during the dissolution experiment was due to incomplete precipitation into methanol. Since this separation technique can be replaced by evaporation, it is assumed that polymer loss can be reduced to a value of no more than 10% loss (90% recovery).

Recovery of glass fiber will be more complicated due to structural considerations of sandwich-type layup structures and large-scale cutting. Therefore, the recovery of fiberglass is estimated to be 50 wt%. The landfill cost is applied to unrecovered material. The maximum resale price for the recovered polymer is set to the market price of PMMA at $2.50/kg. The maximum resale price of the recovered fiberglass is set to the upper range of chopped E-glass fiber at $4.00/kg.

Given this set of assumptions, the price knockdown (a fractional reduction from the maximum resale price) is varied from 0% to 100% for each material to generate the plot shown in Figure 13. The bold contour represents the breakeven point for recycling a wind turbine blade. What this line suggests is that in the best-case scenario of full resale value of the polymer, the recovered fiberglass in the wind turbine blade needs to be sold at 7% of the price for chopped E-glass fiber, corresponding to $0.28/kg. The labor requirement is also shown to greatly affect the viability of recycling and, in fact, represents the most sensitive variable to the ultimate cost of running the facility at a value of $960/FTE/blade.

The feasibility of recycling wind turbine blades based on a dissolution technique is also contingent on the quality of the materials recovered. If the materials have a large knockdown for resale, then the facility will not be feasible. It is plausible that the polymer recovered from the dissolution process could be sold with minimal knockdown because the polymer would not have been significantly degraded from a single extrusion process. However, retaining or creating value in the recovered glass fiber would be significantly more challenging. A potential application for these fibers is feedstock into polymer compounding machines. The state of the art for fiber compounding is to pull continuous fiber off of spools into the compounder in order to maintain maximum fiber length in the final product (Hawley and Jones, 2005). Rovings recovered from the recycled blades could be used in this manner, though they would likely need to be manually fed into a compounder.

It is important to consider the implications that this recycling technique could have on carbon fiber composites. Carbon fiber is a few times more expensive than glass fiber with prices ranging from 11 to 25 $/kg (Baker and Rials, 2013). Carbon fiber reinforced thermoplastics can incur significant economic benefit to the supply chain since carbon fiber is 3 to 6 times more expensive. The review of Oliveux *et al*. documents 46 studies conducted examining solvolysis and most of these are directed toward carbon fiber recovery (Oliveux et al., 2015). However, *none* of these studies exploit room-temperature dissolution of thermoplastic composites, as is presented here. Dissolution is simpler and can be carried out at much lower temperatures than solvolysis, thereby facilitating economical material recovery.

Table 2.Thermoplastic blade recycling facility inputs and cost summary.

Recycling costs		
Process or input value	Quantity	Units
Dissolution energy requirements	15.3	MJ/kg of resin
Devolatilization energy requirement	2.6	MJ/kg of resin
Resin mass in blade	5,322	kg/blade
Cost of energy	0.079	$/kWh
Total cost for dissolution & processing	**2,123**	**$/blade**

Cost of operating facility		
Process or input value	Quantity	Units
Equipment capital cost	3,000,000	$
Equipment installation cost	10	% of capital cost
Equipment maintenance costs	10	% of capital cost over lifetime of

		equipment
Equipment life (number of cycles)	2,000	cycles (or blades)
Average downtime	10	%
Building floor space	1,500	m^2
Building cost	1,200,000	$
Non-process electricity	228,690	kWh
General laborers	10	FTE
Unskilled direct wages	20	$/h
Runtime for one blade (cycle time)	48	h
Total cost to operate facility	**11,767**	**$/blade**

Material resale value

Process or input value	Quantity	Units
Market price of PMMA	2.5	$/kg
Percent resin recovered	90	%
Market price of fiberglass	4	$/kg
Fiberglass per blade	12,077	kg/blade
Percent recovered fiberglass	50	%

Conclusions

Table 3 lists the advantages and disadvantages of the recycling techniques investigated in this study. Pyrolysis experiments show that relatively little energy is required to decompose the polymer matrix from composites when compared to other recovery techniques; however, the loss of the high-embedded-energy polymer is a disadvantage of this recovery option. This work tabulates the properties of short-fiber-reinforced dog bone specimens fabricated from regrind material obtained from a prototypical thermoplastic wind turbine blade spar cap. While mechanical grinding and pyrolysis are mature recycling methods, the thermoplastic resin has the potential advantage over its common thermoset counterparts because the resin can be recovered from a dissolution process. Glass fiber rovings recovered from a composite part separated by dissolution are shown to have equal tensile strength and only 12% reduced stiffness compared to rovings from virgin samples of the same material. This retention of mechanical properties demonstrates advantage over the pyrolysis process where the mechanical properties of glass fiber are diminished. A section of the prototypical thermoplastic spar cap was straightened by thermoforming. This unique property of thermoplastic composites would allow wind turbine blades to be down-cycled into other products such as skateboards, as is presented here.

Table 3.Advantages and disadvantages for potential thermoplastic composite recycling methods.

Recycling process	Advantage	Disadvantage
Grinding	• Simple • mature technology	• Fiber length reduction
Pyrolysis	• Fiber length maintenance • mature technology	• Fiber mechanical property degradation • Lose polymer matrix
Dissolution/ distillation/extrusion	• Fiber length & mechanical property maintenance • Recover polymer matrix	• Expensive to separate solvents • Volatile solvent required

Dissolution/ evaporation/ extrusion	• Fiber length & mechanical property maintenance • Recover polymer matrix	• Volatile solvent required

An economic analysis indicates that recovery of constituent materials from a thermoplastic composite part can be economically feasible when they can displace virgin materials in the supply chain. This feasibility is contingent on reducing labor costs, obtaining a minimal knockdown on the polymer, and maximizing the glass fiber resale. The economic feasibility of this process will increase by 3 to 6 times for carbon fiber composites.

Acknowledgements

The authors gratefully acknowledge financial support from the State of Colorado Office of Economic Development and International Trade Advanced Industries Program (program manager Katie Woslager) and Colorado Higher Education Competitive Research Authority (CHECRA) through their commitment to the Institute for Advanced Composites Manufacturing and Innovation (IACMI) Wind Energy program. This material is based upon work supported by the U.S. Department of Energy's Office of Energy Efficiency and Renewable Energy (EERE) under the support of the Task 4.2 of Institute for Advanced Composites Manufacturing Innovation (IACMI), Award Number DE-EE006926 managed by John Winkel from DOE and John Unser from IACMI. Academic and National Laboratory partners for this project are: Derek Berry and David Snowberg (National Renewable Energy Lab), Aaron Stebner (Colorado School of Mines), Nathan Sharpe (Purdue), Dayakar Penumadu (University of Tennessee), Douglas Adams (Vanderbilt). Industrial consortium was led by Dana Swan (Arkema), Mingfu Zhang (Johns Manville), and Stephen Nolet (TPI Composites). The views and opinions of authors expressed in this paper or referenced documents do not necessarily state or reflect those of the United States Government or the identified collaborating partners. Authors also acknowledge that important insight and ideas were obtained from academic and industrial collaborators during the project activities who are not being formally acknowledged in this manuscript as co-authors. Materials supplied and manufacturing methods developed by the industrial collaborators are gratefully acknowledged. The authors would also like to thank Aaron Frary of Liqwood Board Sports for help fabricating the prototypical skateboard.

References

Abeykoon, C., Kelly, A.L., Brown, E.C., Vera-Sorroche, J., Coates, P.D., Harkin-Jones, E., Howell, K.B., Deng, J., Li, K., Price, M., 2014. Investigation of the process energy demand in polymer extrusion: A brief review and an experimental study. Appl. Energy 136, 726-737.

Alder, C.M., Hayler, J.D., Henderson, R.K., Redman, A.M., Shukla, L., Shuster, L.E., Sneddon, H.F., 2016. Updating and further expanding GSK's solvent sustainability guide. Green Chem. 18(13), 3879-3890.

Arias, F., 2016. Assessment of Present/Future Decommissioned Wind Blade Fiber-Reinforced Composite Material in the United States. City College of New York, New York, NY.

Arkema, Inc., 2018. Elium® resins for composites. https://www.arkema.com/en/products/product-finder/range-viewer/Elium-resins-for-composites/

Asmatulu, E., Twomey, J., Overcash, M., 2013. Recycling of fiber-reinforced composites and direct structural composite recycling concept. J. Compos. Mater. 48(5), 593-608.

American Wind Energy Association, 2017. U.S. Wind Industry Third Quarter 2017 Market Report.

ASTM D 638, 1941. Standard Test Method for Tensile Properties of Plastics. ASTM International, West Conshohocken, PA.

Bai, Y., Wang, Z., Feng, L., 2010. Chemical recycling of carbon fibers reinforced epoxy resin composites in oxygen in supercritical water. Mater. & Design 31(2), 999-1002.

Beyler, C.L., Hirschler, M.M., 2016. Thermal Decomposition of Polymers, SFPE Handbook of Fire Protection Engineering. Springer.

Boustead, I., 2005. Eco-profiles of the European Plastics Industry: Polymethyl Methacrylate (PMMA). Plastics Europe. Association of Plastics Manufacturers.
Bridgwater, A.V., 2012. Review of fast pyrolysis of biomass and product upgrading. Biomass Bioenergy 38, 68-94.
Correia, J.R., Almeida, N.M., Figueira, J.R., 2011. Recycling of FRP composites: reusing fine GFRP waste in concrete mixtures. J. Clean. Prod. 19(15), 1745-1753.
Cousins, D.S., Lowe, C., Swan, D., Barsotti, R., Zhang, M., Gleich, K., Berry, D., Snowberg, D., Dorgan, J.R., 2017. Miscible blends of biobased poly(lactide) with poly(methyl methacrylate): Effects of chopped glass fiber incorporation. J. Appl. Polym. Sci. 134, 44868.
Cunliffe, A.M., Williams, P.T., 2003. Characterisation of products from the recycling of glass fibre reinforced polyester waste by pyrolysis. Fuel 82(18), 2223-2230.
D'Amore, G.K.O., Caniato, M., Travan, A., Turco, G., Marsich, L., Ferluga, A., Schmid, C. Innovative thermal and acoustic insulation foam from recycled waste glass powder. J. Clean. Prod. 165, 1306-1315.
Daugaard, D.E., Brown, R.C., 2003. Enthalpy for Pyrolysis for Several Types of Biomass. Energy Fuels 17(4), 934-939.
European Commission, 1999. Directive 1999/31/EC of the European Parliament and of the Council of 26 April 1999 on Landfill of Waste. Official Publications of the European Communities, Luxembourg.
Fox, T.R., 2016. Recycling wind turbine blade composite material as aggregate in concrete. Iowa State University. Ames, IA.
Fu, S.-Y., Lauke, B., 1996. Effects of fiber length and fiber orientation distributions on the tensile strength of short-fiber-reinforced polymers. Compos. Sci. Technol. 56(10), 1179-1190.
Hawley, R.C., Jones, R.F., 2005. In-line Compounding of Long-fiber Thermoplastics for Injection Molding. J. Thermoplast. Compos. Mater. 18(5), 459-464.
Hirschler, M.M., 1986. Thermal decomposition (STA and DSC) of PVC compounds under a variety of atmospheres and heating rates. Eur. Polym. J. 22(2), 153-160.
Hosgor, E., Kucuk, T., Oksal, I.N., Kaymak, D.B., 2014. Design and control of distillation processes for methanol–chloroform separation. Comput. Chem. Eng. 67(Supp. C), 166-177.
Howarth, J., Mareddy, S.S.R., Mativenga, P.T., 2014. Energy intensity and environmental analysis of mechanical recycling of carbon fibre composite. J. Clean. Prod. 81, 46-50.
IACMI, 2018. About IACMI. https://iacmi.org/about-us/
Jacob, A., 2011. Composites can be recycled. In: Reinforced Plastics. May/June 2011, 45-46. Elsevier Ltd.
Kaminsky, W., Franck, J., 1991. Monomer recovery by pyrolysis of poly(methyl methacrylate) (PMMA). J. Anal. Appl. Pyrolysis 19, 311-318.
Keoleian, G.A., Blanchard, S., Reppe, P., 2000. Life-Cycle Energy, Costs, and Strategies for Improving a Single-Family House. J. Indust. Eco. 4(2), 135-156.
Knappich, F., Hartl, F., Schlummer, M., Mäurer, A., 2017. Complete Recycling of Composite Material Comprising Polybutylene Terephthalate and Copper. Recycling 2(2), 9.
Kouparitsas, C.E., Kartalis, C.N., Varelidis, P.C., Tsenoglou, C.J., Papaspyrides, C.D., 2002. Recycling of the fibrous fraction of reinforced thermoset composites. Polym. Compos. 23(4), 682-689.
La Rosa, A.D., Banatao, D.R., Pastine, S.J., Latteri, A., Cicala, G., 2016. Recycling treatment of carbon fibre/epoxy composites: Materials recovery and characterization and environmental impacts through life cycle assessment. Compos. Part B: Eng. 104, 17-25.
Larsen, K., 2009. Recycling wind turbine blades. Renewable Energy Focus 9(7), 70-73.
Li, X., Bai, R., McKechnie, J., 2016. Environmental and financial performance of mechanical recycling of carbon fibre reinforced polymers and comparison with conventional disposal routes. J. Clean. Prod. 127, 451-460.
Liu, Y.-L., Hsiue, G.-H., Lee, R.-H., Chiu, Y.-S., 1997. Phosphorus-containing epoxy for flame retardant. III: Using phosphorylated diamines as curing agents. J. Appl. Polym. Sci. 63(7), 895-901.

Liu, Y., Liu, J., Jiang, Z., Tang, T., 2012. Chemical recycling of carbon fibre reinforced epoxy resin composites in subcritical water: Synergistic effect of phenol and KOH on the decomposition efficiency. Polym. Degrad. Stab. 97(3), 214-220.
Liu, Y., Farnsworth, M., Tiwari, A., 2017. A review of optimisation techniques used in the composite recycling area: State-of-the-art and steps towards a research agenda. J. Clean. Prod. 140, 1775-1781.
Longana, M.L., Ong, N., Yu, H., Potter, K.D., 2016. Multiple closed loop recycling of carbon fibre composites with the HiPerDiF (High Performance Discontinuous Fibre) method. Compos. Struct. 153, 271-277.
López, F.A., Martín, M.I., Alguacil, F.J., Rincón, J.M., Centeno, T.A., Romero, M., 2012. Thermolysis of fibreglass polyester composite and reutilisation of the glass fibre residue to obtain a glass–ceramic material. J. Anal. Appl. Pyrolysis 93, 104-112.
López, F.A., Rodríguez, O., Alguacil, F.J., García-Díaz, I., Centeno, T.A., García-Fierro, J.L., González, C., 2013. Recovery of carbon fibres by the thermolysis and gasification of waste prepreg. J. Anal. Appl. Pyrolysis 104, 675-683.
Mamanpush, S.H., Li, H., Englund, K., Tabatabaei, A.T., 2018. Recycled wind turbine blades as a feedstock for second generation composites. Waste Manage. (Oxford) 76, 708-714.
Mazumdar, S., Karthikeyan, D., Pichler, D., Benevento, M., Frassine, R., 2017. State of the Composites Industry Report for 2017, Composites Manufacturing Magazine.
Murray, R.E., Jenne, S., Berry, D., Cousins, D., Snowberg, D., 2018. Techno-Economic Analysis of a Megawatt-Scale Thermoplastic Resin Wind Turbine Blade. Accepted: Renewable Energy.
Nauman, E.B., Lynch, J.C., 1989. Polymer recycling by selective dissolution. U.S. Patent US5198471A. Rensselaer Polytechnic Institute United States of America.
NIST Webbook, 2018a. Quarts (SiO2) - Solid Phase Heat Capacity (Shomate Equation). U.S. Department of Commerce. http://webbook.nist.gov/cgi/cbook.cgi?ID=C14808607&Type=JANAFS&Table=on
NIST Webbook, 2018b. Acetone. U.S. Department of Commerce. https://webbook.nist.gov/cgi/cbook.cgi?ID=67-64-1
NIST Webbook, 2018c. U.S. Department of Commerce. Trichloromethane. U.S. Department of Commerce. https://webbook.nist.gov/cgi/cbook.cgi?ID=C67663&Mask=4#ref-5
Oasmaa, A., Czernik, S., 1999. Fuel Oil Quality of Biomass Pyrolysis OilsState of the Art for the End Users. Energy Fuels 13(4), 914-921.
Offringa, A.R., 1996. Thermoplastic composites—rapid processing applications. Compos. Part A: Appl. Sci. Manuf. 27(4), 329-336.
Oliveux, G., Dandy, L.O., Leeke, G.A., 2015. Current status of recycling of fibre reinforced polymers: Review of technologies, reuse and resulting properties. Prog. Mater Sci. 72, 61-99.
Palmer, J., Savage, L., Ghita, O.R., Evans, K.E., 2010. Sheet moulding compound (SMC) from carbon fibre recyclate. Compos. Part A: Appl. Sci. Manuf. 41(9), 1232-1237.
Papadakis, N., Ramírez, C., Reynolds, N., 2010. Chapter 16: Designing composite wind turbine blades for disposal, recycling or reuse. In: Management, Recycling and Reuse of Waste Composites. Woodhead Publishing, pp. 443-457.
Petersen, R.C., Liu, P.-R., 2016. Mechanical Properties Comparing Composite Fiber Length to Amalgam. J. Compos. 2016, 13.
Pickering, S.J., 2006. Recycling technologies for thermoset composite materials—current status. Compos. Part A: Appl. Sci. Manuf. 37(8), 1206-1215.
Pimenta, S., Pinho, S.T., 2011. Recycling carbon fibre reinforced polymers for structural applications: Technology review and market outlook. Waste Manage. (Oxford) 31(2), 378-392.
Piñero-Hernanz, R., Dodds, C., Hyde, J., García-Serna, J., Poliakoff, M., Lester, E., Cocero, M.J., Kingman, S., Pickering, S., Wong, K.H., 2008. Chemical recycling of carbon fibre reinforced composites in nearcritical and supercritical water. Compos. Part A: Appl. Sci. Manuf. 39(3), 454-461.
Ramakrishna, S., K. Tan, W., Teoh, H., Lai, O.M., 1998. Recycling of Carbon Fiber/Peek Composites. In:

Key Engineering Materials, Polymer Blends and Polymer Composites.
Ribeiro, M.C.S., Meira-Castro, A.C., Silva, F.G., Santos, J., Meixedo, J.P., Fiúza, A., Dinis, M.L., Alvim, M.R., 2015. Re-use assessment of thermoset composite wastes as aggregate and filler replacement for concrete-polymer composite materials: A case study regarding GFRP pultrusion wastes. Resources, Conservation and Recycling 104, 417-426.
Rwei, S.-P., Kao, S.-C., Liou, G.-S., Cheng, K.-C., Guo, W., 2003. Curing and pyrolysis of epoxy resins containing 2-(6-oxido-6H-dibenz(c,e)(1,2)oxaphosphorin-6-yl)-1,4-naphthalenediol or bisphenol S. Colloid. Polym. Sci. 281(5), 407-415.
Rybicka, J., Tiwari, A., Alvarez Del Campo, P., Howarth, J., 2015. Capturing composites manufacturing waste flows through process mapping. J. Clean. Prod. 91, 251-261.
Rybicka, J., Tiwari, A., Leeke, G.A., 2016. Technology readiness level assessment of composites recycling technologies. J. Clean. Prod. 112, 1001-1012.
Shuaib, N.A., Mativenga, P.T., 2016a. Effect of Process Parameters on Mechanical Recycling of Glass Fibre Thermoset Composites. Procedia CIRP 48, 134-139.
Shuaib, N.A., Mativenga, P.T., 2016b. Energy demand in mechanical recycling of glass fibre reinforced thermoset plastic composites. J. Clean. Prod. 120(Supp. C), 198-206.
Song, Y.S., Youn, J.R., Gutowski, T.G., 2009. Life cycle energy analysis of fiber-reinforced composites. Compos. Part A: Appl. Sci. Manuf. 40(8), 1257-1265.
Subramanian, P.M., 1995. Recovery of polyamide using a solution process. U.S. Patent US5430068A. Invista North America SARL.
Torres, A., de Marco, I., Caballero, B.M., Laresgoiti, M.F., Legarreta, J.A., Cabrero, M.A., González, A., Chomón, M.J., Gondra, K., 2000. Recycling by pyrolysis of thermoset composites: characteristics of the liquid and gaseous fuels obtained. Fuel 79(8), 897-902.
U.S. Department of Defense, 2000. The Composite Materials Handbook - MIL17 - Polymer Matrix Composites: Materials Properties. Technomic Publishing Co., Inc. & Materials Sciences Corporation.
Walters, R.N., Hackett, S.M., Lyon, R.E., 2000. Heats of combustion of high temperature polymers. Fire Mater. 24(5), 245-252.
Wankat, P.C., 2012. Separation Process Engineering. Prentice Hall.
Witik, R.A., Teuscher, R., Michaud, V., Ludwig, C., Månson, J.-A.E., 2013. Carbon fibre reinforced composite waste: An environmental assessment of recycling, energy recovery and landfilling. Compos. Part A: Appl. Sci. Manuf. 49, 89-99.
Yang, Y., Boom, R., Irion, B., van Heerden, D.-J., Kuiper, P., de Wit, H., 2012. Recycling of composite materials. Chem. Eng. Proc.: Proc. Intens. 51, 53-68.
Yao, S.-S., Jin, F.-L., Rhee, K.Y., Hui, D., Park, S.-J., 2018. Recent advances in carbon-fiber-reinforced thermoplastic composites: A review. Composites Part B: Engineering 142, 241-250.
Zia, K.M., Bhatti, H.N., Ahmad Bhatti, I., 2007. Methods for polyurethane and polyurethane composites, recycling and recovery: A review. React. Funct. Polym. 67(8), 675-692.

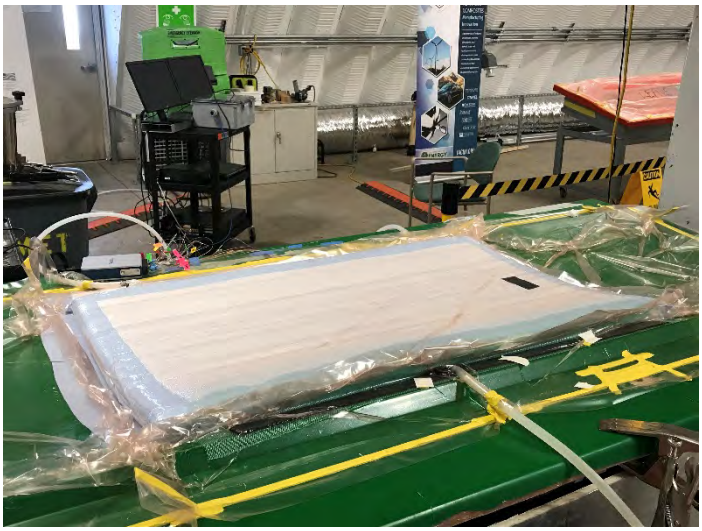

Figure 1. Elium® spar cap component fabricated at the National Wind Technology Center.

Figure 2. Elium® spar cap component after de-molding.

Figure 3. Strips of spar cap component (left) and subsequent ground composite material passed through a 3.5 standard mesh screen (foil pan) and a 7 standard mesh screen (round bucket).

Figure 4. Dog bones fabricated for tensile testing of the regrind material.

Figure 5. Thermoplastic Elium® composite (top) can be separated into fibers (left) and the polymer resin (right) by dissolution. This separation and recovery is not possible with thermoset composites.

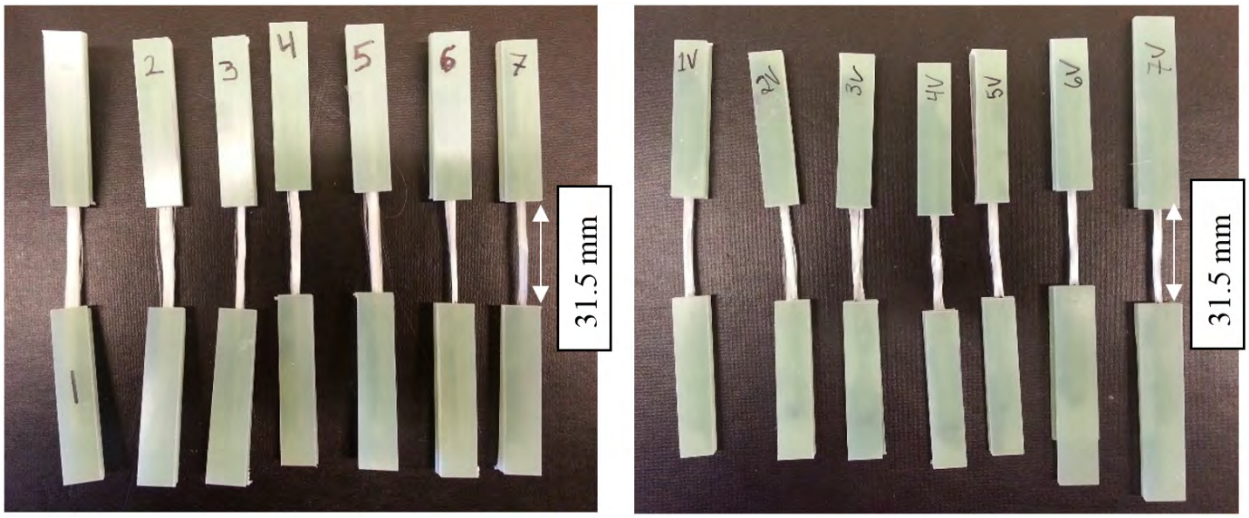

Figure 6. Fiber roving specimens for tensile testing from the dissolution experiment (left) and from a roll of virgin Johns Manville StarRov 086 (right).

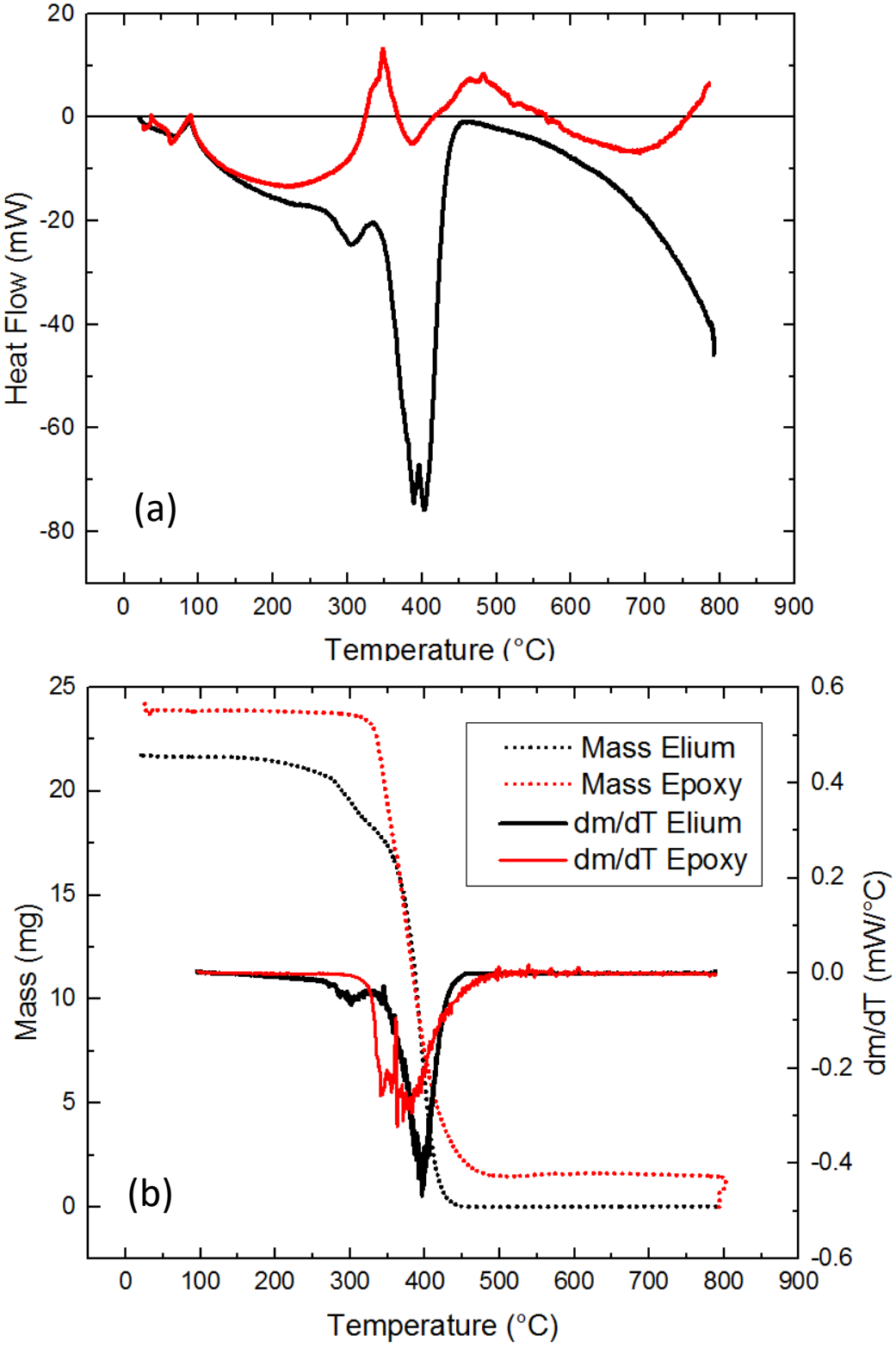

Figure 7. Measurements from simultaneous thermal analysis (combined DSC and TGA). (a) Heat flow as a function of temperature for Elium® (black) and epoxy (red). (b) Mass loss profiles and mass loss derivative of Elium® (black) and epoxy (red) as a function of temperature.

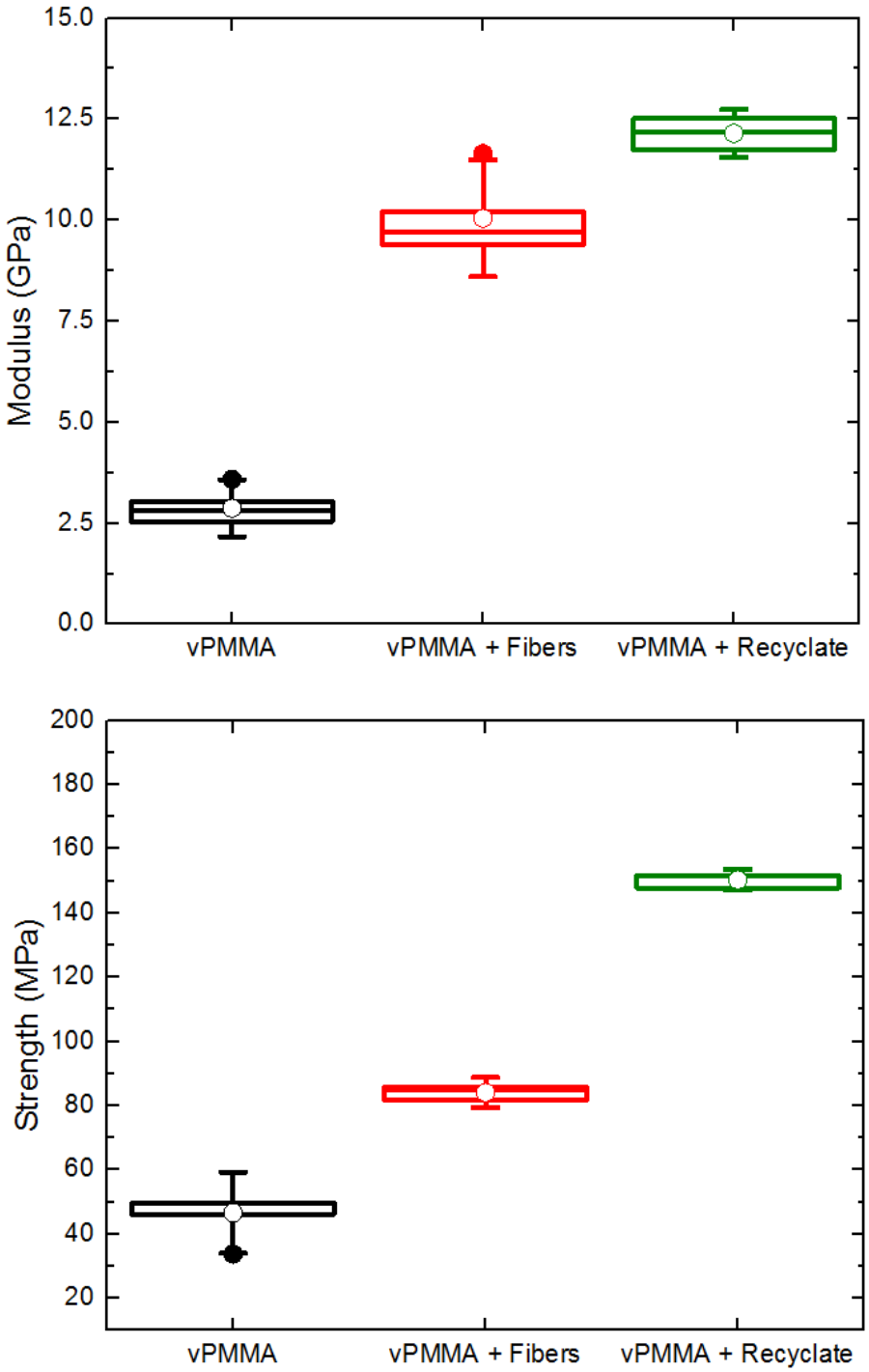

Figure 8. Tensile modulus (top) and tensile strength (bottom) of PMMA blended with recyclate (vPMMA + Recyclate) compared to virgin PMMA (vPMMA) and virgin PMMA plus chopped fibers (vPMMA + Fibers). Error bars represent standard deviations. All values have been normalized to a fiber volume fraction of 0.22 according to Eq. (1). The center point (○) represents the mean, the center line the median, the box is the inter-quartile range, the whiskers are 1.5 times the standard deviation, and outliers are represented by closed circles (●).

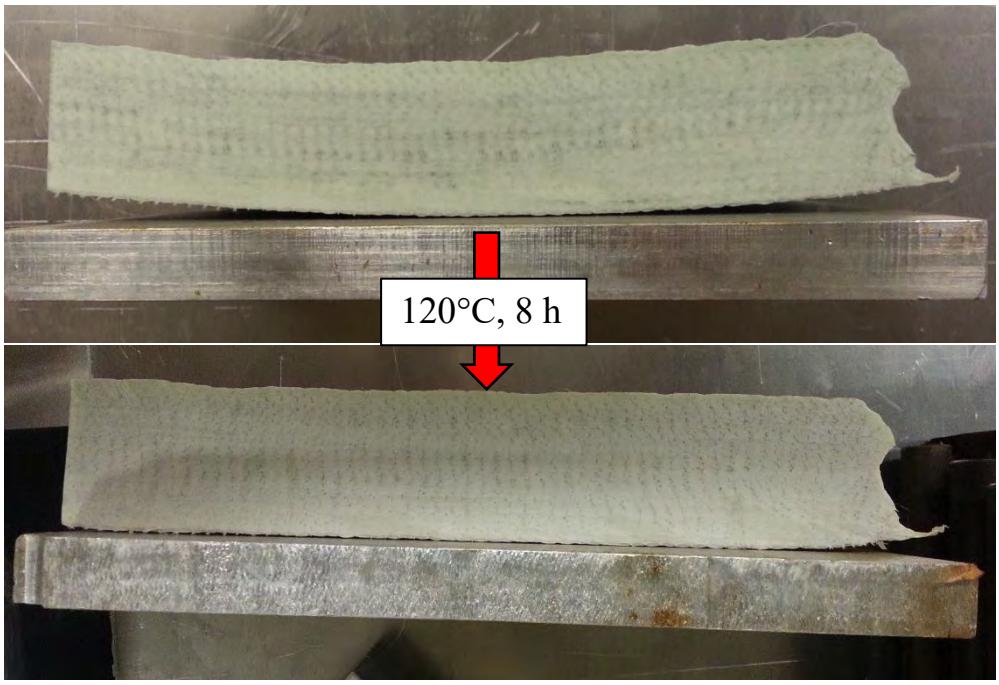

Figure 9. A section of the prototypical thermoplastic spar cap that has been thermoformed into a straight shape. In this way, the material can be planed into strips that have maximum fiber continuity.

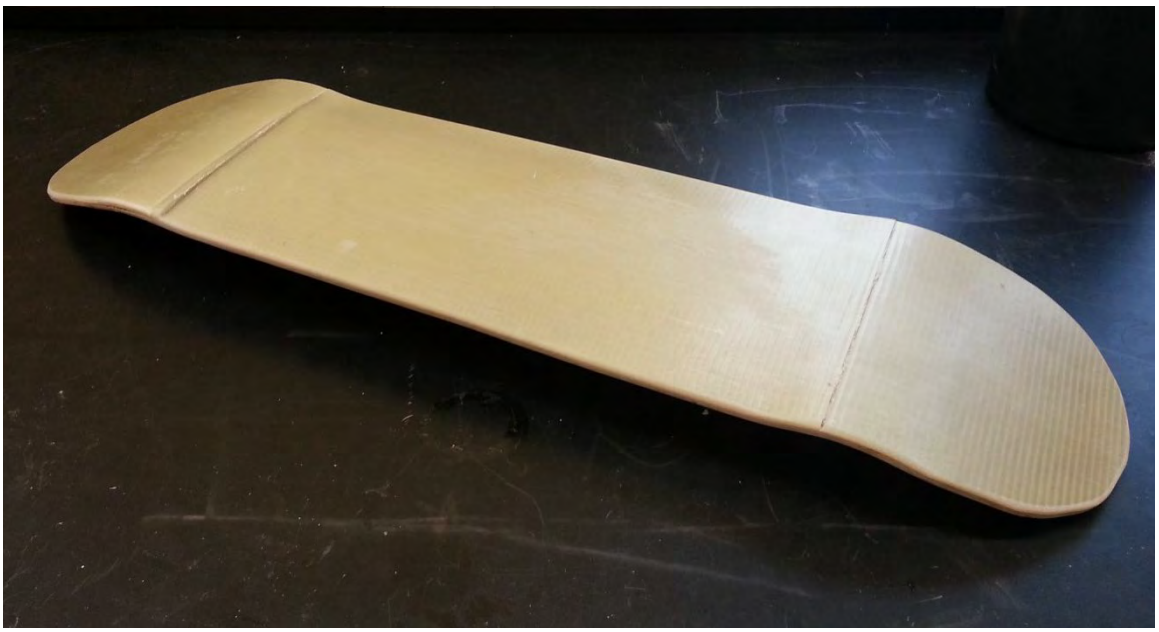

Figure 10. A prototypical skateboard fabricated in part by thermoforming an Elium/ glass fiber test panel as reinforcement.

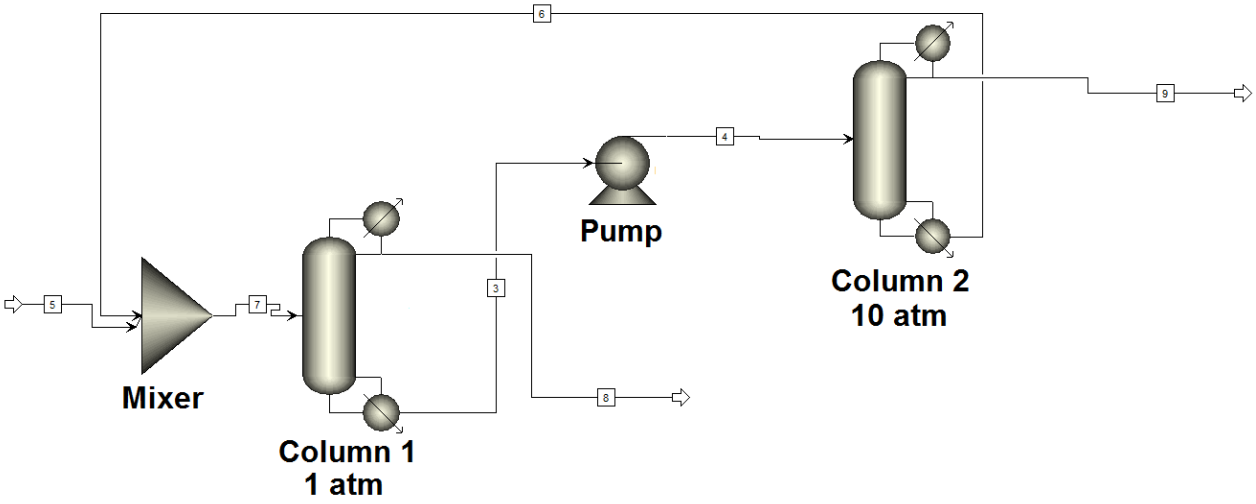

Figure 11. Process flow diagram for pressure swing distillation of a chloroform/methanol mixture.

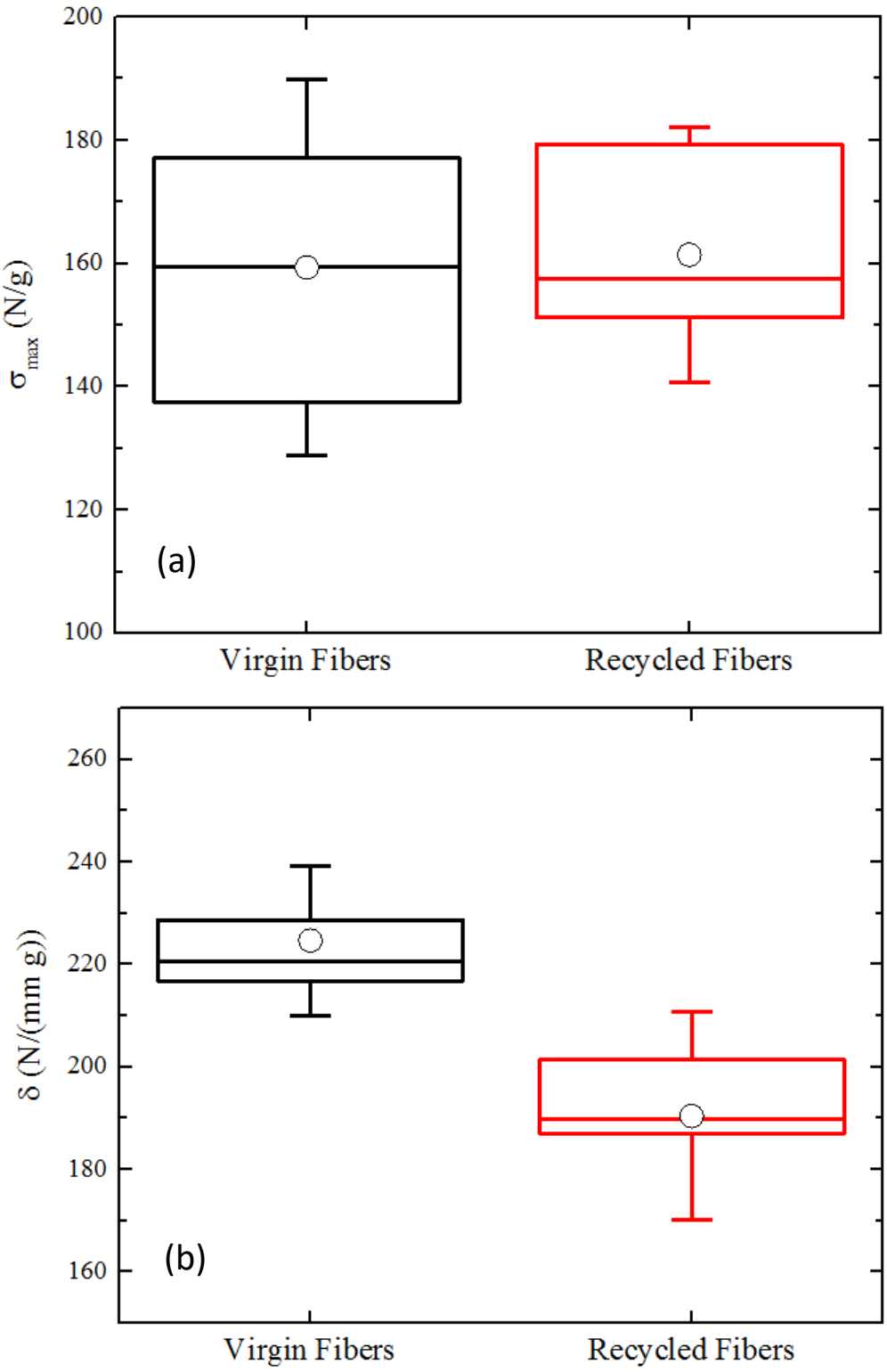

Figure 12. Mass normalized tensile properties of glass fiber rovings recovered from dissolution of the thermoplastic part compared to those of virgin JM 086 StarRov fibers. (a) Mass-normalized force at break, σ_{max}. (b) Mass-normalized slope of the load-displacement curve, δ. The center point (○) represents the mean, the center line the median, the box is the inter-quartile range, and the whiskers are 1.5 times the standard deviation.

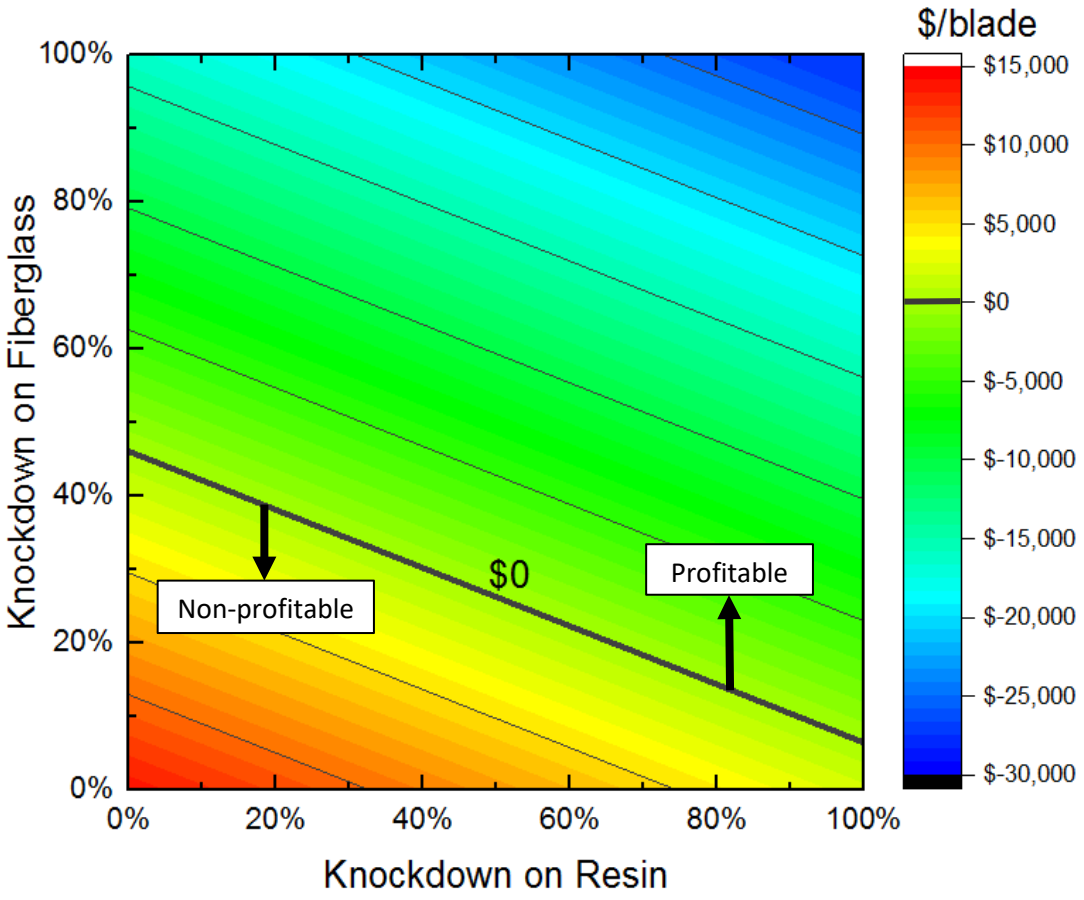

Figure 13. Cost per wind turbine blade for variation in the knockdown rate of fibers and resin given the figures in Table 2. The bold line ($0) represents the break-even point for the recycling operation.